Title
Primary and Secondary Three Dimensional Microbatteries

Author
Cirigliano, Nicolas

Publication Date
2013

Peer reviewed|Thesis/dissertation

UNIVERSITY OF CALIFORNIA
Los Angeles

Primary and Secondary Three Dimensional Microbatteries

A dissertation submitted in partial satisfaction of the

requirements for the degree Doctor of Philosophy

in Materials Science and Engineering

By

Nicolas Cirigliano

2012

ABSTRACT OF THE DISSERTATION

Primary and Secondary Three Dimensional Microbatteries

By

Nicolas Cirigliano

Doctor of Philosophy in Materials Science and Engineering

University of California, Los Angeles, 2012

Professor Bruce S. Dunn, Chair

Today's MEMS devices are limited more so by the batteries that supply their power than the fabrication methods used to build them. Thick battery electrodes are capable of providing adequate energy, but long and tortuous diffusion pathways lead to low power capabilities. On the other hand, thin film batteries can operate at significant current densities but require large surface areas to supply practical energy. This dilemma can be solved by either developing new high capacity materials or by engineering new battery designs that decouple power and energy.

Three dimensional batteries redesign traditional configurations to create nonplanar interfaces between battery components. This can be done by introducing hierarchical structures into the electrode shape. Designs such as these provide a maximum surface area over which chemical reactions can occur. Furthermore, by maintaining small feature sizes, ion diffusion and electronic transport distances can remain minimal. Manipulating these properties ensures fast

kinetics that are required for high power situations. Energy density is maximized by layering material in the vertical direction, thus ensuring a minimal footprint area.

Three dimensional carbon electrodes are fabricated using basic MEMS techniques. A silicon mold is anisotropically etched to produce channels of a predetermined diameter. The channels are then filled using an infiltration technique with electrode slurry. Once dried, the mold is attached to a current collector and etched using a XeF_2 process. Electrodes of varying feature sizes have been fabricated using this method with aspect ratios ranging from 3.5:1 to 7:1. 3D carbon electrodes are shown to obtain capacities over 8 mAh/cm^2 at 0.1 mA/cm^2, or nearly 700% higher than planar carbon electrodes. When assembled with a planar cathode, the battery cell produced an average discharge capacity of 40 J/cm^2 at a current density of 0.2 mA/cm^2. This places the energy density values slightly less than thick-film microbatteries but with power density values larger than thin-film batteries. A 3D zinc-air battery was also fabricated by electrodepositing zinc into a silicon mold. This battery obtained over 12 mAh/cm^2 and utilized 93% of the available material.

The dissertation of Nicolas Cirigliano is approved.

_____
Chang Jin Kim

_____
Jane Pei-Chen Chang

_____
Bruce Dunn, Committee Chair

University of California, Los Angeles
2012

To My Wife, Parents and Sisters

Table of Contents

LIST OF FIGURES

LIST OF TABLES

Acknowledgements

Wow, where do I even begin? Eleven (!) years is a long time. The number of people who have impacted my life throughout my tenure at UCLA is extensive, almost to the point of disbelief. I wish it was as simple as categorizing family, friends and colleagues, but the lines that divide each is faded beyond the point of distinction. I suppose I'll try my best though.

I'll begin with Professor Bruce Dunn, who I can describe as so much more than a "principle investigator". From my involvement with various groups across multiple departments, I can comfortably state that Dr. Dunn is the best advisor a graduate student can possibly have. His experience and expertise encompasses more topics than should be possible, yet he seems to handle it all with ease and, may I be so bold as to say, swagger. More importantly, he is eager to impart his knowledge with the informality necessary for a lowly graduate student to understand yet not feel like a nuisance for asking. Between granting me the freedom to perform my own experiments to allowing me to take a dive into the Killmotor Hill money bin, you have spoiled me as an employee, Dr. Dunn. The experience acquired under his tutelage is priceless, and I am truly honored to have been a part of his plans.

Next come the DunnLab Dunnians (?). An individual's performance is only as good as his supportive cast. Dr. Jimmy Lim comes first for taking me under his wing while I was a wandering undergraduate unsure of his future. Your advice and direction was far more than I expected when signing up for that SRP. And then there's Vegas. "In love, out of luck." I honestly haven't won at a craps table since I met Michelle. Peter Malati and Veronica Augustyn are next on my list. To this day I'm still not sure how we became the core of the electrochemistry

group, but we did it, against all odds it seemed at times. The brainstorming sessions we had helped me learn so much more about the dark arts than any text book could. I only hope the younger students didn't pay attention when we were completely wrong. We'll always have the Westwood Circuit to remember. The rest of the members, both past and present: Wade Richardson ("Over the line!"), Jason Kim (soccer), Daniel Membreno (post resistivity), Joy Trujillo (diamond saw), Leland Smith (MLBtv), Danielle Casillas (SEM), Jesse Ko (your orientation), Jimmy Kim (soccer), Dr. Emilie Perre (French 3D batteries!), Dr. Enrico Della Gaspera (Italian who doesn't like soccer or wine), Dr. Jonathon Fang (resident badminton expert), Dr. Grant Umeda (top secret rock star), Dr. John Wang (stocks), Dr. Derek Min (3D zinc air) and Dr. Tim Yeh (3D lithium ion). Every one of you has given me an extremely meaningful and memorable experience at UCLA.

To Brian, Matt, Steven, Luke, Anthony, Bert, Kip, Charles, McCarthy, Evan, Mike, Pat and Terry who I endearingly call the craziest people I've ever met: now that we got those years out of our system, I'm excited to see what the future has for us. It's scary to think that we are tomorrow's lawyers, doctors, engineers and businessmen. Never once did I feel I had to impress any one of you. It's hard to find guy friends who are more than simply "drinking buddies", and I am lucky to have found so many. I leave with a quote that sums us up: "Some of us are leaving, and that is sad, but this isn't the end. No way. We're gonna show this world a thing of two. We're gonna show…"

My family has been always been a constant source of encouragement and support. My parents are a tough act to follow having already set the bar so high. Discussing the future with

them that night in Montreux made me realize the amount of hard work that is necessary to be successful. To my beautiful wife, who stuck by my side the entirety of graduate school. I know it wasn't the easiest of times, but this experience taught us about ourselves and brought us so much closer as a couple. Your patience, love, insight and silliness have kept me going through the good and the bad. Jill and Nat, you always know what to say, even when I don't know I need to hear it. I couldn't ask for better sisters.

Finally I'd like to thank the MSE department staff for all of the behind-the-scenes work. A special thanks goes out to DARPA for financially supporting this work.

Vita

February 1, 1984	Born, San Mateo, California
2007	B.S. Materials Science and Engineering University of California, Los Angeles Los Angeles, CA
2007-2013	Graduate Student Researcher Department of Materials Science and Engineering University of California, Los Angeles
2010	M.S. Materials Science and Engineering University of California, Los Angeles Los Angeles, CA

Publications and Presentations

Y. Perng, J. Cho,D. Membreno, N. Cirigliano, B. Dunn, F. Toney, J. Chang, "Engineering LiAlSiO4 thin films as a three dimensional battery electrolyte." *In preparation*

T. Arthur, D. Bates, N. Cirigliano, D. Johnson, P Malati, J. Mosby, E. Perre, M. Rawls, A. Prieto, B. Dunn, "Three dimensional electrodes and battery architectures." *MRS Bulletin*, 36, 2011

J. Lim, N. Cirigliano, J. Wang, B. Dunn, "Direct electron transfer in nanostructured sol-gel electrodes containing bilirubin oxidase." *Physical Chemistry Chemical Physics*, 2007, 9, 1809

N. Cirigliano, E. Perre, P. Malati, J. Fang, G. Sun, C.J. Kim, B. Dunn, "Modeling and Characterization of 3D Battery Electrode Arrays" *Materials Research Society Fall Meeting 2011*, oral presentation, Boston, MA, December, 2011

N. Cirigliano, P. Malati, J. Hur, S. Tolbert, C.J. Kim, B. Dunn, "Three dimensional architectures for the miniaturization of batteries and their constraints." *Materials Research Society Spring Meeting 2009*, poster session, San Francisco, CA, April, 2009

N. Cirigliano, P. Malati, J. Hur, S. Tolbert, C.J. Kim, B. Dunn, "Three dimensional architectures for the miniaturization of batteries and their constraints." *UCLA Tech Forum*, **Awarded Runner -up for Best Poster Presentation**, Los Angeles, CA, March 2009

N. Cirigliano, P. Malati, J. Hur, S. Tolbert, C.J. Kim, B. Dunn, "Three dimensional architectures for the miniaturization of batteries and their constraints." *CNSI-JAIST Workshop*, poster session, Los Angeles, CA January 2009

Y.-C. Perng, J. Cho, D. Membreno, N. Cirigliano, B. Dunn and J. P. Chang, "Engineering LixAlySizO Ion Conducting Thin Films by Atomic Layer Deposition for Lithium-ion Battery Applications," *AVS 58th International Symposium & Exhibition*, oral presentation, Nashville, TN, November, 2011

Y.-C. Perng, J. Cho, D. Membreno, N. Cirigliano, B. Dunn and J. P. Chang, presentation on "Engineering LixAlySizO Ion Conducting Thin Films by Atomic Layer Deposition for Lithium-ion Battery Applications," *2011 AIChE Annual Meeting*, oral presentation, Minneapolis, MN, October, 2011.

Y.-C. Perng, J. Cho, D. Membreno, N. Cirigliano, M. F. Toney, B. Dunn and J. P. Chang, presentation on "Engineering LixAlySizO Thin Films as a Solid Electrolyte for 3D Microbatteries," *11th International Conference on Atomic Layer Deposition*, oral presentation, Cambridge, MA, June, 2011

L. Dudek, Y.C. Perng, E. Nemanick, J. Cho, D. Membreno, R. Thompson, N. Cirigliano, S. Tolbert, C.J. Kim, B. Dunn, J. Chang, "Materials and Architectures for 3D Microscale Batteries*." N/MEMS S&T Fundamentals Program Review*, poster session, Newport Beach, CA, May, 2011

Chapter 1

INTRODUCTION TO BATTERIES

1.1 Objectives

The objective of this research is to develop a microbattery with superior energy and power densities using commercially available materials. This is accomplished by redesigning battery electrodes to accommodate the active battery material in a hierarchical fashion. By maintaining small feature sizes, transport distances remain minimal and ensure high power. Conversely, stacking material vertically rather than horizontally results in large energy density. Three dimensional batteries represent a unique method of improving battery performance without the complex process of materials development.

This dissertation is divided into six chapters. The first chapter provides a detailed background of the energy storage process. Electrochemical theory and testing methods are thoroughly explained followed by an introduction to energy storage. The remainder of the chapter focuses on 3D battery characterization and benchmark performances for the various designs. Chapter two provides insight to design restrictions and cell optimization based on geometrical modeling of the electrode features. The ability to quantify electrode performance based on its features is essential to determining the practicality of such designs. The calculations also display the ability of concentric tube-based electrodes to achieve large areal capacities using various feature sizes.

The next chapter presents half-cell data for carbon-based electrodes. The advantages of using a 3D structured electrode are clearly seen when compared to a planar electrode. The

performance of 3D electrodes is also shown to be dependent on a variety of factors including feature sizes, slurry composition and testing conditions. Chapter four describes the performance of a 3D carbon electrode when arranged in battery-like conditions. Using a thick planar cathode, the cell achieved exceptional energy and power densities. The discussion then addresses the progress made in the processing steps necessary to fabricate a full solid state 3D lithium ion battery.

Chapter five veers from lithium chemistry and presents the advantages of using a 3D design for zinc-air cells. In this case, a 3D structure allows the active zinc to maintain a direct electrical connection to the current collector, allowing for efficient material utilization. The problem of zinc corrosion and shelf-life is also addressed in a study of possible organic corrosion inhibitors. The final chapter summarizes the expressed achievements and offers possible directions for future 3D battery generations.

1.2 Motivation

The invention of the transistor forever changed the history of electronics. Instead of the bulky, expensive vacuum tube, a transistor could be used to perform identical tasks in a cheaper and more efficient manner [1]. Increasing the computing power became as simple as increasing the number of transistors on a chip. The next logical route was to reduce the size of the transistor and its components rather than increase the size of the device. In 1958, a team from Texas Instruments invented the first integrated circuit, which consisted of a transistor, 3 resistors and a capacitor. Gordon Moore predicted in 1965 that the number of transistors placed on an integrated circuit should double every two years, thus doubling the computing capabilities [1] [2]. Moore's

law has been consistent for almost 50 years. Today, Intel's i7 quad core processor contains 731 million transistors over 9.5 cm^2 (Fig 1.2.1) [3].

With the miniaturization of the integrated circuit came the miniaturization of electronic devices. It was quickly realized that the same lithographic techniques used to fabricate the chips could also be used to build small devices. Microelectromechanical systems (MEMS) emerged in the 1970s as microscale devices that were used as sensors or actuators. Today, MEMS are used in various applications, ranging from small devices, such as robotic flies and microfluidics, to very large structures, such as automobiles. MEMS devices can be fabricated using a number of materials through 3 basic steps of patterning, depositing and etching [4].

The recent demand for mobile electronics has led to exponential growth of the MEMS market. The desire for products to be both faster and smaller has led to the fabrication of complex devices such as Smart Dust (Fig 1.2.2) [5]. This device integrates an energy source, processor, sensor, converter and communication device on a footprint area of a few square millimeters. Unfortunately, the resultant energy requirements (> 100 J/cm^2) for such devices

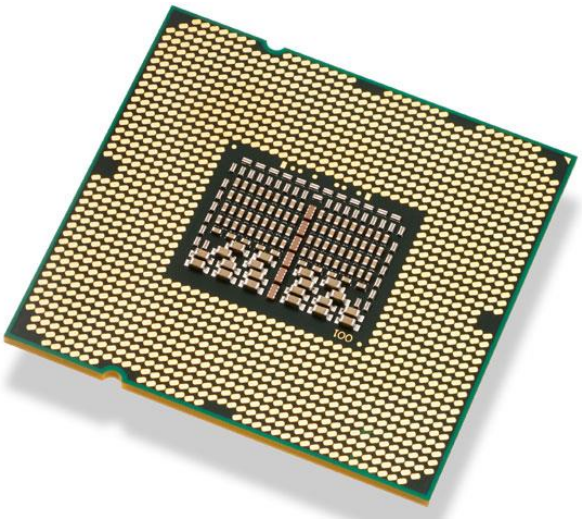

Figure 1.2.1: Intel i7 quad core processor is currently the most powerful commercial chip on the market **[3]**

Figure 1.2.2: Smart dust mote can sense and communicate over a surface area of a few square millimeters. The device requires greater than 100 J/cm^2 of energy to operate. **[5]**

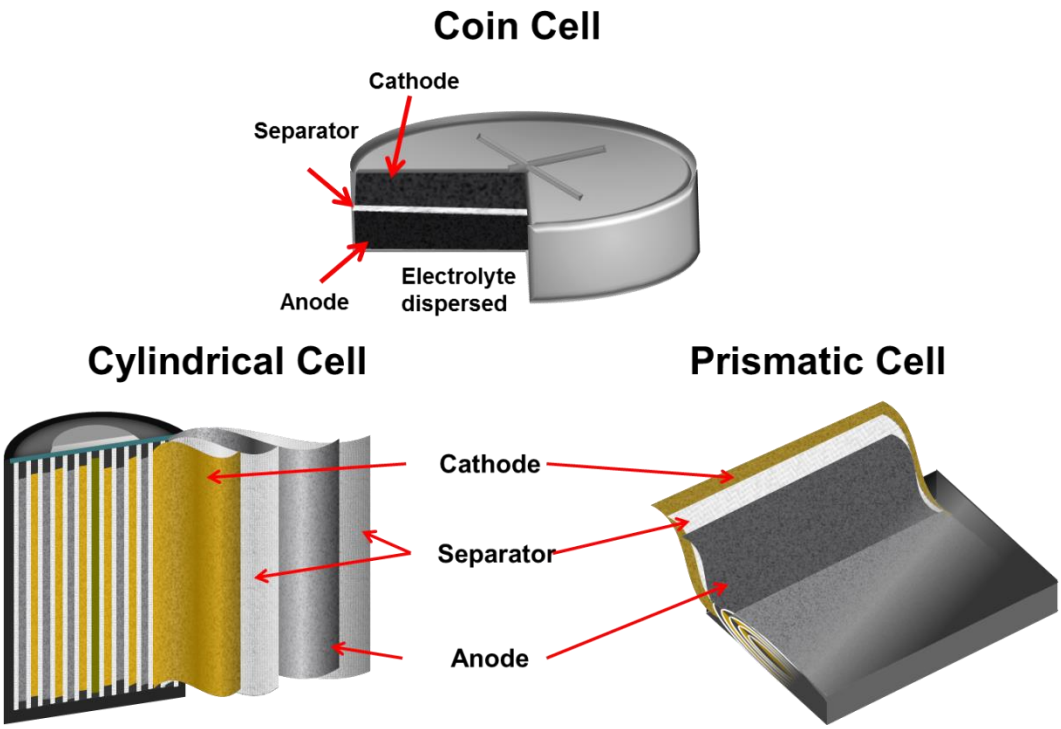

Figure 1.2.3: Typical packaging arrangement for commercially available batteries

have surpassed the capabilities of current battery technology. While integrated circuits have consistently doubled computing capabilities every two years, energy storage capabilities have increased at a rate of only 10% per year. Rolison et al have attempted to explain this by relating the number of transport functions (n) to the annual performance improvement (P) in the following equation [6]:

$$P = {}^{1}/_{2^n} \qquad (1.2.1)$$

Whereas integrated circuits have only one transport function in the form of electronic transport, energy storage devices have 3 transport functions: electronic transport, ionic transport and mass transport. Substitution gives an annual performance improvement of 12.5% for energy storage devices and 50% for integrated circuits, a fairly accurate estimation.

There are two ways to improve the energy storage capabilities of a battery. The first involves the development of new, high capacity materials. This can be a costly and time-

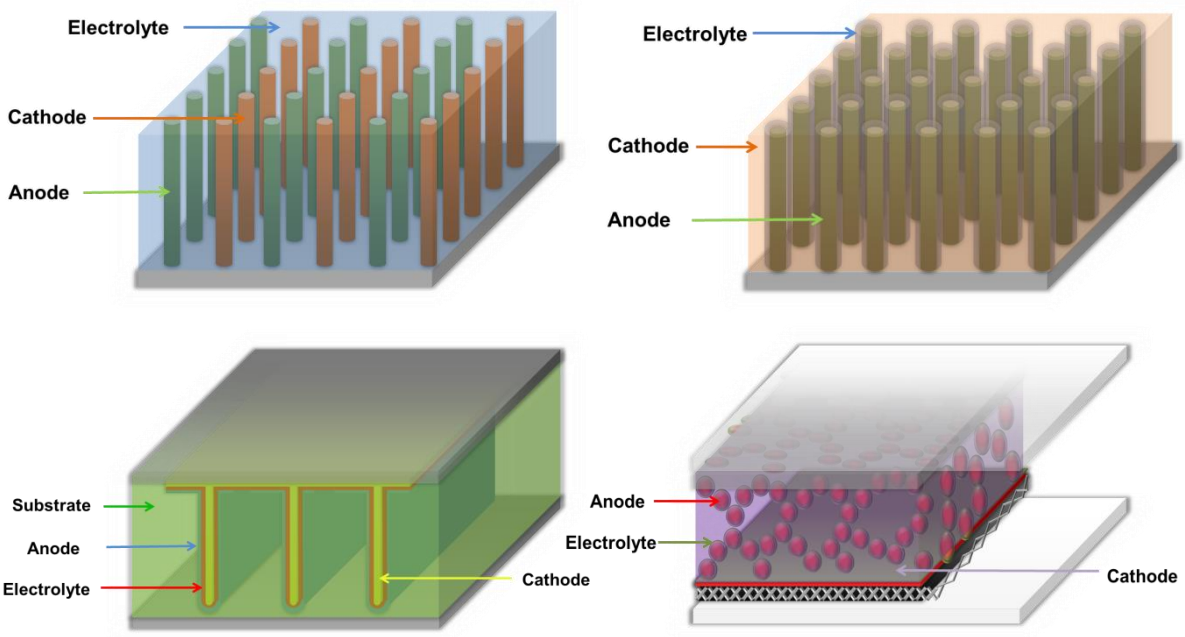

Figure 1.2.4: Examples of 3D battery architectures **[7]**

consuming process that involves many years of materials development followed by numerous characterization techniques. The second method is to engineer an entirely new design for the battery. This approach can lead to immediate results and possibly implement new materials as they are developed. Three dimensional batteries fall into this category.

Three dimensional batteries can be defined as energy storage devices whose positive and negative electrodes share a non-planar interface [7]. Commercial batteries are traditionally assembled in one of three architectures: cylindrical, such as the AA battery, prismatic, such as cell phone batteries, and the coin cell, such as watch batteries (Fig 1.2.3). These three designs are intrinsically related in that the interface between the anode and cathode is two dimensional. This is achieved by spirally winding, stacking or folding the components tightly together in order to load the battery to a desired capacity. Therefore, most commercial research is targeted at making the battery components thinner in order to maximize the loading. Unfortunately, this battery

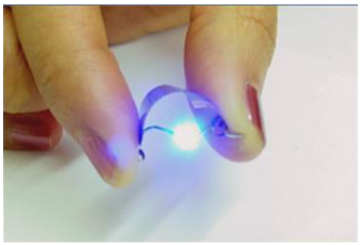

	Seiko MS412FE	Panasonic ML414S	STM EFL700A39	Front Edge Technology
Thickness	0.16 cm	0.14 cm	0.02 cm	0.03 cm
Voltage	3.0 V	3.0 V	3.9 V	4.0 V
Current Density	**0.055 mA/cm²**	**0.03 mA/cm²**	**0.16 mA/cm²**	**0.1 mA/cm²**
Areal Energy Density	5.5 mAh/cm² 17 mWh/cm² **60 J/cm²**	6.6 mAh/cm² 20 mWh/cm² **72 J/cm²**	0.1 mAh/cm² 0.4 mWh/cm² **1.5 J/cm²**	0.2 mAh/cm² 0.7 mWh/cm² **2.6 J/cm²**
Volumetric Energy Density	34.5 mAh/cm³ 104 mWh/cm³ **373 J/cm³**	47 mAh/cm³ 142 mWh/cm³ **511 J/cm³**	5.4 mAh/cm³ 21 mWh/cm³ **76 J/cm³**	6 mAh/cm³ 24 mWh/cm³ **86 J/cm³**
Power Density	**0.17 mW/cm²**	**0.08 mW/cm²**	**0.6 mW/cm²**	**0.4 mW/cm²**

Table 1.2.1: Comparison of commercially available miniature batteries. Seiko and Panasonic coin cells are thick electrodes offering large energy density but low power density. STM and Front Edge are thin film batteries offering large power density but low energy density **[52] [53] [54] [55]**

design is incompatible with the size restrictions imposed on miniature devices. Microbatteries are emerging as the model power source for such devices.

The ideal microbattery is small enough to maintain a device's footprint area while simultaneously providing the power and energy needed to run complex tasks for an extended period of time. For any given battery chemistry, the energy is directly related to the amount of material loaded on an electrode. Therefore, a high energy density battery requires large electrodes in order to accommodate the necessary mass. As battery sizes decrease, so does the available energy density. To compensate, more active material must be introduced. The resulting thicker electrodes introduce larger diffusion distances which, at higher current densities, hinder

the battery's ability to quickly access the necessary energy. Thus, power and energy density are inherently coupled in two dimensional batteries (Table 1.2.1). Three dimensional batteries address this problem by manipulating the battery architecture to incorporate large mass loadings while simultaneously keeping diffusion distances and footprint areas small (Fig 1.2.4).

1.3 Electrochemistry Background

In order to study the working mechanisms of energy storage devices such as batteries, there must be a keen understanding of electrochemistry. Electrochemistry is the study of electrical currents and the resulting chemical effects and vice versa. Electrochemical techniques monitor the transfer of charge between electrode/electrolyte interfaces and provide information about the kinetics and thermodynamics of a given system.

1.3.1 Thermodynamics

The driving force for an electrochemical cell can be determined by starting with the Gibbs free energy of a redox reaction, ΔG_r^o. If the cell is open, or no net current is flowing, then the Gibbs free energy of species *i* in phase *j* can be defined as,

$$\Delta\mu_i = \Delta G_j \qquad 1.3.1$$

This equation implies that the Gibbs free energy of the cell is equal to the chemical potential that is available due to a concentration gradient in the electrolyte [8] [9]. However, because of the inherent voltage difference between the electrodes, there also exists an electrostatic force equal and opposite to that of the chemical potential (Fig 1.3.1). This electrostatic force, chemical potential and Gibbs free energy are balanced by,

$$\Delta\mu_i = \Delta G_j = -z_i FE \qquad 1.3.2a$$

$$\Delta\mu_i^o = \Delta G_j^o = -z_i FE^o \qquad 1.3.2b$$

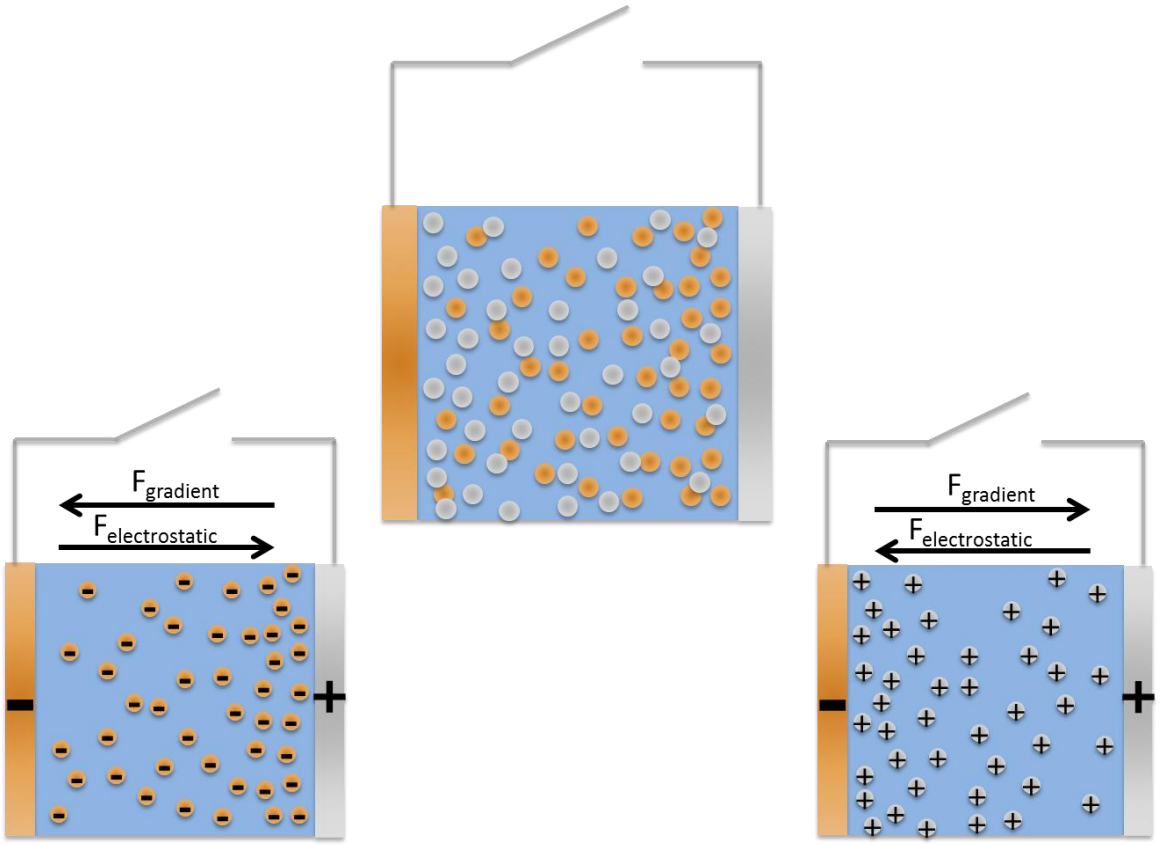

Figure 1.3.1: Open circuit potential occurs due to force balance between concentration gradient and electrostatics

where z is the charge of the ion, F is the Faraday constant, E is the electric potential and superscript indicates standard state conditions. From this equation, it is possible to determine properties such as spontaneity of a reaction, redox potentials and chemical potentials for a system based on the Gibb's free energy of the reaction. Using the thermodynamic relationship between chemical potential and activity (a) of a species, Equation 1.3.2 can be written as,

$$\Delta G_j = -z_i F E = \Delta G_j^o + RT ln(a_i^r / a_i^o) \qquad 1.3.3$$

where a_i^r is the reducing agent activity and a_i^o is the oxidizing agent activity. Rearranging equation 1.3.3 and introducing the equilibrium constant, K, yields the Nernst equation,

$$E = -\frac{\Delta G_f}{zF} = E^o + \frac{RT}{zF} ln(K) = E^o + \frac{RT}{zF} ln\left(\frac{[Ox]}{[Red]}\right) \qquad 1.3.4$$

where E^o is the standard redox potential. The standard redox potential is the potential measured at standard state (ie 1M reactive species, 25*C, 1 atm) and can be determined by extrapolating the activity of a species from experimentally derived formal redox potentials. The formal redox potential ($E^{o\prime}$) takes into consideration unknown side reactions occurring at the electrode interface. Therefore, it is not a value based purely upon thermodynamics, but rather experimental results [10] [11] [12]. Often, the formal redox potential replaces the standard redox potential in the Nernst equation. The Nernst equation directly relates the reduction potential of a reaction to the concentration of the reduced and oxidized species. If a system always follows this relationship, it can be considered electrochemically reversible. The Nernst equation can also be used to relate the voltage of a cell to any other thermodynamic property defined by the activity of a species such as the active analyte concentration and the Gibbs free energy of formation of the products [8].

Taking a closer look at our cell, it can be seen that two spontaneous reactions are occurring: an oxidation reaction at the anode and a reduction reaction at the cathode. This means that each electrode potential, E_c and E_a, can be defined by the redox potential of the reaction determined by the Nernst equation. In other words,

$$E_{cell} = E_c - E_a = \left(E_c^o + \frac{RT}{zF} ln\left(\frac{[Ox]_c}{[Red]_c}\right)\right) - \left(E_a^o + \frac{RT}{zF} ln\left(\frac{[Ox]_a}{[Red]_a}\right)\right) \qquad 1.3.5$$

Note that only differences in reduction potentials can be measured. In some cases, the reduction potential of one of the reactions stays constant even when a small current is applied. This can then be considered to be a reaction that all other reactions can be normalized to and is

called a reference electrode [12] [9]. The use of a reference electrode allows us to monitor individual electrode reactions since it reduces the number of variables in a cell.

Electrochemical cells which use reference electrodes are called half-cells. Half-cell experiments give information about the studied electrode's (working electrode) ability to be oxidized or reduced. For instance, if the electrode is positive relative to the reference electrode, it will tend to be reduced in order to achieve equilibrium. Therefore, the electrode is an oxidizing agent. The more positive the electrode potential, the stronger the oxidizing properties. However, if the electrode is negative relative to the reference electrode, it is considered to be a reducing agent. It is convenient to express the standard reduction potential of reactions as referenced to a standard hydrogen electrode (SHE). An electrode will be oxidized when paired with an electrode that has a more positive potential, and reduced when paired with an electrode that has a more negative potential. In general, the preceding relationships predict where a reaction should

Figure 1.3.2: Potential scale showing a few common reactions referenced to hydrogen

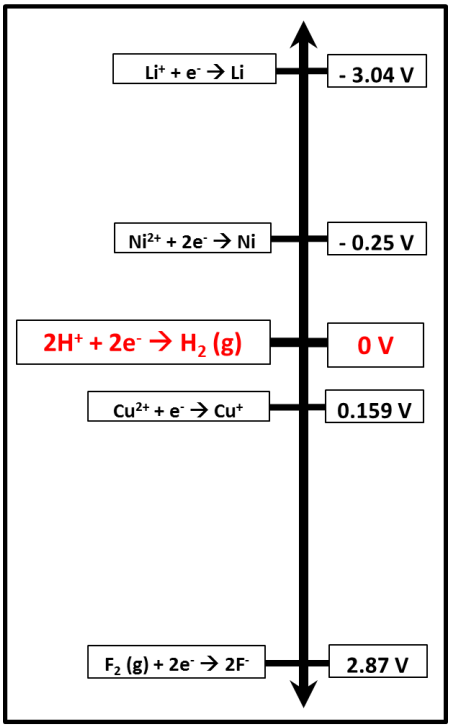

thermodynamically occur on the potential scale (Fig 1.3.2).

1.3.2 Kinetics

Thermodynamics helps predict if and at what potential a reaction should occur. However, it offers no information about how quickly the reaction will occur. Reaction kinetics, on the other hand, allow us to predict the reaction rates based on physical parameters such as electron transfer rates and diffusion. All electrochemical reactions involve the transfer of electrons, ions or both across the electrode/electrolyte interface. The ability to drive a reaction increases as the voltage between two electrodes increases. Other physical processes such as mass transport, atomic rearrangement and adsorption also determine how quickly a reaction will occur.

Consider an electrode undergoing the reaction,

$$Ox + e^- \overset{k_{red}}{\longleftrightarrow} Red \qquad 1.3.6$$

When an electrochemical cell is not polarized and immersed in an electrolyte, the net flux, J_n, at an electrode undergoing an oxidation and reduction reaction is described by,

$$J_n = J_f - J_b = k_{red} C_{O,s} - k_{ox} C_{R,s} = \frac{i}{zF} \qquad 1.3.7$$

where k_{red} and k_{ox} are the reaction rate constants for a reduction and oxidation reaction, and $C_{O,s}$ and $C_{R,s}$ are the surface concentrations of the oxidized and reduced species, respectively. Ionic flux is influenced by three conditions: convection, electric field gradients and concentration gradients [9] [10]. The effects of each will be considered when deriving a relationship between current and voltage.

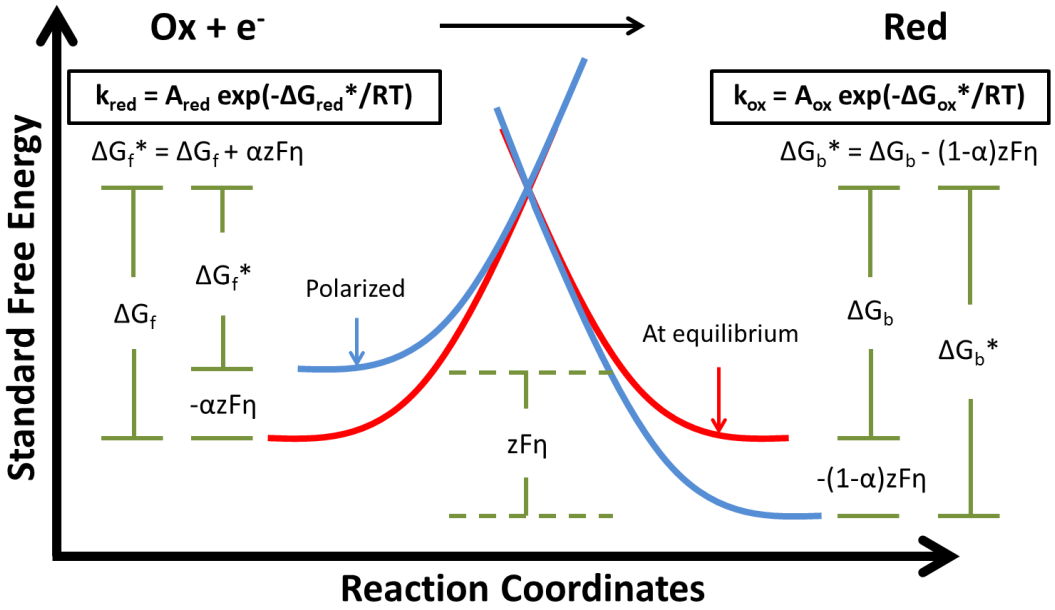

Figure 1.3.3: Energy distribution curve for system at equilibrium (red) and polarized (blue). The forward reaction is defined as a reduction process. Electrochemical rate constants can be derived from energy levels. Modified from **[9]**

From an energy perspective, we can think of anodic oxidation and cathodic reduction as requiring a finite amount of energy in order to overcome an activation barrier. The resulting reaction rates can be defined using an Arrhenius relation defined by the Maxwell-Boltzmann energy distribution curve (Fig 1.3.3),

$$k_{red} = k' exp\left(-\frac{\alpha zF\eta)}{RT}\right) \qquad 1.3.8$$

$$k_{ox} = k' exp\left(\frac{(1-\alpha)zF\eta)}{RT}\right) \qquad 1.3.9$$

where α is a constant dependent on the symmetry of the potential barrier, η is the overpotential and k′ is the standard rate constant. From the inclusion of the Gibb's free energy term (Fig 1.3.3), it can be seen that the standard rate constant represents the difficulty for a reaction to occur. A large k′ value translates to fast kinetics while a small k′ value means slow kinetics [10]. At the formal redox potential, the reduction and oxidation rate constants are equal. Overpotential can be

defined as the difference between the applied potential and the formal reduction potential of the reaction ($\eta = E\text{-}E^{o'}$). Physically, it is the extra energy necessary to drive an oxidation or reduction reaction. A cathodic current flows when polarizing the cell to a more negative potential ($\eta < 0$), and an anodic current dominates when polarizing the cell to a more positive potential ($\eta > 0$). Plugging these into the flux equation defined earlier, the net current can be derived as,

$$i = zFk'\left\{C_{O,s}exp\left(\frac{\alpha zF\eta}{RT}\right)_{red} - C_{R,s}exp\left(-\frac{(1-\alpha)zF\eta}{RT}\right)_{ox}\right\} \qquad 1.3.10$$

At equilibrium, the net current is zero and the surface concentration can be assumed to be equal to the bulk electrolyte concentration ($C_{O,b}$, $C_{R,b}$). Therefore, equation 1.3.10 can be reduced to,

$$i_o = Fk'C_{O,b}^{(1-\alpha)}C_{R,b}^{\alpha} \qquad 1.3.11$$

This is called the exchange current density and represents the background current present when a cell is at its equilibrium voltage, also known as the open circuit potential or corrosion potential [10] [12].

If a system is polarized from equilibrium and well stirred so that the surface concentration is similar to the bulk concentration, then equation 1.3.10 can be simplified to

$$i = i_o\left\{exp\left(\frac{\alpha zF\eta}{RT}\right)_{red} - exp\left(-\frac{(1-\alpha)zF\eta}{RT}\right)_{ox}\right\} \qquad 1.3.12$$

This is known as the Butler-Volmer (BV) equation and describes the current response in the absence of mass transfer effects in a polarized cell (Fig 1.3.4) [10] [9]. The BV equation can be generalized under two conditions. If the overpotential is low (< ~10 mV), the current response is considered to be due to polarization and is linear. Using a series expansion, the BV equation can be approximated to,

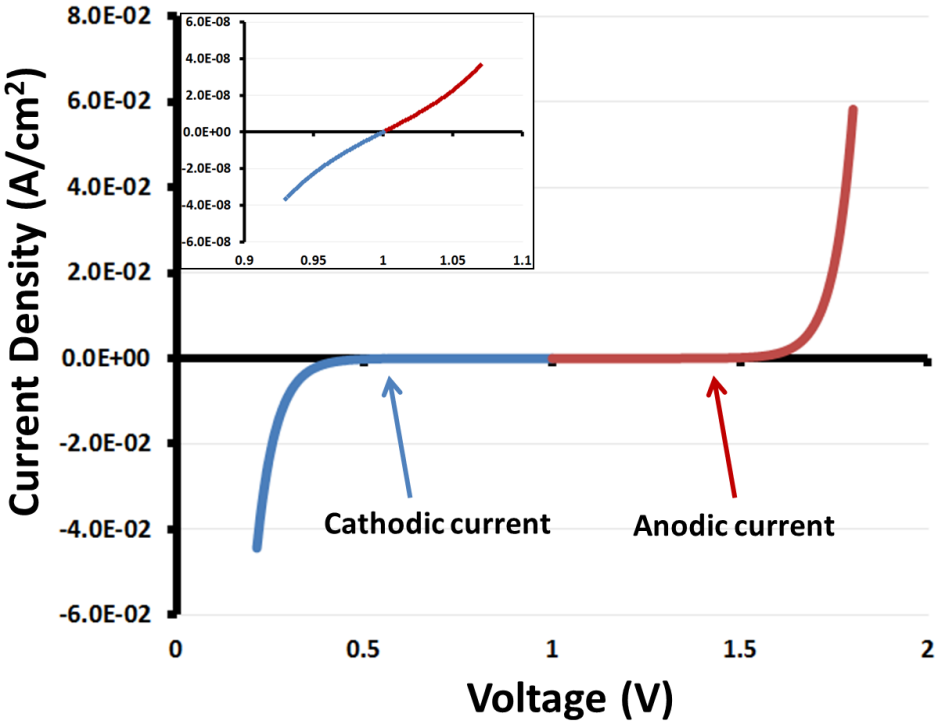

Figure 1.3.4: Generated Butler Volmer curve modeling a system completely governed by activation overpotential. Inset is expanded at open circuit displaying linear relationship.

$$i \approx i_o \left(\frac{zF\eta}{RT}\right) \qquad 1.3.13$$

At large overpotentials, one exponential term in equation 1.3.12 will be much greater than the other. For instance, if the overpotential is very negative, then the resulting reduction current can be described by the following equation,

$$i = i_o exp\left(\frac{\alpha zF\eta}{RT}\right) \qquad 1.3.14$$

This equation describes the current response when the reaction is limited by the activation overpotential. Therefore, the current is limited by the charge-transfer process of the slowest reaction step.

Solving for overpotential gives the Tafel equation,

$$\eta = 2.303\frac{RT}{\alpha zF}\log\left(\frac{i}{i_o}\right) = a + b\log(i) \quad 1.3.15$$

where

$$a = -\frac{2.303RT}{\alpha zF}\log(i_o) \quad 1.3.16$$

$$b = \frac{2.303RT}{\alpha zF} \quad 1.3.17$$

The Tafel equation is useful for determining corrosion rates of metals, which will be discussed later.

As an electrode is further polarized from equilibrium, it eventually reaches a condition at which the surface concentration of active species becomes depleted at the electrode/electrolyte interface. Ions must then diffuse from the bulk electrolyte to the electrode surface in order to continue the reaction. The reaction is now no longer limited by the transfer of charge but instead by the diffusion of active species. This is known as concentration polarization [9]. In order to describe this system, we must begin with the Faraday equation for current density in one dimension,

$$i = zF\frac{m}{A_w tA} = zFJ \quad 1.3.18$$

where J is the molar flux of ions that passes through an area, A. The movement of ions may occur due to convection of the liquid (J_c), migration across an electric field (J_m), or diffusion down a concentration gradient (J_d).

Molar flux due to convection of the host liquid can be described as,

$$J_c = Cv \tag{1.3.19}$$

where C is the concentration of active species and v is the velocity of particles. Under the influence of an electric field, the migration molar flux J_m can be described as,

$$J_m = -CB\frac{d\mu}{dx} = -CBzq_e\frac{d\varphi}{dx} = -\frac{zFCD}{RT}\frac{d\varphi}{dx} \tag{1.3.20}$$

where B is the mobility of ions, q_e is the charge of an electron, φ is the potential field and $F=q_eN_A$. It can be shown that

$$\varphi = \varphi_o \exp(\frac{-x}{\delta}) \tag{1.3.21}$$

where $\varphi_o = RT/zF$ and δ represents the length of the diffusion layer which is typically 300-600 μm. This layer should not be confused with the diffuse layer of the electrical double layer which is typically about 100 Å and describes a region in which ions are loosely bound due to a charged surface. The diffusion layer δ is the distance ions must diffuse from the bulk to react with the electrode and varies with time [9] [13]. Substituting this into 1.3.21 gives,

$$J_m = \frac{DC_s}{\delta} \tag{1.3.22}$$

In the absence of convection and potential gradients, the movement of ions can be described by Fick's first and second laws of diffusion in one dimension,

$$J = -D\frac{\partial C}{\partial x} \tag{1.3.23}$$

$$\frac{\partial C}{\partial t} = D\frac{\partial^2 C}{\partial x^2} \tag{1.3.24}$$

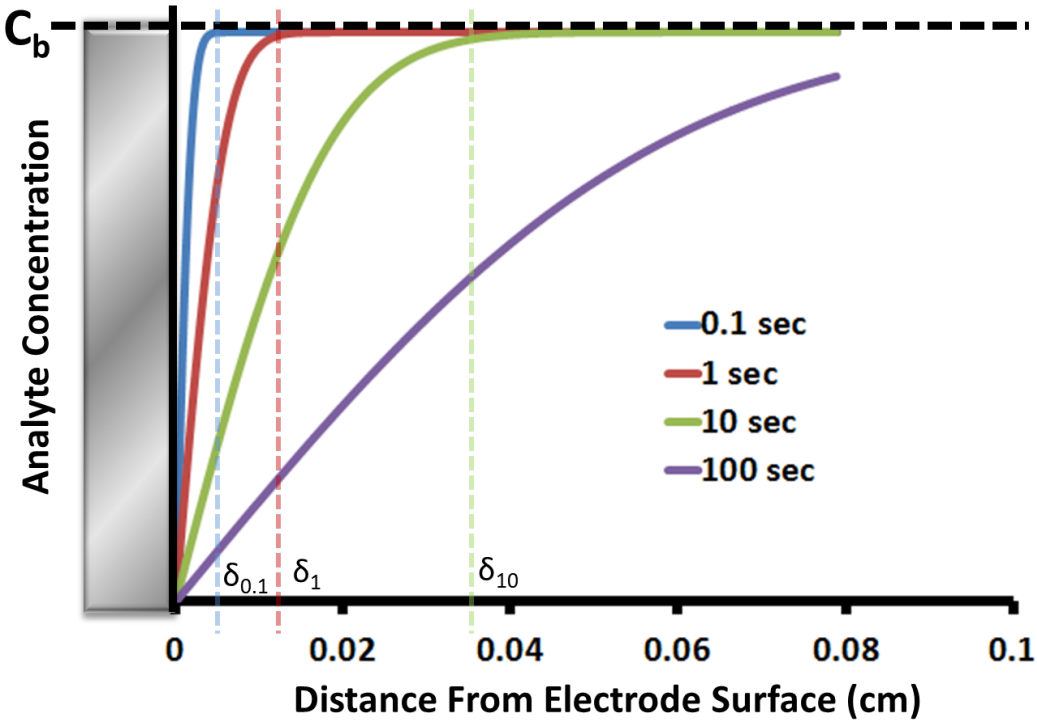

Figure 1.3.5: Concentration profile of oxidized species at 0.1 sec (blue), 1 sec (red), 10 sec (green) and 100 (purple) sec after polarization. Vertical dashed lines are diffusion layer lengths for the respective times.

These equations describe a system in which ions undergo random walk down a concentration gradient with respect to time and space. Solving for Fick's second law in the x-direction yields an equation describing the concentration of a species as a function of distance from the electrode surface (Fig. 1.3.5) The expression for concentration when the bulk concentration is greater than the electrode surface concentration ($C_b > C_s$) is,

$$C_x = C_s + (C_b - C_s)erf\left(\frac{x}{\sqrt{4Dt}}\right) \qquad 1.3.25$$

and when the surface concentration is greater than the bulk concentration ($C_s > C_b$) is,

$$C_x = C_s - (C_s - C_b)erf\left(\frac{x}{\sqrt{4Dt}}\right) \qquad 1.3.26$$

The first derivative of both equations yields,

$$\frac{\partial C}{\partial x} = -\frac{C_s - C_b}{\sqrt{\pi D t}} exp\left(-\frac{x^2}{4Dt}\right) \quad 1.3.27$$

which can be simplified to,

$$\frac{\partial C}{\partial x} = \frac{C_s}{\sqrt{\pi D t}} \quad 1.3.28$$

$$\frac{\partial C}{\partial x} = -\frac{C_s}{\sqrt{\pi D t}} \quad 1.3.29$$

for concentration polarization ($C_b >> C_s$) and activation polarization ($C_s >> C_b$) conditions, respectively. Plugging the derivative term into the equation for diffusional flux yields,

$$J_d = \frac{DC_s}{\sqrt{\pi D t}} = \frac{DC_s}{\delta} \quad 1.3.30$$

With the three flux terms defined, a general equation for the current generated due to molar flux can be established using equation 1.3.18 [10] [14]

$$i = zF(J_c + J_m + J_d) = zF\left(Cv + \frac{2DC_o}{\delta}\right) \quad 1.3.31$$

In the absence of a strong electrical field and stirring, the current is only limited by the diffusion of active species to the electrode interface. This condition is described by the Cottrell equation,

$$i = \frac{zFD(C_b - C_s)}{\delta} \quad 1.3.32$$

From this equation it can be seen that the maximum limiting current (i_L) occurs when the concentration of the active species at the surface (C_s) is zero [13].

A relationship between current and voltage that takes into consideration both activation and concentration overpotential conditions is governed by Fick's second law describing the concentration profiles of both active species,

$$\frac{\partial C_O(x,t)}{\partial t} = D_O \frac{\partial^2 C}{\partial x^2} \quad 1.3.33$$

$$\frac{\partial C_R(x,t)}{\partial t} = D_R \frac{\partial^2 C}{\partial x^2} \quad 1.3.34$$

Solving these equations using Laplace transforms and substituting the solutions into the flux equation (eq 1.3.18) yields,

$$i = \frac{i_L}{1+\xi\theta} \pi^{1/2} H t^{1/2} \left[exp(H^2 t) erfc\left(Ht^{1/2}\right)\right] \quad 1.3.35$$

where

$$H = \frac{k_{red}}{D_O^{1/2}} (1 + \xi\theta) \quad 1.3.36$$

$$\theta = \frac{C_{O,s}}{C_{R,s}} = exp\left(\frac{zF\eta}{RT}\right) \quad 1.3.37$$

$$\xi = \left(\frac{D_O}{D_R}\right)^{1/2} \quad 1.3.38$$

and i_L is the limiting current described by the Cottrell equation when C_s is equal to zero. The term in brackets of Equation 1.3.35 can be considered to be a measure of reversibility. A system's reversibility is largely controlled by the k′ value of the reaction [10]. For a reversible system with a large k′ value, the bracketed term will approach unity, and the current is a result of Butler-Volmer kinetics and Cottrell diffusion. This system will approach the limiting current

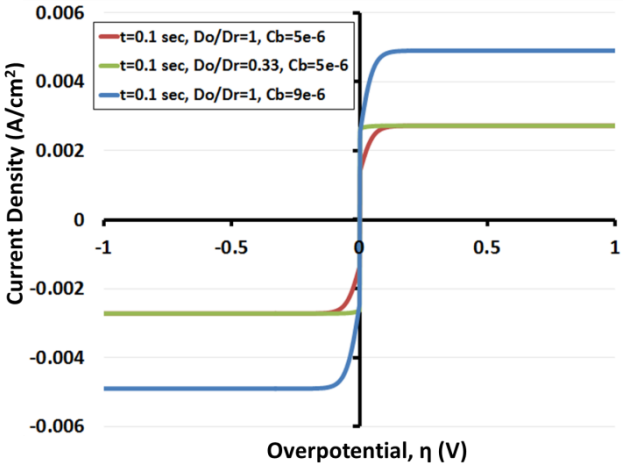

Figure 1.3.6: Generated voltammogram curves displaying effects of diffusion constant and bulk concentration of oxidized species

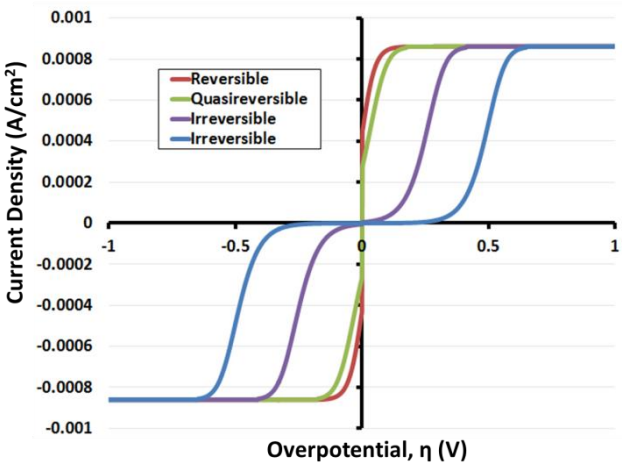

Figure 1.3.7: Generated voltammogram curves displaying k' effects on a system's reversibility. Low k' values result in irreversible systems with large overpotentials, while large k' values have high reversibility

very close to the formal redox potential. Figure 1.3.6 shows how diffusion constants and initial oxidation concentrations affect the shape of a reversible voltammogram. Quasireversible and totally irreversible systems are plagued by small k' values. Therefore, the bracketed term will be less than one and reach the limiting current at larger overpotentials (Fig. 1.3.7).

Equation 1.3.35 describes the current response during step voltammetry experiments in which the working electrode is stepped to voltages from rest while the current is recorded. Each time the electrode is stepped from rest, the current experiences a large transient charging response followed by a steady state response (Fig. 1.3.8). This initial response is due to an increased flux of ions to the electrode as the surface concentration becomes zero. As a result, the sampling time, t, can also determine a system's reversibility [10] [15]. For a reversible system, sampling the current at faster timescales simply increases the limiting current (Fig. 1.3.9). However, for a system with slow kinetics, fast sampling also causes the bracketed term of equation 1.3.35 to deviate from unity. This condition pushes the potential at which limiting

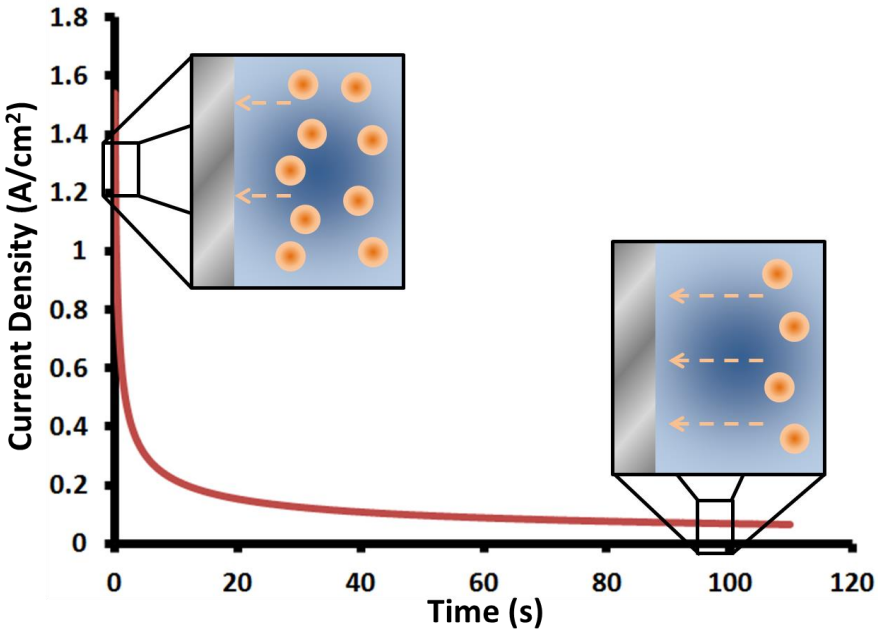

Figure 1.3.8: Sampling time dependence on Cottrell limiting current. Fast sampling times result in large limiting currents due to transient response. Slow sampling times result in lower limiting currents due to steady state conditions.

current is reached to higher overpotentials. On the other hand, if the timescale sampling is slow for the same sluggish system, the reaction is given more time to complete and can result in a reversible system (Fig. 1.3.10).

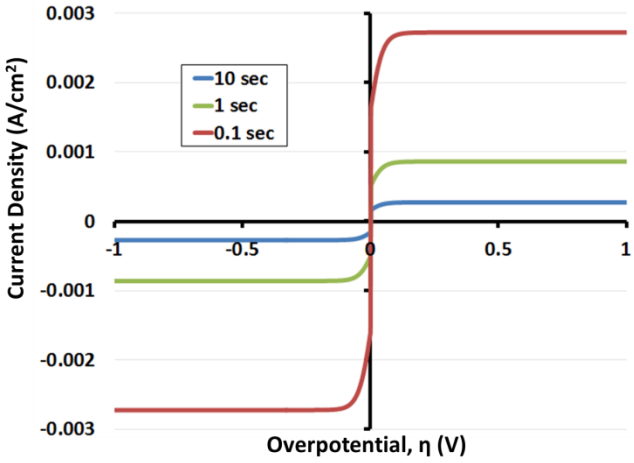

Figure 1.3.9: Generated voltammogram showing effects of sampling time on a reversible system. Fast sampling times result in larger limiting currents.

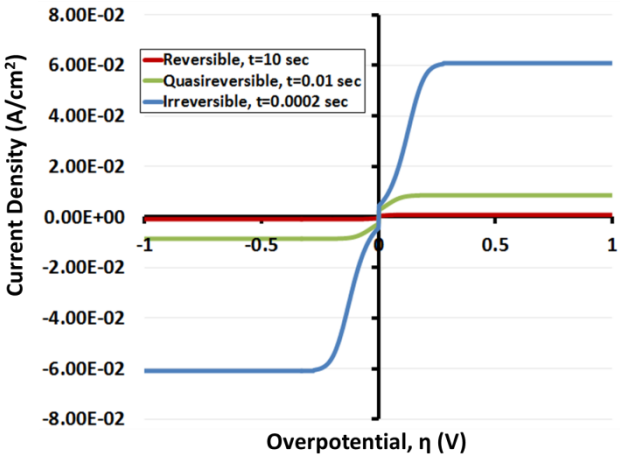

Figure 1.3.10: Generated voltammogram showing effects of sampling time for irreversible system. Increasing the sampling time allows the system to reach steady state and act as a reversible system.

In summary, kinetics are arguably more important when considering a system's practicality as an electrochemical device. Thermodynamics may define a possible purpose, yet kinetics ultimately makes the final decision.

1.3.3 Electrochemistry Experiments

Experiments can be carried out using two-electrode or three-electrode configurations (Fig. 1.3.11). A three-electrode set-up consists of a reference electrode, working electrode and counter electrode. In a two-electrode set-up, the counter and reference electrodes are connected as a single electrode. Three-electrode arrangements are preferred when working electrode voltages must be closely regulated. In order to do this, the reference electrode must meet three conditions [11] [13]. First, the electrode voltage must obey the Nernst equation and not change with time. Simply stated, the reaction must be both chemically and electrochemically reversible. Second, the electrode potential must not change when a very small current is drawn. Third, the electrode must have a small thermal coefficient of potential. If a reference electrode does not meet all of these conditions, it is known as a pseudo reference electrode. Typical reference

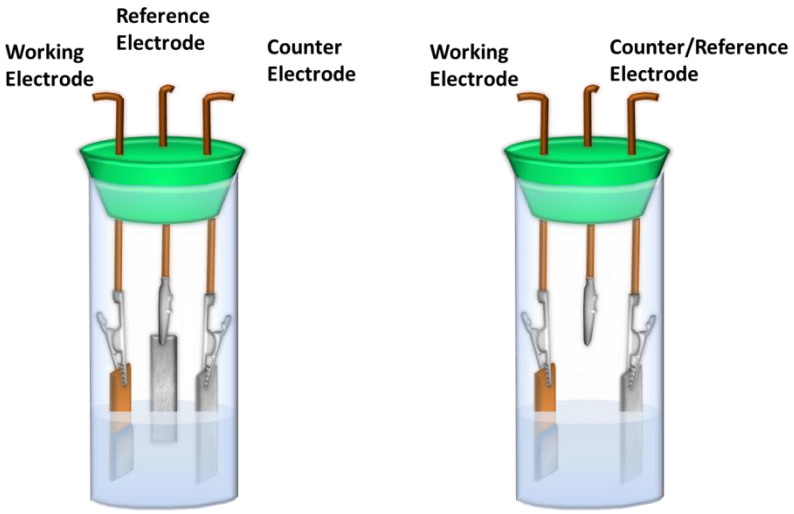

Figure 1.3.11: Example of experimental setup for 3-electrode (left) and 2-electrode (right) cell

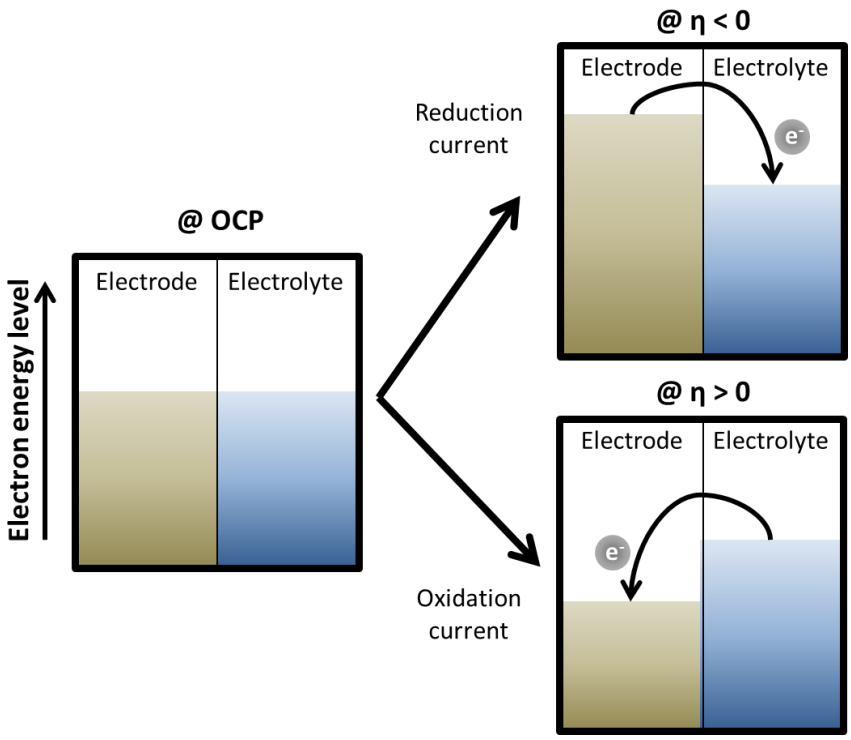

Figure 1.3.12: Applying a negative bias increases the electrode energy level, inducing a reduction current. Applying a positive bias reduces the electrode energy level, inducing an oxidation current. Modified from **[10]**

electrodes are standard hydrogen electrodes (SHE), silver/silver chloride electrodes (Ag/AgCl) and saturated calomel electrodes (SCE). Common pseudo reference electrodes are metal wires such as platinum or silver.

For all electrochemical experiments, the reaction which is being investigated occurs at the interface of the working electrode and electrolyte. Polarizing the working electrode induces a current response that is directly related to the kinetics of a chemical reaction (Fig. 1.3.12). The role of the counter electrode is to maintain electroneutrality of the electrochemical cell. The surface area of the counter electrode should be much larger than that of the working electrode in order to ensure it is not limiting the overall cell reaction or undergoing adverse reactions. The voltage of the counter electrode is regulated only to match the current of the working electrode

and so can swing to very large values if the surface area is too low. In a galvanic (discharging) cell, it acts as the anode, while in an electrolytic (charging) cell, it acts as the cathode. When physically assembled, all electrodes should be as close as possible without touching each other or disrupting the electric field between the counter and working electrodes.

Galvanostatic cycling is a technique in which current is held constant while the voltage between the working and reference electrodes is monitored. A positive current denotes a flow of electrons from the working electrode to the counter electrode, while a negative current results in electrons flowing from the counter electrode to the working electrode. Put simply, a positive current charges the cell, and a negative current discharges the cell. The shape of the discharge curve can reveal information about the thermodynamics and kinetics of a system [8]. From a thermodynamic perspective, the Gibb's phase rule will determine whether the curve is flat, curved or S-shaped depending on the number of intensive properties necessary to define the rest of a system. The Gibb's phase rule is,

$$F = C - P + 2 \qquad 1.3.33$$

where C is the number of active elements, P is the number of phases and F is the degrees of freedom. In a system containing two phases and two elements, such as the zinc anode in a zinc-air battery, then the number of intensive properties that defines the entire system (F) is two. Therefore, setting two simple intensive variables such as temperature and pressure constant means that all other intensive properties such as chemical potential will remain fixed. The resulting discharge curve will remain flat throughout any composition change (Fig. 1.3.13). However, if a system contains two elements in a single phase such as a solid solution, then the number of intensive properties needed to define the system is three. Maintaining a constant

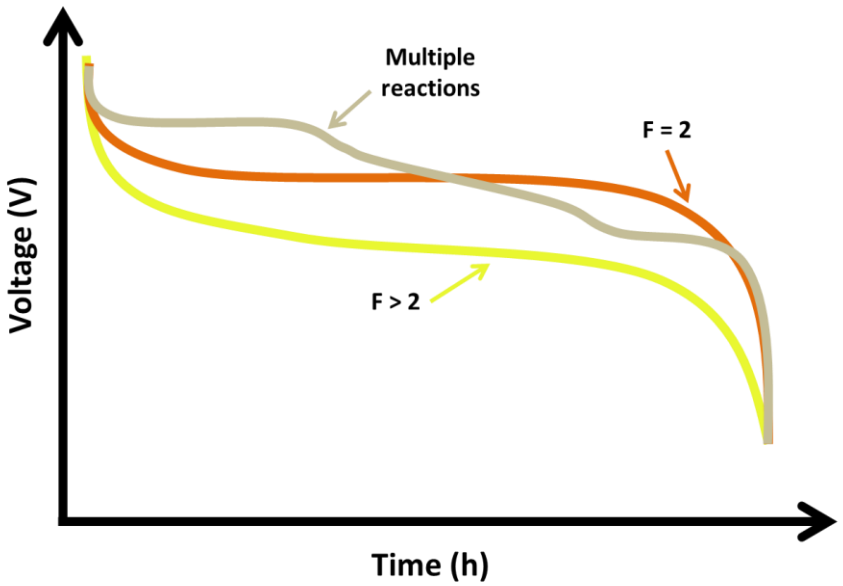

Figure 1.3.13: Diagram illustrating the influence of Gibb's phase rule over the shape of a discharge curve

temperature and pressure is no longer enough to define the other properties. Since the chemical potential is now dependent on the electrode composition, the discharge curve will have an S-shaped appearance. It is also possible for an electrode to have multiple reaction steps, thus giving a discharge curve with various features related to the particular reaction occurring at that voltage.

In practice, individual plateaus are difficult to distinguish due to the kinetics of the system and side reactions. It should be pointed out that recent theories are now challenging commonly accepted explanations for the shape of a discharge curve [16]. Gibb's phase rule, while perhaps not as definitive as once thought, is still a good starting point when analyzing a discharge curve.

Kinetically speaking, electrodes succumb to three types of polarization during the discharge process (Fig. 1.3.14). Initially, the voltage drops almost instantaneously due to the cell resistance. Next, the cell may experience activation overpotential due to extra energy being

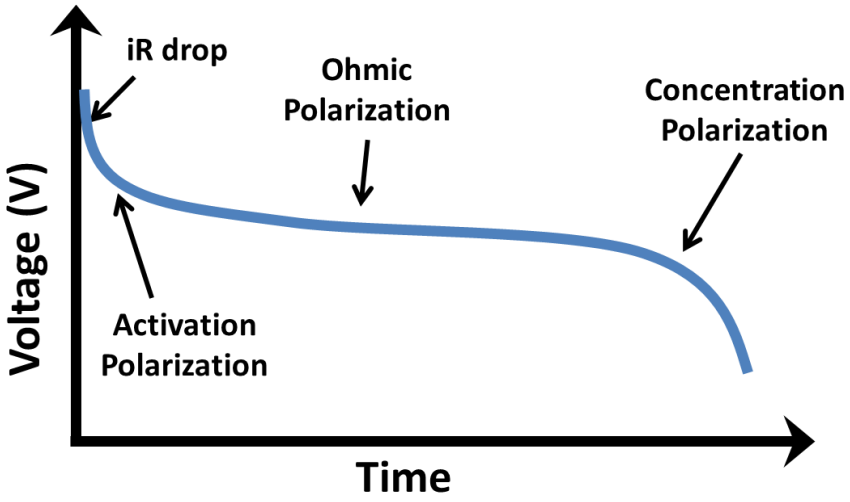

Figure 1.3.14: Kinetic polarization processes that are present during a galvanostatic discharge experiment.

needed to start a reaction. This is more distinguished when large energy barriers need to be overcome to drive a reaction. While in a steady discharge state, the voltage profile will remain flat or slightly curved. The voltage at which this portion occurs is affected by the ohmic polarization. This may come from a number of sources of resistance such as the electrolyte, contacts, film formation or poor electrode conductivity. Ohmic polarization may also affect the slope of this portion. Finally, as ions become depleted near the electrode/electrolyte interface, mass transfer becomes difficult and concentration polarization occurs. These three polarization processes can become more pronounced with larger current densities, especially if the kinetics are slow [17]. This is evident by an increase in the slope of the discharge curve and a decrease in active material utilization (Fig. 1.3.15).

Cyclic voltammetry (CV) is an electrochemical technique that sweeps the working electrode between two potentials at a given rate. Sweeping from negative to positive potentials (anodic sweep) decreases the energy of the working electrode and produces distinct peaks

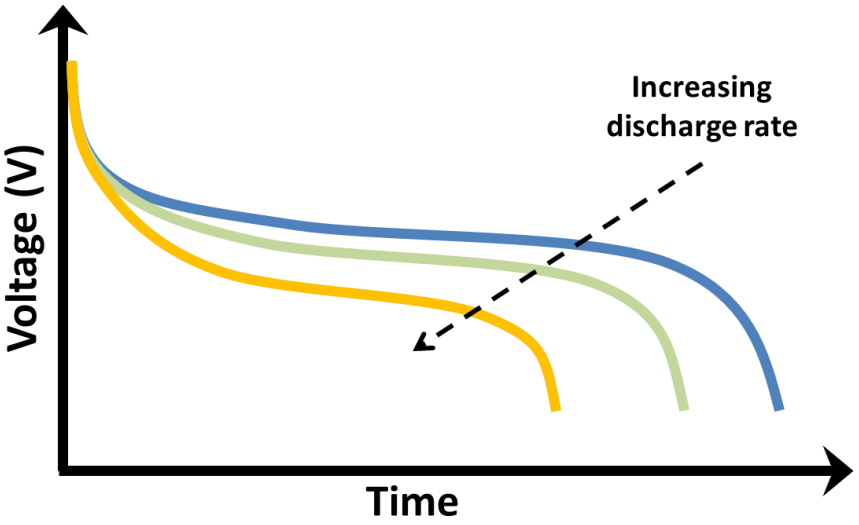

Figure 1.3.15: As discharge rate increases, the working voltage decreases due to polarization effects.

indicative of oxidation reactions. Sweeping in the negative direction (cathodic sweep) increases the energy of the working electrode and produces distinct peaks indicative of reduction reactions. This technique differs from the potential step method described earlier in that it constantly varies the voltage with time instead of bringing the electrode to rest between each step.

Peaks occur due to the relationship between ion flux and surface concentration (Fig. 1.3.16). As an electrode is swept towards its redox potential, a faradaic current begins to flow. Initially, only a limited number of molecules are used, keeping the surface concentration similar to the bulk and the driving force for diffusion minimal. When the redox potential has been reached, the electrode surface concentration becomes zero and creates a large diffusion gradient over a small diffusion layer. The driving force for diffusion is now very large and results in a maximum flux of ions to the surface. Eventually, the ion flux decreases as the diffusion reaches a steady state [11] [14]. This correlates with an increase in diffusion layer size with time. This process is very similar to Cottrell behavior and can be thought of as a summation of successive voltage steps each responding with the proper version of equation 1.3.3. (Fig 1.3.17).

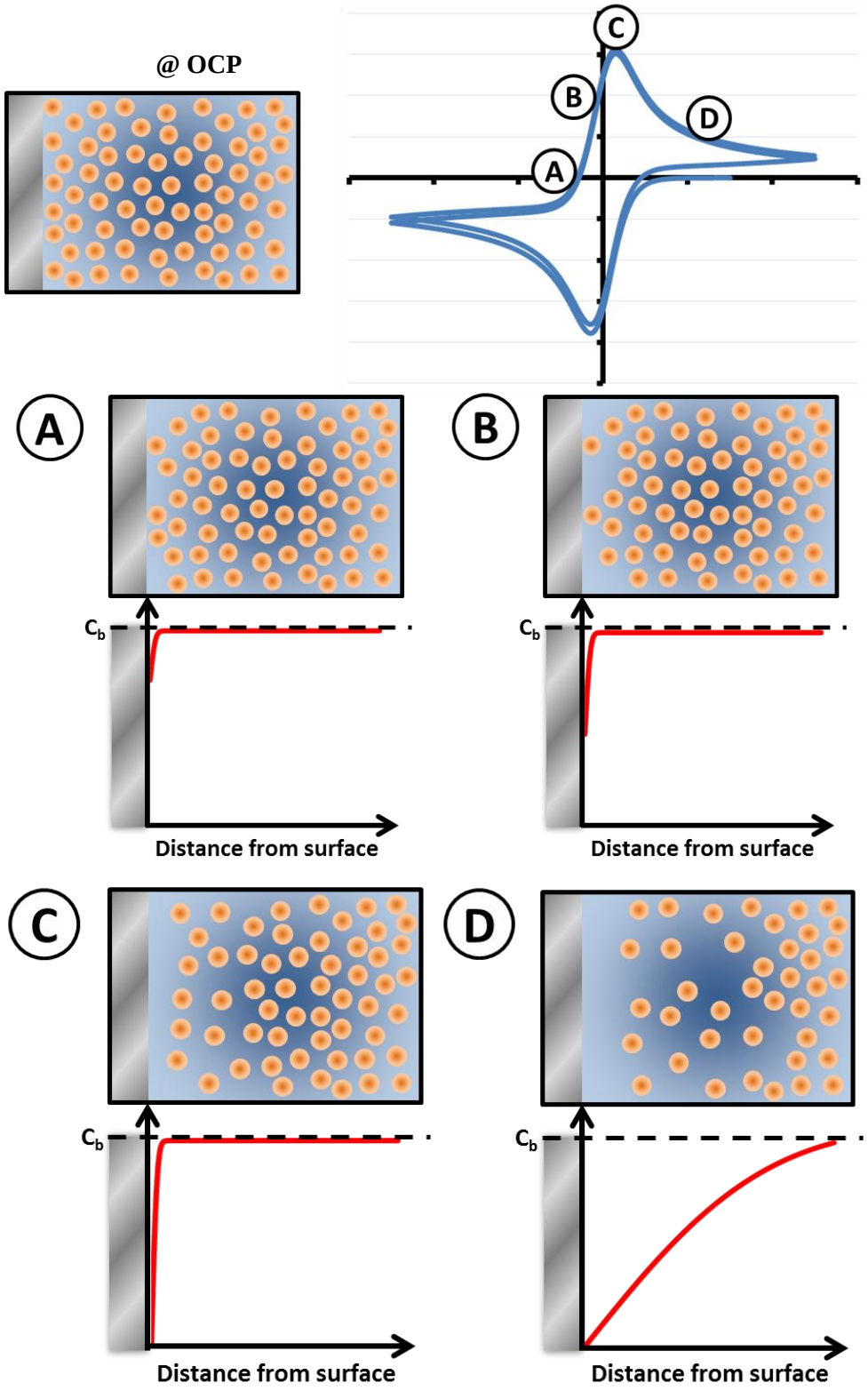

Figure 1.3.16: Diagram showing relationship between concentration gradient, ion flux and current. Peaks in cyclic voltammograms occur due to these three processes.

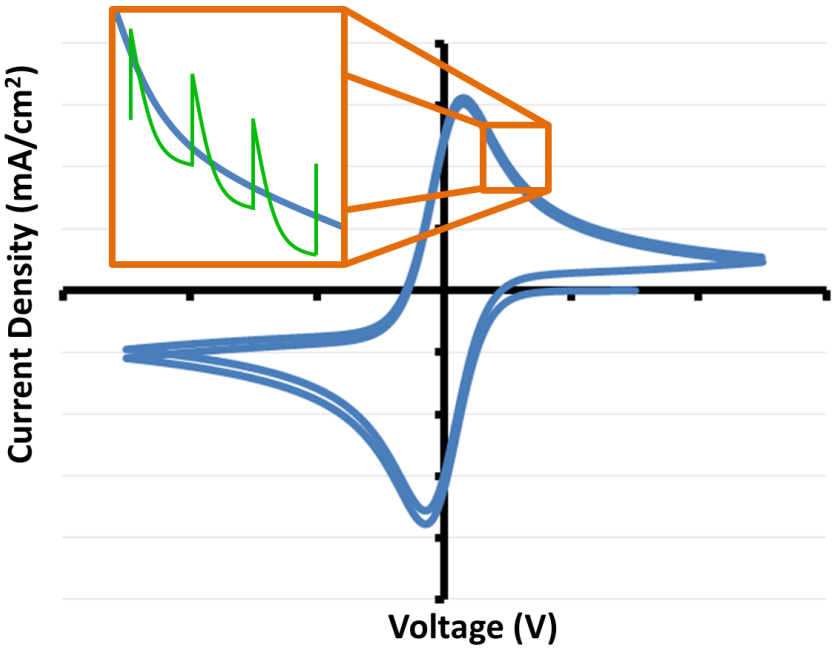

Figure 1.3.17: A CV is composed of many voltage steps. Each step has a current response governed by the Cottrell equation. Adapted from **[11]**

The derivation of the current-voltage relationship for a cyclic voltammogram involves similar boundary conditions as the previous voltammetry experiments but becomes more complex due to the voltage now being time-dependent [10] [18] [19]. For a reversible system, the relationship is again governed by the Nernst equation and Fick's laws of diffusion. Using convolution theorem, derivations and substitutions, we end up with the integral,

$$\int_0^{\sigma t} \frac{\chi(z)dz}{\sqrt{(\sigma t - z)}} = \frac{1}{1+\xi\theta S(\sigma t)} \qquad 1.3.34$$

where S(σt) is a function of E. Any value for this parameter will result in a value for χ(σt) by solving the equation. Rearranging the chi function eventually results in the current equation,

$$i = zFC_{O,b}\sqrt{\pi D_O \sigma}\chi(\sigma t) \qquad 1.3.34$$

Nicholson and Shain were among the first to solve equation 1.3.34 using numerical methods and developed a table of current functions for a reversible charge transfer. From this table, peak current (i_p) and voltage (E_p) values can be derived to be,

$$i_p = 0.4463\left(\frac{zF^3}{RT}\right)^{1/2} C_{O,b} D_O^{1/2} v^{1/2} \qquad 1.3.35$$

$$E_p = E^{o\prime} - 1.109\frac{RT}{zF} \qquad 1.3.36$$

An irreversible system is controlled by Fick's laws of diffusion and Butler-Volmer kinetics. Using the same methods for a reversible system, it is possible to end up with the integral equation,

$$1\text{-}\int_0^{bt} \frac{\chi(z)dz}{\sqrt{bt-z}} = (e^{u-bt})\chi(bt) \qquad 1.3.37$$

which can also be solved using numerical solutions. Again, rearrangement gives the current equation for an irreversible reaction as,

$$i = zFC_{o,b}(D_O v\pi)^{\frac{1}{2}}\left(\frac{\alpha F}{RT}\right)^{\frac{1}{2}}\chi(bt) \qquad 1.3.38$$

A new table of current functions for irreversible charge transfer yields peak current and voltage values to be,

$$i_p = 0.4958\left(\frac{\alpha F^3}{RT}\right)^{1/2} D_O^{1/2} C_{O,b} v^{1/2} \qquad 1.3.39$$

$$E_p = E^{o\prime} - \frac{RT}{\alpha F}\left[0.78 + ln\left(\frac{D_O^{1/2}}{k'}\right) + ln\left(\frac{\alpha F v}{RT}\right)^{1/2}\right] \qquad 1.3.40$$

Figures 1.3.18 and 1.3.19 illustrate the peak current and voltage dependence on scan rate for a reversible and irreversible system, respectively.

Alternatively, a single equation governing reversible, irreversible and quasi-reversible reactions can be derived using a semi-integral technique [11]. By defining the surface concentrations of the oxidized and reduced species as,

$$C_{O,s} = C_{O,b} + \frac{1}{nFA\sqrt{D}} \frac{d^{-\frac{1}{2}} I(t)}{dt^{-\frac{1}{2}}} \qquad 1.3.41$$

$$C_{R,s} = \frac{1}{nFA\sqrt{D}} \frac{d^{-\frac{1}{2}} I(t)}{dt^{-\frac{1}{2}}} \qquad 1.3.42$$

and combining with the Butler-Volmer equation (Eq. 1.3.12), a general current-voltage equation can be expressed as,

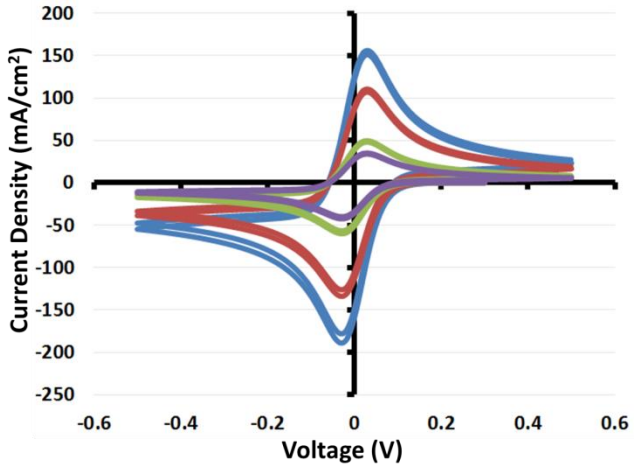

Figure 1.3.18: Effect of scan rate on the shape of a CV for a reversible system.

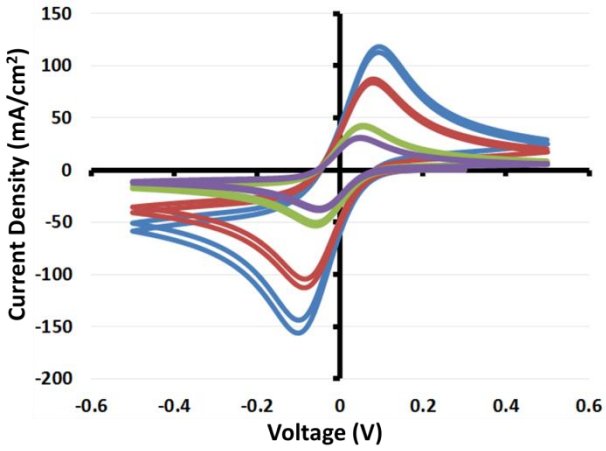

Figure 1.3.19: Effect of scan rate on the shape of a CV for an irreversible system.

$$i(t) = -\left\{zFk'C_{O,b} + \frac{k'd^{-\frac{1}{2}}}{\sqrt{D}dt^{-\frac{1}{2}}}i(t)\right\}\exp\left[-\frac{\alpha zF}{RT}\left(E_i - vt - E^{0'}\right)\right] -$$

$$\left\{\frac{k'd^{-\frac{1}{2}}}{\sqrt{D}dt^{-\frac{1}{2}}}i(t)\right\}\exp\left[-\frac{\alpha zF}{RT}\left(E_i - vt - E^{0'}\right)\right] \qquad 1.3.43$$

It can be shown that as k′ approaches large values, Equation 1.3.43 describes a reversible system, whereas smaller values of k′ describe an irreversible system (Fig. 1.3.20). This equation is extremely complex and requires advanced numerical simulations in addition to experimental fitting in order to utilize it fully.

A simple method to determine the reversibility of a system is by monitoring the peak to peak separation. For a reversible system, the difference between the anodic and cathodic peak voltages (ΔE_p) is 57/*z* mV, where z is the number of electrons transferred. However, a peak-to-peak separation of 90/*z* mV is also generally considered to be in the reversible to quasireversible regime. The peak-to-peak separation of a reversible system will also be independent of sweep rate, whereas the ΔE_p of an irreversible system will shift 30/α*z* mV every decade change in scan rate, where α is the potential barrier symmetry constant [11] [14].

The previous derivations assume that the current response is coming only from faradaic reactions. It is well known that the existence of an electrical double layer also contributes to the current response when an electrode is stepped to a potential. The double layer is composed of charged ions held at the interface by electrostatic interactions. The weak bonding allows the double layer structure to produce charging currents immediately upon a voltage change. Since the voltage is constantly changing in a cyclic voltammogram, then a charging current is also constantly present. The presence of a large charging current may increase the peak current value and should be subtracted from the current response (Fig. 1.3.21). If the electrode is modeled as a

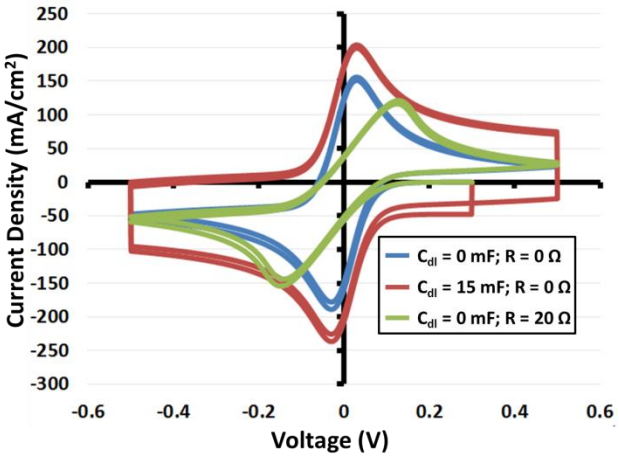

Figure 1.3.20: Effect of capacitance and resistance on CV shape of reversible system. Capacitance increases overall current response. Resistance mimics system with low k'.

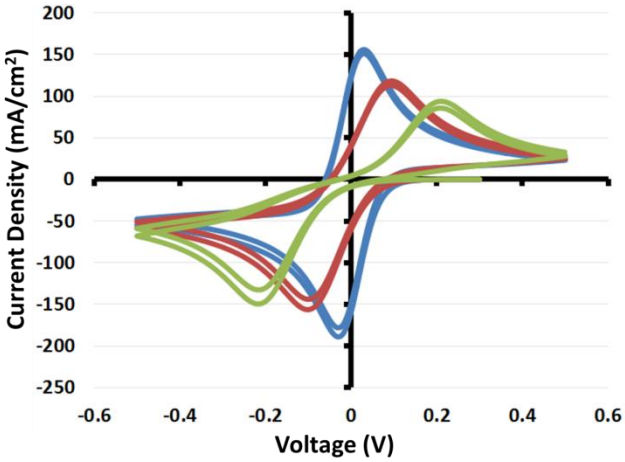

Figure 1.3.21: Effect of rate constant k' on CV. Reversible systems have large k' values while irreversible systems have small k' values.

simple RC circuit, where R_u is the uncompensated solution resistance and C_{dl} is the double layer capacitance, then the transient charging current present during a cyclic voltammogram can be defined as,

$$i_c = vC_{dl} + \left[{}^{E}/_{R_u} - vC_{dl}\right] exp\left({}^{-t}/_{R_u C_{dl}}\right) \qquad 1.3.44$$

This is an important relationship since it implies that the charging current is proportional to v whereas the faradaic peak current is proportional to $v^{1/2}$. Therefore, at fast scan rates or low concentrations, the charging current may be the dominant response [11]. This places practical limits on scan rates that should be chosen for a given system. In reality, the current response is a combination of various background currents along with the faradaic and charging currents [14] [15].

In addition to kinetics and thermodynamics, experimental parameters may also affect the shape of the voltammogram. Uncompensated resistance is defined as the solution resistance plus

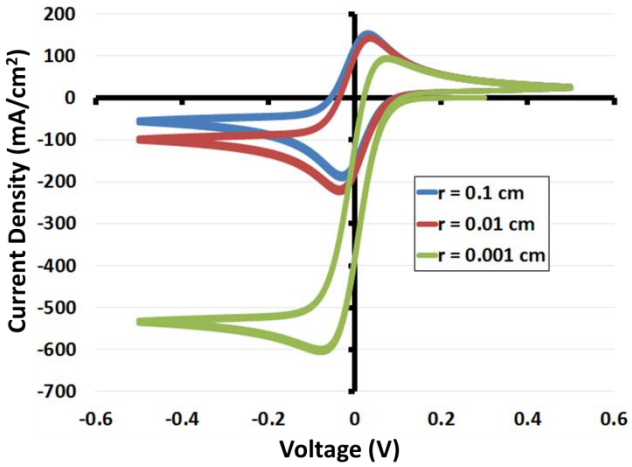

Figure 1.3.22: Electrode size effects on shape of CV. As electrode size decreases, diffusion behavior changes from linear to spherical. Reaction is now kinetically limited, as evident by plateau of limiting current.

any additional resistance due to the working electrode [11]. Depending on the electrolyte resistance, the distance between the working and reference electrodes may drastically increase the uncompensated resistance. This initially affects the shape of the curve by suppressing the peak current. Because of the exponential term in 1.3.44, the cell has a time constant defined as $\tau = R_u C_d$. Increasing the time constant increases the time it takes to charge the double layer. Therefore, in addition to suppressing the peak current, the peak potential shifts to larger overpotentials (Fig. 1.3.21). This effect is exaggerated with increasing scan rate and can mimic certain kinetic phenomena. Uncompensated resistance effects can also introduce a voltage gradient across the working electrode if it is not parallel to the reference electrode.

The size of the electrode can also influence the shape of the curve. If the electrode surface area is of the same size as the diffusion layer, the diffusion behavior of the active species can no longer be considered planar, and the current response becomes independent of the scan rate (Fig. 1.3.22) [11]. In other words, it obtains the limiting current described in section 1.3.2. This phenomenon occurs either when the electrode surface area is small or when the scan rate is

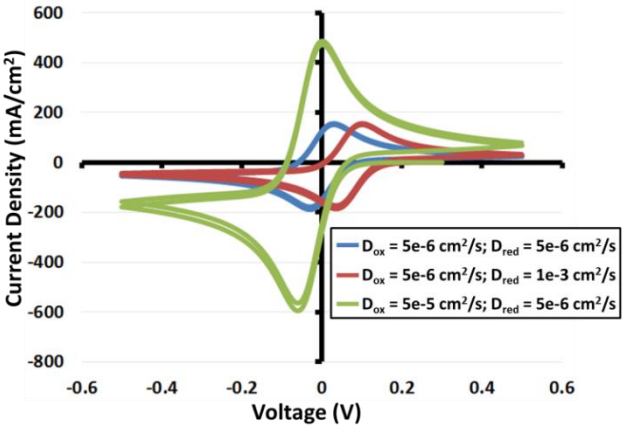

Figure 1.3.23: Effects of diffusion constants on shape of CV. Increasing the D_{red} shifts the oxidation peak to higher overpotentials. Increasing D_{ox} shifts the redution peak to higher overpotentials and increases the peak currents.

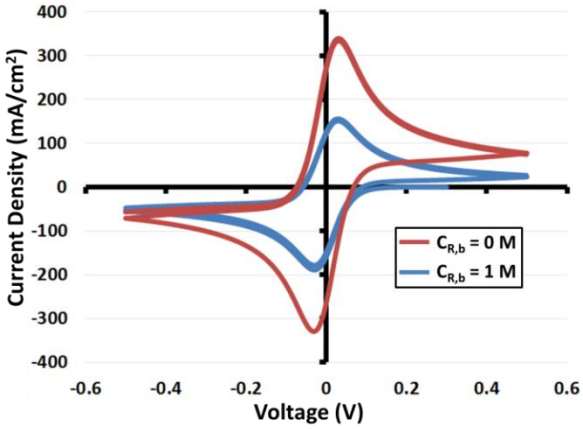

Figure 1.3.24: Effects of bulk reduced species concentrations. Increase in $C_{R,b}$ increases peak currents and shifts oxidation baseline to higher currents.

slow enough to create a large diffusion layer. When the latter occurs, it is often considered to be the lower limit of acceptable scan rates. A scan rate is too slow when the size of the diffusion layer creates natural convection that negates the concentration gradient within the electrolyte. To avoid this situation, a good estimate can be made using a maximum distance of 500 µm in the diffusion layer equation. The calculated time represents the maximum length of time an electrode should sit at the limiting current [14]. Other effects of various parameters on the shape of voltammogram curves are shown in Figure 1.3.23 and Figure 1.3.24.

Cyclic voltammetry is a powerful technique that can give you information about the kinetics of a particular system. However, it is considered to be more qualitative than quantitative. One of its strengths comes from the ability to perform experiments on multiple timescales. In doing this, it is possible to monitor both heterogeneous charge transfer reactions and homogeneous chemical reactions that may occur in the same system [10] [11]. A common example is a reversible charge transfer step followed by a reversible chemical reaction, described

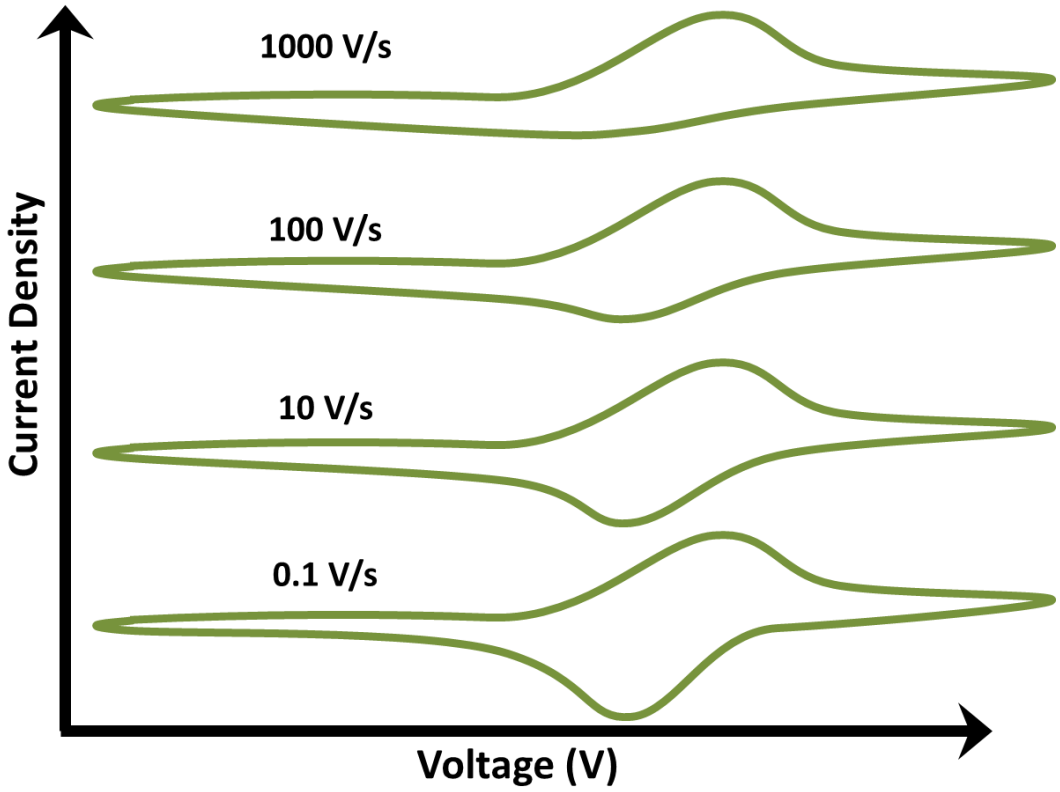

Figure 1.3.25: CV shape dependence on scan rate for reversible charge transfer followed by reversible chemical reaction [A + e^- ↔ B] [B ↔ C]. Assumed $k_f > k_b$ for the chemical reaction. At slow scan rates, chemical compounds B and C can reversibly form. At faster scan rates, chemical reaction C→B is not given enough time to occur. As a result, the charge transfer reaction [B → A + e^-] cannot occur during the reverse sweep.

in Figure 1.3.25. Unfortunately, a CV cannot give information about reaction mechanisms and must be used in conjunction with other characterization techniques to determine this type of data.

1.4 Battery Fundamentals

In 2010, the world consumed 552 exajoules, or 153 petawatt-hours, of energy [20]. At the present rate, this is expected to jump to 812 exajoules by 2035, an increase of 47% (Fig. 1.4.1). The task of supplying this energy becomes even more daunting when considering the environmental impact fossil fuels will have if used as the primary source for these demands. Possibly more than ever, the world is looking to alternative energy technologies as a viable complement to carbon-based fuels. Aside from reducing carbon emissions, an important requirement for future energy use is energy efficiency. Electrochemical energy devices meet these requirements by storing energy as it is harvested and providing continuous power when generators are inoperable.

1.4.1 Supercapacitors, Fuel Cells and Batteries

Electrochemical devices convert chemical energy directly into electrical energy, and, in some cases, vice versa. The three main categories of devices are electrochemical capacitors, fuel cells and batteries. Electrochemical capacitors utilize electrostatics to store charge at the

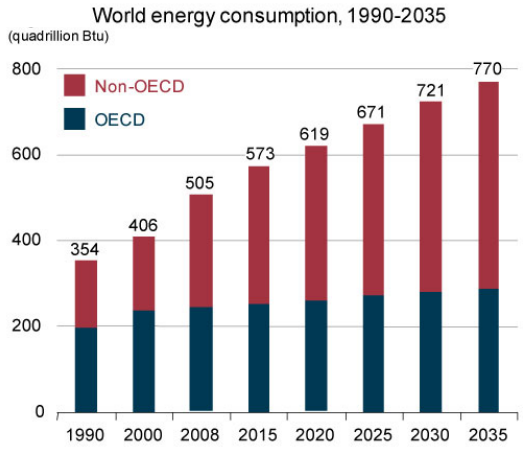

Figure 1.4.1: World energy consumption and projected values in quadrillion btu. OECD = Organization for Economic Cooperation and Development **[20]**

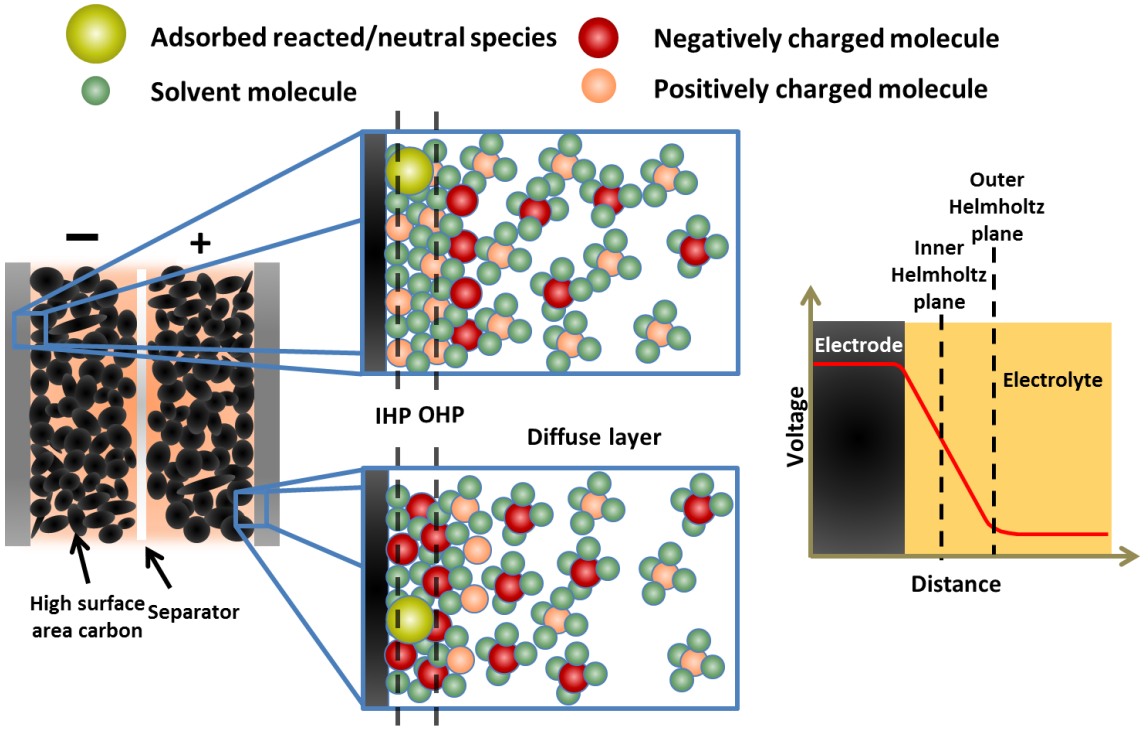

Figure 1.4.2: Structure of an electrochemical double layer. Inner Helmholtz plane defines layer of adsorbed ions and molecules. Outer Helmholtz plane describes layer of charged particles tightly bound by electrostatic forces. Diffuse layer is composed of loosely bound charged particles. Voltage drop across OHP is uniform through bulk electrolyte.

electrode/electrolyte interface, whereas fuel cells and batteries exploit redox reactions. For batteries and fuel cells, the operating voltage is dictated by the complementary chemical reactions occurring at each electrode. The voltage of an electrochemical supercapacitor is determined by the stability of the materials [17].

Electrochemical capacitors have been coined as "supercapacitors" due to their ability to store significant amounts of energy when compared to traditional ceramic or MIM capacitors. The basic principle behind its operation is the electrical double layer (Fig. 1.4.2). When a charged plate is immersed in an ionic solution, ions of opposite charge accumulate at the surface and are anchored by the local charge density in the electrode. Therefore, the charge storage mechanisms are similar to traditional capacitors in that only electrostatic interactions exist, but

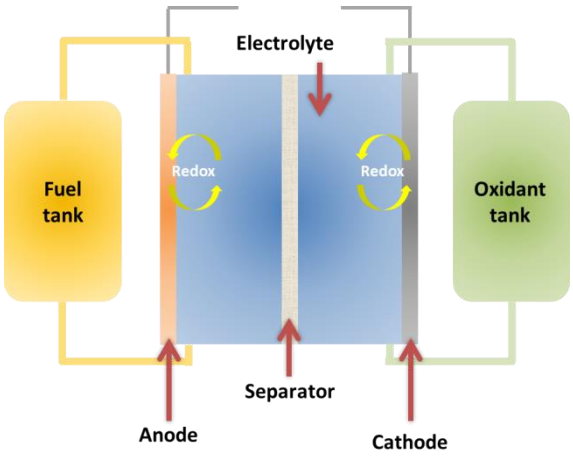

Figure 1.4.3: A fuel cell stores the active masses in separate tanks

the size of the dielectric layer is on the order of nanometers rather than microns. Many complex models exist in an effort to explain the double-layer structure for intricate pore structures [11]. However, it is generally accepted that an electrode can supply between 10 – 40 μF/cm^2 of actual surface area. The energy stored in a double-layer can be delivered in seconds to minutes due to the lack of faradaic reactions. Furthermore, supercapacitors can be cycled hundreds of thousands of times since there is no physical change to the electrode components. Current research is focused on improving the charge storage capabilities by introducing a fast redox couple or by utilizing materials that can withstand large voltages [21]. Supercapacitors are presently restricted to energy harvesting applications in automobiles and other large mechanical machines due to their high cost. However, there is great potential for supercapacitors to be used as power sources for memory devices if the price can be reduced.

A fuel cell is an open system in which the fuel, or active mass, is stored separately from the reaction compartment (Fig. 1.4.3) [21]. The reaction compartment contains two electrodes that exist solely as electron transfer sites. Electrical energy is generated once the fuel is introduced to the catalyst. Faradaic reactions involving fuels such as hydrogen, methanol and sugars are able to provide a substantial amount of energy. The counter reaction at the opposite

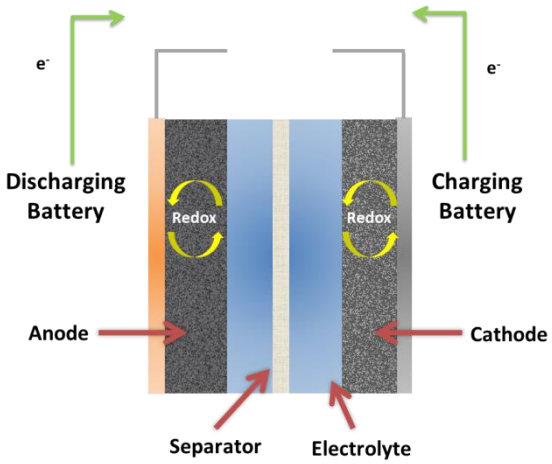

Figure 1.4.4: Batteries generate electricity using redox reactions. Active masses are located at electrode.

electrode is the reduction of an oxidant, typically oxygen, which must also be supplied. Once a fuel has been depleted, the storage unit must be replaced. In some cases, the cell must be cleaned between re-fuels. Thus, the complex manufacturing and operation of a fuel cell is a major drawback of this device. Despite the upkeep, fuel cells are ideal stationary power sources for buildings and cell phone towers. Fuel cells are also popular in space applications. Unfortunately, power restrictions have kept fuel cells out of the mobile electronics and automotive market.

Similar to fuel cells, batteries utilize redox reactions to create electricity. However, the active masses are located at each electrode, placing the conversion and storage sites in the same compartment (Fig 1.4.4) [17]. This requires the active mass to remain electrochemically inert until a load is placed between the two terminals. Upon closing the circuit, energy can be generated almost instantly. This feature also allows the device to manage varying current densities throughout its delivery. Batteries are extremely versatile since they can be a source for both intermittent and constant power. Depending on the chemistry, a battery can be further characterized as primary or secondary. A primary battery must be discarded after a single

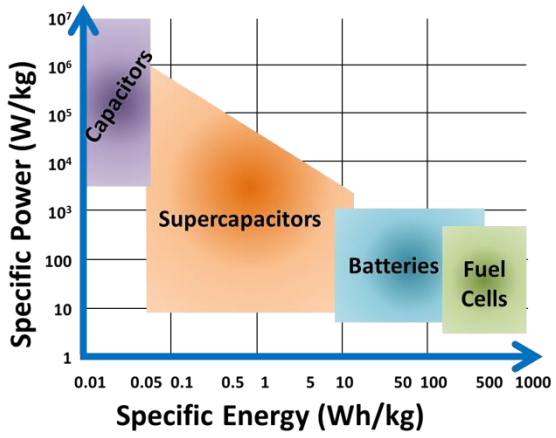

Figure 1.4.5: Ragone chart plotting relationship of energy and power for various energy storage devices. Adapted from **[17]**.

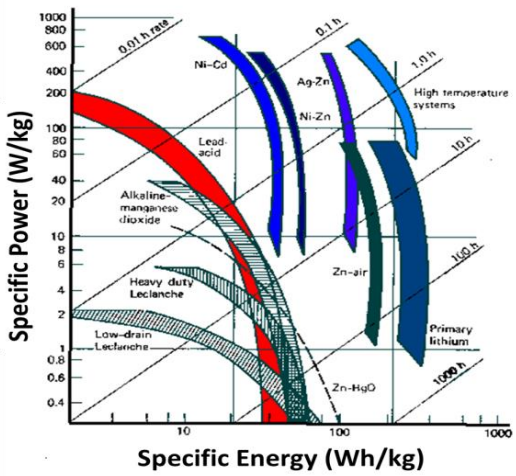

Figure 1.4.6: Ragone chart for various battery systems **[56]**

discharge, while some secondary batteries have been shown to discharge for thousands of cycles. Currently, batteries are the principal power source for all electronic devices. If the cost per kilowatt-hour can decrease by developing cheaper or higher energy density materials, batteries will most likely have a significant role in the automotive industry as well.

Figure 1.4.5 is known as a Ragone chart and plots the relationship between power and energy for each electrochemical device. From the figure, it can be concluded that supercapacitors store the least amount of energy but can deliver it very quickly when necessary. Fuel cells sit at the opposite end of the chart and can offer the most energy albeit at very low power. Bridging the gap between fuel cells and supercapacitors are batteries, which can provide medium amounts of energy and power. Another Ragone plot (Fig. 1.4.6) of only battery systems illustrates the wide range of capabilities available to different chemistries. It is this versatility that has brought so much recent attention to battery research.

1.4.2 Battery Components

A battery, like all electrochemical devices, consists of four main components: an anode, cathode, electrolyte and separator. A cell's performance is highly dependent upon the materials that are chosen for each. If any one of these components fails, an unsafe condition or even failure of the battery may occur. This section will be mostly focused on battery systems. However, the underlying concepts can be extended to nearly all electrochemical systems.

The electrolyte defines the voltage that all other materials must work within. In its most basic description, an electrolyte is a medium that conducts ions but not electrons. Typically this is composed of a salt dispersed in a liquid solvent, but there have been advances in the development of solid and gel electrolytes. Table 1.4.1 summarizes a few typical electrolyte systems and their properties. In addition to their conductive properties, all electrolytes must meet several requirements [22]. First, an electrolyte must be chemically and electrochemically inert over a wide voltage and temperature range. Any side reactions that occur due to electrolyte activity are considered parasitic and reduce the efficiency of the cell. Furthermore, this directly implies that the electrolyte has no influence over the theoretical energy density of a battery. However, any kinetic limitation associated with electrolyte resistance may influence the total

Table 1.4.1: Summary of properties for various electrolyte systems

Electrolyte	Type	Ionic Conductivity ($x10^{-3}$ S/cm)	Electrochemical Window (V)
0.1 M H_2SO_4	Aqueous	48	1.5
1.0 M HCl	Aqueous	330	1.5
1.0 M KCl	Aqueous	110	1.5
0.1 M $LiClO_3$	Aqueous	89	1.5
0.5 M KOH	Aqueous	290	1.5
1.0 M $LiClO_4$ in EC/DMC	Liquid organic nonaqueous	7	3.2
1M LiTFSI in EMI-TFSI	Ionic liquid	2	~ 3.8
LiTFSI-P(EO/MEEGE)	Polymer	0.1	~ 4.7
$Li_{4-x}Ge_{1-x}P_xS_4$	Inorganic solid	2.2	~ 5.0
$LiAlCl_4 + SO_2$	Inorganic liquid	70	~ 4.4

energy output of a battery. It should also be noted that in some cases, a limited reaction with the electrode is beneficial. Such passivation layers will be discussed later. Next, an electrolyte must be in contact with the electrode at all times regardless of any volume change that may occur. As mentioned previously, all electrochemical reactions occur at the electrode/electrolyte interface. Any discontinuity results in fewer reaction sites. Finally, the materials should be cheap and safe. This encompasses any flammability and toxicity issues.

Whereas the electrochemical definitions of anode and cathode covered in the previous chapter are very precise, the assembled device definitions can be vague. When discussing batteries, the term anode describes the material that is oxidized in a discharging battery, and cathode describes the material that is reduced under the same conditions. This method typically ignores traditional electrochemical electrode assignment and implies the user is aware of what battery system is being studied. For instance, carbon is always referred to as a lithium ion anode material regardless of the testing conditions. However, carbon can also be referred to as a cathode material for a Leclanche cell. Therefore, it is important to identify the battery system before comparing anode and cathode materials.

The anode and cathode reaction potentials should be as close to the electrolyte voltage limits as possible in order to maximize the operating voltage of the battery (Fig 1.4.7). Reactions occurring outside the electrochemical window will result in electrolyte degradation and an increase in cell impedance. In some arrangements, a current collector is necessary to include as part of the electrode. This acts as a nonreactive, electronically conducting substrate that links the active material to the outside circuit. Because the anode and cathode operate at different voltages, the same metal may not be compatible at both electrodes. Current collector degradation can lead to electrolyte poisoning and increased cell impedances.

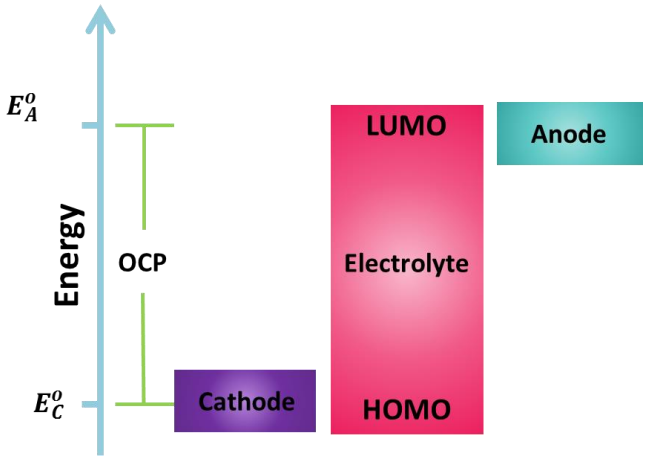

Figure 1.4.7: Redox energy levels of the anode and cathode should be as close to the electrolyte limits as possible. Adapted from **[22]**

Separators are physical barriers between the anode and cathode that prevent an electrical short. Therefore, the separator must be an electronic insulator but also not interfere with ion diffusion. The first separators were simple porous filters. Today's separators are quite complex and designed for specific battery systems. Examples of separator considerations are electrolyte wettability, porosity, corrosion resistance, mechanical integrity and thermal management [23]. Because it does not participate in the electrochemical process, separators are thought of as dead space in a battery. Therefore, efforts are focused on reducing the size and weight without sacrificing functionality. Future separators will most likely evolve to take on the role of electrolytes as new methods for depositing nanometer thick, ionically conducting ceramics are developed.

1.4.3 Battery Terms and Concepts

1.4.3.1 Energy and power

The most important metrics of a battery are energy and power. Energy can be defined as the battery's ability to do work and power is defined as how quickly that work can be performed

[8]. It is sometimes easier to relate work and power to the performance of a car. In this analogy, energy is comparable to the distance the car can drive, and power is comparable to how fast it can drive. Energy can be expressed in watt-hours (Wh) or joules (J), and power is expressed in watts (W). The amp-hour (Ah) is another common unit and is a measurement of charge storage, or capacity. Because an amp is one coulomb per second, an amp-hour is simply 3600 coulombs. Similarly, a watt-hour is 3600 joules. Notice that the capacity and energy only differ by a voltage term, implying that it is impossible to calculate energy from a half-cell experiment. Therefore, most reported figures are capacity measurements.

Energy and power are commonly normalized for comparison reasons. When normalized by weight, this term is known as specific energy and power, whereas energy and power density is normalized by volume or area. Mass normalized values are of importance for large vehicular applications such as automobiles or spacecraft. Volumetric normalizations are mostly used for miniature mobile electronics or stationary power sources where space is limited. Areal normalizations are useful for half-cell electrode comparisons or when an assembled battery has not been realized.

The total capacity available is directly related to the battery chemistry and mass of active material [23]. The theoretical specific capacity (mAh/g) can be calculated using Faraday's Law,

$$Theo\ Cap = \frac{zF}{3.6(MW)} \qquad 1.4.2$$

where z is the number of electrons transferred per mole of product, and MW is the molecular weight of the material. Multiplying by the expected operating voltage yields the theoretical specific energy density of a material.

1.4.3.2 Rate capability testing

Battery and electrode performance are analyzed using the galvanostatic discharge technique. There are two methods for testing the rate capabilities of a cell, the most common being the C-rate [8]. To calculate the C-rate, simply divide the applied current by the maximum capacity of the electrode. For example, if an electrode is loaded with 1 mAh and discharged at 0.5 mA, then this is called C/2.C-rates can also be converted to specific current as illustrated in Figure 1.4.8. Note that the C-rate method actually represents a percentage of the maximum capacity and therefore should be thought of as a material utilization measurement rather than a benchmark figure. C-rates are especially useful when investigating new materials or synthesis methods to determine the extent of completion for a reaction. Unfortunately, C-rates of different electrodes are not comparable since it offers no insight to the current distribution or electrode properties. The shortcomings of C-rates can be exposed in two hypothetical examples.

Assume Electrode A has 5 mg of 100 mAh/g active material for a total of 0.5 mAh, and Electrode B has 5 mg of 1000 mAh/g active material for a total of 5 mAh. Therefore, the respective C/5 currents are 0.1 mA and 1 mA. If both achieve the same efficiency, a comparison

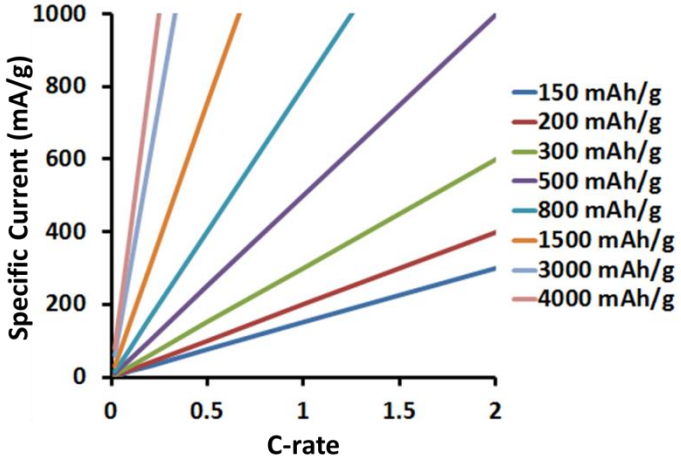

Figure 1.4.8: Relationship between C-rate and specific current (mA/g) testing methods.

would conclude both electrodes performed equally, even though Electrode B obtained a higher capacity while operating at a higher current. Now let's assume there is a third Electrode C loaded with 0.5 mg of 100 mAh/g active material for a maximum capacity of 0.05 mAh. If Electrode 1 reached 90% of its theoretical capacity at a C/5 rate and Electrode 3 obtained 100% efficiency at a C-rate, then a comparison would conclude Electrode 3 outperformed Electrode 1. Upon closer inspection, Electrode 1 actually obtained 0.45 mAh under 0.1 mA while Electrode 3 only obtained 0.05 mAh at 0.05 mA. In both situations, the C-rate comparisons failed to distinguish proper performance values. Therefore, a fair comparison can only be made if two electrodes are the same size and loaded with the same maximum capacity.

A useful analysis metric to complement the C-rate is the area normalized current density. Current density enables accurate electrode testing condition comparison since it gives information on the current distribution throughout the electrode size. This standard allows one to determine the current densities at which local irregularities begin to adversely affect a cell's performance. This is useful when setting limits on power distribution of a device. The two most important merits of an electrode are performance and efficiency. Unfortunately, no single normalization can accurately report both properties. Therefore, it is good practice to report the current and capacity results using multiple normalization standards.

1.4.3.3 Coulombic efficiency, capacity fade and self-discharge

Rechargeable batteries often involve various physical changes during cycling that can affect the charge storage capabilities of the material. Two properties that measure cycling inefficiencies are coulombic efficiency and capacity fade. Coulombic efficiency refers to the ratio of discharge capacity to charge capacity during a single cycle. This value can be higher than

99% for commercial batteries. Capacity fade, on the other hand, is the difference in discharge capacity between successive cycles. Commercial batteries are required to maintain 80% of the original capacity over 300 cycles and 60% over 800 cycles. This strict benchmark requires a capacity fade of less than 0.1% (Figure 1.4.9). Issues that cause these losses include increased diffusion tortuosity, loss of electrical contact, mechanical failure and ion trapping. In some cases, parasitic side reactions such as the continued formation of a passivation layer are significant sources of irreversible losses [8] [23].

Self-discharge of a battery helps predict how a battery will behave when no current is drawn. This includes shelf-life and other situations such as a powered down electronic device. Self-discharge can be quantized by charging a cell then monitoring the open circuit voltage for an extended length of time. Lithium ion batteries are known to have low self-discharge, whereas nickel metal-hydride batteries can lose 40% of their charge in the first 24 hours of open circuit [23].

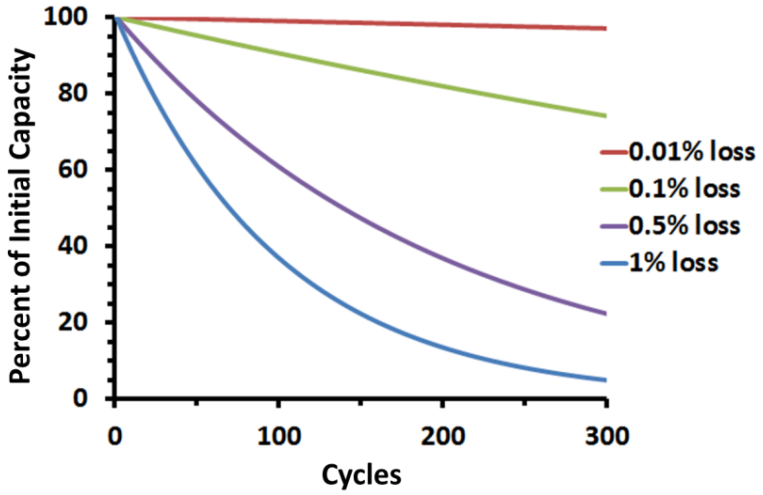

Figure 1.4.9: Chart illustrating average capacity fade requirements for commercial batteries.

1.4.4 Material Limits on Batteries

Currently, Envia Systems claims the highest specific energy for a packaged lithium ion battery (400 Wh/kg) and Samsung claims the largest energy density (600 Wh/l), also for a fully packaged battery. It is interesting that both companies use very different approaches. Envia pushes the limits by implementing state of the art anode and cathode material, whereas Samsung uses traditional, albeit improved, electrode materials in conjunction with advanced nonactive components. Although efforts are focusing on improving each component of a battery, the major progress in battery performance will come from the development of anode and cathode materials. Table 1.4.2 lists the anode and cathode materials for a few well-known battery systems. All calculations were based strictly on the solid active material and did not include the weight of any packaging or electrolyte.

From the table, it is apparent that there is no perfect electrode material. Some materials such as sulfur demonstrate high specific capacities but are unable to offer large volumetric capacities. Other materials, such as lead, have the exact opposite properties. The table combined with equation 1.4.1 reveals that a fine balance must exist between a material's density, the mass of the atoms involved and the governing chemical reaction. Mathematically, the ideal electrode would have light elements arranged in a very small crystal lattice and involve more than one mole of electrons per reaction. In practice, a lithium ion material with that description would most likely have an unstable crystal structure like that of $LiCoO_2$ or succumb to a massive volume change similar to silicon. Thus, the development of new materials and chemistries is an essential and gradual part of improving the energy storage capabilities of batteries.

Material	Electrode	Battery	Type	Material Density (g/cm^3)	Specific Capacity (mAh/g)	Volumetric Capacity (mAh/mL)	Theoretical Voltage (V)	Specific Energy (mWh/g)	Volumetric Energy (mAh/cm^3)	Chemical Reaction	Notes
MnO_2	Cathode	Zn-MnO_2	Aqueous primary	5.03	308	1549	1.5	462	2324	$2MnO_2 + H_2O + 2e^- \rightarrow Mn_2O_3 + 2OH^-$	
Zinc	Anode	Zn-air Zn-MnO2	Aqueous primary	7.24	824	5966	1.65	1360	9844	$Zn + 2OH^- \rightarrow ZnO + H_2O + 2e^-$	
Aluminum	Anode	Al-air	Aqueous primary	2.7	2978	8041	2.7	8041	21710	$Al + 4\ OH^- \rightarrow Al(OH)_4^- + 3e^-$	
Lithium	Anode	Li-air	Aqueous primary	0.5	3830	1915	3	11490	5745	Multiple reaction types	* does not include mass of products
Cadmium	Anode	NiCd	Aqueous secondary	8.65	479	4143	1.3	623	5386	$Cd + 2OH^- \rightarrow Cd(OH)_2 + 2e^-$	
Metal Hydride	Anode	NiMH	Aqueous secondary	6.5	97	631	1.4	136	883	$MH + OH^- \rightarrow M + H_2O + e^-$	* assumes mass of MH = 276
NiOOH	Cathode	NiMH NiCd	Aqueous secondary	6.5	291	1892	1.4	407	2648	$NiOOH + H_2O + e^- \rightarrow Ni(OH)_2 + M$	* does not include mass of water
Lead	Anode	Pb-acid	Aqueous secondary	11.3	260	2938	2.1	546	6170	$Pb + SO_4^{2-} \rightarrow PbSO_4 + 2e^-$	
PbO_2	Cathode	Pb-acid	Aqueous secondary	9.8	224	2195	2.1	470	4610	$PbO_2 + SO_4^{2-} + 4H^+ + 2e^- \rightarrow PbSO_4 + 2H_2O$	
Carbon	Anode	Li-ion	Nonaqueous secondary	2.2	372	818	3.0 - 4.5	1,116 - 1,674	2,450 - 3,680	$Li^+ + e^- + 6C \rightarrow LiC_6$	* discharge = 0.1 V vs Li
Lithium	Anode	Li-ion	Nonaqueous secondary	0.5	3830	1915	3.0 - 4.5	11,580 - 17,370	5,790 - 8,690	$Li^+ + e^- \rightarrow Li$	* discharge = 0 V vs Li
Silicon	Anode	Li-ion	Nonaqueous secondary	2.3	4200	9660	3.0 - 4.0	12,600 - 16,800	28,980 - 38,640	$4.4Li^+ + 4.4e^- + Si \rightarrow Li_{4.4}Si$	* discharge = 0.5 V vs Li; 300% volume change
Tin	Anode	Li-ion	Nonaqueous secondary	7.3	990	7227	3.0 - 4.0	2,970 - 3,960	21,680 - 28,910	$4.4Li^+ + 4.4e^- + Sn \rightarrow Li_{4.4}Sn$	* discharge = 0.65 V vs Li; 400% volume change
Aluminum	Anode	Li-ion	Nonaqueous secondary	2.7	990	2673	3.0 - 4.0	2,970 - 3,960	8,020 - 10,690	$Li^+ + e^- + Al \rightarrow LiAl$	* discharge = 0.4 V vs Li
$LiCoO_2$	Cathode	Li-ion	Nonaqueous secondary	5.15	150	773	3.9	585	3013	$Li + e^- + CoO_2 \rightarrow LiCoO_2$	* practical capacity is 150 mAh/g
$LiFePO_4$	Cathode	Li-ion	Nonaqueous secondary	3.7	170	629	3.3	561	2076	$Li + e^- + FePO_4 \rightarrow LiCoPO_4$	
$LiNiO_2$	Cathode	Li-ion	Nonaqueous secondary	4.8	220	1056	3.8	836	4013	$Li + e^- + NiO_2 \rightarrow LiNiO_2$	
$LiMn_{0.3}Ni_{0.3}\ Co_{0.3}O_2$	Cathode	Li-ion	Nonaqueous secondary	4.7	300	1410	3.6	1080	5076	$Li + e^- + Mn_{0.3}Ni_{0.3}\ Co_{0.3}O_2 \rightarrow LiMn_{0.3}Ni_{0.3}\ Co_{0.3}O_2$	* practical capacity is 200 mAh/g
$LiMn_2O_4$	Cathode	Li-ion	Nonaqueous secondary	4.2	154	647	4	616	2587	$Li^+ + e^- + Mn_{0.3}Ni_{0.3}\ Co_{0.3}O_2 \rightarrow LiMn_{0.3}Ni_{0.3}\ Co_{0.3}O_2$	
$LiMnO_2$	Cathode	Li-ion	Nonaqueous secondary	4.2	308	1294	4.1	1263	5304	$Li + e^- + MnO_2 \rightarrow LiMnO_2$	* practical capacity is 150 mAh/g
$LiNi_{0.8}Co_{0.15}Al0_{0.5}O_2$	Cathode	Li-ion	Nonaqueous secondary	4.8	300	1440	3.8	1140	5472	$Li^+ + e^- + Ni_{0.8}Co_{0.15}Al0_{0.5}O_2 \rightarrow LiNi_{0.8}Co_{0.15}Al0_{0.5}O_2$	* practical capacity is 180 mAh/g
Sodium	Anode	Na-S	Nonaqueous secondary	0.97	479	465	2.1	1006	976	$2Na^+ + 2e^- \rightarrow 2Na$	
Sulfur	Cathode	Na-S	Nonaqueous secondary	1.8	558	1004	2.1	1172	2109	$3S + 2e^- \rightarrow S_3^{2-}$	* must be in liquid state;

Table 1.4.2: Summary of the maximum energy storage capabilities for various battery materials. Mass of packaging and electrolyte were not included in calculations.

1.5 Three Dimensional Batteries: Description and Classification

The idea to improve battery performance by designing high surface area electrodes is somewhat contradictory to accepted battery theory. It is well known that large surface areas increase the number of irreversible side reactions, thus limiting the battery's cycle life and energy density. However, in 2003 the idea of engineering an electrode based on designs of the current photonic devices was suggested by Hart et al [24]. It was believed that both diffusion and charge transport distances can be kept at a minimum using this design. In addition, energy densities can be maintained by simply stacking the material vertically rather than horizontally. This concept was coined as three dimensional batteries.

Since the introduction of 3D batteries, a number of designs have been proposed. This has mostly been attributed to the improvement of fabrication methods. Each design has a unique approach to accomplish both high energy and power density and therefore come with its own unique set of challenges. Unfortunately, as the movement for 3D batteries gains momentum, the definition of a true 3D battery has been lost among the many attempts to be classified as three-dimensional. This stems from the numerous methods possible to make a structure three dimensional on both the nano- and micro-scale. The following discussion will analyze current 3D-based electrode performances and attempt to classify the designs into three categories: 3D batteries, 3D electrodes and 3D nanostructures. Most performance figures will be normalized per footprint area rather than volume since reported results often lack comparable testing volumes.

1.4.1 3D Batteries

A design can be categorized as a 3D battery if the electrode/electrode and electrode/electrolyte interfaces are nonplanar (Fig 1.5.1). Feature sizes such as posts, scaffolds or

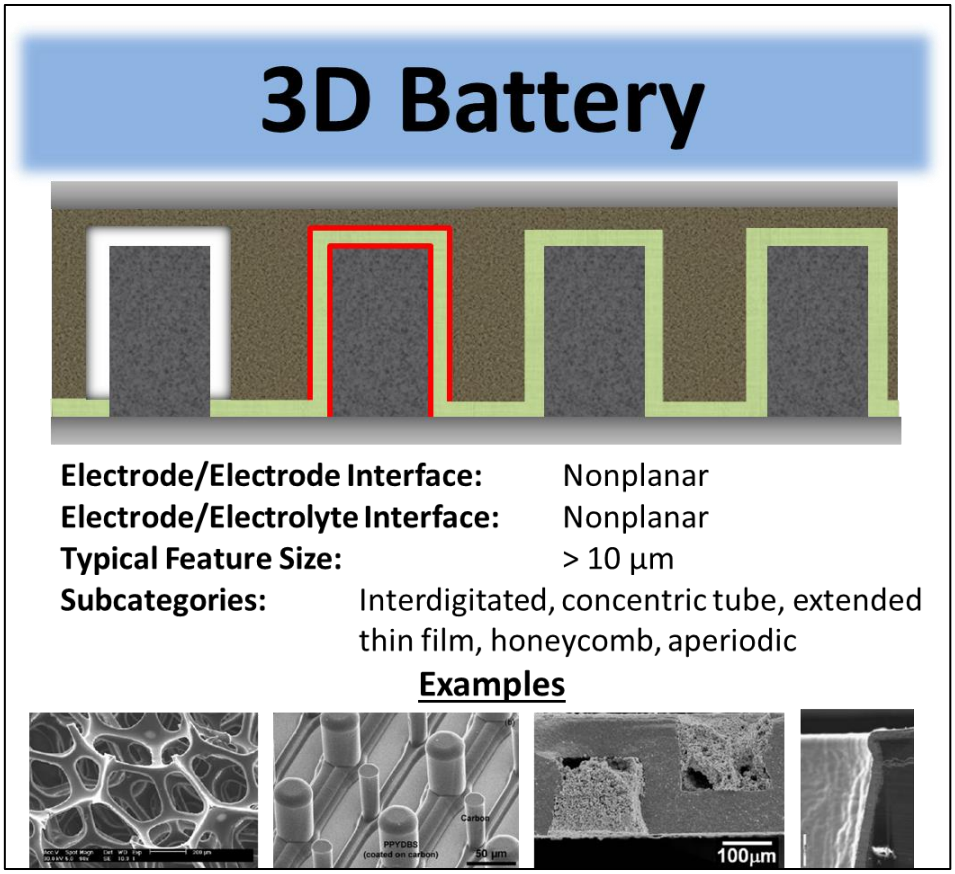

Figure 1.5.1: Definition and examples of a 3D battery. Red interface shows nonplanar electrode/electrolyte interface. White interface shows nonplanar electrode/electrode interface.

pores must be large enough to accommodate the necessary battery materials. A typical process flow for a 3D battery involves fabrication of a nonplanar electrode followed by the introduction of an electrolyte and separator. The final step incorporates the counter electrode material through various techniques. 3D batteries can be further categorized into the concentric tube, interdigitated, honeycomb, extended thin-film or aperiodic designs.

Min et al [25] demonstrated one of the first 3D batteries adopting the interdigitated rod design. Using alternating rods of carbon and PPYDBS, a capacity of 0.011 mAh/cm^2 was achieved at a current density of 0.02 mA/cm^2. Recently, Yoshima et al [26] fabricated a 3D battery using interdigitated plates of $LiCoO_2$ and $Li_4Ti_5O_{12}$ and achieved 0.27 mAh/cm^2 at a rate

of 0.42 mA/cm^2, albeit at a low voltage. The interdigitated design is among the easiest of 3D batteries to fabricate, but has an inherent limit on the maximum volumetric energy density due to the large volume occupied by electrolyte. However, batteries of this kind can offer insight to the electrochemical properties of high surface area, nonplanar interfaces.

The interdigitated design gradually led to the concentric tube architecture. This design maximizes the volumetric energy density by using a thin solid electrolyte separator to confine the electrolyte to a limited volume. Furthermore, depending on the fabrication method, it may be possible to incorporate numerous types of active material. In 2007, Chamran et al [27] reported areal capacities of 1.6 mAh/cm^2 at a rate of 0.05 mA/cm^2 and 2 mAh/cm^2 at 0.02 mA/cm^2 for vanadium oxide nanoroll (VONR) and mescarbon microbead (MCMB) half-cells prepared by colloidal processing methods, respectively. The biggest challenge of concentric tube batteries is the deposition of a conformal solid electrolyte separator over irregular surfaces. Shadowing effects of the large features often lead to uneven layering or pinholes that eventually cause electrical shorts. However, advances in deposition techniques are yielding promising results in the first generation of 3D batteries. In one example, Proell et al [28] managed to create $LiMn_2O_4$ cones using a UV laser. Lithium vanadium silicon oxide and aluminum were RF sputtered as the solid electrolyte separator and anode, respectively. This structure obtained 0.03 mAh/cm^2 at a rate of 0.024 mA/cm^2 but suffered from large capacity fade.

Honeycomb structures circumvent the conformal coating issue by using a solid electrolyte separator as the starting material. Kotobuki et al [29] accomplished this by machining a $Li_{0.35}La_{0.55}TiO_3$ solid electrolyte and filling the wells with active material. The resulting battery obtained 0.0073 mAh/cm^2 at a current density of 0.00625 mA/cm^2. The biggest challenge with

this design is preparing a starting material that is mechanically capable of handling the filling process but also thin enough to facilitate lithium ion diffusion.

The extended thin film design uses a structured scaffold as a template over which a thin film of the necessary materials is layered. In one case, Baggetto et al [30] etched 20 micron-deep wells in a silicon substrate and layered a thin film of amorphous silicon over the template. This electrode achieved 0.255 mAh/cm^2 at a rate of 0.025 mA/cm^2. In another design, Golodnitsky et al [31] [32] [33] utilized microchannel plates composed of 500 µm deep pores 50 µm in diameter to act as a template for the deposition of active materials. They have shown that chemical vapor deposition, electrochemical deposition and electrophoretic deposition techniques can produce very uniform films of CuS, $LiFePO_4$, TiN, and MoS_2. To date, their best device has been a 2.5D battery consisting of a lithium anode and a 3D CuS cathode which achieved 2.5 mAh/cm^2 at a current density of 0.2 mA/cm^2. The extended thin film construct is capable of operating at fairly large current densities. However, because of the volume occupied by the scaffold, the volumetric energy densities are severely limited. Furthermore, this design is limited only to the materials compatible with the deposition techniques.

Various aperiodic designs have been proposed using aerogels, foams or inverse opal structures as the skeleton of the electrode. Similar to the extended thin film design, aperiodic structures can handle fairly large current densities, but tend to have low volumetric energy densities. This architecture typically involves a three dimensional scaffold prepared by sol-gel methods or heat treatments. The scaffold is either one of the active components or acts as a current collector. The other battery components are then electrochemically deposited or filled using vacuum infiltration. Surprisingly, Ergang et al [34] used this fabrication technique to successfully build an aperiodic 3D battery with nanosized features. In the study, a carbon inverse

opal structure was coated with polymer electrolyte and infiltrated with a V_2O_5 aerogel. The battery only achieved 0.0065 mAh, yet showed the potential for this particular fabrication technique. In another example of an aperiodic design, Johns et al [35] electrodeposited manganese dioxide onto reticulated vitreous carbon (RVC). When assembled with a planar lithium anode, the device achieved 14.3 mAh/cm^2, but faded to less than 3 mAh/cm^2 after only fifteen cycles.

When comparing 3D batteries, it can be seen that feature sizes are typically greater than 10 μm in order to accommodate the necessary battery components. As a result, aspect ratios of 3D batteries are rarely larger than 10:1. It is also evident that very few 3D batteries have been realized because of the challenges involved with solid electrolyte separator coatings. However, as deposition techniques mature, the possibility of using previously unknown materials as solid electrolytes becomes a reality.

Group	Category	Sub-category	Cell Type	Capacity (mAh/cm^2)	Current Density (mA/cm^2)	Active Mass Loading (mg/cm^2)	Notes
Min et al	3D Battery	Interdigitated	Battery	0.011	0.02	0.82	**Anode** – pyrolized carbon posts **Cathode** – electrodeposited PPYDBS on carbon posts
Yoshima et al	3D Battery	Interdigitated	Battery	0.27	0.42	~ 1.4	**Anode** – $LiCoO_2$ wall **Cathode** – Li_4Ti_5O wall
Izumi et al	3D Battery	Concentric Tube	Half-cell	1.0 – 0.9	1.0 – 5.0	6.25	**Anode** – Lithium foil **Cathode** – micro printed $Li_4Ti_5O_{12}$ wall
Chamran et al	3D Battery	Concentric Tube	Half-cell	1.6	0.05	5.57	Colloidal processing of vanadium oxide nanoroll posts
Chamran et al	3D Battery	Concentric Tube	Half-cell	2.0	0.02	9.1	Colloidal processing of MCMB posts
Teixidor et al	3D Battery	Concentric Tube	Half-Cell	0.35	0.076	~ 3.0	Posts of pyrolyzed SU8 photoresist with MCMB attached
Proell et al	3D Battery	Concentric Tube	Battery	0.03	0.024	1.1	**Anode** – Lithium foil **Cathode** – Laser etched $LiMn_2O_4$ cones
Kotobuki et al	3D Battery	Honeycomb	Battery	0.0073	0.00625	~ 11	**Anode** – $LiMn_5O_{12}$ wells in machined solid electrolyte **Cathode** – $LiCoO_2$ wells in machined solid electrolyte
Baggetto et al	3D Battery	Extended Thin Film	Half-cell	0.255	0.025	< 1.0	LPCVD thin film of polycrystalline silicon
Mazor et al	3D Battery	Extended Thin Film	Battery	2.3 – 2.1	0.05 – 0.2	~ 3.0	**Anode** – Lithium foil **Cathode** – Electrodeposition of CuS thin film on $LiFePO_4$
Nathan et al	3D Battery	Extended Thin Film	Battery	2.0 – 1.0	0.2 – 1.0	~ 11	**Anode** – Spin coat MCMB in wells **Cathode** – Electrodeposited $Li_xMoO_yS_z$ thin film
Ergang et al	3D Electrode	Inverse Opal	Battery	-	-	-	**Anode** – inverse opal carbon structure **Cathode** – vacuum infiltrated V_2O_5 aerogel
Johns et al	3D Battery	Aperiodic	Battery	14.3 – 2.2	1.4	-	**Anode** – Lithium foil **Cathode** – MnO_2 electrodeposited on RVC
Roberts et al	3D Battery	Aperiodic	Battery	1.5	0.35	9.09	**Anode** – Lithium foil **Cathode** – $LiFePO_4$ spin coated on RVC

Table 1.5.1: Comparison of 3D battery results in literature

1.5.2 3D Electrodes

Most structured three dimensional architectures found in literature fall under the 3D electrode category. When assembled as a battery, a 3D electrode has a nonplanar electrode/electrolyte interface, but a planar electrode/electrode interface (Fig 1.5.2). Examples of 3D electrodes are core-shell nanowires, vertically aligned nanotubes and some aerogel structures [36] [37] [38] [39] [40].

The most common 3D electrodes reported in literature are core-shell nanowires. These electrodes are composed of vertically aligned metallic nanotubes grown using either top-down or bottom-up methods. A thin layer of active material is then formed around each nanotube

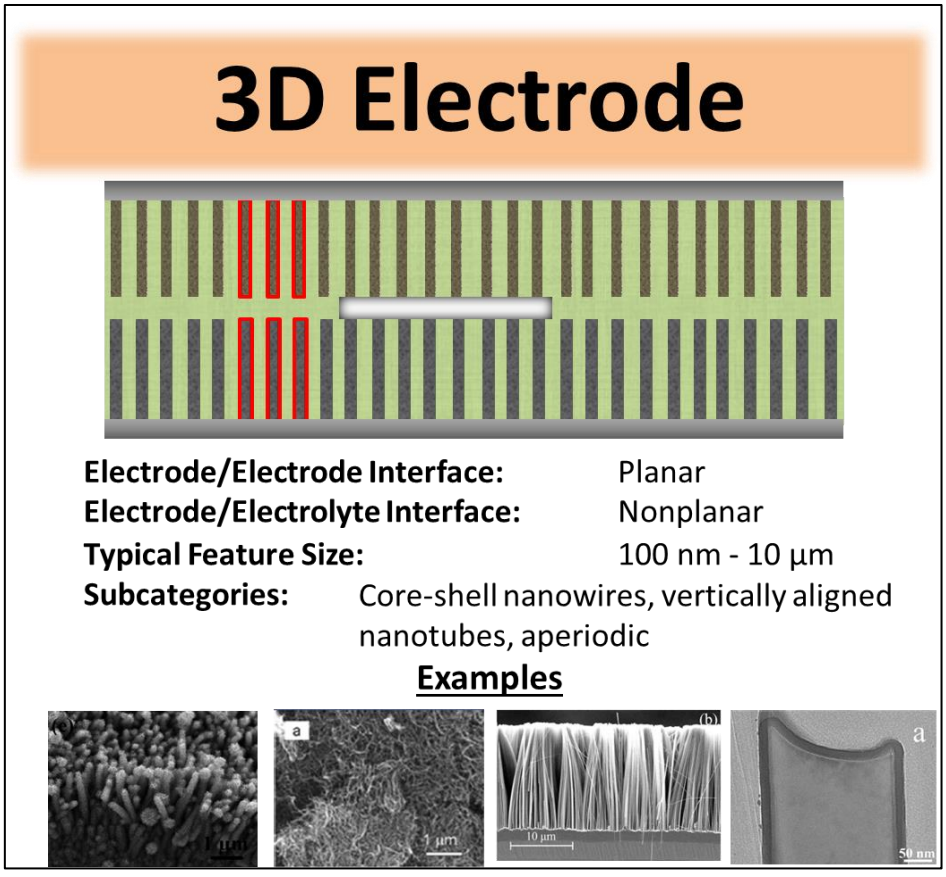

Figure 1.5.2: Definition and example for 3D electrodes. Red interface shows nonplanar electrode/electrolyte interface. White interface shows planar electrode/electrode interface.

allowing the metallic array to act as a three dimensional current collector. In one instance, a network of nickel nanowires was coated with TiO_2 using ALD and discharged at 0.016 mA/cm^2 [39]. The resulting areal capacity was 0.16 mAh/cm^2. In another example, Zeng et al [41] coated an array of ZnO with SnO_2 followed by a coating of Fe_2O_3 using an aqueous wet chemical process. This electrode obtained a stable 0.9 mAh/cm^2 at a discharge rate of 0.1 mA/cm^2. Recently, Fe_3O_4 nanotubes were coated with glucose and pyrolyzed to form a low-cost anode. When discharged at a rate of 0.02 mA/cm^2, the electrode achieved 0.637 mAh/cm^2 [42].

Another popular 3D electrode design utilizes vertically aligned nanotubes of the active material. Chan et al [43] [44] showed that silicon and germanium nanowires can achieve high rate capabilities and maintain their mechanical integrity despite extreme volume expansion upon lithiation. In another example, Tian et al [45] achieved an impressive 4.3 mAh/cm^2 at 1.7 mA/cm^2 using a low quality porous anodized alumina template to grow Ni-Sn nanowire networks by electrodeposition.

3D electrode aperiodic designs such as those pioneered by Rolison et al [46] are similar to 3D battery aperiodic designs in that they both have high porosity and non-repeating features. New aperiodic designs other than aerogels and foams are also beginning to be realized. In 2011, Lai et al [47] discovered that sintering $LiCoO_2$ particles forms a porous network of active material that doesn't require carbon additives or a binder. This electrode obtained 5.6 mAh/cm^2 at a rate of 1.7 mA/cm^2 when assembled as a battery with a lithium anode.

The main difference between 3D batteries and 3D electrodes lays in the ability to incorporate the remaining battery materials. Whereas 3D battery features are on the micron scale, 3D electrode features are typically nanosized. The combination of small pores and large aspect ratios makes it extremely difficult to efficiently introduce a solid electrolyte and complementary

electrode material. Furthermore, most 3D electrodes have a limited amount of active material available due to the time consuming nature of the deposition techniques required to coat nano features. Therefore, it is often difficult to obtain the proper mass loadings necessary for a high energy density battery. However, the increased surface area leads to the ability to operate at relatively high current densities and larger capacities compared to thin film batteries. Finally, it should be pointed out that 3D electrode surface area gains are much larger than those of 3D batteries. It is expected that most 3D electrodes will be prone to irreversible side reactions and suffer from large capacity fade.

Group	Category	Sub-category	Cell Type	Capacity (mAh/cm^2)	Current Density (mA/cm^2)	Active Mass Loading (mg/cm^2)	Notes
Wang et al	3D Electrode	Core-shell Nanowire	Half-cell	0.726	1.4	0.9	Sn sputtered on Cu nanowires
Wang et al	3D Electrode	Core-shell Nanowire	Half-cell	0.16	0.016	1.6	Ni nanowire network coated with TiO_2
Shaijumon et al	3D Electrode	Core-shell Nanowire	Battery	0.12	0.024	0.86	**Anode** – Lithium foil **Cathode** – Al nanorods coated with $LiCoO_2$
Xie et al	3D Electrode	Core-shell Nanowire	Half-cell	0.637	0.02	0.8	Anodized Fe_3O_4 nanotubes coated with carbon shell
Wang et al	3D Electrode	Core-shell Nanowire	Half-cell	1.94	1.87	1.0	$Si_{1-x}Ge_x$ sputtered on Cu nanowires
Gowda et al	3D Electrode	Core-shell Nanowire	Battery	0.032	0.04	< 1.0	**Anode** – Lithium foil **Cathode** – PANI coated porous gold nanowires
Gowda et al	3D Electrode	Vertically Aligned Nanowires	Half-cell	0.9	0.12	2.0	Ni-Sn nanowires coated with PMMA solid electrolyte separator
Zeng et al	3D Electrode	Vertically Aligned Nanowires	Half-cell	0.9	0.1	0.752	$SnO_2/\alpha\text{-}Fe_2O_3$ nanowires
Tian et al	3D Electrode	Vertically Aligned Nanowires	Half-cell	4.3	1.7	8.6	Nanowire network of Ni-Sn alloy
Lai et al	3D Electrode	Aperiodic	Battery	5.9	1.7	36	**Anode** – Lithium foil **Cathode** – porous sintered $LiCoO_2$
Gerasopolous et al	3D Electrode	Other	Battery	0.038	0.009	0.27	**Anode** – Lithium foil **Cathode** – V_2O_5 layerd on Cu nanorods grown on gold micro pillars

Table 1.5.2: Comparison of 3D electrode results in literature.

1.5.3 3D Nanostructures

The vast majority of research in three dimensional energy storage falls under the category of high surface area 3D nanostructures. Electrodes fabricated using these materials are no different than commercial batteries in that all interfaces are defined by only two dimensions (Fig 1.5.3). However, the nanoscale surface area is immense due to the incorporation of irregular features. A review of achievements for this category is out of the scope of this chapter due to the substantial number of publications. However, a brief description of common materials and methods used to fabricate these electrodes is in order.

The goal of 3D nanostructures is to create an electrode with the highest possible

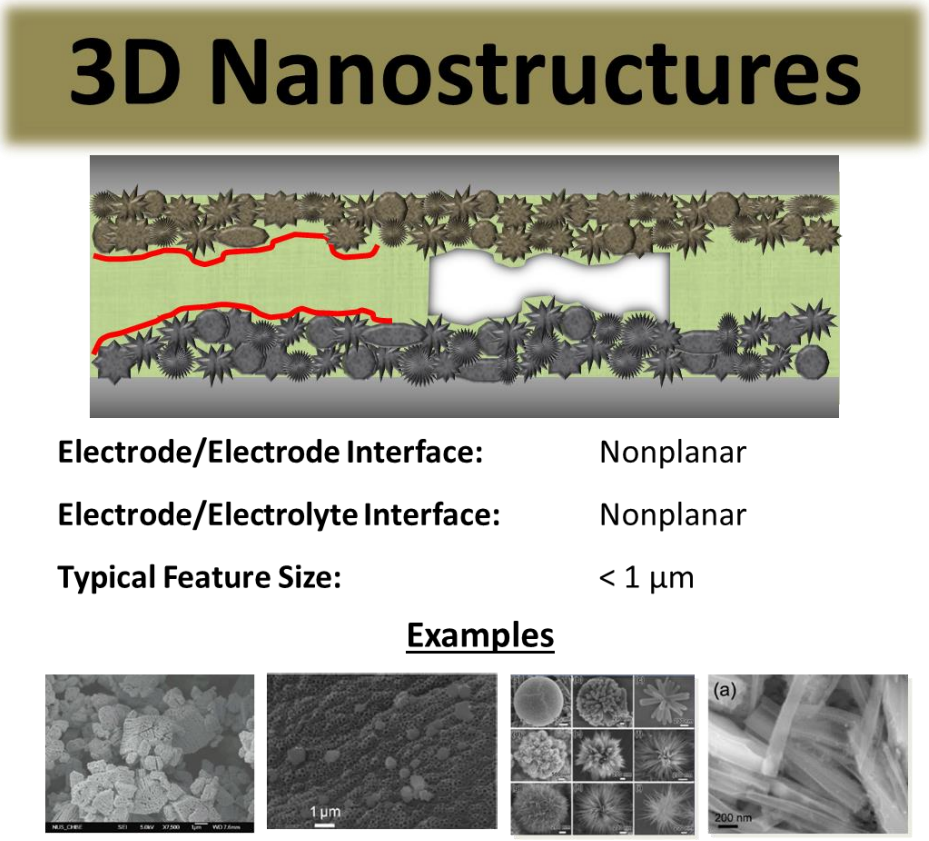

Figure 1.5.3: Definition and example for 3D nanostructures. Red interface shows nonplanar electrode/electrolyte interface. White interface shows nonplanar electrode/electrode interface.

interfacial surface area. The most common method for this involves controlling the shape of the nanoparticles [48]. This can be done by tuning the nucleation and growth properties during synthesis. It has been shown that growth occurs preferentially along certain directional planes in the presence of surfactants. It is also possible to create nanoparticles with highly irregular surfaces by removing linker molecules all together. A nanoparticle with a rough surface guarantees high surface area electrodes.

Another popular technique to increase the interfacial surface area is to combine nanoparticles with graphene sheets [49] [50] [51]. A common nanocomposite is composed of anode or cathode nanoparticles layered between graphene. Another similar design coats the nanoparticles with graphene layers. In this case, the graphene serves two purposes. First, it can act as a conductive pathway for electrons between the nanoparticles. Second, it may improve the charge storage capabilities through surface adsorption or double-layer effects. It should be pointed out that graphene does not increase capacity through intercalation methods since the layers are spaced too far apart.

As pointed out earlier, extremely high surface areas are often prone to detrimental side reactions. More often than not, electrodes of this type can produce high gravimetric capacities at significant discharge rates but rarely exhibit good cycling behavior. However, if interfacial instabilities are improved, then the future of fast reacting nanoparticles is promising.

1.6 References

[1] R. G. Arms, "The other transistor: early history of the metal-oxide-semiconductor field-effect transistor," vol. 7, no. 5, 1998.

[2] J. Kilby, "Invention of the integrated circuit," vol. 23, no. 7, 1976.

[3] "Intel Corporate Website," [Online]. Available: http://ark.intel.com/products/64887/Intel-Core-i7-3920XM-Processor-Extreme-Edition-(8M-Cache-up-to-3_80-GHz).

[4] R. Ghodssi and P. Lin, MEMS Materials and Processes Handbook, Springer, 2011.

[5] B. Warneke, M. Scott, B. Leibowitz, L. Zhou, C. Bellew, J. Chediak, J. Kahn, B. Boser and K. Pister, "An autonomouse 16mm3 solar powered node for distributed wireless sensor networks," *Sensors, Proceedings of IEEE,* vol. 2, pp. 1510-1515, 2002.

[6] D. Rolison and L. Nazar, "Electrochemical energy storage to power the 21st century," *MRS Bulletin,* vol. 36, pp. 486-493, 2011.

[7] T. Arthur, D. Bates, N. Cirigliano, D. Johnson and P. e. a. Malati, "Three dimensional electrodes and battery architectures," *MRS Bulletin,* vol. 36, pp. 523-531, 2011.

[8] R. Huggins, Advanced Batteries: Materials Science Aspects, Springer, 2009.

[9] N. Perez, Electrochemistry and Corrosion Science, Kluwer Academic Publishers, 2004.

[10] A. Bard and L. Faulkner, Electrochemical Methods: Fundamentals and Applications, John Wiley and Sons, 2001.

[11] F. Scholz, Electroanalytical Methods: Guide to Experiments and Applications, Springer, 2010.

[12] A. Bard, G. Inzelt and F. Scholz, Electrochemical Dictionary, Springer, 2008.

[13] D. Sawyer, A. Sobkowiak and J. Roberts, Electrochemistry for Chemists, John Wiley and Sons, 1995.

[14] J. Bockris and A. Reddy, Modern Electrochemistry 2A: Fundamentals of Electrodics, Kluwer Academic Publishers, 2002.

[15] J. Bockris and A. Reddy, Modern Electrochemistry: Ionics, Kluwer Academic Publishers, 1998.

[16] D. Cogswell and M. Bazant, "Coherency strain and the kinetics of phase separation in LiFePO4 nanoparticles," *ACS Nano,* vol. 6, no. 3, pp. 2215-2225, 2011.

[17] M. Winter and R. Brodd, "What are batteries, fuel cells and capacitors?," *Chemical Reviews,* vol. 104, no. 10, 2014.

[18] R. Nicholson and I. Shain, "Theory of stationary electrode polarography," *Analytical Chemistry,* vol. 36, no. 4, pp. 706-723, 1964.

[19] R. Nicholson, "Theory and application of cyclic voltammetry for measurement of electrode reaction kinetics," *Analytical Chemistry,* vol. 37, no. 11, pp. 1351-1355, 1965.

[20] US Energy Information Administration, 2010. [Online]. Available: http://www.eia.gov/forecasts/ieo/.

[21] R. Liu, L. Zhang, X. Sun, H. Liu and J. Zhang, Electrochemical Technologies for Energy Storage and Conversion, John Wiley and Sons, 2012.

[22] J. Goodenough and Y. Kim, "Challenges for Rechargeable Li Batteries," *Chemistry of Materials,* vol. 22, pp. 587-603, 2010.

[23] C. Daniel and J. Besenhard, The Handbook of Battery Materials, Wiley-VCH, 2011.

[24] R. Hart, H. White, B. Dunn and D. Rolison, "3-D Microbatteries," *Electrochemistry Communications,* vol. 5, pp. 120-123, 2003.

[25] H. Min, B. Park, L. Taherabadi, C. Wang, Y. Yeh, R. Zaouk, M. Madou and B. Dunn, "Fabrication and properties of a carbon/polypyrrole three-dimensional battery," *Journal of Power Sources,* vol. 178, pp. 795-800, 2008.

[26] K. Yoshima, H. Munakata and K. Kanamura, "Fabrication of micro lithium-ion battery with 3D anode and 3D cathode by using polymer wall," *Journal of Power Sources,* vol. 208, pp. 404-408, 2012.

[27] F. Chamran, Y. Yeh, H. Min, B. Dunn and C.-J. Kim, "Fabricatoin of high aspect ratio electrode arrays for three dimensional microbatteries," *Journal of microelectromechanical systems,* vol. 16, no. 4, pp. 844-852, 2007.

[28] J. Proell, R. Kohler, A. Mangang, S. Ulrich, C. Ziebert and W. Pfleging, "3D structures in battery materials," *Journal of Laser Micro/Nanoengineering ,* vol. 7, no. 1, pp. 97-104, 2012.

[29] M. Kotobuki, Y. Suzuki, H. Munakata, K. Kanamura, Y. Sato, K. Yamamoto and T. Yoshida, "Fabrication of three dimensional battery using ceramic electrolyte with honeycomb structure by sol-gel process," *Journal of Electrochemical Society,* vol. 157, no. 4, 2010.

[30] L. Baggetto, H. Knoops, R. Niessen, W. Kessels and P. Notten, "3D negative electrode stacks for integrated all-solid-state lithium-ion microbatteries," *Journal of Materials Chemistry,* vol. 20, pp. 3703-3708, 2010.

[31] H. Mazor, D. Golodnitsky, L. Burstein and E. Peled, "High power copper sulfide cathodes for thin film microbatteries," *Electrochemical and Solid-State Letters,* vol. 12, no. 12, 2009.

[32] H. Mazor, D. Golodnitzky, L. Burstein, A. Gladkich and E. Peled, "Electrophoretic deposition of lithium iron phosphate cathode for thin film 3D-microbatteries," *Journal of Power Sources,* vol. 198, pp. 264-272, 2012.

[33] M. Nathan, D. Golodnitsky, V. Yufit, E. Strauss, T. S. I. Ripenbein, S. Menkin and E. Peled, "Three dimensional thin film Li-ion microbatteries for autonomous MEMS," *Journal of Microelectromechanical Systems,* vol. 14, no. 5, 2005.

[34] N. Ergang, M. Fierke, Z. Wang, W. Smyrl and A. Stein, "Fabrication of a fully infiltrated three dimensional solid-state interpenetrating electrochemical cell," *Journal of the Electrochemical Society,* vol. 154, no. 12, 2007.

[35] P. Johns, M. Roberts and J. Owen, "Conformal electrodeposition of manganese dioxide onto reticulated vitreous carbon for 3D microbattery applications," *Journal of Materials Chemistry,* vol. 21, 2011.

[36] K. Gerasopoulos, E. Pomerantseva, M. McCarthy, A. Brown, C. Wang, J. Culver and R. Ghodssi, "Hierarchical three dimensional microbattery electrodes combining bottom-up self-assembly and top-down micromachining," *ACS Nano,* vol. 6, no. 7, 2012.

[37] S. Gowda, A. Reddy, X. J. H. Zhan and P. Ajayan, "3D nanoporous nanowire current collectors for thin film microbatteries," *Nano Letters,* vol. 12, 2012.

[38] J. Wang, N. Du, H. Zhang, J. Yu and D. Yang, "Cu-Sn core-shell nanowire arrays as three dimensional electrodes for lithium ion batteries," *The Journal of Physical Chemistry C,* vol. 115, 2011.

[39] W. Wang, M. Tian, A. Abdulagatov, S. George, Y.-C. Lee and R. Yang, "Three dimensional Ni/TiO2 nanowire network for high areal capacity lithium ion microbattery applications," *Nano Letters,* vol. 12, pp. 655-660, 2011.

[40] J. Wang, N. Du, H. Zhang, J. Yu and D. Yang, "CuSiGe cor shell nanowire arrays as three dimensional electrodes for high-rate capability lithium ion batteries," *Journal of Power Sources,* vol. 208, pp. 434-439, 2012.

[41] W. Zeng, F. Zheng, R. Li, Y. Zhan, Y. Li and J. Liu, "Template synthesis of SniO2/Fe2O3 nanotube array for 3D lithium ion battery anode with large areal capacity," *Nanoscale,* vol. 4, 2012.

[42] K. Xie, Z. Lu, H. Huang, W. Lu, Y. Lai, J. Li, L. Zhou and Y. Liu, "Iron supported C@Fe3O4 nanotube array: a new type of 3D anode with low-cost for high performance lithium ion batteries," *Journal of Materials Chemistry,* vol. 22, 2012.

[43] C. Chan, H. Peng, G. Liu, K. McIlwrath, X. Zhang, R. Huggins and Y. Cui, "High-performance lithium battery anodes using silicon nanowires," *Nature Nanotechnology*, 2007.

[44] C. Chan, X. Zhang and Y. Cui, "High capacity Li ion battery anodes using Ge nanowires," *Nano Letters,* vol. 8, no. 1, pp. 307-309, 2008.

[45] M. Tian, W. Wang, Y. Wei and R. Yang, "Stable high areal capacity lithium ion battery anodes based on three dimensional Ni-Sn nanowire networks," *Journal of Power Sources,* vol. 211, pp. 46-51, 2012.

[46] C. Rhodes, J. Long, M. Doescher, B. Dening and D. Rolison, "Charge insertion into hybrid nanostructures: mesoporous manganese oxide coated with poly(phenylene) oxide," *Journal of Non-Crystalline Solides,* vol. 350, pp. 73-79, 2004.

[47] W. Lai, C. Erdonmez, T. Marinis, C. Bjune, N. Dudney, F. Xu, R. Wartena and Y.-M. Chiang, "Ultrahigh energy density microbatteries enabled by new electrode architecture and micropackaging design," *Advanced Energy Materials,* vol. 22, 2010.

[48] D. Deng and J. Lee, "Linker-free assembly of 3D assembly of nanocrystals with tunable unit size for reversible lithium ion storage," *Nanotechnology,* vol. 22, 2011.

[49] H. Kim, B. Han, J. Choo and J. Cho, "Three dimensional porous silicon particles for use in high performance lithium secondary batteries," *Angewandte Chemie,* vol. 47, 2008.

[50] M. Nagao, M. Otani, H. Tomita, S. Kanzaki, A. Yamada and R. Kanno, "New three-dimensional electrode structure for the lithium battery: nano-sized Fe2O3 in a mesoporous carbon matrix," *Journal of Power Sources,* vol. 196, pp. 4741-4746, 2011.

[51] X. Xin, X. Zhou, F. Wang, X. X. X. Yao, Y. Zhu and Z. Liu, "A 3D porous architecture of Si/graphene nanocomposite as high-performance anode materials for Li-ion batteries," *Journal of Materials Chemistry,* vol. 22, 2012.

[52] Seiko Instruments, "MicroBattery," [Online]. Available: http://www.sii.co.jp/components/battery/topEN.jsp.

[53] Panasonic, [Online]. Available: http://www.panasonic.com/industrial/batteries-oem/.

[54] STMicroelectronics, "EnFilm," [Online]. Available: http://www.st.com/web/en/catalog/sense_power/FM142/CL848/SC1107.

[55] Front Edge Technology, [Online]. Available: http://www.frontedgetechnology.com/tech.htm.

[56] PowerStream, [Online]. Available: http://www.powerstream.com/BatteryFAQ.html.

[57] G. Teixidor, R. Zaouk, B. Park and M. Madou.

[58] S. Gowda, A. Reddy, M. Shaijumon, X. Zhan, L. Ci and P. Ajayan, "Conformal coating of thin polymer electrolyte layer on nanostructured electrode materials for three-dimensional battery applications," *Nano Letters*, vol. 11, 2011.

[59] Y. Yu, L. Gu, C. Zhu, S. Tsukimoto, P. van Aken and J. Maier, "Reversible storage of lithium in silver coated three dimensional macroporous silicon," *Advanced Materials*, vol. 22, p. 2247, 2010.

Chapter 2

MODELING OF 3D BATTERIES

2.1 Geometric Considerations

Basic modeling of a 3D electrode is essential in determining its practicality as an energy storage device. While many 3D designs exist, very few offer the ability to obtain the areal capacities required by miniature devices. This is often a direct result of low mass loadings associated with the electrode design features [1]. Because of the simplicity of the concentric tube design, it is possible to determine the expected electrode capacity using the various design features. It should be stressed that only geometrical designs were considered, and any increase in electrode resistance due to an increased aspect ratio was not incorporated into the calculations.

Calculations were based on three main variables: radius *r*, pitch *p* and height *h*. Electrolyte thickness *t* (if necessary) and footprint area *A* are also involved in most of the equations. All terms are physically defined in Figure 2.1.1 and Figure 2.1.2. A sixth variable, spacing *s*, is interrelated to pitch and can be defined mathematically as the diameter subtracted

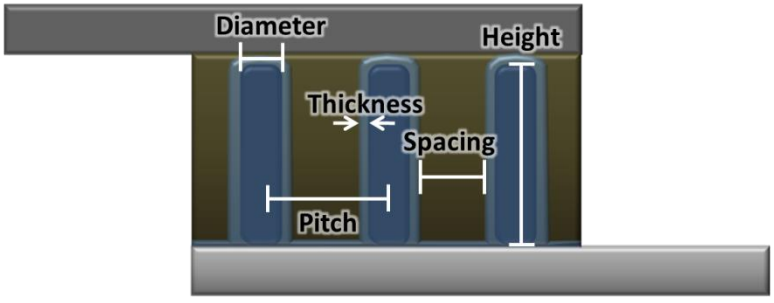

Figure 2.1.1: Physical parameters used for calculating expected areal capacities of 3D lithium ion electrodes

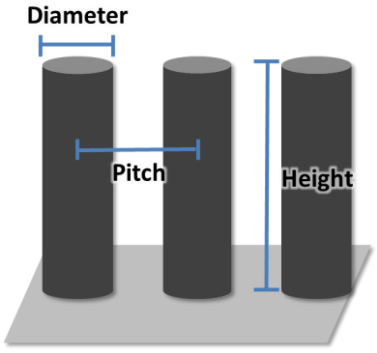

Figure 2.1.2: Physical parameters used for calculating expected areal capacities of 3D zinc-air electrodes

from the pitch. Physically, it is simply the distance between the edges of two nearest neighbor posts. To begin, two variables must be held constant. By varying the third, it is possible to calculate the expected areal capacity (mAh/cm^2) based on,

$$Areal\ Cap = C_{th} * m/A = C_{th} * V * \rho/A \quad (2.1.1)$$

where C_{th} is theoretical gravimetric capacity (mAh/g) of the given material, *m* is mass, *V* is the total volume of electrode material and ρ is density. If the total volume of the electrode material is the volume of each individual post (v_p) times the number of posts (n), Equation 2.1.1 can be further reduced to,

$$Areal\ Cap = \frac{C_{th}\rho v_p n}{A} = \frac{C_{th}\rho(\pi r^2 h)n}{A} \quad (2.1.2)$$

Determining the number of posts for a given area requires a consistent boundary condition when variables are changed. For a specified footprint area *A,* defined by a length *l,* and width *w*, it was assumed that the first post, which may also be surrounded by the electrolyte thickness *t,* is positioned at the edge of the current collector. Using these assumptions, the total number of posts for a given area is,

$$n = \left(\frac{l+s}{2(r+t)+s}\right)\left(\frac{w+s}{2(r+t)+s}\right) \quad (2.1.3)$$

Plugging *n* into Equation 2.1.2 will give the theoretical capacity in mAh/cm^2 for a 3D post electrode. The final equation ensures that only the mass of active electrode material is used for capacity measurements, while electrolyte thickness is considered to determine how many posts fit in a given area.

Lithium ion batteries utilize two unique materials for lithium intercalation, one for the anode and the other for the cathode. Because the materials have dissimilar theoretical gravimetric capacities, a situation may arise in which one electrode is limiting the capacity of the overall

battery [2]. Therefore, it is necessary to calculate the theoretical capacity of the complementary electrode. In this case, the electrode will consist of active material deposited between posts. The total volume of this electrode can be calculated by subtracting the volume of the electrolyte-coated rods from the total volume of the battery material,

$$V_{sed} = (l * w * h) - \pi(r + t)^2 hn \quad (2.1.4)$$

Plugging this into Equation 2.1.1 will give the areal capacity for the electrode.

2.2 Lithium Ion Systems

Material properties play an important role in determining electrode capacities. For all anode calculations, it was assumed that the density of the dried composite was 1.45 g/cm^3, and MCMB accounted for 90% of the mass. Cathode calculations assumed the dried composite was 1.9 g/cm^2, and 75% of the mass was $LiCoO_2$. Using these values and the theoretical capacities, it was determined that 71% of a given volume must be dedicated to the cathode in order to maximize the battery capacity. Any change in slurry composite mass ratio or density will vary this percentage. Due to the high volume percentage necessary for the cathode, it was decided to model the 3D battery using anode posts.

The relationship between aspect ratio and areal capacity for a given pitch when holding the diameter constant is shown in Figure 2.2.1. By comparing capacities of both electrodes, it can be seen that the value of the pitch determines which electrode limits the battery capacity. For instance, if the pitch is 151 μm, the MCMB electrode is capable of producing approximately 11 mAh/cm^2 at an aspect ratio of 5. At the same aspect ratio, the $LiCoO_2$ electrode is only capable of storing 5 mAh/cm^2. For this arrangement, the $LiCoO_2$ electrode is the limiting factor.

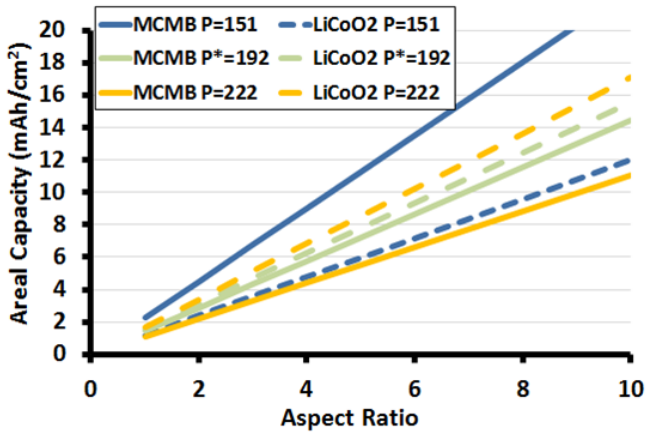

Figure 2.2.1: Relationship between areal capacity and aspect ratio of anode and cathode when post diameter held constant at 110 µm. Critical pitch occurs at 192 µm.

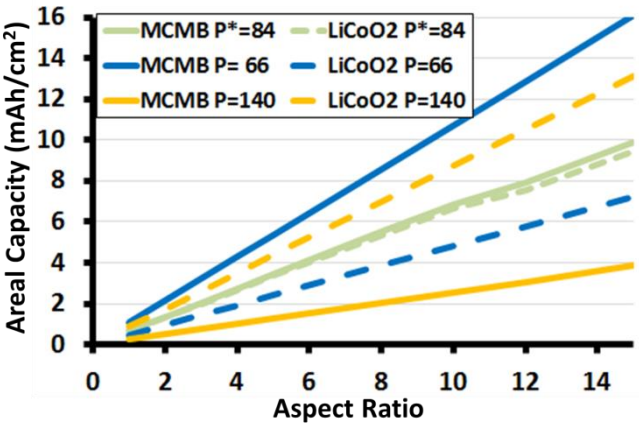

Figure 2.2.2: Relationship between areal capacity and aspect ratio of anode and cathode when post diameter held constant at 50 um. Critical pitch occurs at 84 um.

However, if the pitch is increased to 222 µm, the $LiCoO_2$ electrode jumps to 8 mAh/cm^2 while the MCMB electrode falls to 5 mAh/cm^2. The limiting factor is now the MCMB electrode.

From the electrode role reversal, it can be concluded that there exists a critical pitch at which both anode and cathode will provide the same areal capacity, as seen in Figure 2.2.1. Therefore, irreversibilities aside, the battery will have maximum energy storage capabilities when both electrodes have similar capacities. As expected, the critical pitch describes a situation when the cathode occupies approximately 71% of the total battery volume. Identical results are obtained when calculating the relationship between aspect ratio and capacity for a structure based on 50 µm diameter posts (Fig 2.2.2). It can be seen that the critical pitch for this particular

Table 2.2.1: Physical parameters of 3D configurations resulting in over 7 mAh/cm^2.

Diameter (µm)	Height (µm)	Aspect Ratio	Areal Capacity (mAh/cm^2)	Expected Energy Density (J/cm^2)	Pitch (µm)
130	520	4:1	7.2	98.6	204
110	550	5:1	7.2	98.6	180
80	640	8:1	8.6	117.7	126
50	600	12:1	7.6	104	79
20	600	30:1	7.5	102.6	33

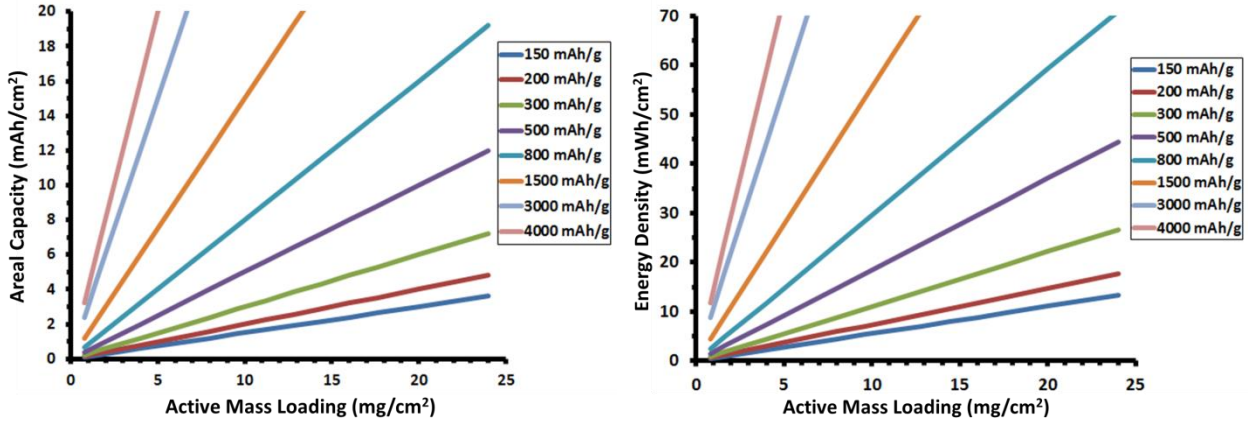

Figure 2.2.3: Relationship between mass loading and areal capacity (left) and energy density (right) for various hypothetical materials

arrangement is 84 μm. Table 2.2.1 shows sample calculations of geometric arrangements that would produce batteries capable of capacities greater than 7 mAh/cm^2.

These calculations bring to light interesting information concerning electrode active mass loading. For example, when considering a 3D carbon electrode composed of 110 μm diameter posts 550 μm tall, the expected areal capacity is 7.2 mAh/cm^2. Assuming the battery has a working voltage of 3.8 V, this translates to 27.4 mWh/cm^2 or 98.5 J/cm^2. Therefore, we know that in order to achieve the benchmark of 100 J/cm^2, an electrode must be loaded to about 7.3 mAh/cm^2. Calculations show that if the capacity of a graphite-based anode is 372 mAh/g, then a minimum active mass loading of 22 mg/cm^2 is necessary to achieve an energy density of 100 J/cm^2 (Fig 2.2.3). This mass loading is nearly double that of commercial cylindrical cell carbon electrodes [2], indicating that planar architectures may not meet the necessary power requirements for small MEMS devices. It should be noted that slurry densities can vary depending on the mass percentage of each component.

Surface area gains can also be calculated for the concentric tube design using the same parameters. Table 2.2.2 summarizes the surface area gains for 50 and 110 μm diameter posts at

Diameter (µm)	Height (µm)	Aspect Ratio	Post Array	3D Surface Area (mm^2)	2D Surface Area (mm^2)	Surface Area Gain (%)
110	100	1	16x16	11.28	9	25
	200	2	16x16	20.12	9	124
	350	3.5	16x16	33.39	9	271
	550	5.5	16x16	51.08	9	468
50	50	1	36x36	12.72	9	41
	100	2	36x36	22.9	9	154
	175	3.5	36x36	38.16	9	324
	275	5.5	36x36	58.52	9	550
	350	7	36x36	73.78	9	720
	550	11	36x36	114.49	9	1172

Table 2.2.2: Surface area gains for various 3D arrangements. All calculations are made using a 3x3 mm footprint area electrode.

various aspect ratios. Both planar and 3D calculations are based on a 3 mm x 3 mm electrode size. The critical pitch was used to determine the number of posts for 3D calculations. It can be seen that even at a low aspect ratio of 1, the surface area gain is 25% and 41% for the 100 µm and 50 µm diameter posts, respectively. This value increases with aspect ratio, reaching over 1000% gain for a 3D electrode designed 550 µm tall with 50 µm diameter posts. These large surface area gains combined with small diffusion distances should lead to a more powerful microbattery.

In conclusion, general trends for 3D architectures show that pitch is controlled by the distance between posts, post size and, electrolyte thickness. In order to maintain superior capacities with a decreasing post diameter, the pitch must be reduced by decreasing post separation or electrolyte thickness, or the aspect ratio must be increased by increasing the post height. These trends are the result of subsequent mass loadings regulated by the geometrical constraints.

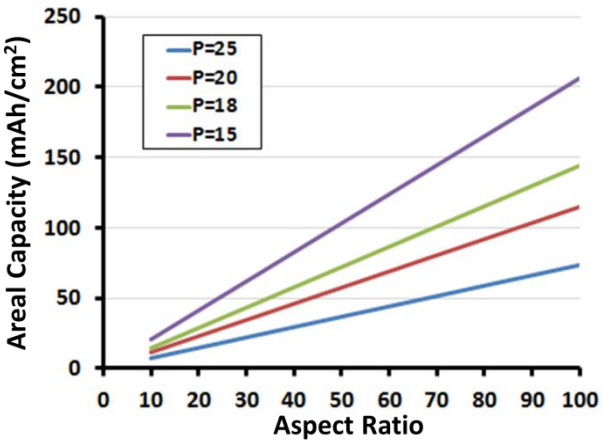

Figure 2.3.1: Calculated areal capacities for 3D zinc anodes based on 10 um diameter posts

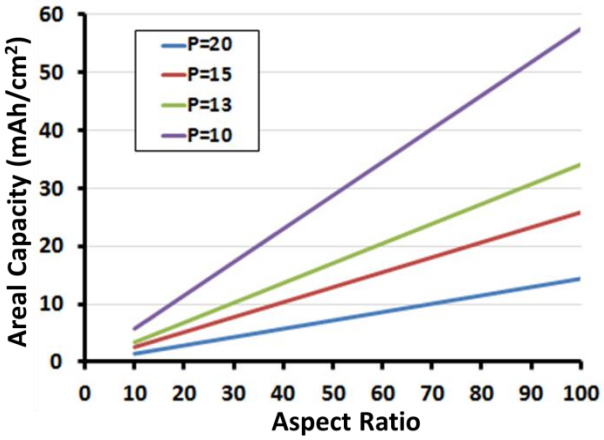

Figure 2.3.2: Calculated areal capacities for 3D zinc anodes based on 5 um diameter posts

2.3 Zinc-Air system

Because the cathode of a zinc air battery does not lead to an easily identifiable energy storage material, the models described below do not consider it as a variable. As a result, there is no limiting electrode or critical pitch that needs to be determined. Also, because 3D zinc air microbatteries are not of the concentric tube design, an electrolyte separator is not necessary to include in the calculations. A density value of 7.14 g/cm^3 was used since zinc is the primary metal being electrodeposited.

Figure 2.3.1 illustrates how the capacity of a zinc electrode changes with varying aspect ratio and pitch values. As expected, increasing the height of the posts increases the estimated areal capacity. By utilizing the vertical direction, more material is allowed to be loaded within the electrode footprint area. Furthermore, because these rods are metallic, little to no resistance drop is expected along the length of each post. Figure 2.3.1 also shows an increase in electrode capacity with decreasing pitch. Calculations show that an electrode composed of 10 μm diameter posts and a pitch of 25 μm produces about 37 mAh/cm^2 at an aspect ratio of 50:1. Decreasing the pitch to 15 microns results in an electrode capable of storing over 100 mAh/cm^2 at the same

aspect ratio. Similar results can be expected from electrodes composed of 5 μm diameter posts (Figure 2.3.2). The effect of pitch on the electrode's capacity can be explained by the increase of zinc material available for discharge. Table 2.3.1 shows that for the 10 micron post diameter electrode, changing the pitch from 20 to 15 microns increases the volume occupied by zinc posts by 15%. Thus, a smaller pitch allows more zinc posts to be placed on a given footprint area, increasing the overall capacity. Table 2.3.1 also illustrates the versatility of the fabrication technique used to create the electrodes, showing many possible configurations resulting in electrodes capable of storing over 10 mAh/cm^2.

As with the lithium ion calculations, it is possible to determine the minimum mass loading to achieve our target. Calculations indicate a minimum of 21.5 mAh/cm^2 is necessary to achieve 100 J/cm^2 if a working voltage of 1.3 V is used to determine the energy density. Therefore, an approximate minimum loading of 26 mg/cm^2 is required to achieve our target. Because only one component in the active material exists, density variations are minimal. It is interesting that although zinc has almost twice the theoretical capacity of a carbon lithium-ion anode, the mass loadings are nearly identical due to the higher working voltage of a lithium ion battery. However, because the density of zinc is so much larger than the carbon slurry, the total volume necessary to accommodate a carbon electrode of equal capacity is nearly 400% more

Diameter (μm)	Height (μm)	Aspect Ratio	Areal Capacity (mAh/cm^2)	Expected Energy Density (J/cm^2)	Pitch (μm)	Volume of Zinc
10	200	20:1	14.8	69	25	13%
	100	10:1	11.5	54	20	20%
	100	10:1	20.6	96	15	35%
5	500	100:1	14.4	67	20	5%
	100	20:1	11.5	54	10	20%

Table 2.3.1: Physical parameters of 3D zinc electrodes resulting in capacities greater than 10 mAh/cm^2.

Diameter (μm)	Height (μm)	Aspect Ratio	Pitch (μm)	Post Density (posts/cm^2)	3D Surface Area (mm^2)	Volume of Zinc (%)
10	350	35	20	250,000	27.7	20
	500	50	20	250,000	39.5	20
	350	35	15	449,000	49.7	36
	500	50	15	449,000	70.9	36
5	350	70	10	1,000,000	55.2	20
	500	100	10	1,000,000	78.7	20
	350	70	8	1,562,500	86.2	30
	500	100	8	1,562,500	123	30

Table 2.3.2: Surface area calculations for various arrangements of 3D zinc electrodes

than that of the zinc.

Surface area gains for 3D zinc electrodes are difficult to calculate since commercial batteries use a zinc powder anode. Table 2.3.2 summarizes the calculated surface area of 3D zinc electrodes. Assuming an FCC stacking mechanism with a particle-to-particle contact angle of 25^o, the surface area of a powder anode with similar mass is of the same order of magnitude as a 3D zinc electrode. In this case, 3D electrode performance is expected to be superior due to each microstructure being directly connected to the current collector.

It can be concluded that in order to maximize the areal capacity of zinc electrodes, we must maximize the volume occupied by active zinc. Calculations show that this can be done by increasing the height of each individual rod and by decreasing the distance between posts. In both cases, this increases the amount of zinc available to be discharged. Furthermore, rod resistivity is expected to be minimal due to the conductive nature of metallic wires.

2.4 References

[1] T. Arthur, D. Bates, N. Cirigliano, D. Johnson and P. e. a. Malati, "Three dimensional electrodes and battery architectures," *MRS Bulletin,* vol. 36, pp. 523-531, 2011.

[2] P. Ramadass, B. Haran, R. White and B. Popov, "Performance study of commercial LiCoO2 and spinel-based Li ion cells," *Journal of Power Sources,* vol. 111, pp. 210-220, 2002.

Chapter 3

3D CARBON ELECTRODES

3.1 Carbon in Lithium Ion Anodes

The first generation of lithium batteries utilized lithium metal as the anode material. This was considered the ideal anode since lithium is the lightest and the most electropositive metal, which allows for high voltage batteries. However, many hazards are associated with a lithium counter electrode, the most relevant being the growth of dendrites [1]. As lithium ions are removed from the metal during a discharge process, microstructural surface irregularities cause local current densities to fluctuate. The resulting preferential delithiation leads to more pronounced surface irregularities. Upon charging, local current densities become focused at micro-crests and create favorable plating sites. This process becomes exaggerated after excessive cycling and eventually leads to the formation of dendrites (Figure 3.1.1). Dendrites can grow millimeters in length and eventually short-circuit the battery.

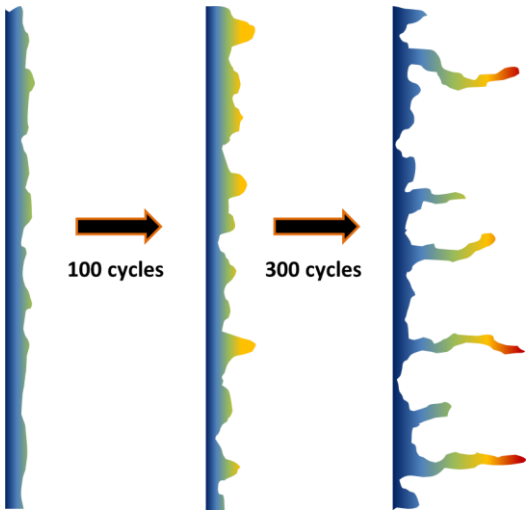

Figure 3.1.1: Dendrite formation on lithium metal anode. Localized current density increases with sharper features.

In the early 1990s, Sony revolutionized the lithium battery market by commercializing a battery using carbon as the anode and lithium cobalt oxide ($LiCoO_2$) as the cathode [2]. This achievement led to the development of high energy density lithium-ion batteries capable of powering a new wave of electronic devices without the safety concerns of lithium batteries. Since then, carbon has been studied extensively in order to determine how specific properties affect lithium intercalation. Today, various forms of carbon can be used in a battery with each having its own purpose.

3.1.1 Carbon as an Active Material

3.1.1.1 Carbon structure and characterization

Carbon in the form of diamond is one of the most expensive materials known and in the form of graphite is one of the cheapest materials known. Fortunately for the battery industry, only the latter phase is useful for energy storage. A network of carbon atoms bonded in the shape of hexagonal rings is called graphene. Carbon atoms are predominantly sp^2-bonded with a small percentage of sp^3-bonds to account for defects and boundaries. Crystallites are composed by stacking graphene layers in either hexagonal ABABA or rhombohedral ABCABC crystal

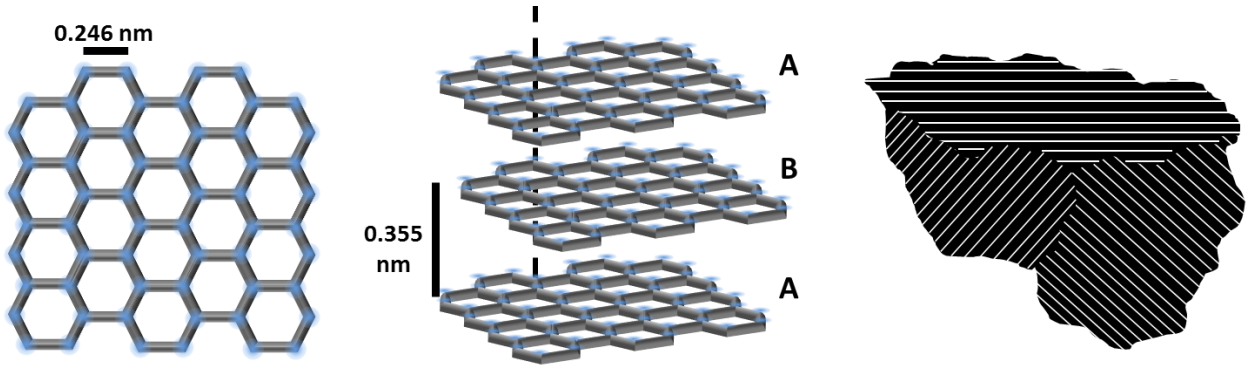

Figure 3.1.2: Left - Hexagonal network of carbon atoms forming a graphene layer. Center - Graphene layers stacked in hexagonal structure. Right - Collection of graphene crystallites makes a graphite particle.

Figure 3.1.3: Structural difference between hard and soft carbon. Hard carbon exhibits high turbostratic nature and amorphous regions (left). Crystallites of soft carbon are closely aligned. (right)

structures. These layers are held together by weak Van der Waals forces. The collection of graphene crystallites is known as graphite (Figure 3.1.2). The textbook definition of graphite requires long range three-dimensional order. However, in practice, long-range c-axis order is rarely found due to stacking defects and layer misorientation. The term turbostratic refers to the amount of disorder in a carbon structure. It is possible to reduce the turbostratic nature of graphite through heat treatment. The degree to which the turbostratic nature is reduced determines whether the carbon is characterized as hard or soft [1] [3] [4].

Hard carbons typically maintain a high degree of turbostratic nature even after heat treatments as high as 3000^{o}C. These types of carbons are produced by the pyrolysis of solid materials that already have a set microstructure. As a result, it is very difficult to rearrange the graphene layers into a more ordered structure. Hard carbons also have a very large volume occupied by nanopores which can lead to capacities greater than 372 mAh/g [1] [5]. However, the lithium storage processes are very slow due to the tortuous diffusion paths within hard carbon grains.

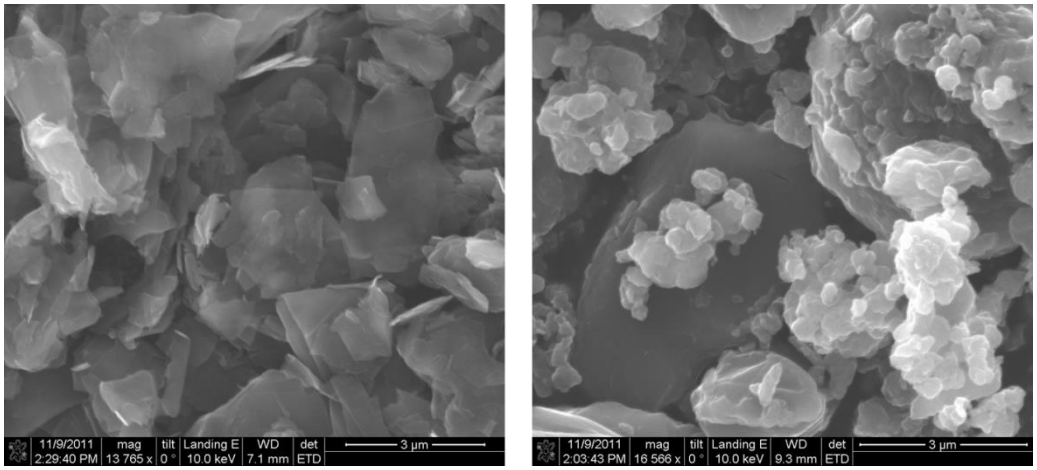

Figure 3.1.4: Physical differences between flaky natural graphite (left) and synthetic MCMB (right)

Soft carbons are produced by the pyrolysis of liquid amorphous material at temperatures of 2000 – 3000^{o}C. At these temperatures, much of the turbostratic disorder is removed. The microstructure resembles large crystallite grains composed of graphene layers oriented in similar directions (Figure 3.1.3) [3] [6]. Soft carbons are often further characterized as natural or synthetic depending on their particle shape (Figure 3.1.4). Thin, flaky natural graphite is capable of delivering reversible capacities up to 350 mAh/g. However, it is limited to slow rates due to the orientation of the graphene layers when pressed on an electrode. This has led to development of the more expensive synthetic graphites such as the spherical-shaped mesocarbon microbeads (MCMB). MCMB has shown to have a similar reversible capacity but does not preferentially align graphene edge-layers perpendicular to the current flow the way natural graphite does. Furthermore, MCMB has a higher packing density than natural graphite, leading to higher energy density electrodes [1].

3.1.1.2 Lithium storage in carbon

Lithium can be stored in carbon by either an insertion process, intercalation process or a combination of both. Intercalation and insertion are often used interchangeably, but it is

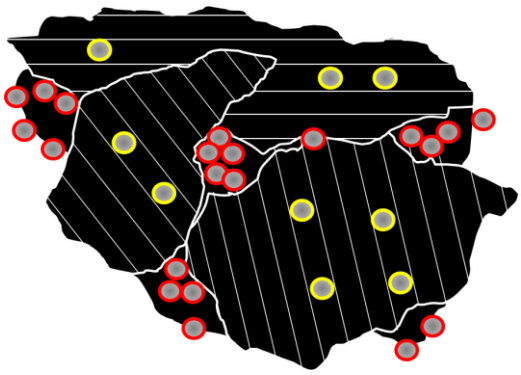

Figure 3.1.5: Lithium interactions with a graphite particle. Red ions part of insertion process and yellow ions are part of the intercalation process.

becoming more common to distinguish the two terms. MCMB stores lithium predominantly through the intercalation, whereas graphene sheets have shown to store lithium through insertion processes. Hard carbons are an example of in which both processes can be present.

The primary difference between lithium insertion and lithium intercalation is the location of the lithium ion in the carbon structure [1]. Lithium insertion suggests ions are stored everywhere except in between graphene layers. Examples of insertion sites include nanopores, crystallite voids, defect sites and basal or edge plane boundaries (Figure 3.1.5). The insertion process is highly dependent upon diffusion pathways and can be fast, as seen in graphene sheets, or very slow, such as in hard carbons [7]. Furthermore, lithium insertion occurs mostly due to concentration gradients and can happen without polarizing an electrode. Intercalation, on the other hand, is a thermodynamically driven chemical reaction that will only occur upon polarization.

Lithium intercalation in carbon has been studied extensively and, although more complex than insertion, is well understood today. The governing chemical reaction is,

$$Li + 6C \rightarrow LiC_6 \qquad 3.1.1$$

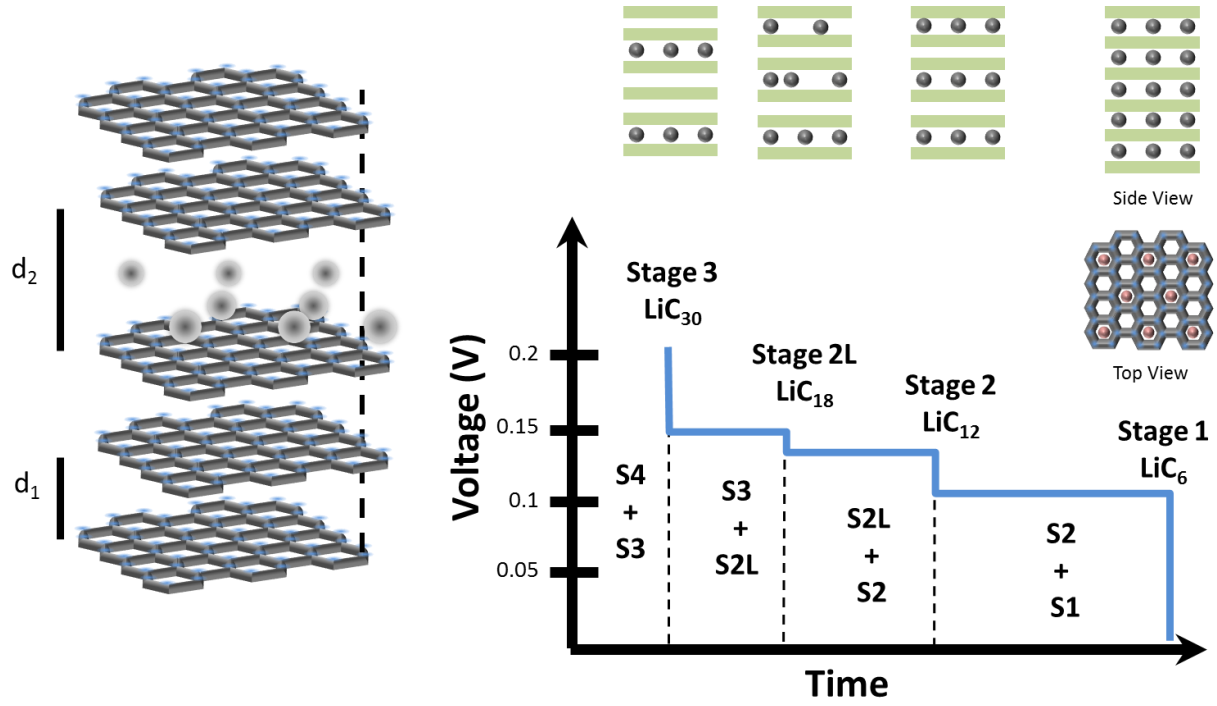

Figure 3.1.6: The staging process of carbon lithiation.

Intercalation has been revealed to occur through a phenomenon known as staging. During this process, carbon undergoes several phase changes defined by the number of lithium ions stored in the host matrix. Each two-phase region can be associated with its own plateau on a discharge curve (Figure 3.1.6). The staging process occurs by intercalating lithium ions into a few Van der Waals gaps, or galleries, at a time. As a gallery is filled, the neighboring graphene layers simultaneously expand and slide to accommodate the cations [3] [4].

Lithium staging proceeds in a manner that results in the smallest Coulombic interaction between intercalated cations [1] [8]. Initially, the carbon undergoes stage-4 intercalation at a voltage greater than 0.2 V. This means there are four graphene layers in between the lithium ion layers. The first distinguished plateau occurs at 0.2 V and indicates a transition from stage-4 to stage-3. When complete, the chemical makeup of the electrode is LiC_{30}. The transition from stage-3 to stage-2 occurs at 0.15 V and is split into two processes due to different packing

densities. The stoichiometry at the end of this process is LiC_{12}. As the lithium layers get closer, the Coulombic repulsion increases. The electrode must be polarized further in order to provide more energy for the lithiation process. The final transition to stage-1 occurs around 0.1 V and typically takes the longest. When every intercalation site is filled, the material sits in the LiC_6 region of the phase diagram. The final volume expansion in natural graphite due to lithium intercalation is about 10%.

The described staging situation is highly idealized. In practice, individual staging plateaus may be difficult to distinguish due to the existence of overpotentials and inhomogeneous intercalation. It has also been widely accepted that the intercalation of solvated groups may occur under some conditions, and that SEI layers, which will be discussed later, can affect lithium intercalation.

It is important that the final intercalation voltage occurs above 0 V as this indicates that the intercalated lithium is still partially ionic. It is believed that the lithium ion becomes more neutral as the staging process progresses, but never completely reaches a metallic lithium state. This is supported by the fact that Coulombic forces influence the staging process. Furthermore, Li-NMR studies have shown elevated electron densities in the graphene surrounding lithium ions [1]. A neutral lithium ion would have exhibited a more homogenous distribution throughout the network. A carbon anode that has been overcharged may develop lithium deposits. Metallic lithium should be avoided since it can lead to excess lithium plating and dendrite formation.

Many studies have been performed on structurally modified carbons and their lithium storage capabilities. Chemical doping with boron is a popular method to increase the crystallite size and facilitate lithium diffusion. Other methods to improve lithium storage involve surface

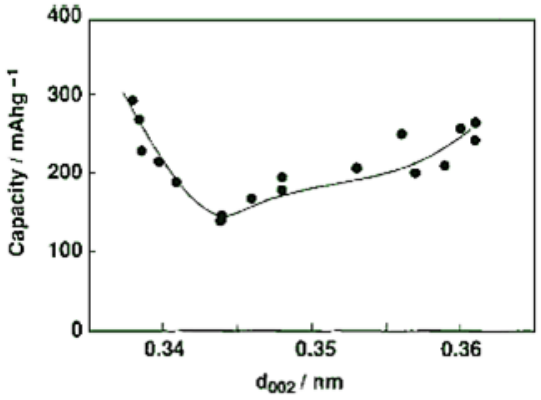

Figure 3.1.7: Relationship between graphene layer spacing and charge storage capabilities. **[3]**

modifications such as mild oxidation or the removal of unfavorable functional groups. A distinct relationship has proven to exist between the interlayer spacing between graphene sheets (d_{002}) and the discharge capacity. Figure 3.1.7 reveals a minimum capacity corresponding to 0.344 nm, the interlayer spacing of a disordered carbon [3]. It is interesting that both decreasing the spacing to increase the crystallinity and increasing the spacing to enhance lithium diffusion results in higher discharge capacities.

3.1.1.3 Solid electrolyte interphase

The solid electrolyte interphase (SEI) is an important passivation layer that exists on the surface of the anode of a lithium ion battery. It plays an important role in cycle life, self-discharge, rate capability, Coulombic efficiency and low temperature performance [9]. Similar to an electrolyte, an SEI layer should be electronically resistive, conduct lithium ions and consistently maintain contact with the electrode. The formation of an SEI is usually associated with a large irreversible capacity in the first discharge due to electrolyte degradation at the electrode surface.

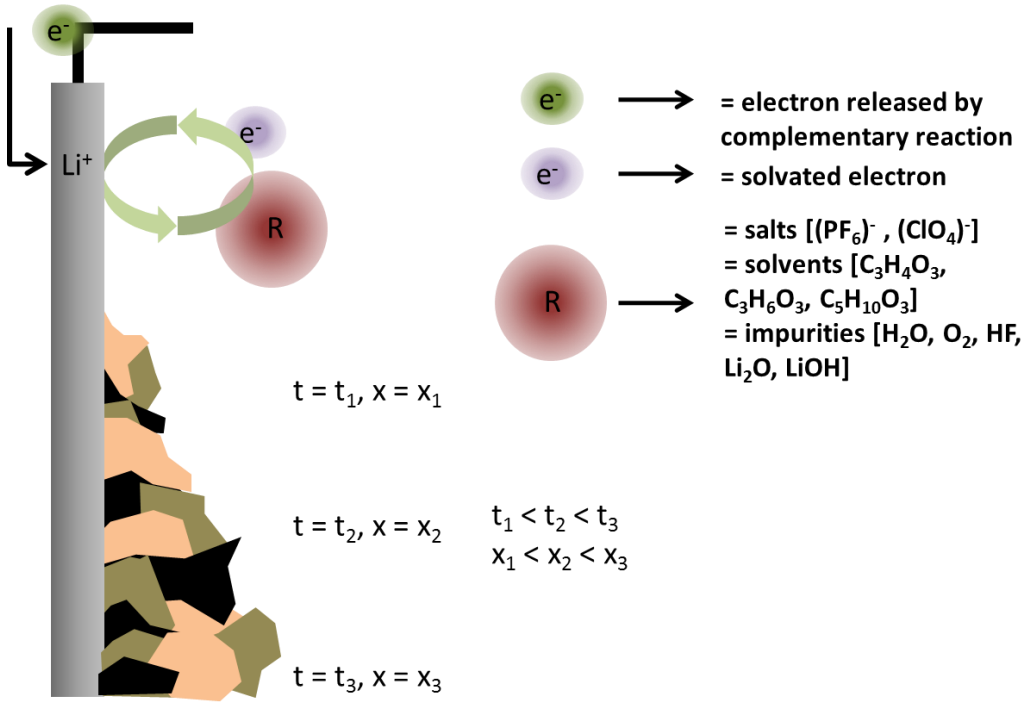

Figure 3.1.8: SEI forms on unpassivated anode surface when electrolyte molecules react with the active material.

Unfortunately, SEI formation is also the largest source of irreversible capacity loss. As mentioned earlier, the SEI forms on an unpassivated anode surface. When polarized outside the electrochemical window, any salts, solvents and impurities will be reduced to form a solid interphase composed of lithium compounds (Figure 3.1.9). This process reduces the number of lithium ions available for intercalation. Repetitive cycling causes the material to expand and contract, continuously exposing unpassivated carbon surface. The re-formation of an SEI acts as a parasitic reaction resulting in Coulombic efficiencies less than one. Substantial capacity fade and increased cell impedance eventually lead to the death of the cell [6].

The exact details of how an SEI operates are still vague, but it is understood that films can function very differently depending on the electrolyte components. For example, it is widely known that the SEI layer formed in propylene carbonate-based electrolytes is permeable to solvated lithium ions. As a result, lithium ions with a large solvation shell are intercalated into

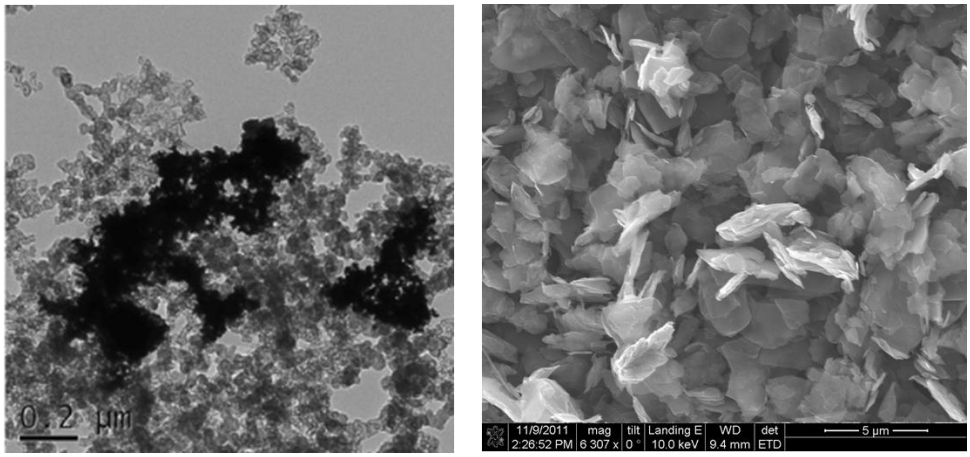

Figure 3.1.9: Ketjen black **[15]** (left) and KS4 graphite (right) are two popular conductive additives. Notice the significant size difference between the two types.

the graphene layers, eventually leading to exfoliation of the carbon from the electrode surface. However, with ethylene carbonate-based electrolytes, the SEI layer is only permeable to bare lithium ions. This development greatly increased the cycle life of lithium ion batteries. Research efforts have discovered new additives such as vinylene carbonate and diethyl carbonate that can create more stable SEI films [10]. Other ideas for more efficient SEI layers include deposition of a solid passivation layer prior to electrolyte introduction and surface modifications.

3.1.3 Carbon as a Conductive Additive

Most active materials for lithium-ion batteries are transition metal oxide-based and as a result have intrinsically low conductivities. Thus, it is common practice to include conductive carbon additives to the slurry in order to reduce the resistivity of the electrode. Additive components can also affect properties such as porosity, binder wetting and electrolyte absorption. These factors play important roles in cell performance and can produce significant cycling improvements if optimized.

The two main types of carbon additives are flaky graphite and carbon black (Figure 3.1.10). While both help reduce the electrode resistivity, they can also significantly alter the physical properties of the electrode. As a rule of thumb, graphite additives can increase the packing density of the electrode, decrease the overall binder content and potentially intercalate lithium ions. However, graphite also reduces the electrolyte penetration in the electrode. On the other hand, carbon black greatly enhances the porosity of the electrode due to its high surface area and nanometer dimensions. As a result, volumetric energy densities are reduced [3].

Choosing the correct amounts of each additive depends on the desired properties of the cell. For example, a cell requiring high rate capabilities may need more carbon black, whereas a cell maximizing its energy density may need more graphite. Because the surface area of both types is typically larger than that of the active carbon, the amount of additive should be no more than 10% to minimize any irreversible side reactions associated with SEI formation or electrolyte degradation.

3.2 2D Mesocarbon Microbead Electrodes

3.2.1 Experimental

Slurry Preparation. Electrodes were prepared using a slurry consisting of mesocarbon microbeads (MCMB), carboxymethyl cellulose (CMC) binder and conductive additives. A 2% binder solution was prepared by dispersing 200 mg of carboxymethyl cellulose (CMC) in 10 mL of deionized water (DI). The solutions were then sonicated for approximately one hour followed by vigorous vortexing to ensure a uniform thickness. MCMB (2.37 g), KS4 natural graphite (0.229 g) and Ketjen black (0.057 g) are then introduced to the solution. This is followed by a treatment of vortexing, sonicating for 1 hour and vortexing one final time. Excess DI may be added until the desired viscosity is reached. The slurry is then placed on a stir plate overnight. The final slurry concentration consists of 83% MCMB , 7% CMC binder, 8% graphite and 2% Ketjen black mixed in a 2% CMC solution. The final mass concentration was typically 0.2 – 0.3 mg/ml.

Electrode preparation. Copper foil was cleaned using sulfuric acid and scratched with a Dremmel to increase slurry adhesion. The current collector is weighed prior to slurry casting in order to determine the weight of the electrode material. Using a glass pasteur pipette, one drop of slurry was placed on the copper and spread evenly over 0.5 cm^2. The electrode was then dried in air or at 120^oC. Typical weights ranged from 1 to 3 mg. Electrodes were vacuum dried and transferred into the glovebox by means of a Schlenk flask.

Electrochemical setup. Electrochemical testing was performed using a BioLogic VMP3 multi-channel potentiostat. Impedance values were obtained over a frequency range of 300kHz to 10 mHz. Electrodes were cycled galvanostatically between 0.01 V and 1.8 V at various current densities. Cyclic voltammetry was carried out using a sweep rate of 0.1 mV/s between 0.01 V

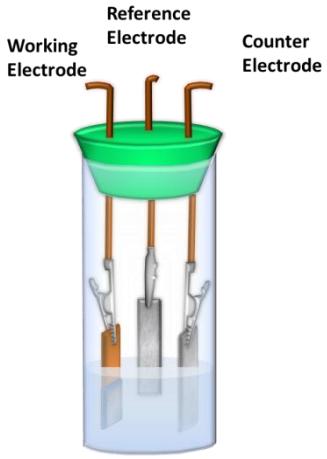

Figure 3.2.1: Experimental setup for half-cell studies.

and 1.4 V. Prior to testing, lithium foil was cleaned using polyethylene and used as the reference and counter electrodes. The prepared carbon electrode acted as the working electrode. The three electrodes were immersed in approximately 8 mL of electrolyte composed of 1 M $LiClO_4$ dissolved in a 50:50 mixture of EC/DMC. Cells were constructed using a cylindrical glass jar and rubber stopper fashioned with three copper wire leads to act as electrical contacts (Figure 3.2.1).

3.2.2 Results and Discussion

Electrochemical impedance was performed on an electrode while at a 0% state of charge and 95% state of charge. The obtained spectra are displayed in Figure 3.2.2. The shape of both Nyquist plots reveals the presence of two semicircles followed by a low frequency Warburg element. Each semicircle represents a particular electrode/electrolyte interface undergoing its respective Faradaic reaction controlled by different charge transfer resistance values. The Warburg portion describes a system that is diffusion controlled. The complete system can be modeled as two parallel RC circuits connected in series. The interface with the largest resistance

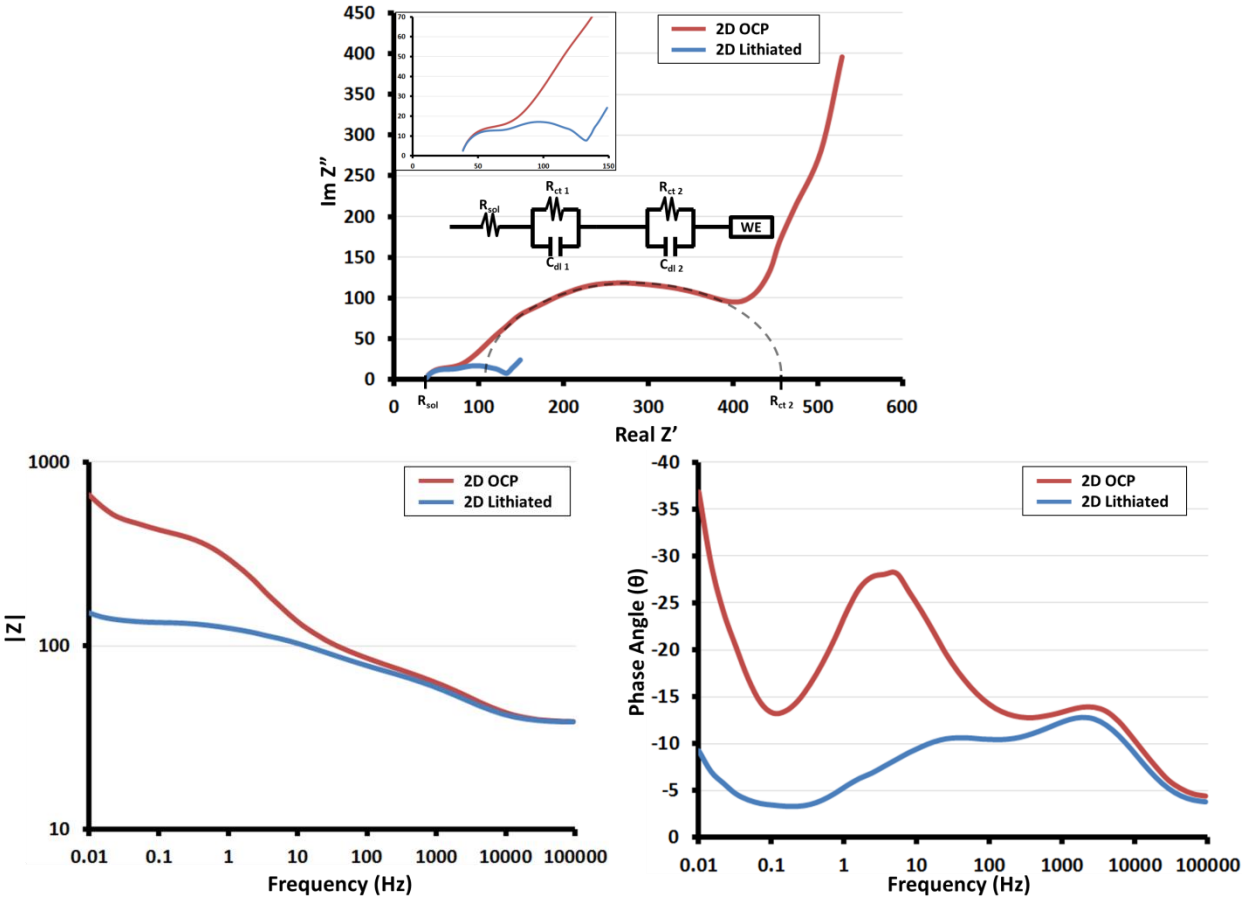

Figure 3.2.2: Nyquist impedance spectra for electrode at 0% and 95% SOC (top). Inset is focused on high frequency x-intercept. Bode plots (bottom) for same experiments. Red lines represent 0% SOC and blue lines represent 95% SOC

determines the overall cell resistance. This is defined as the location where the semi-circle crosses the x-axis. The high frequency x-intercept represents the electrolyte resistance [11].

It can be seen that the cell resistance decreases from approximately 450 Ω to 130 Ω upon lithiation. This is expected behavior since the intercalated lithium ions are close to a metallic state. The fact that both semicircles of the lithiated carbon experiment are almost identical in size supports this model. Upon closer inspection, it can be seen that only the size of the second semicircle varies with the state of charge. This suggests that the first semicircle represents the lithium/electrolyte interface since its behavior should be unaffected by the carbon lithiation.

	PLANAR ELECTRODE 1					PLANAR ELECTRODE 2					
Mass (mg)	1.39					1.79					
Footprint Area (cm^2)	0.5					0.5					
Active Mass Loading (mg/cm^2)	2.4					3.1					
Max Areal Capacity (mAh/cm^2)	0.9					1.16					
Current Density (mA/cm^2)	0.15	0.25	0.5	1.0	2.0	0.1	0.15	0.25	0.5	1.0	2.0
Current Density (mA/g)	62	103	207	413	827	32	48	80	161	321	642
C-Rate	C/6	C/3.6	C/1.8	1.1C	2.2C	C/11.6	C/7.7	C/4.6	C/2.3	C/1.2	1.7C
Average Areal Discharge (mAh/cm^2)	0.76	0.72	0.66	0.48	0.14	1.0	0.97	0.95	0.86	0.59	0.18
Average Areal Charge (mAh/cm^2)	0.74	0.72	0.66	0.48	0.14	0.97	0.97	0.94	0.86	0.59	0.18
Average Gravimetric Discharge (mAh/g)	313	297	273	199	58	321	314	304	277	189	58
Average Gravimetric Charge (mAh/g)	307	298	273	199	58	312	312	303	276	189	57

Table 3.2.1: Summary of 2D electrode performance when cycled through various current densities.

Bode plots are also displayed for the two experiments. The lithiated sample clearly has a lower magnitude of impedance than the unlithiated sample. A decrease and shift in the phase angle are also indicative of decreased impedance values.

Planar electrodes were cycled as a half cell in order to establish benchmark capacities for comparisons against 3D electrodes. Table 3.2.1 summarizes the properties of two planar electrodes. Electrode 1 was loaded with 1.21 mg of MCMB for an active mass loading of 2.4 mg/cm^2 and a maximum areal capacity of 0.9 mAh/cm^2. Electrode 2 was loaded with 1.56 mg of

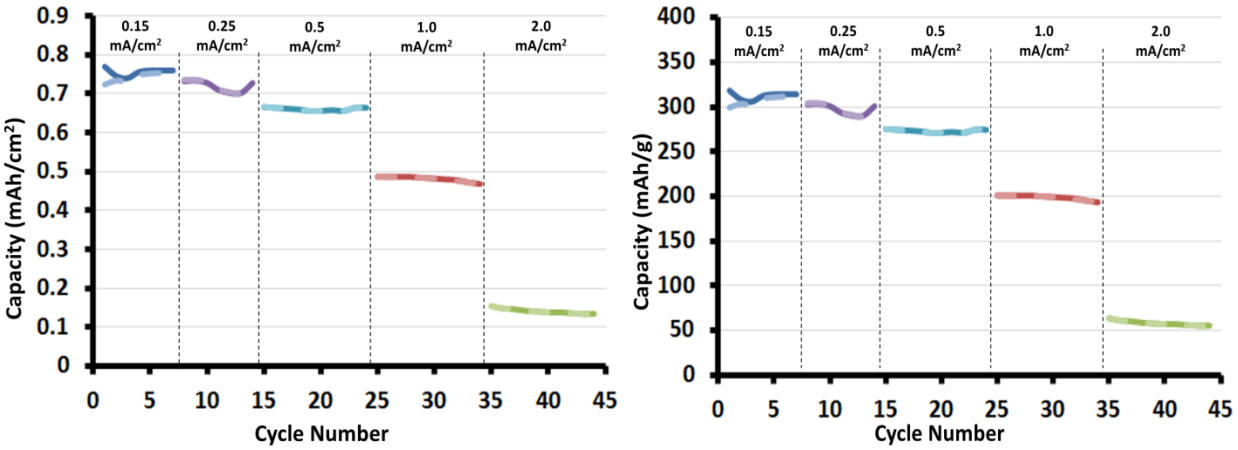

Figure 3.2.3: Planar Electrode 1 **r**ate capability and cycling data normalized by footprint area (left) and mass of MCMB (right).

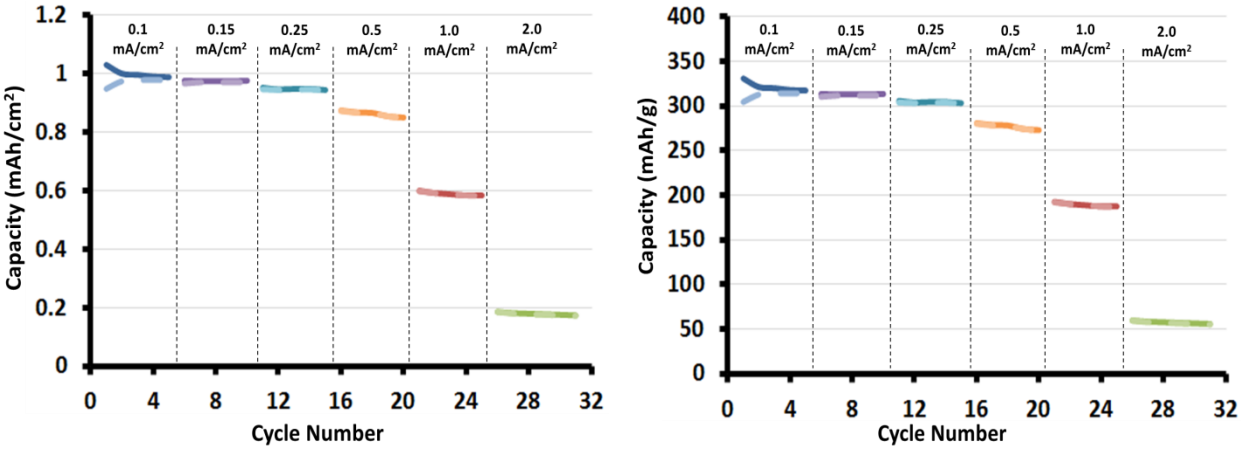

Figure 3.2.4: Planar Electrode 2 rate capabilities and cycling data normalized by footprint area (left) and mass of MCMB (right).

MCMB for an active mass loading of 3.1 mg/cm^2 and a maximum areal capacity of 1.16 mAh/cm^2.

Rate capability and cycling data for Electrode 1 and Electrode 2 are presented in Figure 3.2.3 and Figure 3.2.4. It can be seen that Electrode 1 obtained an average areal discharge capacity of 0.76, 0.72, 0.66, 0.48 and 0.14 mAh/cm^2 at current densities of 0.15, 0.25, 0.5, 1.0 and 2.0 mA/cm^2. These values correspond to material utilization efficiencies of 84%, 80%, 73%, 53% and 15%. Electrode 2 achieved an average discharge capacity of 1.0, 0.97, 0.95 0.86, 0.59

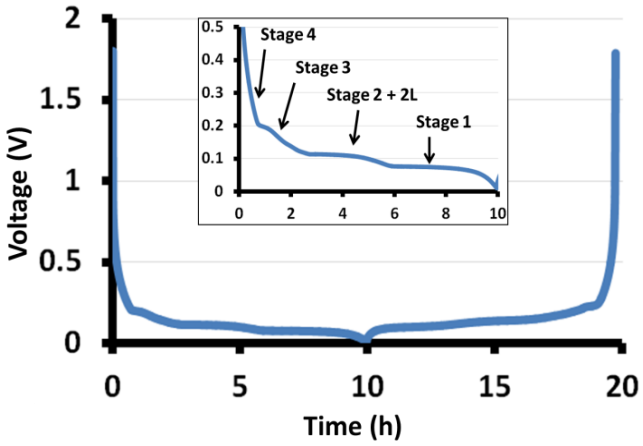

Figure 3.2.5: Typical discharge/charge profile for lithium intercalation in carbon. Inset zooms in on intercalation voltages showing staging plateaus.

and 0.18 mAh/cm^2 at a rate of 0.1, 0.15, 0.25, 0.5, 1.0 and 2.0 mA/cm^2, respectively (Table 3.2.1). These capacities correspond to a material utilization efficiency of 86%, 84%, 82%, 74%, 51% and 15%. Excluding the first cycle, both electrodes maintained a Coulombic efficiency of 97% or greater. It is interesting that for both planar electrodes, a significant decrease in material utilization begins to occur around 0.5 mA/cm^2, as evident by a 7% drop in utilization efficiency. The transition between 0.5 mA/cm^2 and 1.0 mA/cm^2 is accompanied by massive 20-25% decrease in material utilization, clearly illustrating the kinetic limitations of lithium intercalation in carbon.

Figure 3.2.5 represents a typical discharge and charge curve of a planar carbon electrode. An applied negative current results in lithium ions leaving the lithium foil counter electrode and intercalating into the MCMB working electrode. The intercalation of lithium ions is associated with the insertion of electrons to maintain electrical neutrality. The introduction of electrons increases the electron energy level of the electrode, thus reducing the working voltage. Charging the cell with a positive current leads to lithium deintercalation at the working electrode and lithium plating at the counter electrode. The inset of Figure 3.2.5 represents a focused portion of

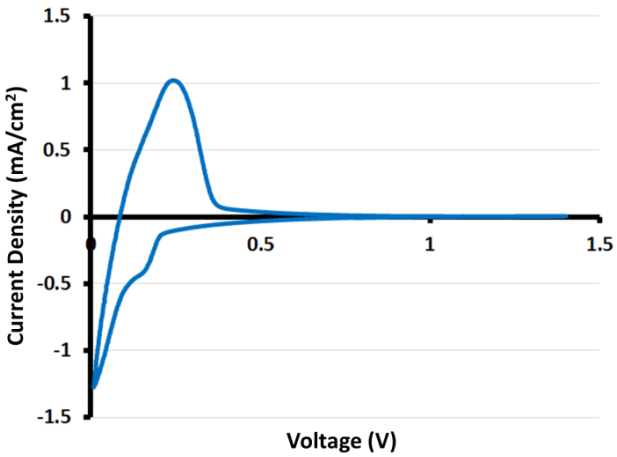

Figure 3.2.6: Cyclic voltammagram of planar electrode. Sweep rate = 0.1 mV/s

the discharge process. The three plateaus clearly show the staging process of lithium intercalation in carbon described earlier. Furthermore, the ability to distinguish staging plateaus suggests there is a minimal kinetic overpotential for the intercalation process at this current density (0.1 mA/cm^2).

Cyclic voltammetry was performed to ensure lithium intercalation was the dominant reaction occurring in the cell (Figure 3.2.6). In the case of intercalation, CV peaks signify a balance between lithium ion diffusion in a liquid and solid medium. Since solid state diffusion is rate limiting, peaks are mostly controlled by lithium diffusion through the active material. Peaks are expected to be broad due to the slow diffusion process and phase transitions that must occur during the staging process. The current-voltage behavior of the planar electrode shows no significant side reactions interfering with the carbon intercalation. In fact, a cathodic sweep to 0.01 mV reveals two distinct intercalation peaks. The onset of the first peak occurs around 0.2 mV, most likely indicating the onset of stage 3 intercalation. The second peak begins near 0.1 mV which is the expected voltage for stage 1 intercalation.

3.3 3D MCMB Electrodes

3.3.1 Experimental

Three-dimensional MCMB electrodes were synthesized using advanced micromachining techniques (Fig 3.3.1). Deep reactive ion etching (DRIE) was used to fabricate inverse templates of various feature sizes based upon earlier geometric calculations. The silicon molds were then filled with the appropriate material using an extrusion process. Next, the filled molds were attached to the current collector using a conductive epoxy and heat treated at 120*C for at least 1 hour. Finally, the silicon was etched using a dry XeF_2 process.

Silicon mold fabrication. Silicon was anisotropically etched using Uniaxis SLR 770 deep reactive ion etcher (DRIE) to form the mold. This machine used fluorine plasma and a proprietary Bosch process to etch deep anisotropic trenches in silicon. The silicon was masked during etching using AZ 4620 positive photoresist (PR). The PR was spin coated on a 4 inch wafer at 3000 RPM for 20 s to form a 10 μm thick film. The PR was soft baked at 100˚C for 7 minutes and patterned using photolithography. It was then hard baked at 120˚C for 10 minutes.

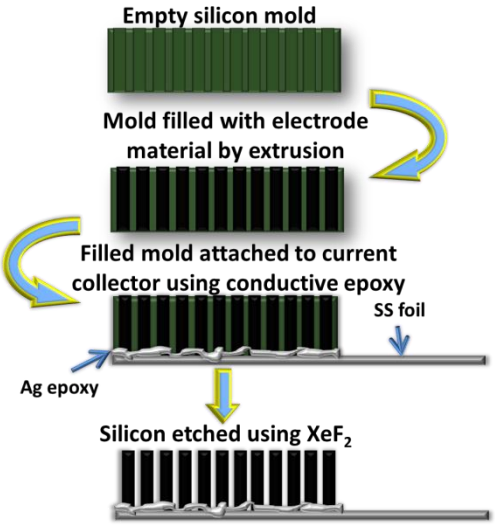

Figure 3.3.1: Process flow for fabrication of 3D MCMB electrode

The last hard bake step was essential for the PR to survive in the DRIE machine for a long period of time. The molds were fabricated by Dr. Guangyi Sun from Professor CJ Kim's group in the MAE department. Details on mold fabrication can be found in reference [12].

Post extrusion. Silicon molds were filled using an extrusion method involving a high pressure syringe pump. It was previously decided to incorporate anode material as the post structure due to the large cathode volume needed to optimize a concentric tube battery. Mesocarbon microbeads (MCMB) have also been shown to successfully intercalate Li ions at moderate current densities for multiple cycles [6]. Furthermore, SEM images of MCMB shows a particle size on the order of 10 microns, which is small enough to fill the channels in the mold (Figure 3.1.4).

MCMB slurry consisting of 7-10 wt% CMC binder was prepared by methods previously described. A filter holder was used to house the silicon mold and placement pieces, as seen in Figure 3.3.2. The silicon mold was placed on top of a Whatman filter membrane and metal filter. A Teflon ring held the mold in place and also helped to funnel the material through the mold. A small piece of Kapton tape could also be used to anchor the mold to the Whatman filter. The slurry was then introduced to the piece through the top opening using a plastic disposable pipette.

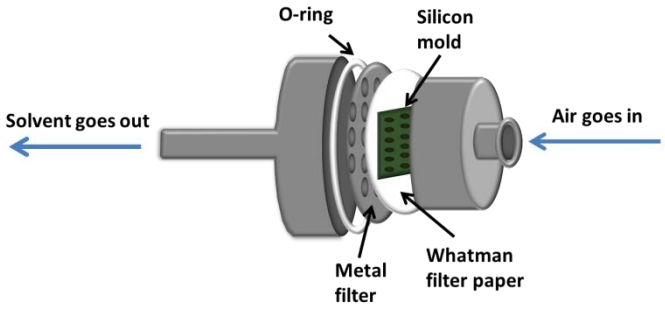

Figure 3.3.2: Assembly of filter holder showing positioning and layering of components

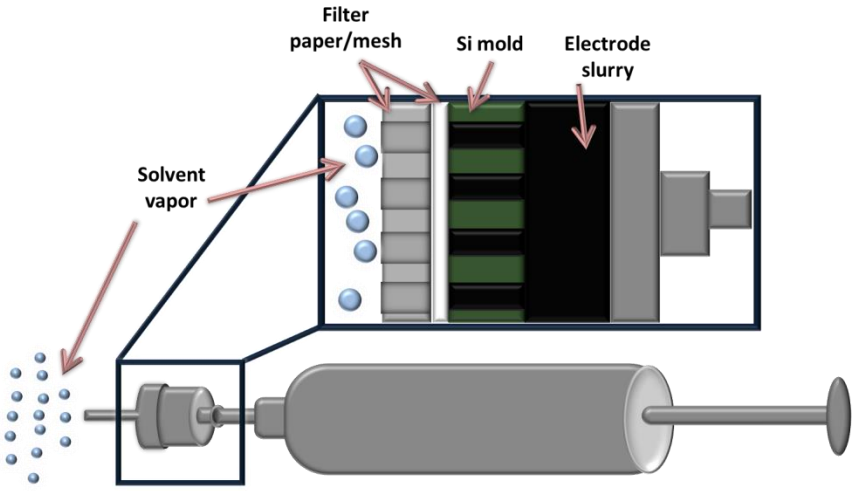

Figure 3.3.3: Diagram of mold filling process. Focused portion is cross section of filter holder holding the silicon mold.

This unit was then attached to a high pressure stainless steel syringe (Harvard Apparatus) at one end and a vacuum pump at the other end (Figure 3.3.3). The high-pressure syringe pump was then used to force the slurry into the mold while the vacuum simultaneously pulled the slurry through. This process was repeated 3-5 times and allowed to sit at high pressure for approximately 5-10 minutes between each refill and pump. After the final injection, the system was allowed to sit until the pressure was relieved. The slurry was then dried either in air or at 120^{O}C.

Attachment to current collector. When the extrusion process was complete, the mold was attached to a current collector using a silver conducting epoxy (Epo-Tek). Filled molds were cleaned by scraping the surface with a sharp blade and weighed to determine the mass of electrode material. Current collectors were either copper or stainless steel. Prior to attachment, holes were drilled through any foil-based current collectors to ensure that a composite-like structure would be created with the conductive epoxy. The epoxy must meet three requirements: supply a low-resistance electrical contact of the posts to the current collector, give structural

support to the free-standing posts and be electrochemically inactive in the working potential range. Separate tests conclude that the silver conducting epoxy meets all of these prerequisites when used for an anode. After attaching the current collector, the electrode was dried in an oven at 100*C for at least 3 hours to cure the epoxy.

Mold releasing. The most important property of the etchant is that it be nonreactive with the active electrode material. Once released, the electrode should remain physically and chemically intact. Vapor phase xenon difluoride (XeF_2) has been shown to both be highly specific to silicon and have fast etch rates [13].

Resistivity measurements. Four-point probe testing was performed to measure the resistivity of individual posts was using a Hewlett-Packard 4284A Precision LCR Meter. The current response is measured when 13 mV is applied at a frequency of 1 kHz.

Electrochemical setup. Electrochemical testing was performed using a BioLogic VMP3 multi-channel potentiostat. Electrodes were galvanostatically cycled between 0.01 V and 1.8 V at various current densities. Cyclic voltammetry was carried out using a sweep rate of 0.1 mV/s

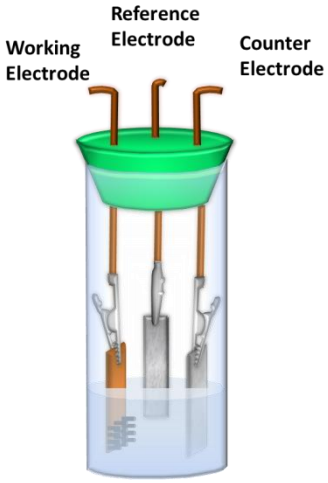

Figure 3.3.4: Experimental setup for 3D electrode half-cell characterization

between 0.01 V and 1.4 V. Prior to testing, lithium foil was cleaned using polyethylene and used as the reference and counter electrodes. The prepared 3D carbon electrode acted as the working electrode. The three electrodes were immersed in approximately 8 mL of electrolyte composed of 1 M $LiClO_4$ dissolved in a 50:50 mixture of EC/DMC. Cells were constructed using a cylindrical glass jar and rubber stopper fashioned with three copper wire leads to act as electrical contacts (Figure 3.3.4).

3.3.2 Results and Discussion

3.3.2.1 Post resistivity

Once the electrode feature sizes have been decided upon, a silicon mold having the inverse structure is constructed using lithographic techniques. The mold is then placed in a filter holder and infiltrated with slurry material using a combination of high pressure and vacuum. Once dried, the mold is attached to a current collector with silver epoxy. The final step involves a dry etch process that leaves behind free standing carbon posts. The precise nature and maturity of these methods allow us to fabricate electrodes of various feature sizes, ranging in aspect ratio from 3.5:1 to 7:1 (Figure 3.3.5 and 3.3.6).

Prior to silicon etching, post resistivity is measured using an LCR meter connected to a probe station. Four tungsten probe tips are positioned so that two tips are in contact with the top of the post while the two remaining tips are in contact with the current collector (Figure 3.3.7). A sinusoidal-varying voltage is applied between two probes while the current response is measured between the other probes. The resulting resistance was then used to calculate the volumetric resistivity.

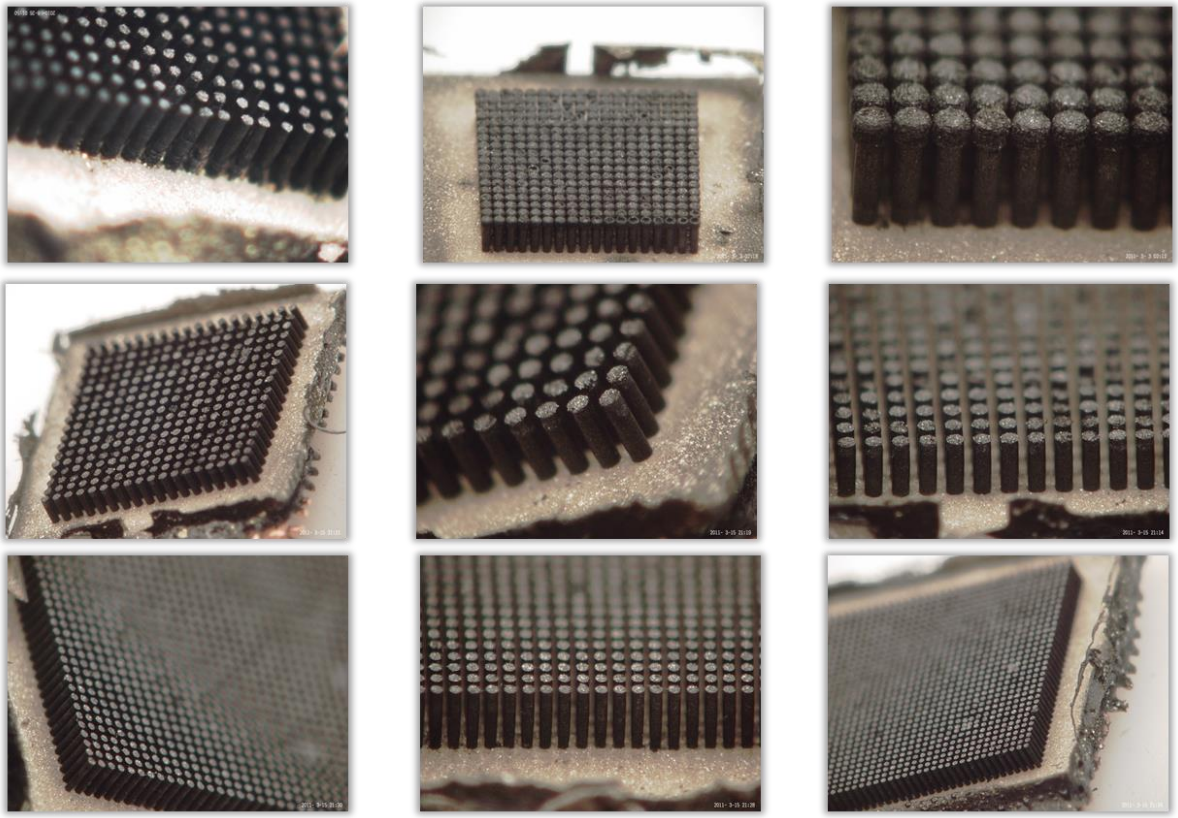

Figure 3.3.5: 3D MCMB electrodes. TOP: 18x18 array, D = 110 µm, H = 550 µm MIDDLE: 18x18 array, D = 100 µm, H = 350 µm BOTTOM: 34x34 array, D = 50 µm, H = 350 µm

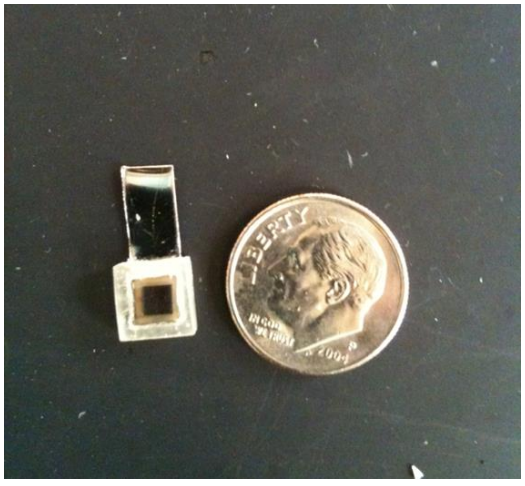

Figure 3.3.6: Size scale of 3D MCMB electrode encased in epoxy. Black square in middle is 18x18 array of carbon posts, 0.09 cm^2

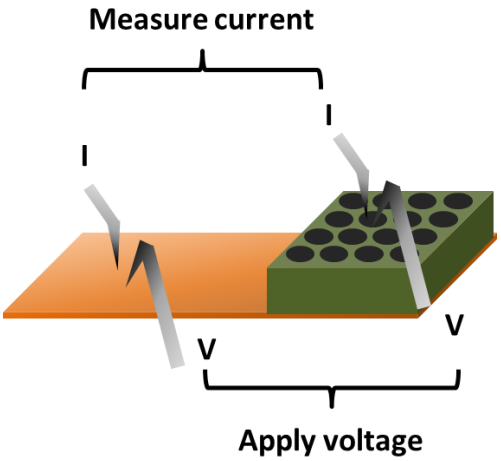

Figure 3.3.7: Experimental setup for post volumetric resistivity measurements**.**

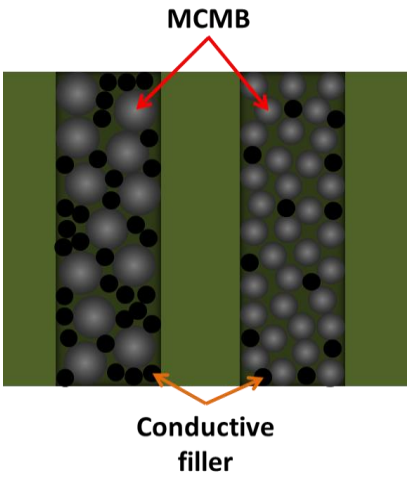

Figure 3.3.8: Effect of MCMB particle size on mold filling

Three post sizes were measured in order to determine how diameter and height affect the electrode resistance. Electrode 3D-1 was 550 µm tall with a diameter of 100 µm, Electrode 3D-2 was 350 µm tall with a diameter of 100 µm and Electrode 3D-3 was 350 µm tall with a diameter of 50 µm. In all samples, the slurry had a mass distribution of 83% MCMB (average particle size = 6 µm) , 7% CMC, 8% natural graphite and 2% Ketjen black. At least 20 posts from each sample were measured to obtain an accurate average value. The average measured rod resistance for electrodes 3D-1, 3D-2 and 3D-3 are 170 Ω, 90 Ω and 420 Ω, respectively. The volumetric resistivities were nearly identical for each sample, yielding 0.24, 0.2 and 0.24 Ω-cm for their respective electrodes (Table 3.3.1). Surprisingly, Electrode 3D-4 had nearly identical features as those of Electrode 3D-1 with the exception that the average particle size was 10 µm rather than 6 µm yet had a volumetric resistivity 58% less than Electrode 3D-1. This may be explained by the fact that Electrode 3D-4 needs almost half the number of MCMB particles to fill a channel in the mold. Furthermore, the larger MCMB particles will have larger interparticle voids that can accommodate more conductive filler (Figure 3.3.8). These two factors are expected to reduce the particle-to-particle contact resistance.

	3D-1	3D-2	3D-3	3D-4
Height (µm)	550	350	350	550
Diameter (µm)	100	100	50	105
Theoretical Active Mass (mg)	1.34	0.85	0.76	1.47
Measured Active Mass (mg)	1.23	0.94	0.63	1.57
Average Post Resistance (Ω)	170	90	420	63
Average Volumetric Resistivity (Ω-cm)	0.24	0.2	0.24	0.1

Table 3.3.1: Physical and electrical properties of various MCMB post sizes

Post resistivity is also dependent upon the mold filling efficiency. This value can be determined using the same modeling boundaries described in Chapter 2. For example, a slurry consisting of 83% MCMB, 7% CMC, 8% graphite and 2% Ketjen black was measured to have a density of about 1.15 g/cm^3. Using this value, an 18x18 array of 100 µm diameter posts 550 µm tall should have 1.34 mg of active material, whereas a 350 µm tall array should have 0.85 mg of active material. The actual measured active mass for a mold of the former size was 1.23 mg, giving a 93% filling efficiency. The experimental mass for molds of other feature sizes is given in Table 3.3.1. Values over 100% are due to thin layers of carbon that remain attached even after

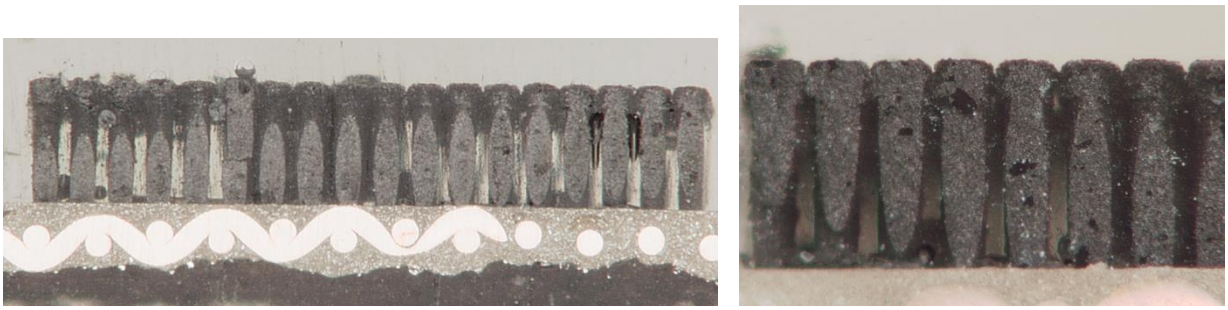

Figure 3.3.9: Cross section of MCMB posts at (left) 200x and (right) 400x.

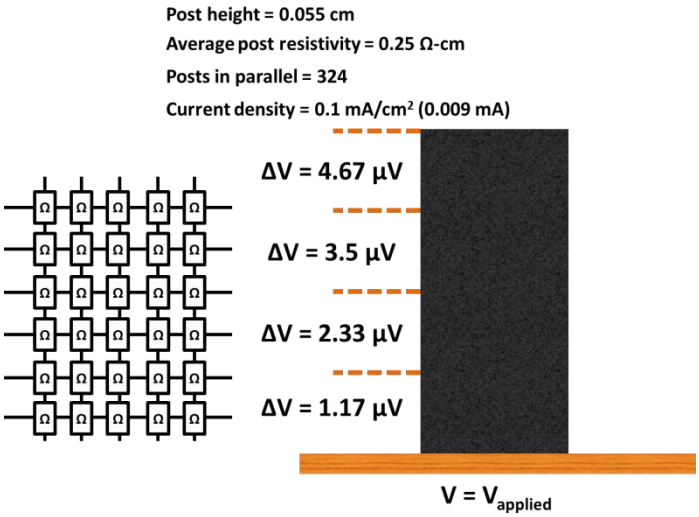

Figure 3.3.10: (left) Circuit model of post arry (right) example of IR drop along post at 0.1 mA/cm^2

cleaning the mold with a blade. High filling efficiency values are further verified by cross section images revealing very few voids throughout the post structure (Figure 3.3.9). Therefore, it can be concluded that the post resistivity values are fairly accurate.

While the post volumetric resistivity values are higher than desired for an electrode, it should be pointed out that the operating currents are very small. This translates to a minimal voltage drop across each post. For examples, if a 3D electrode is to be modeled as an 18x18 array of 168 Ω resistors connected in parallel, then the system is governed by,

$$I = V\left[\frac{324}{168\ \Omega}\right] \qquad 3.3.1$$

Substituting 0.009 mA for I yields a voltage drop of only 0.0046 mV (Figure 3.3.10). Therefore, even at a current density of 10 mA/cm^2, the top of the posts will only see a difference of about 5 mV compared to the voltage applied to the current collector.

3.3.2.2 Electrode impedance

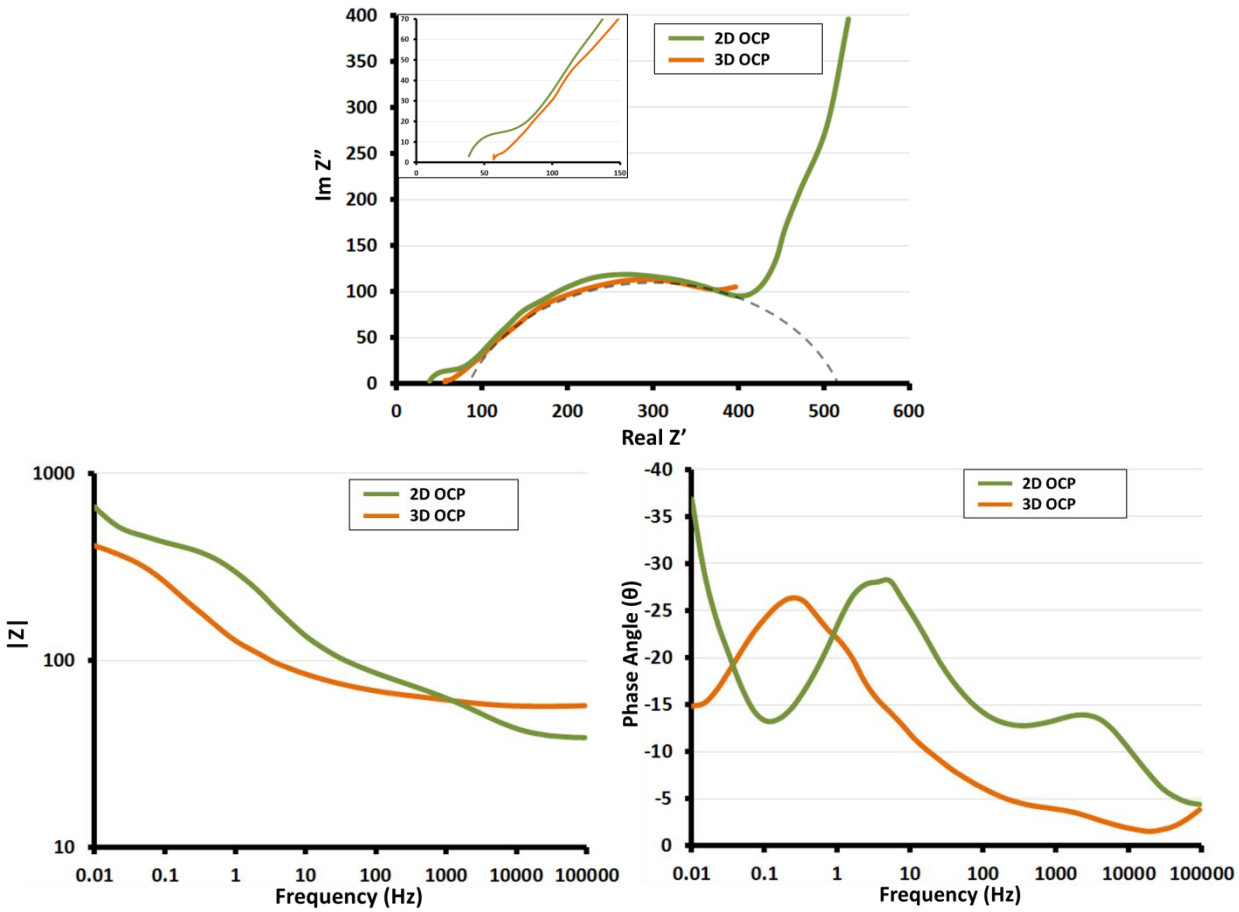

Figure 3.3.11: Nyquist (top) and Bode (bottom) plots comparing 2D (green) and 3D (orange) cells at 0% SOC. Inset of Nyquist plot is focused on high frequency range.

Impedance spectra of a 3D electrode at 0% state of charge is presented in Figure 3.3.11 and compared to a planar electrode. A Nyquist plot reveals what appears to be one large semicircle instead of two. This suggests the cell is limited by a single charge transfer resistance of considerable magnitude. The cell resistance of a 3D MCMB electrode is approximately 500 Ω, which is surprisingly similar to the 2D electrode cell resistance. However, nearly all of that resistance is associated with the reaction resistance at a single electrode. The lack of a Warburg element provides more evidence of a system that is under kinetic control [11].

The Bode plot displaying phase angle as a function of frequency shows a shift of the peak to a lower frequency when compared to a planar cell. This behavior is explained by a

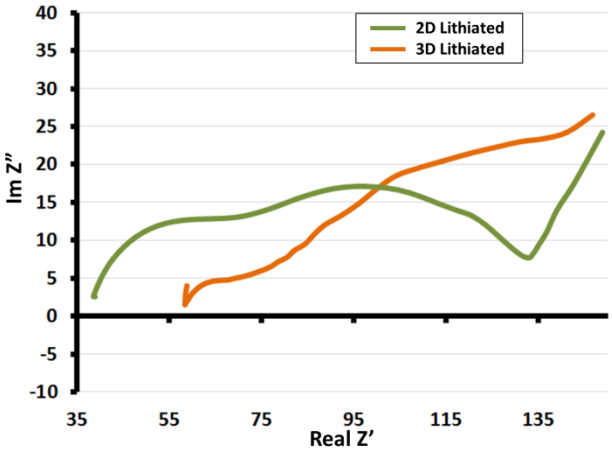

Figure 3.3.12: Nyquist plot comparing 2D (green) and 3D (orange) cells at 95% SOC

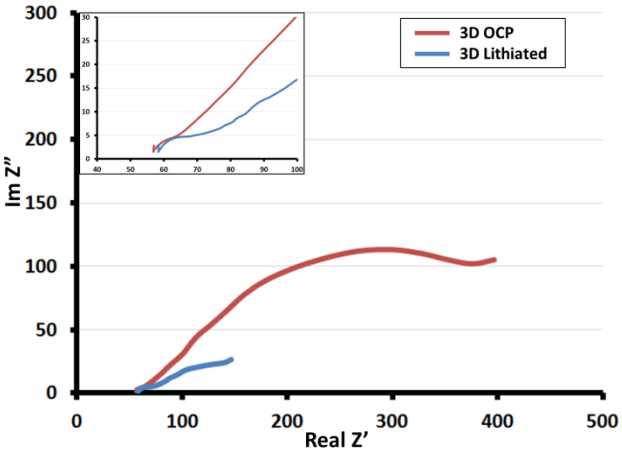

Figure 3.3.13: Nyquist plot comparing 0% (red) and 95% (blue) SOC of 3D MCMB cell

combination of the higher electrolyte and charge transfer resistances of the 3D cell. A plot of impedance as a function of frequency suggests that the 3D cell has a smaller resistance than the 2D cell. However, Nyquist plots such as these fail to display any information about the kinetics of a system. As a result, low frequency diffusion resistance is indistinguishable from the electronic resistance. This is a good example of how displaying data in various graphical representations can explain ambiguous results.

A comparison of lithiated 3D and planar electrodes is displayed in Figure 3.3.12. It can be seen that the cell impedance is decreased to about 170 Ω, which is similar to the 2D cell resistance of 135 Ω. This is low enough to now distinguish a second semicircle occurring at the high frequencies. It can be concluded that the resistance of a 3D cell behaves similarly to a 2D cell in that the carbon electrode is the limiting step. Furthermore, the lithiation process greatly decreases the electrode resistance by altering the electronic structure of the carbon (Fig 3.3.13).

3.3.2.3 Rate Capabilities: 2D vs. 3D comparisons

Rate capability tests were performed to compare 3D storage capabilities to those of the previously tested planar samples. In all presented data, the first 2-6 cycles of 3D electrodes are omitted due to the presence of a thin layer of silver silicide that has shown to intercalate lithium. Control experiments reveal that under similar testing conditions, the layer is no longer active after at most 6 cycles.

The top half of Table 3.3.2 compares the physical properties of a 2D and 3D electrode. It is apparent that the active mass loading of the 3D electrode is far greater than that of the 2D electrode. This in turn directly places the 3D electrode at a distinct advantage for the maximum charge storing capabilities. While the planar electrode is limited to only 1.16 mAh/cm^2, the 3D

Table 3.3.2: 2D vs. 3D comparison of physical properties and rate capabilities.

	PLANAR ELECTRODE 2						3D-7						
Mass (mg)	1.79						2.21						
Footprint Area (cm^2)	0.5						0.09						
Active Mass Loading (mg/cm^2)	3.1						22.1						
Max Areal Capacity (mAh/cm^2)	1.16						8.21						
Current Density (mA/cm^2)	0.1	0.15	0.25	0.5	1.0	2.0	0.1	0.25	0.5	1.0	1.5	2.0	3.0
Current Density (mA/g)	32	48	80	161	321	642	4.5	11.6	22.6	45.2	67.8	90.5	135.9
C-Rate	C/12	C/7.7	C/4.6	C/2.3	C/1.2	1.7C	C/82	C/33	C/17	C/8	C/6	C/5	C/3
Average Areal Discharge (mAh/cm^2)	1.0	0.97	0.95	0.86	0.59	0.18	7.67	5.58	3.67	1.81	1.14	0.77	0.4
Average Areal Charge (mAh/cm^2)	0.97	0.97	0.94	0.86	0.59	0.18	6.85	5.14	3.54	1.79	1.14	0.77	0.4
Average Gravimetric Discharge (mAh/g)	321	314	304	277	189	58	347	252	166	82	52	35	18
Average Gravimetric Charge (mAh/g)	312	312	303	276	189	57	310	233	162	81	52	35	18

electrode has the ability to store 8.21 mAh/cm^2 due to a massive loading of 22.1mg/cm^2. This is a direct consequence of using the active material to build a three-dimensional structure. In this arrangement, there is no dead space occupied by scaffolds or templates, thus maximizing the energy storage capabilities.

The rate capabilities of 2D and 3D electrodes are displayed in the lower half of Table 3.3.2. The 3D electrode achieved a maximum average capacity of 7.67 mAh/cm^2 when discharged at 0.1 mA/cm^2, an increase of nearly 670% when compared to the 2D electrode. It can be seen that the 3D electrode outperformed the 2D electrode by at least 200% at each current density. In fact, the capacity of the 3D electrode does not fall below the maximum of the 2D electrode until it is discharged at a very fast rate of 2.0 mA/cm^2. The superior performance can again be attributed to the 3D nature of the electrode. By assembling the material into a high surface area post array, a more effective system of charge storage is established by increasing the number of sites available for a chemical reaction.

Another interesting effect of the increased mass loading available to 3D electrodes is the increased discharge time. For instance, a current density of 0.1 mA/cm^2 is equivalent to a C/12 rate for the planar electrode. However, because of the large active mass loading associated with the 3D electrode, a current density of 0.1 mA/cm^2 is equal to a C/82 rate (Figure 3.3.14). This is important for device power delivery since this means a system requiring the battery to output 0.1 mA/cm^2 will be capable of running 700% longer between battery charges. This is assuming the battery is capable of holding the proper voltage as well.

Cyclic voltammetry was also performed under the same conditions as the planar experiments. From Figure 3.3.15, it is evident that the 3D nature does not disrupt a normal lithium intercalation/deintercalation process. This is confirmed by the peak near 0.15 V that is

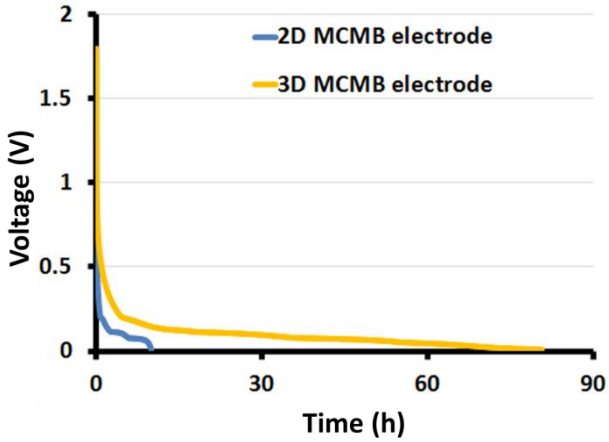

Figure 3.3.14: Discharge curves of planar and 3D electrode at 0.1 mA/cm^2. 3D discharge is nearly 700% longer at same current density

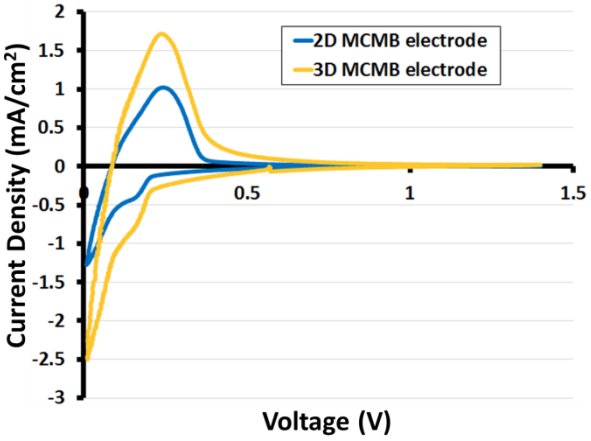

Figure 3.3.15: Comparison of CV curves for planar and 3D electrodes

identical to that found in the curve of the planar sample. Furthermore, the absence of extra peaks indicates that the lithiation/delithiation process is the dominant reaction occurring in the cell. Because the current response is directly related to the number of ions flowing across an interface, it can also be confirmed that the enhanced surface area of the 3D electrode facilitates more reactions per footprint area than a planar electrode.

It has been shown that the 3D electrode has superior charge storage capabilities when compared to a planar electrode. However, one metric which it underperformed in is material utilization. Whereas the planar sample experienced a material utilization drop of only 4% between 0.1 mA/cm^2 and 0.25 mA/cm^2, the 3D sample dropped by 25% over the same rate step. The next rate step, from 0.5 mA/cm^2 to 1.0 mA/cm^2, was accompanied by another 23% loss in material utilization. By the last rate test, the 3D electrode was only using 5% of the available material, or equal to 18 mAh/g.

A possible explanation for this may come from the cell orientation. Previously, it was determined that the voltage drop along the post was less than 1 mV. Therefore, it can be assumed that there is no preferential lithiation due to voltage effects. It can also be shown that the volume

of an individual post 550 μm tall with a diameter of 100 μm is $4.32x10^{-6}$ cm^3, which translates to about $4.1x10^{-7}$ mol of carbon per post. Since the spacing between posts is 60 μm, then we can assume a shell that is extended 30 μm in each direction exists around the post. The volume of this shell is $7.28x10^{-6}$ mL containing $7.28x10^{-9}$ mol of lithium ions in an electrolyte containing 1 M lithium salt. For full lithiation, the ratio of lithium to carbon should be 1:6. However, the ratio is about 1:60 in this situation. Thus, only about 10% of the carbon will be lithiated from this shell while the remaining lithium ions will diffuse from the bulk of the electrolyte or from the counter electrode.

It is has been suggested that because the lithium diffusion coefficient in electrolyte ($D \sim 10^{-5}$ cm^2/s) [6] is orders of magnitude greater than lithium diffusion in MCMB ($D \sim 10^{-8}$ cm^2/s) [14], the surface concentration of lithium ions will be constant and won't limit the intercalation process. However, it can easily be shown that if every lithium ion within the electrolyte shell were deposited on the surface of the carbon post, the ions would need to intercalate 2.5 μm to account for 10% of the post lithiation. This process would take approximately 6.2 seconds. In reality, a portion of the ions need to diffuse 30 μm in the electrolyte to reach the surface, a process that would take at least 9 seconds. Therefore, it can be assumed that the surface concentration will be close to zero and not act as a constant source for ions.

Since it is now assumed that the depletion region around a post is greater than 30 μm, it can also be assumed that the electrolyte between posts will have a minimal lithium ion concentration. Since there is no voltage driven lithiation preference, the remaining lithium will preferentially intercalate at the point of the electrode closest to the counter electrode. In the experimental set-up, the 3D electrode essentially has a planar interface with the counter

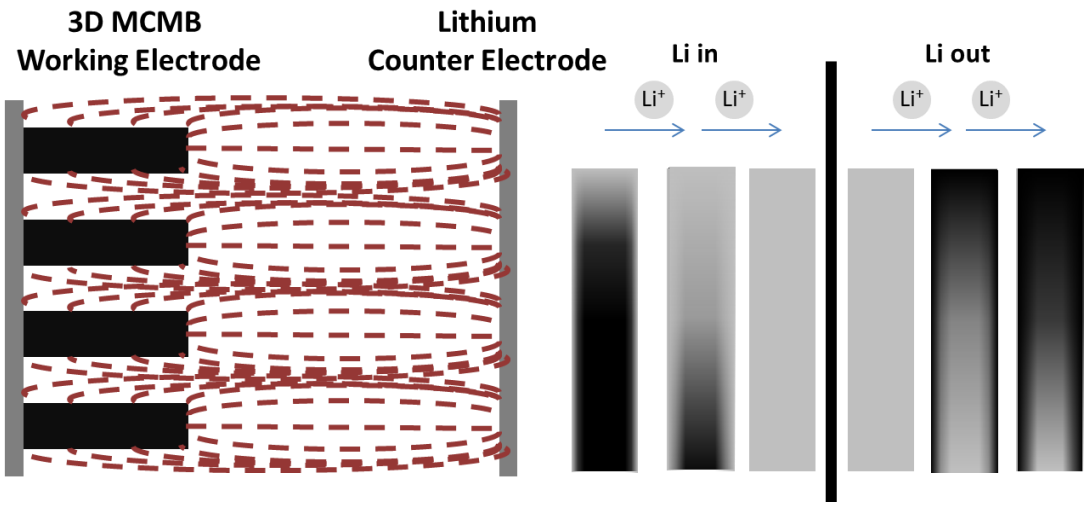

Figure 3.3.16: Possible source for poor material utilization in 3D MCMB electrodes. Lithium ions diffuse mostly through the top of the posts due to a combination of its proximity to the counter electrode and interfering electric fields between posts. Deintercalation through the length of the post results in lithium trapping within posts.

electrode, creating an electric field that runs parallel to the posts. Therefore, most of the lithiation will occur at the top of the posts and diffuse axially to accommodate more lithium ions (Figure 3.3.16). This translates to ion diffusion distances on the order of hundreds of microns. A diffusion process this tortuous would be expected to result in low material utilization along with possible trapping of ions in the host matrix.

The described situation should be evaluated further using advanced simulation programs that can also consider the effects of overlapping electric fields between neighboring posts. However, it can be successfully concluded that the true benefits of a 3D electrode cannot be exploited unless assembled with a 3D counter electrode. This is the only approach to accurately test a 3D electrode with the proper electric field distribution and diffusion behavior.

3.3.2.4 Rate Capabilities: Feature sizes and slurry content

Tests were also performed to determine the effects of feature sizes on electrode performance. Initial comparisons between electrodes of varying feature sizes illustrate the

difference in active mass loading capabilities that parallel the comparisons to planar electrodes. Electrode 3D-2, composed of 350 μm tall rods, can only accommodate 10.4 mg/cm^2 of MCMB, resulting in a maximum areal capacity of 3.9 mAh/cm^2, whereas Electrode 3D-1, composed of 550 μm tall rods, can accommodate 13.6 mg/cm^2 for a maximum capacity of 5.1 mAh/cm^2. Electrode 3D-5, composed of posts 50 μm in diameter and 350 μm tall, had the lowest mass loading of 6.4 mg/cm^2 for a maximum capacity of 2.4 mAh/cm^2.These results are in line with the modeling figures obtained by previously described methods.

Figure 3.3.17 and Figure 3.3.18 show the cycling data for Electrode 3D-1 and Electrode 3D-2, respectively. These electrodes have identical diameters, but different heights. From the figures, it can be seen that Electrode 3D-1 achieved a maximum discharge capacity of 4.94 mAh/cm^2 but a stable average discharge capacity of 2.7 mAh/cm^2 when operated at 0.1 mA/cm^2. At the same current density, Electrode 3D-2 achieved a maximum discharge capacity of 3.79 mAh/cm^2 but a stable average discharge capacity of 1.4 mAh/cm^2. The 29% capacity increase between Electrode 3D-2 and Electrode 3D-1 is directly due to the nearly identical increase in mass loading. The rate capabilities of Electrode 3D-5 are illustrated in Figure 3.3.19. It can be seen that the electrode achieved a maximum capacity of 2.32 mAh/cm^2 but stabilized around 1.2 mAh/cm^2 when cycled at 0.1 mA.cm^2. For comparison, Electrode 3D-2, which has posts of identical height but doubled in diameter, achieved 63% more capacity than Electrode 3D-5. Again, this can be attributed to the larger active mass loading associated with larger feature sizes and proves that 3D batteries can successfully increase electrode capacity by stacking material vertically. Full details of each electrode's rate capabilities are presented in Table 3.3.3.

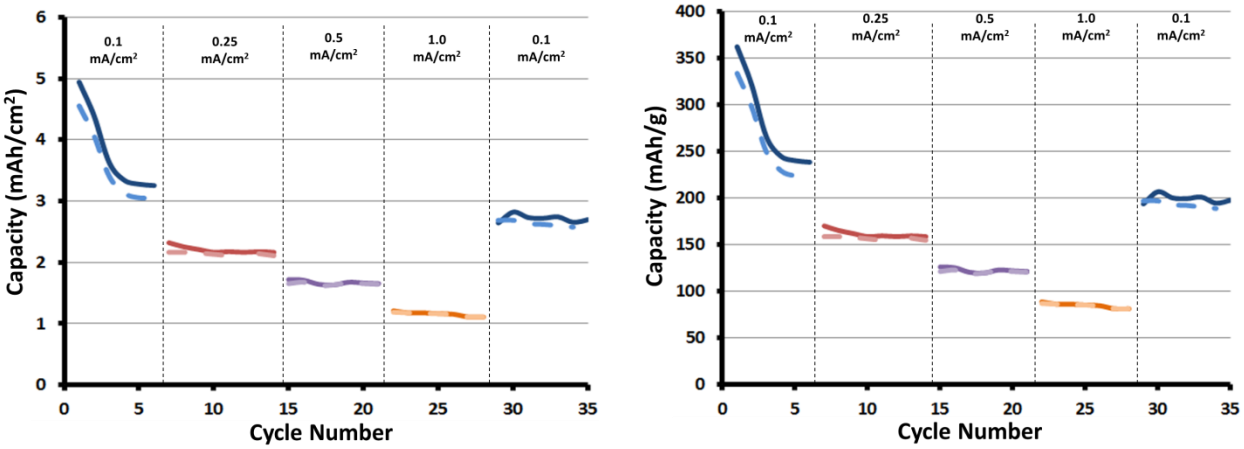

Figure 3.3.17: Electrode 3D-1 rate capability and cycling data normalized by footprint area (left) and active mass of MCMB (right); D = 100 µm, H = 550 µm

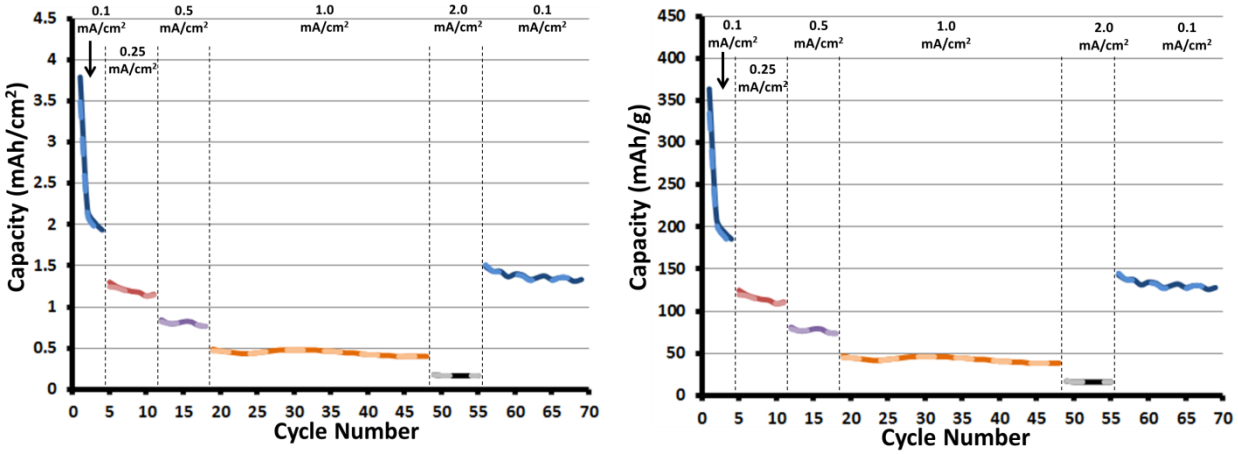

Figure 3.3.18: Electrode 3D-2 rate capability and cycling data normalized by footprint area (left) and active mass of MCMB (right). D = 100 µm, H = 350 µm

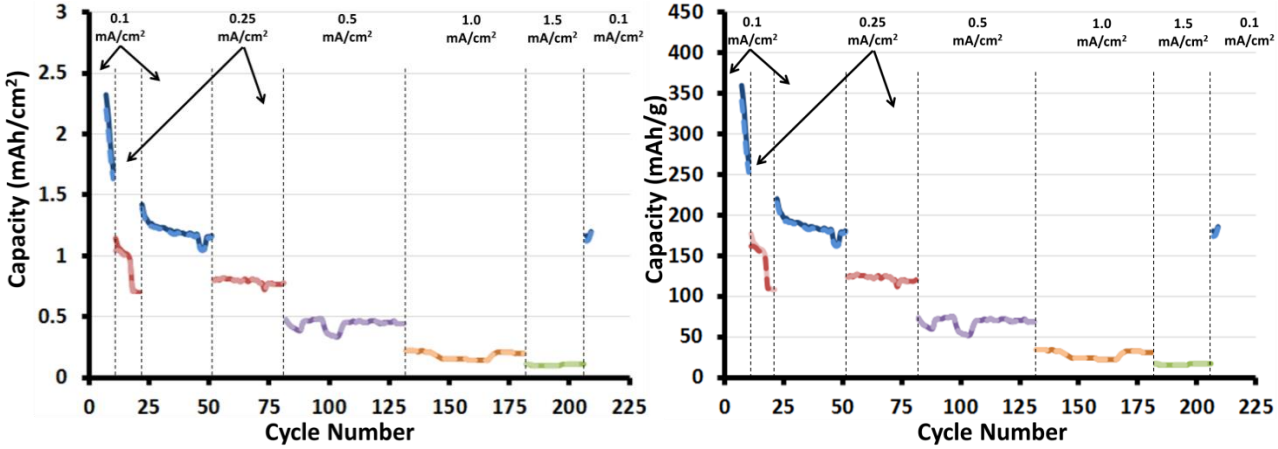

Figure 3.3.19: Electrode 3D-5 rate capability and cycling data normalized by footprint area (left) and active mass of MCMB (right) D = 50 µm, H = 350 µm

Figure 3.3.20: Effect of Ketjen black on physical properties of dried slurry. Deposited slurry on left has zero Ketjen black and slurry on right has 13% Ketjen black.

Electrode efficiencies are determined by comparing gravimetric capacities. Interestingly, the material utilization when cycled at 0.1 mA/cm^2 is about 50% for Electrode 3D-1, but only 37% for Electrode 3D-2. This is surprising considering Electrode 3D-1 has the larger feature sizes. The results comparing post diameter effects are also inconclusive. The material utilization for Electrode 3D-5 was 50%, 33%, 18% and 8% at rates of 0.1, 0.25, 0.5 and 1.0 mA/cm^2, respectively. At the same respective rates, Electrode 3D-2 obtained 37%, 31%, 21% and 11%. It is interesting that the electrode composed of smaller diameter posts outperformed the larger posts only at low current densities. Even more surprising is the fact that Electrode 3D-1 had the highest material utilization of any electrode at every current density (Table 3.3.3). This may be another consequence of the experimental setup. It is likely that overlapping electric fields from adjacent posts or undesirable diffusion behavior results in the inability to fully appreciate the qualities of the 3D electrode.

Slurry properties were also shown to affect the overall performance of 3D electrodes. The amount of Ketjen black can greatly affect the porosity and density of a dried slurry (Figure 3.3.20). The increase in porosity can allow for greater electrolyte penetration and thus improve

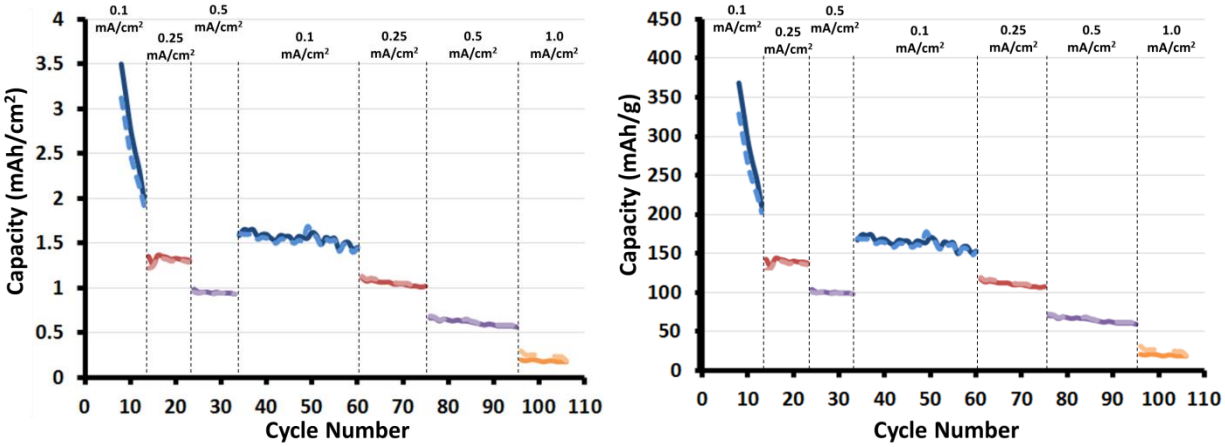

Figure 3.3.21: Electrode 3D-6 rate capability and cycling data normalized by footprint area (left) and active mass of MCMB (right). 13% Ketjen black

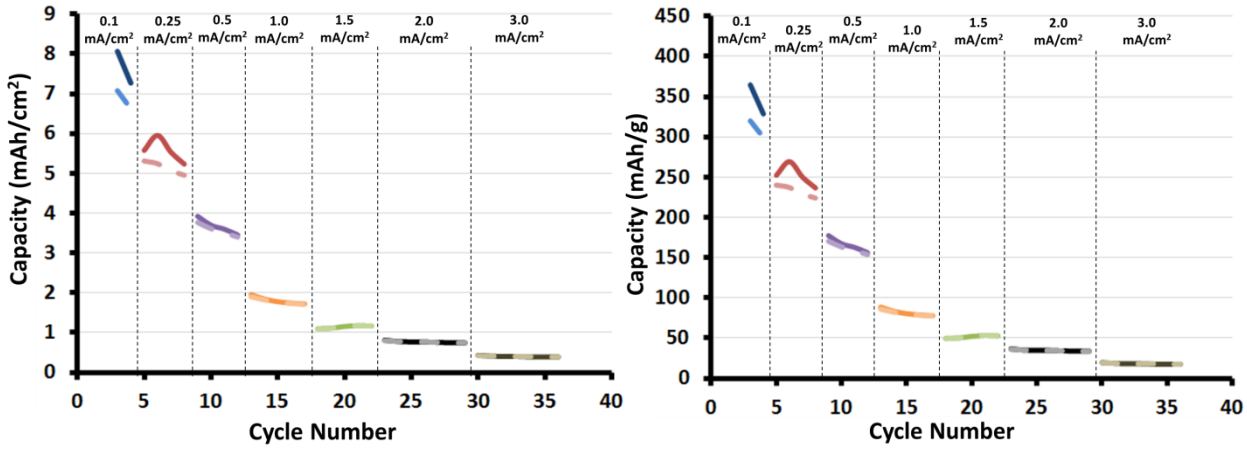

Figure 3.3.22: Electrode 3D-7 rate capability and cycling data normalized by footprint area (left) and active mass of MCMB (right). 0% Ketjen black

the ionic conductivity. However, the high porosity may also create poor electrical connection between particles. Figure 3.3.21 shows the rate capabilities results for an electrode with high Ketjen black content (Electrode 3D-6), while Figure 3.3.22 represents the data for an electrode with no Ketjen black (Electrode 3D-7). It is immediately apparent that the low density of the Ketjen black slurry severely limits the electrode mass loading capabilities (Table 3.3.3). As a result, the maximum discharge capacity is only 3.5 mAh/cm^2, which is much less than the maximum discharge capacity of 8.07 mAh/cm^2 obtained by Electrode 3D-7. The material

utilization during stable cycling is also less than that of Electrode 3D-4 and Electrode 3D-5. By comparison, Electrode 3D-6 only utilized 164 mAh/g of material at a rate of 0.1 mA/cm^2 whereas both Electrodes 3D-1 and 3D-5 achieved 200 and 187 mAh/g, respectively, at the same rate. This low utilization is most likely an effect of the poor network connection that comes with low density slurries.

The physical effects of cycling lithium into and out of the carbon posts were also investigated. From Figure 3.3.23, it can be seen that few microstructural changes occur to the posts as a result of the lithiation process. In fact, most of the structural changes seem to occur at the top of the posts. The posts are also shown to remain in contact with the current collector even after many cycles. The fractured posts are a result of capillary forces during the drying process.

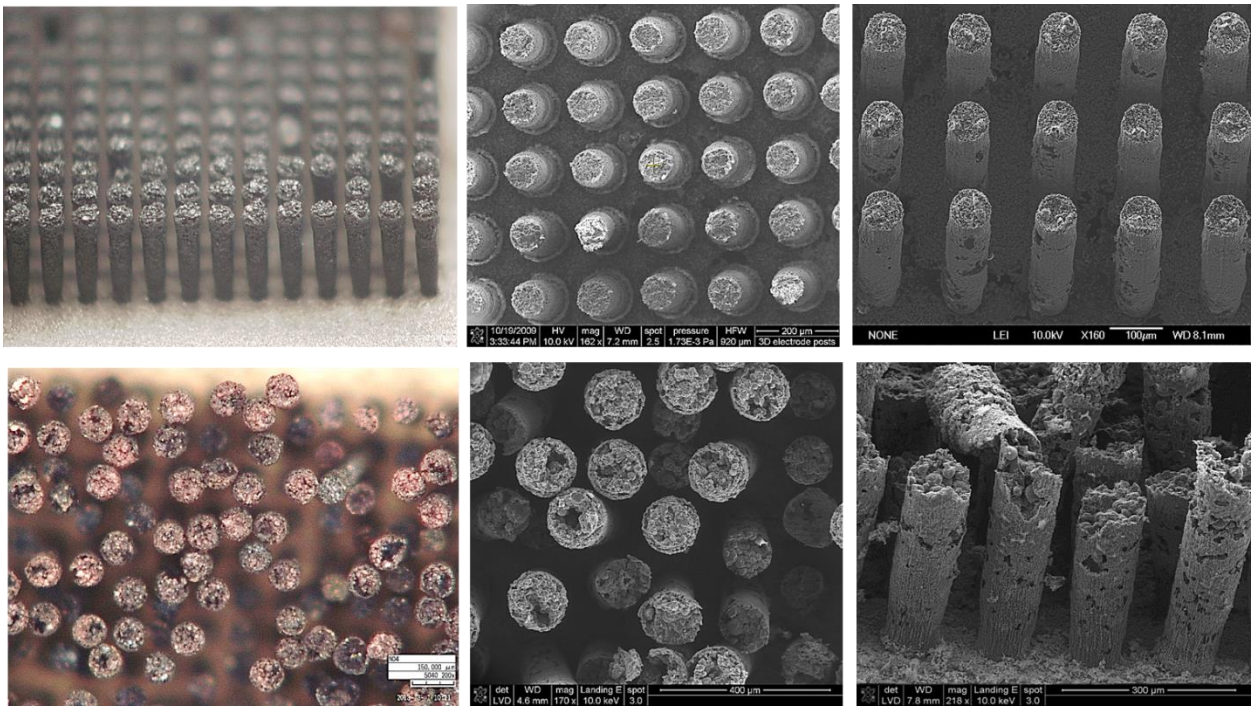

Figure 3.3.23: Comparison of fresh electrodes (top) to lithiated electrodes (bottom). Posts remain intact showing minor structural changes.

	3D-1 83% MCMB, 7% CMC, 8% graphite, 2% CB				3D-2 83% MCMB, 7% CMC, 8% graphite, 2% CB					3D-5 83% MCMB, 7% CMC, 8% graphite, 2% CB					3D-6 77% MCMB, 10% CMC, 13% CB				3D-7 90% MCMB, 10% CMC						
Mass (mg)	1.48				1.13					0.7					1.11				2.21						
Height (μm)	550				350					350					550				550						
Diameter (μm)	100				100					50					110				110						
Active Mass Loading (mg/cm^2)	13.7				10.4					6.45					9.5				22.1						
Max Areal Capacity (mAh/cm^2)	5.08				3.88					2.4					3.53				8.21						
Current Density (mA/cm^2)	0.1	0.25	0.5	1.0	0.1	0.25	0.5	1.0	2.0	0.1	0.25	0.5	1.0	1.5	0.1	0.25	0.5	1.0	0.1	0.25	0.5	1.0	1.5	2.0	3.0
Current Density (mA/g)	7.3	18.7	36.6	73.3	9.6	48	96	192	384	15.5	39.6	77.5	154.9	232.4	10.5	26.9	52.7	105	4.5	11.6	22.6	45.2	67.8	90.5	135.9
C-Rate	C/51	C/20	C/10	C/5	C/39	C/16	C/8	C/4	C/2	C/24	C/10	C/5	C/2.5	C/1.8	C/35	C/14	C/7	C/3.5	C/82	C/33	C/17	C/8	C/6	C/5	C/3
Average Areal Discharge (mAh/cm^2)	2.72	2.21	1.67	1.16	1.4	1.2	0.8	0.44	0.17	1.19	0.79	0.44	0.18	0.11	1.56	1.05	0.62	0.19	7.67	5.58	3.67	1.81	1.14	0.77	0.4
Average Areal Charge (mAh/cm^2)	2.64	2.14	1.65	1.15	1.4	1.19	0.8	0.44	0.17	1.19	0.79	0.44	0.18	0.11	1.54	1.07	0.63	0.25	6.85	5.14	3.54	1.79	1.14	0.77	0.4
Average Gravimetric Discharge (mAh/g)	200	162	123	85	137	115	77	43	16	185	122	68	28	16	164	111	65	20	347	252	166	82	52	35	18
Average Gravimetric Charge (mAh/g)	196	157	121	84	137	114	77	43	16	184	122	68	28	16	162	112	66	26	310	233	162	81	52	35	18

Table 3.3.3: Summary of physical properties and charge storage capabilities at various current densities.

3.4 Conclusions

Basic lithography techniques were used to fabricate three dimensional MCMB electrodes with various feature sizes. Volumetric resistivities were determined using a probe station to access individual rods and calculated to be about 0.25 Ω-cm. This value can be considered to be fairly high, yet basic calculations predict minimal losses at the low currents being used. The electrodes were electrochemically characterized using galvanostatic and cyclic voltammetry methods. Results showed superior areal capacities at various current densities when compared to planar electrodes. However, the material utilization of 3D MCMB was much less than that of the 2D sample. It is believed that the experimental set-up may generate electric fields that results in diffusion behavior not representative of a fully assembled 3D battery.

The effects of feature sizes and slurry content on cycling behavior were also studied. The results did not show any significant enhancement in cycling capabilities when the post height and diameter were reduced. Initial cycling at 0.1 mA/cm^2 suggests material utilization values of close to 100%. However, repeated cycling sees this value stabilize closer to 50% with increasing losses for every increase in current density. This may be a result of lithium ions diffusing axially through the posts rather than through the sidewalls. Thus, it can be concluded that the full benefits of a 3D MCMB electrode are not being realized.

The physical properties of the posts also showed to have an effect on rate capabilities. Cycling data of highly porous posts proved that particle connectivity plays an important role in charge storage behavior. Although the increased porosity can allow for greater electrolyte penetration, the resulting poor mechanical integrity of the posts leads to low material utilization.

Since it was shown that high post volumetric resistivities do not produce drastic iR losses, then efforts should be focused on increasing the density of the posts.

Arguably, the most important aspect of a 3D electrode is the means by which it accommodates the active mass. Large active mass loadings are essential to achieving high areal capacity electrodes. However, how the mass is distributed and maintaining the integrity of the electrode material needs to be addressed as well. It can be concluded that final 3D active mass loadings are highly dependent upon the post feature sizes, slurry properties and filling efficiency.

3.5 References

[1] G. Nazri and G. Pistoia, Lithium Batteries: Science and Technology, Springer, 2003.

[2] K. Ozawa, "Lithium-ion rechargeable batteries with LiCoO2 and carbon electrodes: the LiCoO2/C system," *Solid State Ionics,* vol. 69, no. 3, p. 212, 1994.

[3] M. Yoshio, R. Brodd and A. Kozawa, Lithium Ion Batteries: Science and Technologies, Springer, 2009.

[4] R. Huggins, Advanced Batteries: Materials Science Aspects, Springer, 2009.

[5] K. Tatsumi, N. Iwashita, H. Sakaebe, H. Shioyama, S. Higuchi, A. Mabuchi and H. Fujimoto, "The influence of graphitic structure on the electrochemical characteristics for the anode of secondary lithium batteries," *The Journal of the Electrochemical Society,* vol. 142, no. 3, p. 716, 1995.

[6] C. Daniel and J. Besenhard, The Handbook of Battery Materials, Wiley-VCH, 2011.

[7] E. Yoo, J. Kim, E. Hosono, H. Zhou, T. Kudo and I. Honma, "Large reversible Li storage of graphene nanosheet families for use in rechargeable lithium ion batteries," *Nano Letters,* vol. 8, no. 8, p. 2277, 2008.

[8] Y. Reynier, R. Yazami and B. Fultz, "Thermodynamics of intercalation into graphites and disordered carbons," *Journal of the Electrochemical Society,* vol. 151, no. 3, 2004.

[9] F. Kong, R. Kostecki, G. nadeau, X. Song, K. Zaghib, K. Kinoshita and F. McLarnon, "In situ studies of SEI formation," *Journal of Power Sources,* vol. 97, p. 59, 2001.

[10] K. Moller, H. Santner, W. Kern, S. Yamaguchi, O. Besenhard and M. Winter, "In situ characterization of the SEI formation on graphite in the presence of a vinylene group containing film-forming electrolyte additives," *Journal of Power Sources,* vol. 119, p. 561, 2003.

[11] A. Bard and L. Faulkner, Electrochemical Methods: Fundamentals and Applications, John Wiley and Sons, 2001.

[12] F. Chamran, Y. Yeh, H. Min, B. Dunn and C.-J. Kim, "Fabricatoin of high aspect ratio electrode arrays for three dimensional microbatteries," *Journal of microelectromechanical systems,* vol. 16, no. 4, pp. 844-852, 2007.

[13] J. Dagata, D. Squire, C. Dulcey, D. Hsu and M. Lin, "Chemical processes involved in the etching of silicon by xenon difluoride," *Journal of Vaccuum Science Technology B,* vol. 5, no. 5, p. 1495, 1987.

[14] Q. Wang, H. Li, X. Huang and L. Chen, "Determination of chemical diffusion coefficient of lithiom ion in graphitized mesocarbon microbeads with potential relaxation technique," *Journal of the Electrochemical Society,* vol. 148, no. 7, 2001.

[15] G. Wang, G. Sun, Q. Wang, S. Wang, J. Guo, Y. Gao and Q. Xin, "Improving the DMFC performance with Ketjen Black EC300J as the additive in the cathode catalyst layer," *Journal of Power Sources,* vol. 180, no. 1, p. 176, 2008.

Chapter 4

3D LI ION BATTERY

4.1 Lithium Ion Battery Basics

4.1.1 History and Development of the Lithium Ion Battery

The safety concerns of using lithium metal as a battery component drove the battery market to search for new materials. A string of discoveries in the early 1980s led by Ikeda, Goodenough and Basu shed light on the abilities of carbon and transition metal oxides to intercalate lithium ions [1]. It wasn't until 1991 that Sony made the first commercial lithium ion battery using a carbon anode and lithium cobalt oxide ($LiCoO_2$) cathode. This revolutionary step was accomplished not only by using new intercalation materials, but also by introducing advanced electronic circuitry for charge/discharge control, the cell internal pressure fail-safe and a shut-down polymer separator.

Initial lithium ion batteries utilized hard carbons as the anode, which were only capable of achieving 200 mAh/g, and had a limited the upper voltage of 4.1 V. It was eventually discovered that the propylene carbonate electrolyte was a source of electrode breakdown. The resulting research was spent searching for ideal electrolyte solvents and additives that would react to form a stable SEI with the carbon electrode. This proved difficult since the solvent interactions were very dependent on the type of carbon used as the anode. The development of a functional electrolyte that included various additives in 1998 led to the introduction of high capacity graphite anodes [2]. Later, in 2003, the same methods were used to increase the stability of the $LiCoO_2$ cathode and pushed the cell voltage to 4.2 V. Today, an 18650 cylindrical cell can

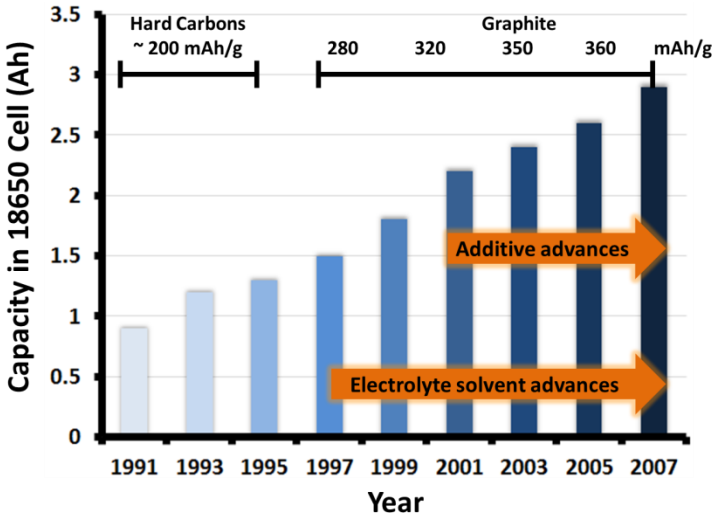

Figure 4.1.1: Development of the 18650 cylindrical lithium ion battery. Adopted from **[2]**

achieve 2.9 Ah, equivalent to 200 Wh/kg or 500 Wh/L, through the use of nickel-based cathode materials and electrolyte additives. The significant achievements of an 18650 cell are charted in Figure 4.1.1. Prismatic cell designs utilizing new polymer gel electrolytes have been able to achieve energy densities of 600 Wh/L [3], while next generation cathode materials are expected to increase specific energy to 450 Wh/kg [4]. Lithium ion batteries are significantly more efficient than the first generation of products, but it should not be overlooked that these advances have taken over 30 years to accomplish.

4.1.2 Basic Working Principles of Lithium Ion Batteries

The term lithium ion battery can be applied loosely to describe all battery systems in which a lithium ion is shuttled between an anode and cathode, but no metallic lithium is present. Typically, this implies the use of two solid active materials, one of which has lithium ions in the crystal structure and therefore acts as the lithium source. When discharging a lithium ion battery, lithium ions are removed from the anode crystal structure. The ions then diffuse through the electrolyte and are incorporated into the cathode crystal structure. The intercalation process of

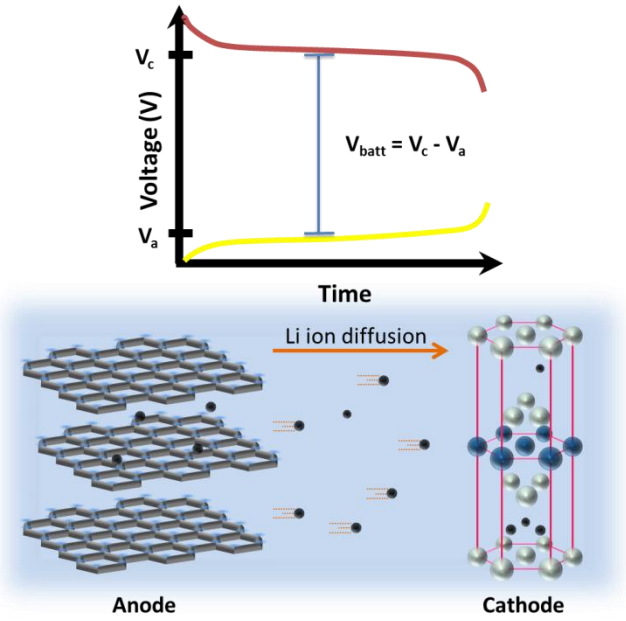

Figure 4.1.2: Discharge mechanisms of a lithium ion battery

both materials occurs simultaneously and coincides with the removal and addition of electrons into the respective electrode [5]. Thus, a reaction may only occur when both electron and ion transfer is possible. The electrode reactions occur at a particular potential with reference to the Li/Li^+ couple. Therefore, the cell voltage is determined by the potential of both reactions (Fig 4.1.2).

The intercalation process is very different from a typical redox reaction that governs other battery chemistries. It is common for an electrode material to rearrange its crystal structure during intercalation and deintercalation. This often leads to structural instabilities and limits a material's cycling capabilities. However, the strong bonds that form between the ions and host structure lead to very low self-discharge rates and result in battery shelf-life of up to ten years. NiMH rechargeable batteries, on the other hand, can lose up to 30% of their capacity in one month [5]. Lithium ion battery kinetics are also slower than other battery chemistries because of the diffusion processes. However, high operating voltages ensure adequate power even at

relatively low current draws. These characteristics combined with large theoretical capacities are why lithium ion batteries dominate the mobile electronics market.

4.1.3 Cathode Materials

Cathode materials utilize various oxidation states of transition metal oxides to store a charge. Ideally, the oxidation state should be as high as possible to ensure a high operating voltage. As with any intercalation material, the host crystal lattice should accommodate as many lithium ions as possible without its sacrificing structural stability. Traditional cathodes are characterized by their crystal structures. Layered structures such as $LiNiO_2$ and $LiCoO_2$ are desirable because of their high capacities and operating voltages [2] [6]. It is also relatively simple to dope these materials with other elements to improve the structural stability and increase the energy density. Spinel materials such as $LiMn_2O_4$ are inexpensive but have lower capacities and shorter cycle life. A new class of olivine cathodes based on $LiFePO_4$ offer excellent stability and low cost [7], but at a lower operating voltage. Among the many available cathode materials, lithium cobalt oxide is the most widely used commercially.

The first lithium ion batteries utilized lithium cobalt oxide ($LiCoO_2$) as the cathode material. Over thirty years later, $LiCoO_2$ is still the preferred cathode for most applications. High temperature synthesized $LiCoO_2$ adopts a layered hexagonal crystal structure. The basic unit cell is composed of oxygen anions sitting in tetrahedral sites arranged in an ABCABC stacking sequence, and lithium and cobalt cations sitting in octahedral sites (Fig 4.1.3). The lithium intercalation/deintercalation process is accompanied by six phase transitions, as shown in Figure 4.1.3. At high lithium contents ($x<0.5$), the crystal structure rearranges into several hexagonal

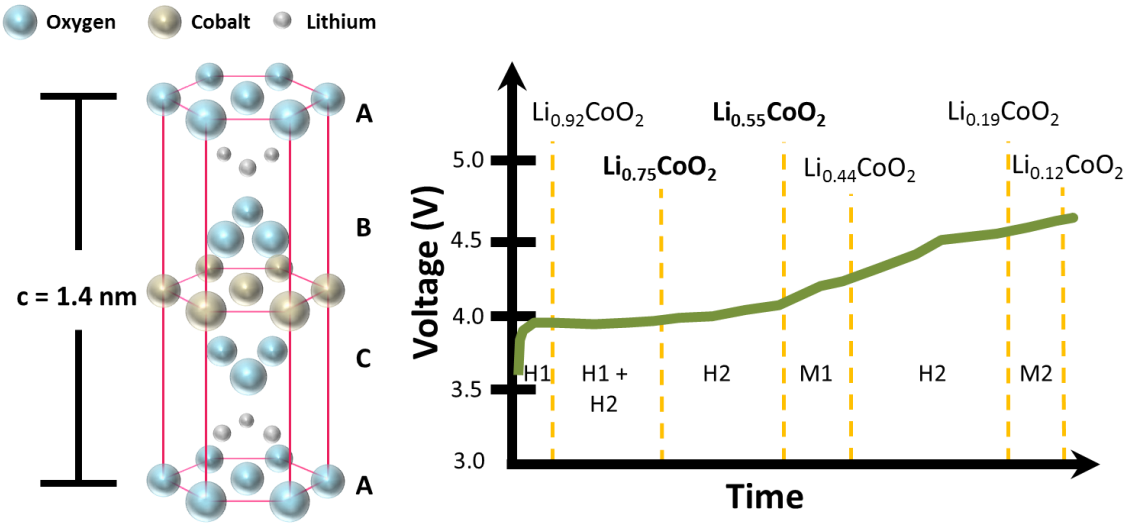

Figure 4.1.3: Crystal structure and voltage profile showing phase transitions of $LiCoO_2$

phases followed by a monoclinic phase. This pattern continues until reaching $Li_{0.12}CoO_2$, at which point the crystal structure is of some question [2] [1].

Of the six phase transitions, two should be discussed in some detail. The first occurs at $Li_{0.75}CoO_2$ and is important because it represents a Jahn-Teller distortion. This type of physical change coincides with an electronic rearrangement and results in a semiconductor-metal transition. In other words, the material becomes more conductive as lithium is removed. Another important transition occurs at $Li_{0.55}CoO_2$, or approximately 4.2 V, at which the crystal structure transforms into a monoclinic phase [1]. It has been shown that cycling this material at voltages beyond this transition results in severe capacity fade. This instability is associated with complex structural rearrangements and severe cobalt dissolution. Consequently, this limits the available capacity of lithium cobalt oxide to about 150 mAh/g, a little more than half of the theoretical 275 mAh/g. Efforts to increase the stability of $LiCoO_2$ above these limits include various electrolyte additives and surface modifications [2]. Today's lithium cobalt oxide cathodes can be successfully be charged to 4.35 V and retain over 80% of their capacity over 400 cycles.

Type	Compound	Theoretical Capacity (mAh/g)	Voltage (V vs Li/Li^+)
Phosphate	$LiMnPO_4$	171	4.1
	$LiCoPO_4$	167	4.8
	$LiNiPO_4$	169	5.1
	$Li_3Co(CO_3)PO_4$	228	4.6, 4.1
	$Li_3Co(CO_3)PO_4$	228	4.6, 4.1
	$Li_2Bi(CO_3)PO_4$	141	4.7, 4.7
	$Li_3Bi(BO_3)PO_4$	140	4.6, 4.3
Silicate	Li_2FeSiO_4	332	4.8, 2.8
	Li_2MnSiO_4	333	4.5, 4.1
	Li_2CoSiO_4	325	5.0, 4.2
	$Li_3Fe(CO_3)SiO_4$	234	4.6, 4.4
Fluorophosphate	$Li(Na)VPO_4F$	156	4.2
	$Na_3V_2(PO_4)_2F_2$	192	4.1
	$Li(Na)_2CoPO_4F$	287	5.0
Fluorosulphate	$LiFeSo_4F$	151	3.6
Carbanosulfate	$Li_6Mn_2(CO_3)_4SO_4$	219	4.7, 3.9
	$Li_6Ni_2(CO_3)_4SO_4$	216	4.7, 4.7
	$Li_6Co_2(CO_3)_4SO_4$	216	4.6, 4.7
Borate	$LiFeBO_4$	220	3.0

Table 4.1.1: Summary of theoretical next generation cathode materials based on computational modeling. A second quoted voltage is associated with removal of a second lithium. Sodium ions can be exchanged for lithium ions during first cycle.

Strong efforts are being made in developing next generation cathode materials that can operate at higher voltages and offer large specific capacities (Fig 4.1.4). New materials based on the tetrahedra backbone of silicates, phosphates, fluorophosphates and borates are being investigated as potential lithium ion cathodes (Table 4.1.1) [8] [9]. Although the materials are new, the issues that need to be addressed are the same as those that plagued today's commercial cathodes in the past, such as structural instability, cation dissolution and gas evolution.

4.1.4 Anode Materials

Characteristics of a good lithium ion anode are high electron energy levels, low operating voltages versus Li/Li^+ and chemical and structural stability [10]. Elemental lithium offers ideal

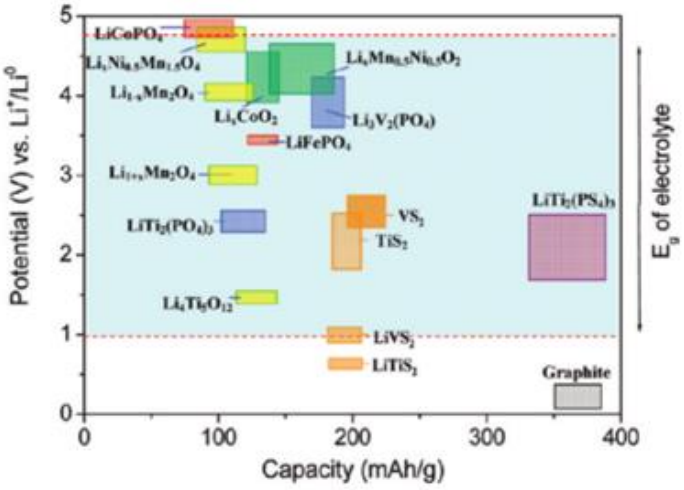

Figure 4.1.4: A voltage versus capacity chart shows the shortcomings of current cathode materials and where some efforts for future materials are being pursued. **[11]**

voltage and capacity qualities but is susceptible to dangerous dendrite growth. The first replacement for lithium metal was graphitic carbon and is still the most widely used anode material. Intercalation occurs through a staging process at voltages nearly identical to metallic lithium, but at a tenth of the capacity. Until recently, this has not been an issue since cathode materials are typically the limiting electrode for lithium ion batteries. However, as new high-capacity cathode materials are developed, research in anode materials has been renewed, especially with the discovery of silicon as a potential anode material.

Next generation anode materials should have larger specific and volumetric capacities than carbon. Currently, most research efforts are focused on silicon-based alloys and a smaller effort focusing on tin or aluminum-based alloys [5] [6]. Silicon is the frontrunner to replace carbon due to its specific capacity of 4200 mAh/g and volumetric capacity of 9700 mAh/mL. Furthermore, silicon intercalates lithium at a voltage very close to that of carbon. However, silicon is limited by two distinct problems. First, the lithium diffusion coefficient in silicon has been shown to be up to three orders of magnitude less than that of carbon. Therefore, silicon-based anodes have limited power capabilities. Second, the material expands by over 300% as it

transitions from a diamond crystal lattice to an amorphous lithium intermetallic phase [11] [12]. Cycling of silicon anodes is severely limited due to the eventual decrepitation of the material and loss of electrical connection to the current collector. Most research is focused on solving the volume expansion problem by creating a core-shell nanostructure or alloying the silicon with another metal. In both cases, the silicon expansion is inhibited by the inclusion of a restrictive force, but at a cost to the specific capacity [6].

4.1.5 Electrolytes

The liquid nonaqueous electrolyte is the most common lithium ion battery electrolyte. The solution is typically composed of a lithium salt dissolved in a combination of organic solvents. Although not part of the energy storage mechanisms, the electrolyte can influence the kinetics of the diffusing ions and the stability of the active electrode materials. One of the most important qualities of a lithium ion electrolyte is its ability to form a stable SEI on the surface of the anode and cathode [6] [5]. A summary of nonaqueous liquid electrolytes is given in Table 4.1.2.

The first liquid electrolytes used propylene carbonate (PC) as the solvent until it was

Salt	Solvent	Ionic Conductivity ($x10^{-3}$ S/cm)	Oxidation Potential (V vs Li/Li^+)
1.0 M $LiPF_6$	1:2 EC/DEC	7.0	4.5
	1:2 EC/DMC	10.0	5.0
1.0 M $LiClO_4$	1:2 EC/DMC	8.4	3.2
	PC	4.32	-
1.0 M $LiAsF_6$	1:1 EC/DME	14.5	4.5
	1:1 EC/DMC	9.9	-
1.0 M $LiBF_4$	1:1 EC/DEC	4.9	3.2
	1:1 EC/DMC	3.2	-
0.8 LiBOB	1:1:3 PC/EC/EMC	4.4	4.25

Table 4.1.2: Physical properties of commonly used liquid nonaqueous electrolyte solutions

discovered to be the source of carbon decrepitation. Since then, electrolyte research has been focused on studying solvent-particle interactions for creating an optimal passivation layer. The greatest success has come from the use of cyclic and open-chain alkyl carbonates such as ethylene carbonate (EC), dimethyl carbonate (DMC), diethyl carbonate (DEC), methylethyl carbonate (MEC) and methyl propyl carbonate (MPC) [2]. A combination of solvents is required in order to increase the boiling temperature and reduce the freezing temperature of the solution. Important properties of solvents include dielectric permittivity, viscosity, polarizability and electrochemical stability window.

Lithium hexafluorophosphate ($LiPF_6$) has emerged as the most frequently used salt. Although not as electrochemically stable or capable of forming a conductive passivation layer, $LiPF_6$ has similar conductivity to and is far less toxic than lithium hexaflouroarsenate ($LiAsF_6$) [14]. Lithium perchlorate ($LiClO_4$) is also an adequate salt that forms conductive SEI layers but is thermally unstable and prone to explosion risks. The main disadvantage of $LiPF_6$ is the formation of HF acid with unavoidable trace water concentrations. HF can form resistive passivation layers and slowly attack any exposed metal such as the current collector or transition metal oxides in the active material. Other salts such as $LiBF_4$, LiBOB, LiFAP and LiDFOB are

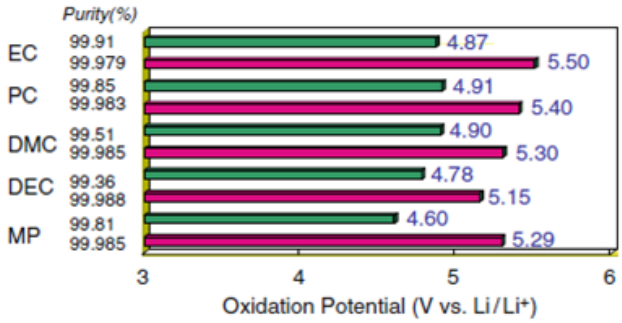

Figure 4.1.5: Effects of purifying solvent on electrochemical windows. Values are quoted after the formation of a stable SEI.

being looked at as potential mass-produced electrolyte salts [6].

Liquid electrolytes can be tailored to a particular system by introducing small percentages of additives. The purpose of additives can range from improving SEI layers and protecting cathode materials to acting as wetting agents or flame retardants. Common additives include vinylene carbonate (VC), 1,3 propanesulton, cyclohexylbenzene (CHB), vinyl acetate (VA), biphenyl (BP) and o-terphenyl (OTP) [14] [2]. Purifying the electrolyte components has also been shown to dramatically improve the properties of a liquid electrolyte (Fig 4.2.5).

Electrolytes are slowly evolving to take on the role of the separator. This is done by using a gelling agent such as PEO to create thin, flexible electrolyte layers or by depositing ionically conductive ceramic thin-films. Although conductivities are generally lower than liquid electrolytes, solid and gel electrolytes can be confined to such small volumes that diffusion times are negligible [6]. The most difficult requirement to address is maintaining the electrode/electrolyte interface. When a material experiences a volume change during the lithiation process, the solid electrolytes remain the same size and shape. As a result, most batteries using solid electrolytes require a small amount of liquid electrolyte as well.

4.2 2.5D Lithium Ion Battery

Cylindrical cells are composed of long electrode sheets wound tightly together. This cell requires a large amount of volume and, if unwound, the individual electrodes do not have the energy density to power complex MEMS devices [15] [16]. The incompatibilities of this design combined with the energy demands of miniature devices pose serious problems for the energy storage industry. A battery with superior electrode capabilities must be developed in order to drive this new market. Implementing three dimensional structures is one such idea to maximize the power and energy densities of an electrode. This approach can offer large mass loadings and minimize diffusion distances by layering material vertically in a structured manner.

The properties of 3D carbon electrodes have already been shown to be greater than planar electrodes. The abilities of the same electrodes tested in a battery arrangement are discussed in this section. Unfortunately, today's cathode materials are unable to match the areal capacity capabilities of a 3D electrode. As a result, cells were prepared with lower capacity 3D carbon electrodes. All of the tests were conducted in a jar cell similar to the three-electrode experiments described in previous chapters in order to make conclusions about the electrode performance rather than the packaging conditions.

4.2.1 Experimental

Anode Fabrication. The 3D MCMB anode was fabricated by extruding slurry through a sacrificial template and attaching it to a current collector. The slurry of 80% MCMB10-28 (Osaka Gas), 10% CMC (DuPont) and 10% KS4 (Timcal) was prepared in water and allowed to stir overnight. A silicon mold having the inverse electrode structure is constructed using lithographic techniques. The mold is then placed in a filter holder and infiltrated with the slurry

material using high pressure at one end and vacuum at the opposite end. Once dried, the mold is attached to a current collector with silver epoxy and etched using XeF_2 gas.

Cathode Preparation. Cathode slurry was prepared by mixing lithium nickel cobalt aluminum oxide ($LiN_{0.8}Co_{0.15}Al_{0.05}O_2$, NEI Corp.), PVDF-HFP copolymer (Arkema) and KS4 (Timcal) in acetone. The final weight percentage was 75%, 5% and 20%, respectively. The solution was sonicated and stirred for at least 3 hours. Aluminum foil (Alfa Aesar) was scratched using a Dremmel and cleaned by alternating treatments of 20% NaOH, DI water and concentrated sulfuric acid. One to two drops of slurry material were pipetted on the current collector and allowed to dry in air. When dried, the electrodes were weighed to obtain the mass of the active material.

Electrochemistry. Electrochemical measurements were performed using a VMP3 potentiostat (Biologic, USA) in a standard glass cell using the 3D MCMB attached as the counter/reference electrodes and the planar cathode electrode as the working electrode (Fig 4.2.1). The electrolyte

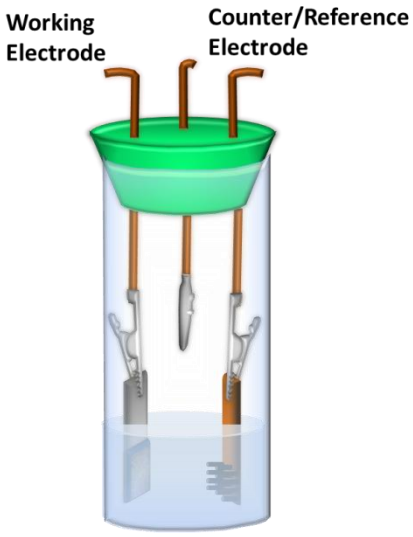

Figure 4.2.1: Experimental setup for two-electrode test

was a 49/49/2 mixture of EC/DMC/VC containing 1 M LiClO4. Planar electrodes had a footprint area of either 0.09 cm^2 or 0.5 cm^2, while 3D electrodes had a footprint area of 0.09 cm2. All experiments were performed in an argon-filled glovebox containing less than 1 ppm of oxygen and water. Both electrodes were dried at 130-150^oC under vacuum for at least 7 hours before being transferred into an Argon filled glovebox. 3D electrodes were vacuum infiltrated with electrolyte for wetting purposes. All chemicals were purchased from Sigma and used without further treatment. Electrodes sat in the electrolyte at open circuit for 10-12 hours prior to any testing to ensure sufficient wetting.

4.2.2 Results and Discussion

Capacity matching is an important aspect of battery assembly. The nominal capacity of a battery is limited by the electrode that is loaded with the smaller capacity. The typical procedure is to load the cathode with excess capacity in order to compensate for irreversible losses [15]. Because the active materials have similar volumetric capacities, the cathode is only slightly thicker than that of the carbon anode even though it requires nearly triple the mass. For this particular cell, the 3D MCMB anode was loaded with 10.2 mg/cm^2 for a theoretical capacity of 3.8 mAh/cm^2. The cathode, on the other hand, was loaded with 29.2 mg/cm^2 for a nominal capacity of 5.3 mAh/cm^2. This cathode loading is extremely high, resulting in a thick electrode that is expected to produce various problems during cycling.

Because the anode has a mixed potential based on the electrolyte interactions with carbon and the silver epoxy, the half-cell open circuit potential is typically higher than that of the cathode. To reduce the OCP, the carbon was lithiated to 5% of its maximum capacity in a three-

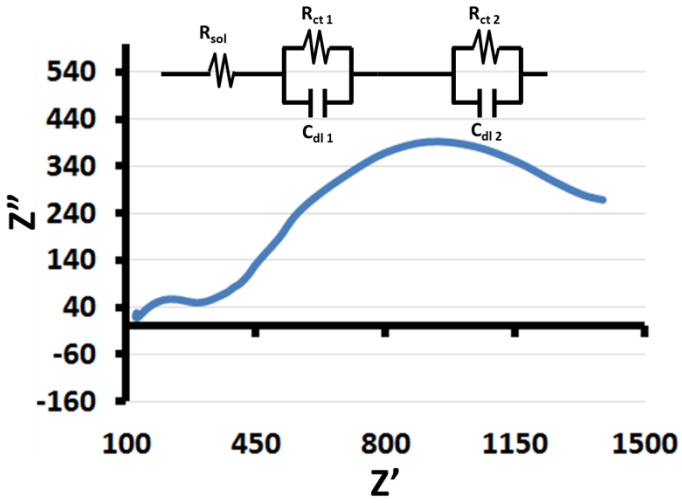

Figure 4.2.2: Electrochemical impedance spectra of two-electrode cell represented as a Nyquist plot

electrode cell and immediately assembled in the two-electrode cell when completed. In this way, the natural open circuit potential of the two-electrode cell is unobtainable.

Cell impedance is displayed as a Nyquist plot in Figure 4.2.2. Each electrode/electrolyte interface can be represented as a parallel RC circuit. Therefore, the two semicircles can be modeled by an equivalent circuit of two parallel RC circuits arranged in series [17]. Comparing the impedance of the two interfaces reveals the charge transfer resistance is much higher at one of the interfaces, most likely the 3D electrode. The electrolyte impedance is approximately 115 Ω due to the distance between electrodes, while the overall impedance of the cell is about 1500 Ω. The lack of a Warburg element implies that charge transfer is the rate-limiting step even at a low frequency of 20 mHz. Diffusion controlled reactions would most likely be seen at much lower frequencies.

The cell was charged using a constant current-constant voltage (CCCV) technique similar to that used by commercial chargers. In this method, the cell is galvanostatically charged to a cut-off voltage of 4.2 V followed by a potentiostatic hold until the current drops to 10% of the

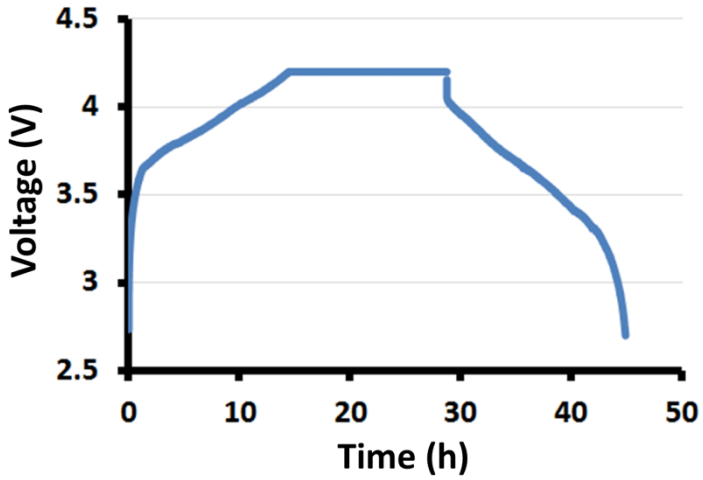

Figure 4.2.3: Voltage profile of two-electrode cell tested in CCCV method at 0.2 mA/cm

charging current. A typical charge-discharge curve of a cell operating at 0.2 mA/cm^2 is shown in Figure 4.2.3. The slope of the voltage plateaus suggests the presence of ohmic polarization which arises from the large cell impedance obtained from previous experiments. The high impedance is also responsible for the dissimilar charge and discharge voltages. It can be seen that the 50% charge voltage is 3.9 V whereas the 50% discharge voltage is 3.65 V.

The cell was cycled at current densities of 1 mA/cm^2, 0.2 mA/cm^2 and 0.1 mA/cm^2 in order to determine rate capabilities (Fig. 4.2.4). Initial cycling at higher rates was performed in an attempt to build a more stable SEI on the surface of both electrodes. The first 2 cycles have been omitted due to the aforementioned silicide reaction. The subsequent cycles yielded charge capacities of 4.1, 3.9, 3.7, 3.6, 3.5 and 3.4 mAh/cm^2 and discharge capacities of 3.8, 3.7, 3.6, 3.4 and 3.3 mAh/cm^2 at a current density of 1 mA/cm^2. This is equal to an average energy density of 15 mWh/cm^2 and 10.8 mWh/cm^2 for charge and discharge, respectively (Table 4.2.1). The discrepancy between charge and discharge energy densities is due to a large hysteresis in working voltages that occurs when operating at such a high current density.

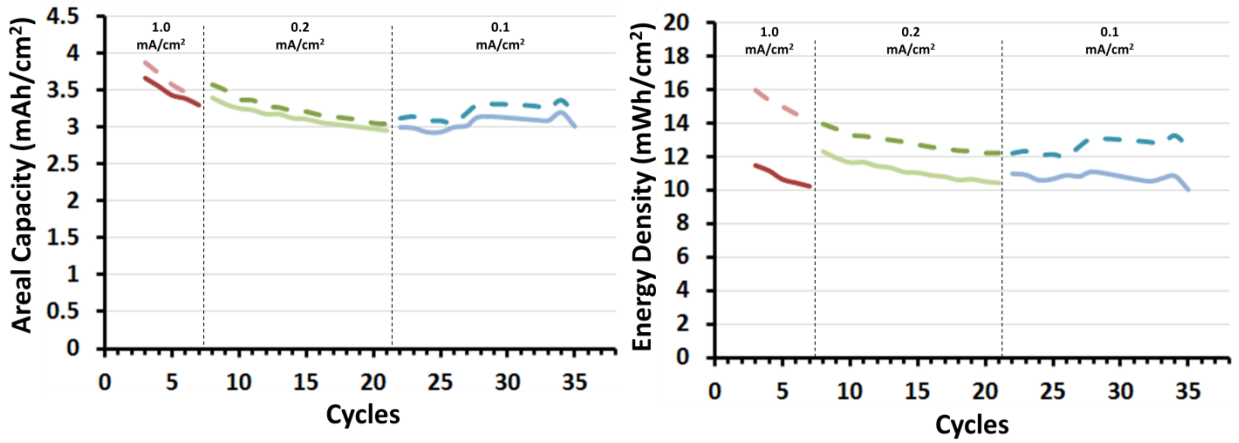

Figure 4.2.4: Two-electrode cell rate capabilities in areal capacity (left) and energy density (right). Dashed lines are values for charging cell, solid lines are values for discharging cell

When reduced to a rate of 0.2 mA/cm^2, the charge capacity increased slightly to 3.6 mAh/cm^2 before gradually fading to 3.0 mAh/cm^2 after 14 cycles. Similarly, the discharge capacity began at 3.4 mAh/cm^2 and faded to 3.0 mAh/cm^2. The respective average charge voltage and energy density was 3.96 V and 12.9 mWh/cm^2, while the average discharge voltage and energy density was 3.56 V and 11.2 mWh/cm^2, respectively. There was also an average discharge fade percentage of 1.07% between each cycle.

The cell was then stepped down to a rate of 0.1 mA/cm^2 and obtained respective average charge and discharge areal capacities of 3.2 and 3.05 mAh/cm^2 over 15 cycles. The average charge and discharge energy densities were calculated to be 12.6 and 10.7 mWh/cm^2 at working voltages of 3.93 V and 3.5 V, respectively. By the last few cycles, noticeable amounts of cathode material were seen at the bottom of the cell. This can lead to an increase in cell impedance, which may explain the voltage hysteresis between the charge and discharge values even at a low rate. Cathode degradation is most likely due to the high mass loading necessary to obtain such large capacities.

Physical Properties	2.5D Battery 1			Seiko MS412FE	STM EFL700A39
$LiCoO_2$ Active Mass Loading (mg/cm^2)	29.2			-	-
MCMB Active Mass Loading (mg/cm^2)	10.2			-	-
Footprint Area (cm^2)	0.09			-	-
Max Areal Capacity (mAh/cm^2)	3.8			-	-
Current Density (mA/cm^2)	1.0	0.2	0.1	0.055	0.16
Average Voltage (V)	C – 4.16 D – 3.11	C – 3.96 D – 3.56	C – 3.93 D – 3.5	3.0	3.9
Average Areal Capacity (mAh/cm^2)	C – 3.61 D – 3.47	C – 3.25 D – 3.13	C – 3.2 D – 3.05	5.5	0.1
Average Energy Density (mWh/cm^2)	C – 15.0 D – 10.8	C – 12.9 D – 11.2	C – 12.6 D – 10.7	17.0	0.4
Average Energy Density (J/cm^2)	C – 54 D - 39	C – 46 D – 40	C – 45 D – 39	60	1.5
Average Discharge Power Density (mW/cm^2)	3.11	0.713	0.35	0.17	0.6

Table 4.2.1: Summary of average performance characteristics for 2.5D battery compared to commercial battery values

Interestingly, capacity fade was not as significant as the prior three-electrode tests. When testing individual 3D electrodes, most cells did not stabilize until about 25 cycles. However, the two-electrode experiments stabilized after only about 7 cycles. Furthermore, the anode material utilization efficiency was very similar for all three current densities. Whereas the three-electrode tests showed significant drops in capacity between rate steps, the average energy and capacity density was nearly identical when the 2.5D cell was cycled at 0.2 and 0.1 mA/cm^2. Equally as impressive is the fact that the coulombic efficiency never dropped below 95%.

The average discharge energy densities were 10.8, 11.2 and 10.7 mWh/cm^2, or 39, 40 and 39 J/cm^2, respectively. These values are comparable to the thick commercial electrodes

mentioned in Section 1.1 but obtained at rates similar to or faster than those of the commercial thin-film batteries. The maximum power delivered was 3.1 mW/cm^2 when the cell was discharged at a rate of 1 mA/cm^2. This value is much higher than that of the four commercial batteries. The power at lower rates is similar to that of the thin film batteries. Considering the testing conditions, including the electrode spacing and thickness of the cathode, the preliminary results of the two-electrode experiments represent a notable benchmark. In conclusion, the two-electrode cell was capable of delivering nearly equal amounts of energy at vastly different power densities. This clearly shows that 3D batteries are fully capable of decoupling power and energy density.

4.3 Concentric Tube 3D Li Ion Battery Assembly

Three dimensional microbatteries must possess a small footprint area while simultaneously support enough material to ensure large energy density. The concentric tube design can achieve this by stacking the electrode material vertically in a post array rather than the traditional planar design of commercial batteries. Furthermore, this particular design does not require inactive scaffold materials, thus ensuring maximum energy density for the allotted volume. Any power requirements can be met by altering the post dimensions to enhance the ion diffusion properties.

The assembly of a concentric tube battery can be broken down into three major steps: post fabrication, electrolyte deposition and cathode sedimentation (Fig 4.3.1). Each step comes with unique challenges that need to be addressed before a commercially available 3D concentric tube battery is realized. The first generation of processing techniques will be discussed in the following sections.

4.3.1 Post Fabrication

Three dimensional post arrays can be fabricated using established MEMS techniques (Fig 4.3.2). A silicon wafer is first masked with the dimensions of the post diameter and pitch. The

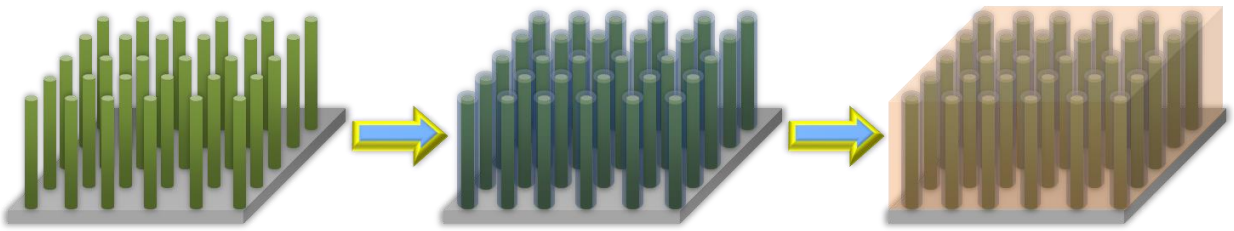

Figure 4.3.1: Three major process steps for fabricating a 3D concentric tube microbattery: post fabrication, electrolyte deposition and cathode sedimentation

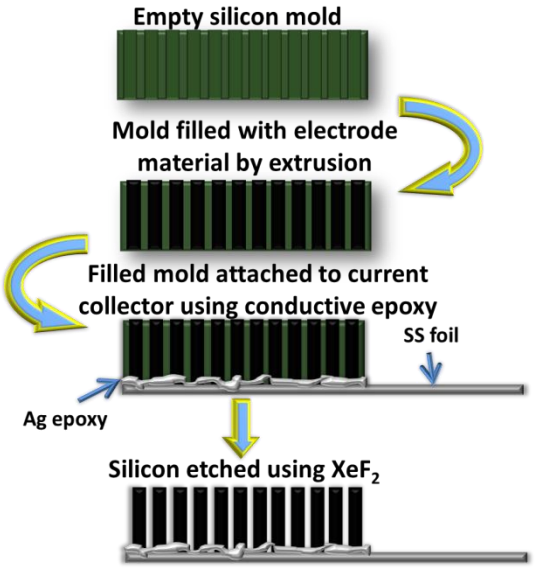

Figure 4.3.2: Process flow for 3D carbon post fabrication

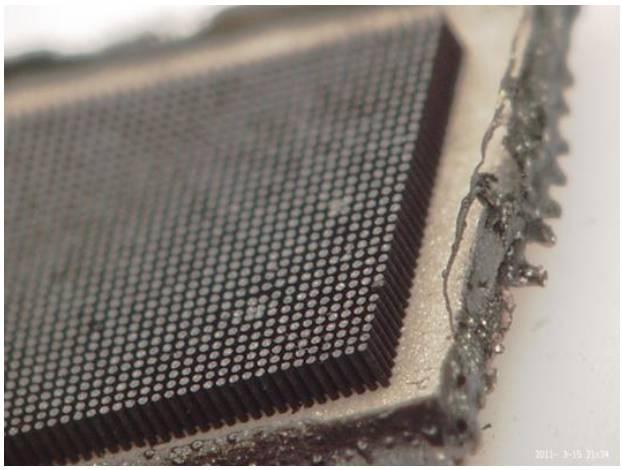

Figure 4.3.3: 3D carbon post anode for concentric tube battery

post height is controlled by the thickness of the wafer. Deep reactive ion etching (DRIE) is then used to anisotropically etch highly ordered channels through the wafer. The final mold will serve as an inverse template for the electrode.

The silicon mold is then positioned on a Whatman filter and placed inside a stainless steel filter holder. The attachment is filled with slurry material and fastened to the end of a high pressure syringe pump. During the pumping process, a vacuum is attached to the bottom of the filter holder to simultaneously pull the slurry material through the silicon mold. This is repeated three to five times and allowed to dry. When dried, the filled mold is connected to a current collector using silver epoxy. The silicon is then etched using xenon difluoride (XeF_2) in order to yield an array of carbon-derived posts (Fig 4.3.3).

4.3.2 Electrolyte Deposition

The most difficult step in the assembly of a 3D concentric tube battery is the deposition of a solid electrolyte separator. This layer must conduct lithium ions but be electronically resistive. Most importantly, the layer must be conformal across the entire surface of the electrode. Any pinholes will result in a short. Two deposition methods were tested for their ability to deposit uniform solid electrolyte layers. Electrochemical and, when applicable, microscopy techniques were used to determine the uniformity of these films.

4.3.2.1 Atomic layer deposition of LASO

Atomic layer deposition (ALD) is a highly controlled method of growing thin films. Over the last decade, advances in ALD technology have increased the number of fields in which the process can be considered beneficial. Similar to CVD and PVD techniques, ALD is a vapor phase deposition. However, unlike the other techniques, ALD is self-limited by the reactions that occur on the surface of a substrate (Figure 4.3.4). This process has been shown to deposit highly uniform films that can be as thin as a few nanometers. Some groups have focused research on using ALD to deposit battery electrode material [18]. However, the time consuming nature of this process makes it extremely difficult to layer enough material to offer desirable capacities.

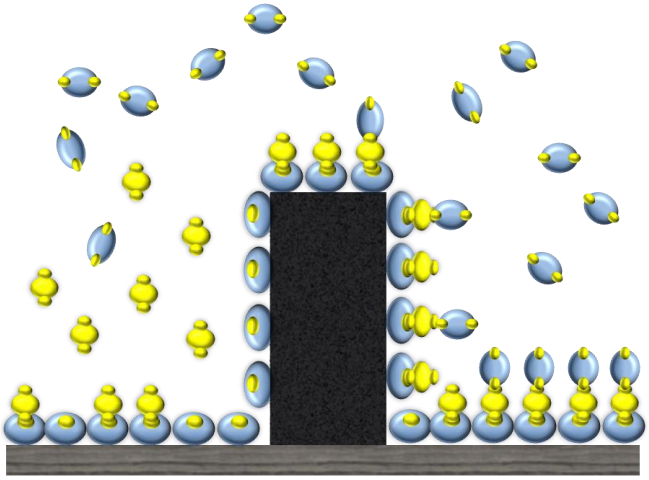

Figure 4.3.4: Atomic layer deposition is a surface controlled thin film growth technique

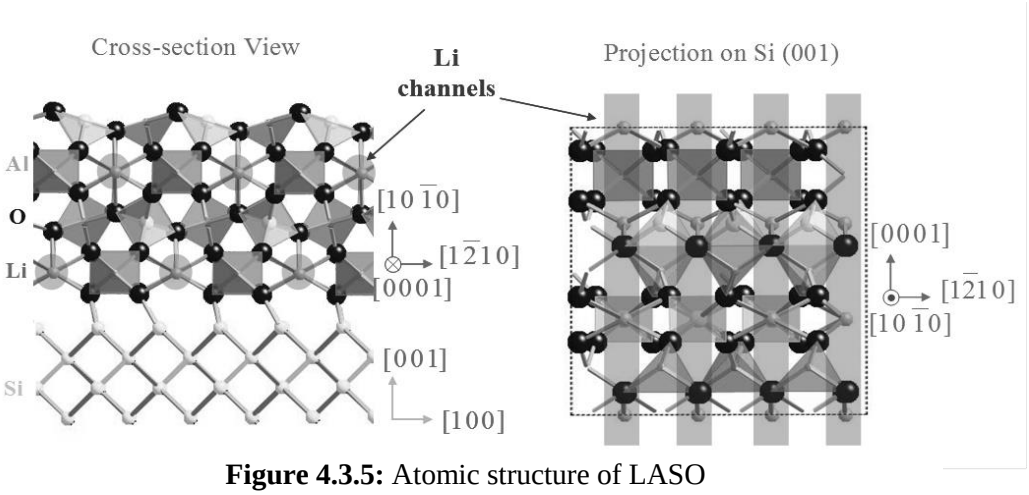

Figure 4.3.5: Atomic structure of LASO

Therefore, the true benefits of ALD can be realized through the deposition of solid electrolyte materials.

The material of interest in this work is beta-lithium aluminosilicate (β-$LiAlSiO_4$). This material is known to possess a relatively high ionic conductivity of $4.7x10^{-5}$ S/cm in single crystal form and yet be electronically insulating enough to prevent shorting. The high ionic conductivity is related to its unique crystalline structure in which lithium ions move along 1D channels formed by shared oxygens located at the corners of Al-O and Si-O tetrahedra (Fig 4.3.5) [19]. Crystalline β-$LiAlSiO_4$ was reported to be ionically conducting over a wider temperature range compared to other solid state lithium ionic conductors, with an activation energy in the range of 0.77~0.95 eV [20]. Another advantage of β-$LiAlSiO_4$ is its conductivity increases with decreasing film thickness. Such properties make this material an attractive candidate for microbatteries that must be engineered at the nanoscale level.

Experimental. $Li_xAl_ySi_zO$ (LASO) thin films were grown by thermal ALD in a hot wall reactor at 290^oC. All samples were prepared by Dr. Sandy Perng and Jea Cho of Dr. Jane Chang's lab in the Chemical Engineering Department. The substrates were either ITO on quartz (CEC020Q,

Präzisions Glas & Optik GmbH, Germany) or a prepared planar MCMB electrode. Organometallic precursors, lithium t-butoxide (LTB), trimethylaluminum (TMA), and tetraethyl orthosilane (TEOS), were used as the source for Li, Al and Si, respectively, with DI water as the oxidant. To grow each constituent oxide, an alternating cycle of a metal precursor and the oxidant is used, denoted as (M-O). The LASO films with thicknesses of 5-12 nm were synthesized with a sequence of a(Li-O)- b(Al-O)-c(Si-O) where a, b ,c represent the number of local ALD cycles for each constituent. The effect of cycle ratios a, b and c on the composition of the ALD LASO films is detailed elsewhere. The film thickness was estimated based on global deposition cycles.

Cyclic voltammetry measurements were used to test for pinholes in the LASO film. In these experiments, the LASO coated samples were immersed in a solution of 1 mM ferrocene (Fc) and 100 mM tetrabutylammonium tetrafluoroborate (TBATFB) in propylene carbonate (PC). The redox properties of the film were characterized using voltammetric sweeps at 10 mV/s (VMP3 potentiostat, BioLogic, USA). Platinum mesh (~ 0.5 cm2) was used as both a reference and a counter electrode (Fig 4.3.6). Although no redox couple exists for the platinum, it can be considered an acceptable quasi-reference electrode since we are only concerned with the current

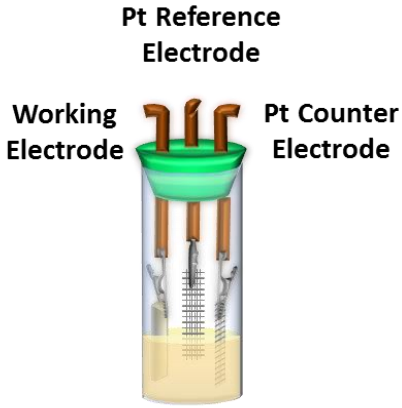

Figure 4.3.6: Experimental setup for pinhole tests

response of the working electrode and not the equilibrium potential of the reaction [17]. The mesh was cleaned between each experiment using sonication treatments in various solvents to remove any adsorbed redox molecules. All experiments were performed in an argon filled glovebox containing less than 1 ppm of water and oxygen.

Results and Discussion. Cyclic voltammetry was used to establish whether pinholes were present in the LASO film. The existence of pinholes is a critical issue for solid electrolytes because such defects can lead to electrical shorts between the anode and cathode. In the present study, the well-established redox chemistry of ferrocene was used to determine the presence of pinholes. The presence of characteristic redox peaks can infer whether or not the molecule effectively penetrates the LASO film. Figure 4.3.7 shows the characteristic current-voltage (I-V) response of a reversible ferrocene reaction at a bare ITO electrode. Sweeping to positive potentials produces a distinctive peak that is attributed to the oxidation of ferrocene (Fc) to ferrocenium (Fc^+), while a sweep in the reverse direction produces a peak signifying the reduction of ferrocenium (Fc^+) to ferrocene (Fc) according to the reaction,

$$Fc^+ + e^- \rightarrow Fc \qquad 4.3.1$$

The peak heights are dependent on the active surface area that is available to facilitate electron transfer.

After coating the ITO substrate with a LASO film 5 layers thick (~10 nm), the characteristic peaks were completely suppressed, indicating that the oxidation and reduction of ferrocene was inactive. This inactivity is credited to the uniform and pinhole-free coverage of the electrically insulating LASO film. The same results were obtained when a film only 3 layers thick (~6 nm) was deposited on an ITO substrate. A carbon electrode was also prepared using

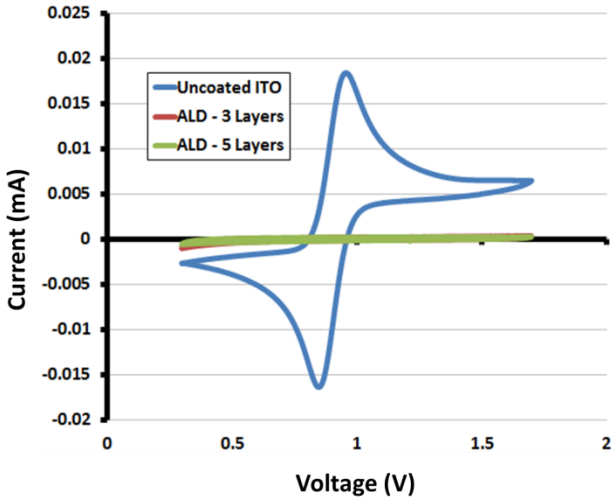

Figure 4.3.7: Comparison of ferrocene activity at an uncoated ITO surface and coated ITO surface. ALD LASO layers completely suppress redox peaks suggesting a pinhole-free coating.

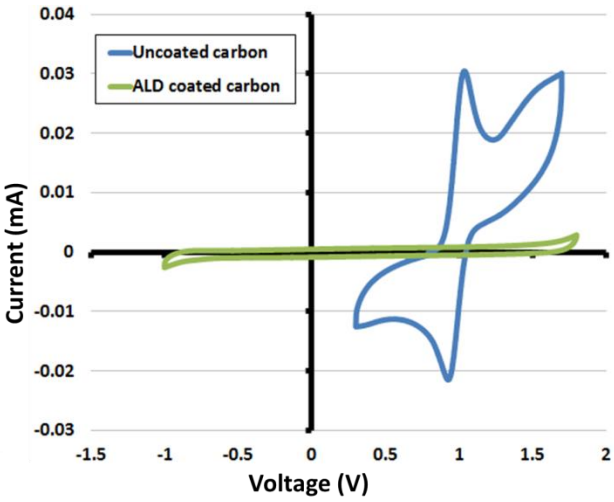

Figure 4.3.8: CV response of uncoated carbon electrode (blue) and LASO coated carbon electrode (green)

MCMB slurry with 7% CMC binder deposited on a stainless steel current collector. The backside of these electrodes were taped to ensure no redox signal appears that can be associated with the current collector. Cyclic voltammetry of an uncoated sample yielded the expected redox peaks associated with ferrocene chemistry. However, a coated surface completely suppressed all redox activity over a 3V window (Fig 4.3.8). This implies that the ALD process is capable of depositing a uniform, pinhole-free coating on microscopically rough surfaces.

4.3.2.2 RF sputtering of LiPON

RF sputtering is similar to direct current sputtering methods except that it utilizes radio waves to ionize the inert gas [21]. The plasma breaks down the target material into a gas which nucleates and grows on a substrate (Fig 4.3.9). RF sputtering can be performed at lower gas pressures resulting in a more direct path for the target molecules to get to the substrate. This

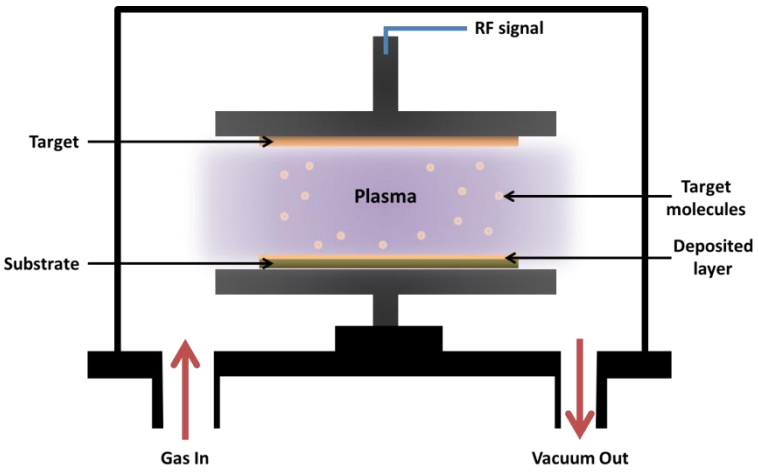

Figure 4.3.9: Schematic of RF sputtering device

technique is also ideal for layering thin films of insulating materials since the target does not suffer from charge build-up.

Lithium phosphorous oxynitride (LiPON) is a popular solid electrolyte material that has been successfully used in planar microbattery applications. It is attractive due to its high ionic conductivity at room temperature ($2x10^{-6}$ S/cm), low electronic conductivity (10^{14} Ω-cm) and electrochemical window of over 5 V versus lithium. Furthermore, batteries using a LiPON electrolyte have shown minimal self-discharge after being stored for over one year. Films can range in conductivity depending on the stoichiometry and crystallinity [22]. Typically, amorphous films are deposited on to a substrate and crystallized accordingly to achieve the desired properties. While various methods have been used to deposit LiPON films, few have been studied for their capabilities to uniformly coat highly irregular surfaces [22] [23].

Experimental. Three dimensional MCMB electrodes were fabricated by methods described previously [22] and shipped to Dr. Nancy Dudney at Oak Ridge National Laboratory. Samples were then deposited with LiPON using RF sputtering techniques. The target was Li_3PO_4 in a nitrogen filled chamber set to 20 mTorr. RF power was held between 130 and 150 W to obtain

deposition rate of approximately 6 nm/min. Previous experiments using posts composed of silver epoxy were performed to optimize the sample alignment in the deposition chamber. Deposition times varied depending on the desired thickness. After sputtering, samples were annealed at 250^{o}C for 10 minutes under argon gas.

Coating conformality was determined by the same electrochemical methods described above. In short, the sample was immersed in an electrolyte composed of 1mM ferrocene and 100 mM TBATFB in PC. Platinum mesh was used as the counter and reference electrodes while the prepared sample was used as the working electrode. Ferrocene redox peaks are expected to be observed if any pinholes are large enough to allow electrolyte to be in contact with a conductive surface. Samples were introduced to electrolyte and placed under vacuum in order to ensure maximum wetting of the 3D structure. All experiments were performed in an argon-filled glovebox.

Results and Discussion. Scanning electron microscopy was used to examine the quality of the LiPON coatings. Figure 4.3.10 is a top-down view of coated 110 µm diameter posts 550 µm tall. Upon inspection, the LiPON coatings look highly uneven when comparing adjacent posts.

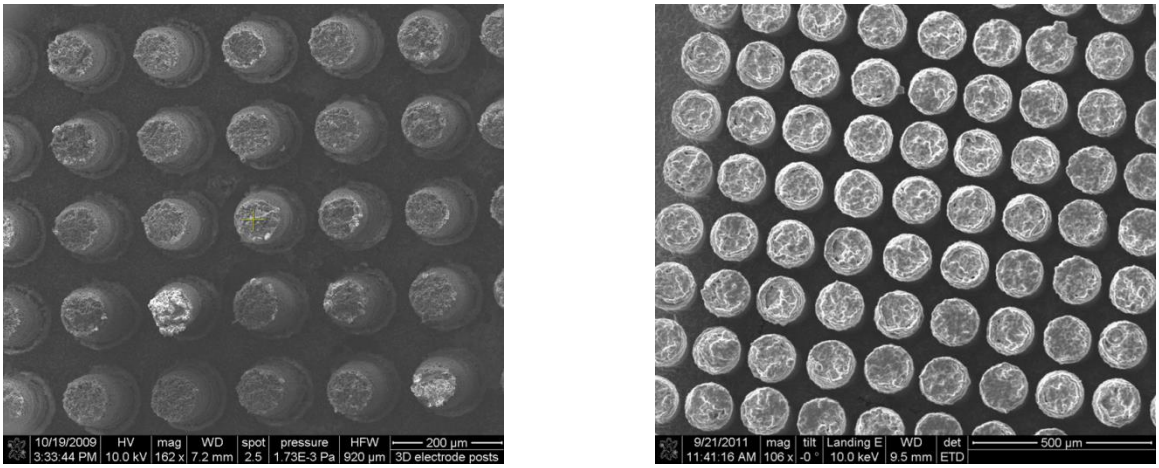

Figure 4.3.10: Uncoated 3D MCMB posts (left) and LiPON coated 3D MCMB posts (right)

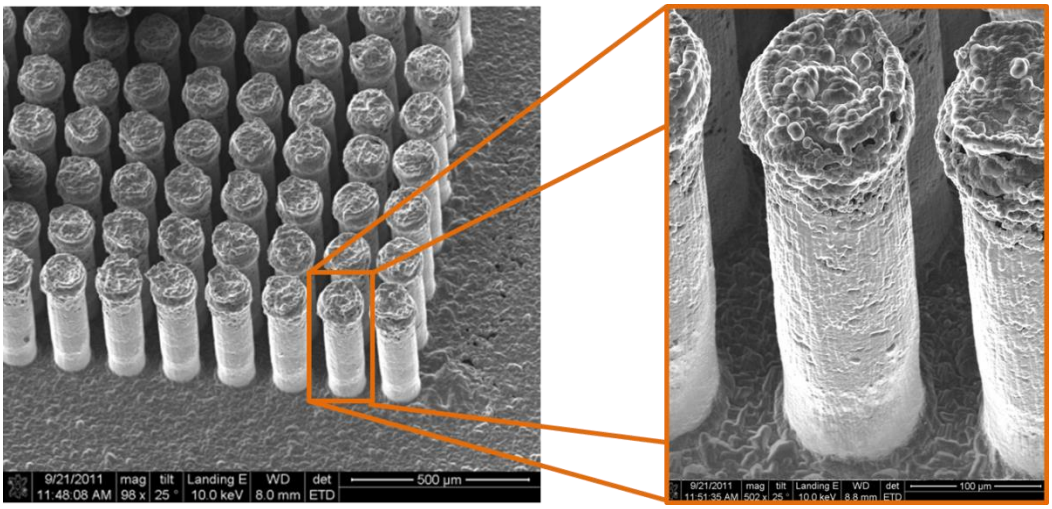

Figure 4.3.11: SEM image of LiPON coatings along post side and current collector. Thickness ranges between 1 – 5 µm.

Furthermore, pinholes on the order of a few microns are clearly visible on some of the posts. Increasing the magnification and tilt reveals more information about the properties of the coating (Fig 4.3.11). It can be seen that the LiPON layer gradually becomes smoother and thinner along the length of the post, with the presence of very few micron sized voids. Furthermore, the striations along the side of the post suggest growth begins at the top and flows to the bottom of the post. This method of growth makes it difficult to predict the thickness of the electrolyte layer, but it is expected to range between 1 and 5 µm. An important aspect of 3D electrolyte separator coatings that is often overlooked is the coating of the electrode floor. While it may not be considered active material, the current collector is still part of the electrode and can result in a short if not adequately coated. Figure 4.3.11 reveals the floor was successfully coated albeit with a few gaps in the coating.

Cyclic voltammetry was also used to determine the uniformity of the electrolyte layer. Prior to silicon mold etching, 3D electrodes were packaged in an epoxy encasement to prevent ferrocene redox from occurring on the backside of the current collector. Figure 4.3.12 compares

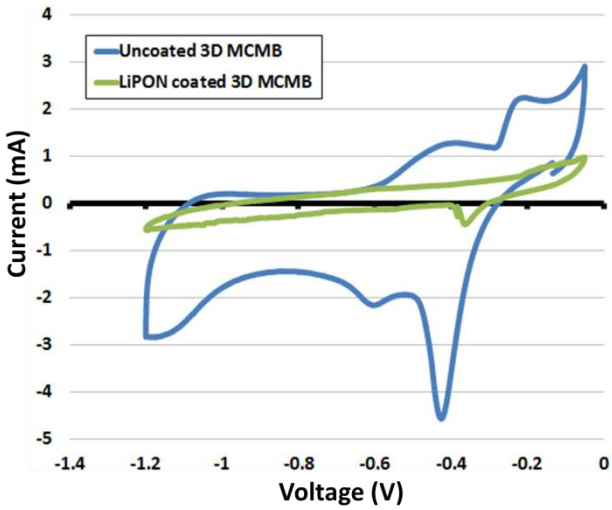

Figure 4.3.12: CV showing ferrocene activity of uncoated 3D MCMB posts (blue) and LiPON coated 3D posts (green). Pinholes in LiPON coating are confirmed by the presence of reduction in peaks. Currents are reduced due to a smaller available surface area.

I-V curves of uncoated and coated 3D samples. The uncoated sample appears to produce two reduction peaks at -0.42 V and -0.6 V. This can be explained by the silver reaction,

$$Ag^{+} + e^{-} \rightarrow Ag(s) \qquad 4.3.2$$

which occurs at a potential 0.12 V more positive than the ferrocene couple [17]. Unfortunately, adsorption effects and side reactions at the quasi-reference electrode shift the reaction potentials and make it difficult to confirm this hypothesis. Coated samples also revealed two reduction peaks at -0.36 V and -0.54 V. However, peak heights were reduced by 90% and 94%, respectively, indicating that almost all of the conductive surface area was coated with insulating LiPON. Furthermore, the slope of the background Faradaic current of the coated sample suggests a large increase in electrode resistance. It can be concluded that RF sputtering technique is very capable of coating a three dimensional structure with LiPON, but the deposition process needs to be optimized before being considered an ideal candidate.

4.3.3 Cathode Sedimentation

The final step in assembling a 3D concentric tube battery is the cathode sedimentation. Various methods have been proposed to accomplish this, ranging from drop-by-drop sedimentation to centrifuge infiltration. There are several concerns that must be addressed before beginning the process, the first being material homogeneity. During sedimentation, heavier metal oxide particles will settle faster than the light carbon additives. If deposited at once, this will result in an electrode structure composed of a thin layer of active material covered by a thick layer of carbon additive. Possible solutions to this problem are laying down thin layers of slurry sequentially or increasing the viscosity of the slurry to prevent material separation. However, too much of an increase in viscosity may result in voids in the structure when dried. Finally, capillary forces should be avoided in order to maintain the integrity of the post structure. Excessive drying and wetting of the electrode will result in post fracturing. The following section will describe a dropwise method using a dilute solution to fill the remaining volume with cathode material.

Experimental. Cathode slurry was prepared by mixing 1.0 g of $LiCoO_2$ (Sigma Aldrich), 0.267 g of KS4 graphite (Timcal) and 0.067 g of PVDF in 5 mL of acetone. The weight ratio of components was 75% active material, 20% conductive additive and 5% binder. The slurry was sonicated for approximately 1 hour and mixed on a stir plate for at least 2 hours. The mixture was diluted by taking 2 mL of slurry solution and adding 8 mL of acetone. The same dilution was repeated once more to make a final solution of about 0.01 g/mL. Each dilution was performed while the solution was being stirred.

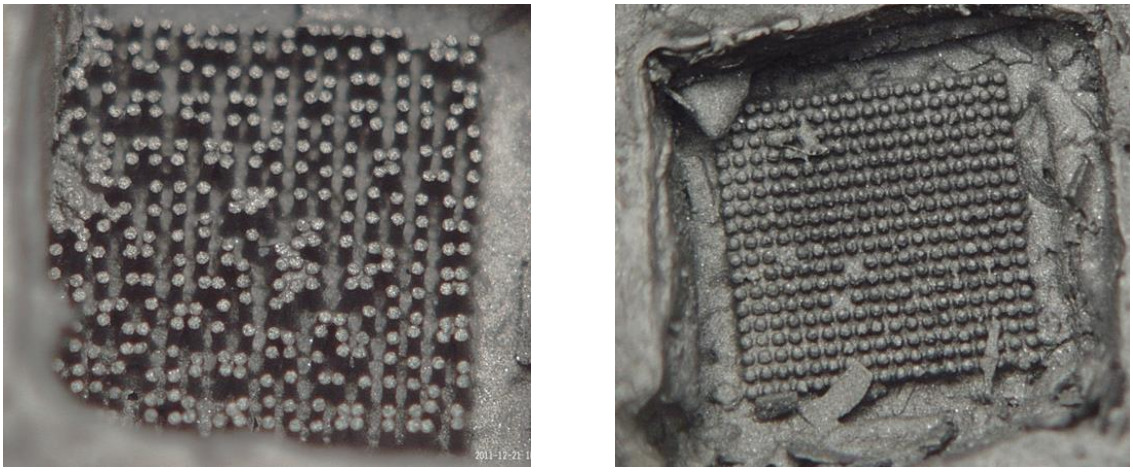

Figure 4.3.13: Effects of evaporation time between successive deposition refills. Excessive drying ruins post integrity (left) but constant wetting maintains post integrity.

Solution containing the cathode material was dropped over the posts and contained by the epoxy packaging unit. The unit was occasionally vortexed very lightly over the course of a few minutes. Two to three drops of solution were taken from a stock being constantly stirred and added to the cell before the solvent had completely dried. This process was repeated until the top of the posts could no longer be seen. A top contact was made by attaching an aluminum current collector to the dried electrode material with nickel epoxy (EpoTek). Optical cross section images were taken using a Hirox digital microscope.

Results and Discussion. Cathode sedimentation was performed by dripping a dilute slurry solution over a 3D post array electrode. Important factors affecting the filling efficiency included evaporation time, mixing and slurry concentration. It was found that the optimum conditions for this method involved filling the cell with the dilute solution, followed by a light vortex treatment for about 5-10 seconds every 2-3 minutes. It was imperative that the acetone solvent was not allowed to dry completely. The repetitive drying simulated a stress cycle due to the presence of strong capillary forces acting between the posts. Therefore, when approximately 80-85% of the liquid had evaporated, the cell was refilled with the slurry solution. Figure 4.3.13 compares the

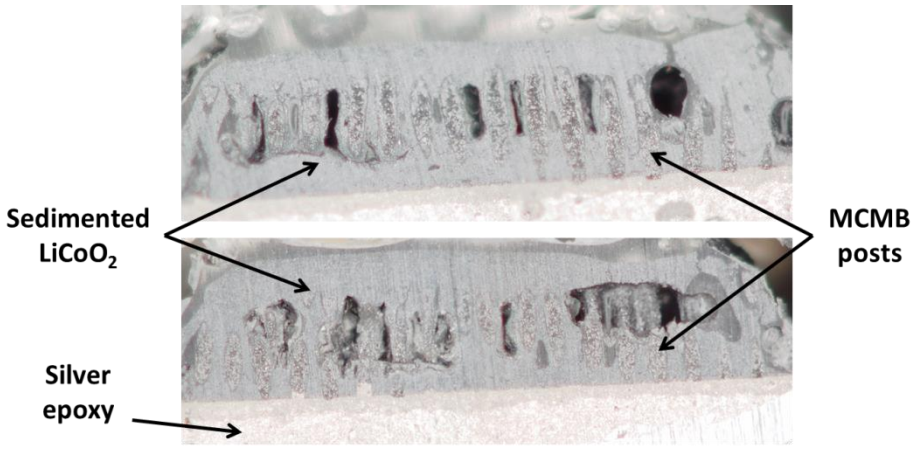

Figure 4.3.14: Cross section of sample filled without vortexing. Similar effects were seen with concentrated slurries.

post integrity of two samples partially filled using different evaporation times. Posts from the sample that was allowed to dry completely between refills have been pulled together at the top, whereas the sample that was constantly wetted maintained its structure.

Cross sections were examined to determine the cathode filling efficiency. Once

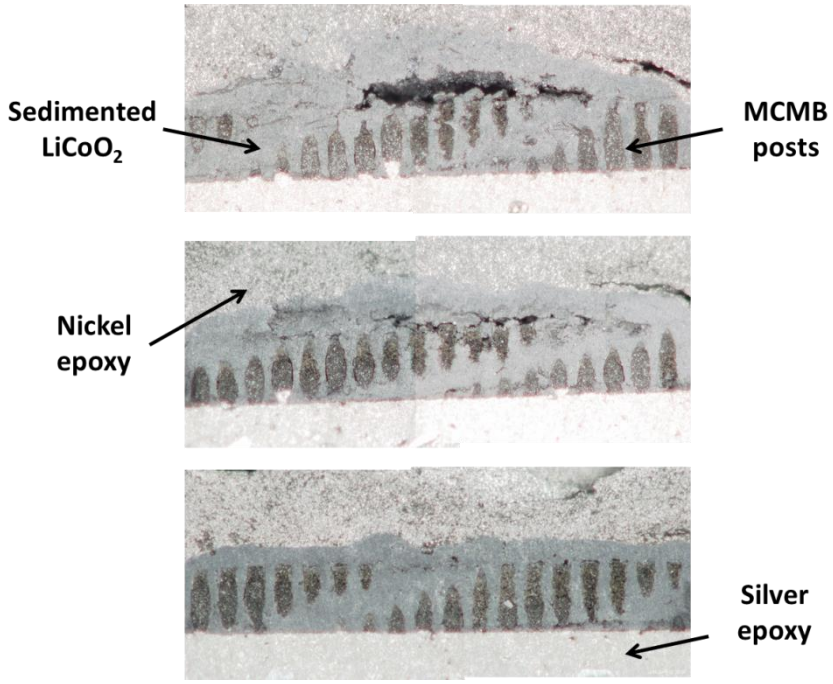

Figure 4.3.15: Cross section of multiple layers for sample that was vortexed during filling process. Void at top was due to increased filling rate near end of process.

assembled, cells were encapsulated in epoxy and polished using 320 and 1200 grit polishing paper. Cross sections were imaged at various points of the polishing process to determine the filling characteristics throughout the cell. Light vortexing proved to be a pivotal step in successfully depositing cathode material in the remaining volume between posts. Figure 4.4.14 reveals the presence of large voids in the cell when vortexing was not performed during the sedimentation process. Trapped bubbles and uneven drying may lead to material clogging between the posts. Unless vortexed, the effects of uneven deposits will compound and eventually result in voids similar to those seen in the figure. The effects of vortexing during cathode sedimentation can be seen in Figure 4.4.15. Cross sections throughout the cell clearly exhibit a more uniform cathode structure. The absence of large voids implies the vortex process distributes the cathode material evenly between the posts. This is further supported by the visibly tight packing of material around the entire length of the rods.

4.4 Conclusions

A 3D MCMB electrode was assembled as a lithium ion battery anode and tested in a two-electrode cell. This 2.5D battery utilized a thick planar cathode that utilized lithium nickel cobalt aluminum oxide as the active material. The cell was then cycled at current densities of 1.0, 0.2 and 0.1 mA/cm^2. At each rate, the battery obtained a discharge capacity between 3.0 and 3.5 mAh/cm^2. The battery was susceptible to capacity fade just as the individual electrodes showed, but to a much lesser extent. Charge and discharge voltages showed a high degree of hysteresis that increased as cycling continued. This is a direct result of two issues. First, the cell impedance was very high due to the thick cathode and resistive posts of the anode. Second, the thick cathode gradually fell apart during the cycling, thus increasing the impedance and resulting working voltages. The cathode pulverization eventually led to massive capacity loss and death of the cell.

The second part of this chapter considered the construction of a concentric tube 3D battery. Battery assembly can be broken down into three steps: post fabrication, electrolyte deposition and cathode sedimentation. The most refined step is the post fabrication. It has been shown that we are capable of fabricating 3D electrodes of various feature sizes due to the precise nature of photolithography manufacturing techniques. Furthermore, the method by which we fabricate the posts allows us to implement any material that is prepared as a slurry.

The ability of ALD and RF sputtering to deposit a conformal electrolyte layer over an irregular surface was tested using electrochemical methods. Although mostly qualitative in nature, this method ensures the evaluation of the entire surface of the electrode. Using the distinct redox chemistry of ferrocene, it was determined that ALD was capable of depositing a highly conformal layer of lithium aluminosilicate over planar ITO and carbon surfaces. The next

step involves deposition over a 3D carbon electrode. The same testing method showed that RF sputtering of LiPON was capable of coating over 90% of a 3D carbon post electrode. Visual investigation by electron microscopy confirmed the presence of gaps in the LiPON coating that were on the order of a few microns. SEM imaging also suggested irregular coating thickness along the length of the posts. Optimizing the process will undoubtedly prepare near perfect coatings. Electrical and electrochemical characterization of LiPON coatings varying in thickness are to be performed in order to determine the optimal composition.

The final step was performed by depositing a dilute solution of cathode material, binder and additive around a packaged 3D array. It was determined that three important aspects of this process need to be considered to ensure tight packing. First, the slurry must be dilute to prevent the trapping of air bubbles. Second, the array must constantly stay wetted to maintain the post integrity. Ideally, the drip process should be optimized to refill after 80% of the solvent has evaporated. Finally, the electrode should be lightly vortexed after the filling step. This step ensures uniform deposition between the posts and reduces the number of large voids in the final dried structure.

4.5 References

[1] G. Nazri and G. Pistoia, Lithium Batteries: Science and Technology, Springer, 2003.

[2] M. Yoshio, R. Brodd and A. Kozawa, Lithium Ion Batteries: Science and Technologies, Springer, 2009.

[3] "Samsung SDI," [Online]. Available: http://www.samsungsdi.com/battery/polymer-rechargeable-battery.jsp.

[4] Envia Systems, [Online]. Available: http://enviasystems.com/.

[5] R. Huggins, Advanced Batteries: Materials Science Aspects, Springer, 2009.

[6] C. Daniel and J. Besenhard, The Handbook of Battery Materials, Wiley-VCH, 2011.

[7] Y. Zhang, Q. Huo, P. Du, L. Wang, A. Zhang, Y. Song, Y. Lv and G. Li, "Advances in new cathode material LiFePO4 for lithium-ion batteries," *Synthetic Metals,* vol. 162, p. 1315, 2012.

[8] G. Hautier, A. Jain, H. Chen, C. Moore, S. Ong and G. Ceder, "Novel mixed polyanions lithium ion battery cathode materials predicted by high throughput ab initio computations," *Journal of Materials Chemistry,* vol. 21, p. 17147, 2011.

[9] Z. Gong and Y. Yang, "Recent advances inthe research of polyanion-type cathode materials for Li-ion batteries," *Energy and Environmental Science,* vol. 4, p. 3233, 2011.

[10] J. Goodenough and Y. Kim, "Challenges for Rechargeable Li Batteries," *Chemistry of Materials,* vol. 22, pp. 587-603, 2010.

[11] P. Limthongkul, Y. Jang, N. Dudney and Y.-M. Chiang, "Electrochemically driven solid-state amorphization in lithium-silicon alloys and implications for energy storage," *Acta Materiala,* vol. 51, no. 4, p. 1103, 2003.

[12] M. Obrovac and L. Christenson, "Structural changes in silicon anodes during lithium insertion/extraction," *Electrochemical and Solid State Letters,* vol. 7, no. 5, 2004.

[13] R. Huggins, Energy Storage, Springer, 2010.

[14] K. Moller, H. Santner, W. Kern, S. Yamaguchi, O. Besenhard and M. Winter, "In situ characterization of the SEI formation on graphite in the presence of a vinylene group containing film-forming electrolyte additives," *Journal of Power Sources,* vol. 119, p. 561, 2003.

[15] P. Ramadass, B. Haran, R. White and B. Popov, "Performance study of commercial LiCoO2 and spinel-based Li ion cells," *Journal of Power Sources,* vol. 111, pp. 210-220, 2002.

[16] K. Ozawa, "Lithium-ion rechargeable batteries with LiCoO2 and carbon electrodes: the LiCoO2/C system," *Solid State Ionics,* vol. 69, no. 3, p. 212, 1994.

[17] A. Bard and L. Faulkner, Electrochemical Methods: Fundamentals and Applications, John Wiley and Sons, 2001.

[18] X. Meng, X. Yang and X. Sun, "Emerging applications of atomic layer deposition for lithium ion battery studies," *Advanced Materials,* vol. 24, no. 27, p. 3589, 2012.

[19] I. Alekseeva, O. Dymshits, V. Ermakov, A. Zhilin, V. Petrov and M. Tsenter, "Raman spectroscopy quantifying the composition of stuffed quartz derivative phases in lithium aluminosilicate glasse-cermaics," *Journal of Non-Crystalline Solids,* vol. 354, no. 45, p. 4932, 2008.

[20] V. Thangadurai and W. Weppner, "Solid state lithium ion conductors: Design considerations by thermodynamic appcroach," *Ionics,* vol. 8, no. 3, p. 281, 2002.

[21] M. Walker, "wiseGEEK," Conjecture Corp, [Online]. Available: http://www.wisegeek.org/what-is-rf-sputtering.htm.

[22] F. Xu, N. Dudney, G. Veith, Y. Kim, C. Erdonmez, W. Lai and Y. Chiang, "Properties of lithium phosphorous oxynitride for 3D solid-state lithium batteries," *Journal of Materials Research,* vol. 25, no. 8, p. 1507, 2010.

[23] C. Lethien, M. Zegaoui, P. Roussel, P. Tilmant, N. Rolland and P. Rolland, "Micro-patterning of LiPON and lithium iron phosphate material deposited onto silicon nanopillar arrays for lithium ion solid state 3D microbattery," *Microelectronic Engineering,* vol. 88, p. 3172, 2011.

[24] R. Liu, L. Zhang, X. Sun, H. Liu and J. Zhang, Electrochemical Technologies for Energy Storage and Conversion, John Wiley and Sons, 2012.

Chapter 5

3D ZINC AIR BATTERIES

5.1 Introduction to Zinc-air Batteries

A zinc air battery generates electricity by simultaneously oxidizing zinc metal and reducing oxygen according to the following,

$$Zn + 4OH^- \rightarrow Zn(OH)_4^{2-} + 2e^- \quad 5.1.1$$

$$Zn(OH)_4^{2-} \rightarrow ZnO + H_2O + 2OH^- \quad 5.1.2$$

$$O_2 + 2H_2O + 4e^- \rightarrow 4OH^- \quad 5.1.3$$

It can be seen that the anodic reaction is actually a two-step process. The first step involves the accumulation of zincate molecules in the electrolyte followed by the precipitation of zinc oxide around the active metal [1]. Zinc air cells may be preferred because of their extremely flat

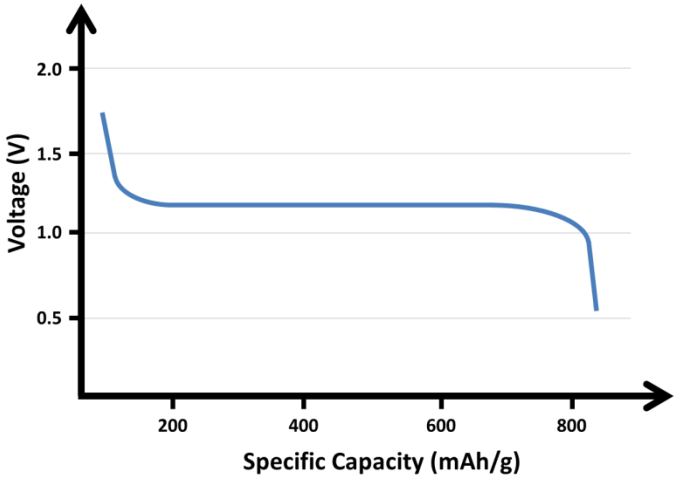

Figure 5.1.1: Typical voltage profile of discharging zinc-air cell

discharge curve and high capacities (Fig. 5.1.1). In fact, the specific capacity (820 mAh/g) and volumetric capacity (5,970 mAh/mL) of zinc are larger than most primary and some secondary lithium ion battery materials [2]. Zinc-air batteries are also considered to be safer than lithium ion batteries due to the use of an aqueous electrolyte and non-toxic materials. Zinc metal is easily recoverable and already has established recycling methods as well [3]. Another main advantage of zinc-air batteries is the low-cost, non-active cathode.

An air electrode is a mixture of a catalyst material such as MnO_2 and carbon pressed on a mesh current collector. Because oxygen is the active material, the electrode acts only as a reaction site and can be made very thin [4] [5]. Properties of a good air electrode include high surface area, high porosity for gas diffusion, large electronic conductivity to reduce iR losses, electrochemical and chemical inactivity and low weight [1]. A hydrophobic binder such as Teflon is used to prevent flooding of the pores with electrolyte. However, the bottom-half of the electrode must also maintain a certain degree of wetting with the electrolyte to facilitate the reaction. This three-phase interface is the source of many problems for a zinc-air battery. Other major concerns include electrolyte evaporation, hydrogen evolution and side reactions with gases other than oxygen.

Commercial cells utilize powder zinc alloyed with small amounts of mercury or indium to prevent hydrogen gas generation [6]. The electrolyte is an aqueous solution of potassium hydroxide, dissolved zinc oxide and a gelling agent such as poly acrylic acid. The zinc oxide facilitates the oxide forming reaction and helps suppress gas evolution, while the gelling component creates a composite-like structure with the zinc powder. The air cathode is placed between a separator on the zinc side and a Teflon barrier on the air side (Figure 5.1.2). The Teflon layer acts as a seal to prevent electrolyte evaporation and water diffusion into the cell [1].

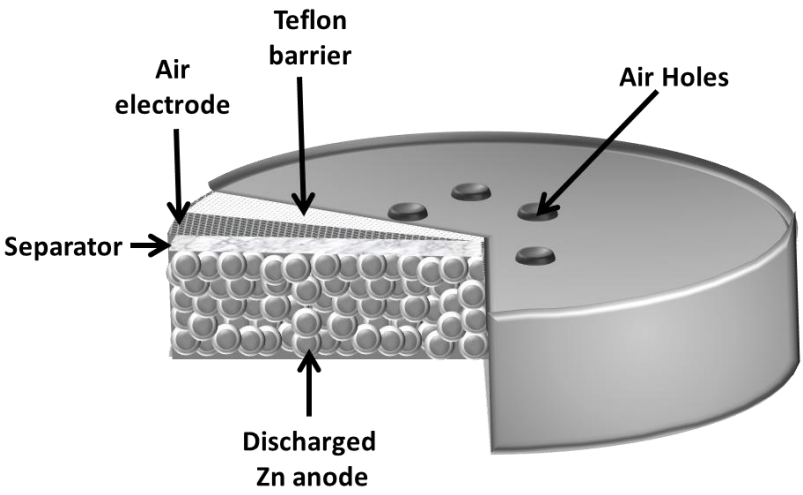

Figure 5.1.2: Commercial zinc-air coin cell

The biggest drawback of a zinc-air cell is its low power. Zinc reacts with hydroxyl ions at 0.2 V vs NHE while oxygen is reduced at -1.45 V vs NHE to give a theoretical cell voltage of 1.65 V [7]. However, practical cells rarely operate at voltages larger than 1.2 V due to overpotentials associated with oxygen diffusion and slow reaction kinetics. Material utilization is also very low for zinc-air batteries due to the zinc oxide that grows around each zinc particle. During discharge, the oxide layer eventually becomes too thick for electron transfer to occur. As a result, zinc-air batteries are limited to low power applications such as hearing aid devices [1] [2].

Zinc-air cells are commercially available only as primary batteries. However, interest in developing a rechargeable zinc-air battery has recently increased. A few concerns must be addressed before a functional rechargeable zinc-air battery is realized. The first difficulty is zinc plating. Similar to a rechargeable lithium anode, a zinc anode suffers from dendrite growth after a limited number of cycles [1]. The growth of whiskers will eventually lead to a short. The second biggest problem is developing an affordable and efficient bifunctional cathode. In order

for a zinc-air cell to be rechargeable, the cathode must reduce oxygen when discharging and oxidize water upon recharging [4]. Unfortunately, most catalysts cannot perform both functions. Such kinetic barriers often lead to a large hysteresis in charge and discharge profiles. Some ideas to circumvent these problems include recharging stations separate from the cell and a flow battery-type design in which the zinc "fuel" can be flowed through the cell [1] [8].

5.2 3D Zinc Air Battery

The reaction between zinc and a hydroxyl ion is plagued by slow kinetics. High surface area powder is employed in commercial zinc-air batteries to reduce the activation overpotential. As the reaction continues, insulating zinc oxide forms around each particle and disrupts the electron migration path to the current collector. The oxide layer eventually inhibits all electron flow and results in the death of the battery. This discharge mechanism results in low material utilization and limits the zinc-air battery to low power applications [1].

High aspect ratio three dimensional zinc posts were fabricated using photolithography and electrochemical methods. The zinc posts were assembled as a battery anode and discharged using an air cathode retrieved from a commercial zinc-air cell. The cell achieved greater material utilization efficiency than commercial cells when discharged at similar rates. This is due to the zinc post being constantly in electrical contact with the current collector. Furthermore, the areal capacity was larger than that of the 3D MCMB electrodes. A major drawback of this design is the inability to alloy the zinc with a hydrogen gas suppressing metal, such as mercury or indium. As a result, the high surface area posts are susceptible to corrosion.

5.2.1 Experimental

3D zinc array fabrication. The zinc posts were fabricated using a combination of photolithography, electrochemical anodization and electrodeposition (Fig 5.2.1). Each electrode was produced by co-worker Dr. Guangyi Sun from Dr. C-J Kim's lab in the Mechanical Engineering Department.

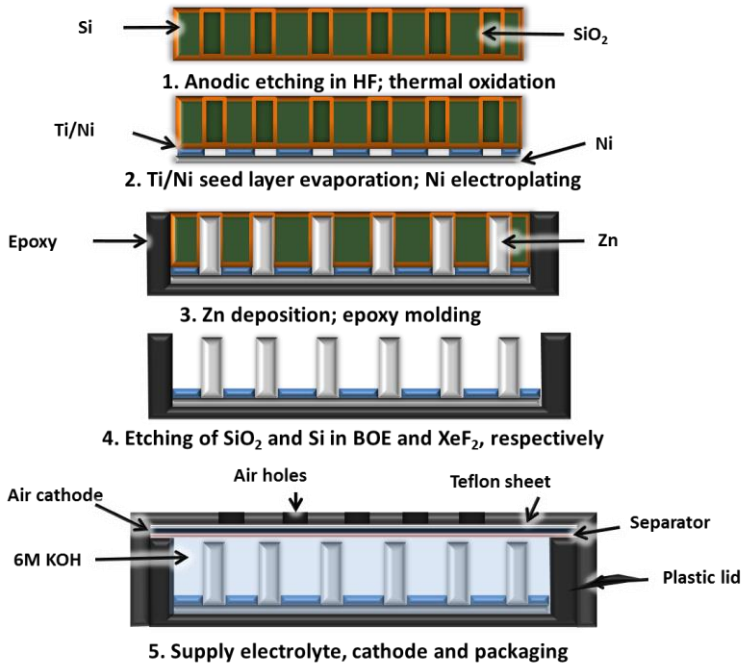

Figure 5.2.1: Process flow for fabrication of 3D zinc electrode and cell

A rectangular n-type silicon sample was patterned and arranged so that a circular portion 2 cm in diameter would be etched. The sample was placed in a bath of HF facing a platinum counter electrode. As the sample was anodized, a light source shone on the back of the silicon to increase the carrier concentration. The process is stopped before the sample is completely etched through. Channels were opened from the bottom by thinning down the sample using blank DRIE. The full details of this method are discussed elsewhere. The resulting trenches were about 5 µm in diameter with a pitch size of 15 µm and height of 250 µm.

A 1500 Å thermal oxide layer was grown on the silicon to electrically isolate the silicon surface during the following electroplating steps. The silicon dioxide prevents the bare silicon from being electroplated and confines the plating to the holes. Next, Ti/Ni (100 Å /1000 Å) was evaporated using CHA E-beam evaporation. This was followed by electroplating 20 µm of

nickel to act as the seed layer for a current collector. This simultaneously closes the silicon holes and provides a seed layer for the subsequent zinc electroplating step.

Commercially available nickel electroplating solution from Technic Inc. was used to deposit the current collector. Plating was performed at 10 mA/cm^2 using nickel foil as the counter electrode. The electrode was then flipped, and zinc was electroplated through the holes using zinc sulfate electroplating solution. The solution was prepared by dissolving zinc sulfate (240 g), ammonium chloride (15 g), aluminum sulfate (30 g) and saccharin (1 g) in one litter of DI water. Zinc was deposited at 20 mA/cm^2 using zinc foil as the counter electrode. The electroplated sample was then diced into smaller samples and packaged accordingly. The silicon dioxide and silicon mold were etched away in the final step. The top oxide was removed in buffered oxide etchant (BOE) to expose the silicon, which was then etched using XeF2. A final BOE dip was performed to remove any residual silicon dioxide.

Cell preparation. Prior to XeF_2 etching, nickel wire is attached to the nickel current collector using conductive silver epoxy. The sample is then packaged by masking the top portion with tape and pouring epoxy into the container. The following day, a thin epoxy layer and the tape are removed with a blade. Because the packaged unit is the shape of the container, the container may be used as the cap of the cell (Fig 5.2.2).

The air electrode of a commercial cell is used as the cathode. The air electrode consists of a separator, catalyst electrode and Teflon barrier (Fig 5.2.3). The separator acts as a physical barrier between the anode and cathode to prevent a short while the Teflon barrier serves to allow air in and keep water out. The catalyst electrode is composed of MnO and carbon pressed on a nickel mesh current collector. Nickel wire is wrapped around the mesh to create an electric lead

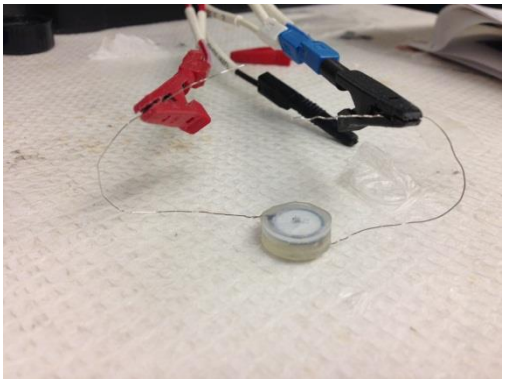

Figure 5.2.2: Cell fashioned from polyethylene container. Cathode is visible on top, anode is below.

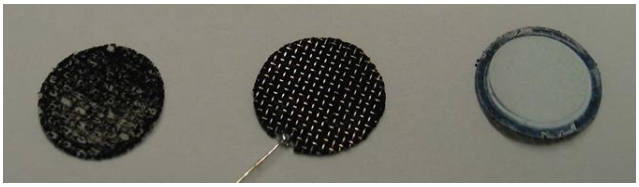

Figure 5.2.3: Components of a commercial air cathode. Separator (left), carbon/MnO_2 catalyst pressed on nickel mesh (center) and Teflon gas diffusion layer (right).

to the cathode. Holes are punched through a polyethylene cap similar to the one used to shape the anode, and the cathode is positioned at the top. Electrolyte is then introduced to the anode, and the cap is placed on the cell. Five minute epoxy may be used to seal the cell around the edges.

Characterization. A potentiostat (VMP3, Biologic USA) was used for all electrochemical characterization. Commercial zinc-air batteries (Energizer 675 & 13) were discharged for comparison. 3D electrodes were tested in a two-electrode arrangement. Measurements were taken by connecting the counter and reference electrode to the zinc anode, while the working electrode was connected to the air cathode. The cell was discharged at a pre-determined current in 6M KOH electrolyte [9] based on the estimated mass of zinc. Optical (Hirox) and electron microscopy (FEI) were used to image the zinc posts before and after discharge.

5.2.3 Results and Discussion

A 3D zinc anode was packaged and discharged using a commercial air cathode. The zinc anode was composed of 450 µm tall posts spaced 10 µm apart. The average diameter of the posts was 6 µm. The mass of the deposited zinc was estimated using the footprint area of the electrode. Using imaging techniques, it was estimated that the zinc was only deposited on

approximately 37.5% of the total electrode area, or about 0.25 cm^2 (Fig 5.2.4). The theoretical mass of zinc that should be deposited over 0.25 cm^2 at 100% yield is 8.9 mg. However, optical images can be used to estimate the yield to be about 45%, resulting in a mass of about 4.0 mg.

A few drops of electrolyte were introduced to the cell using a plastic pipette. Bubbles immediately formed upon electrolyte immersion, indicative of hydrogen evolution. The cell was then closed with a cap fashioned from a polyethylene tube and sealed using 5 minute epoxy. A current density of 0.28 mA/cm^2, or C/47 rate, was chosen as the discharge rate. A long, flat discharge profile typical of zinc air batteries is obtained (Fig 5.2.5). The voltage appears to be very stable at 1.0 V. The discharge capacity is 12.1 mAh/cm^2, which represents the highest areal capacity reported for a microbattery. This demonstrates the massive potential for zinc as an active material in batteries. The energy density is equivalent to 12.1 mWh/cm^2 when discharged at a power density of 0.28 mW/cm^2. It is interesting to note that the 3D MCMB battery obtained the same energy density (40 J/cm^2) due to the higher operating voltage of lithium ion batteries.

Discharged zinc posts are pictured in Figure 5.2.6. Optical images show the posts have

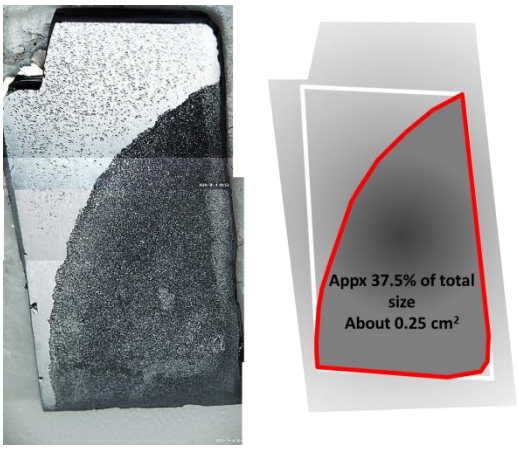

Figure 5.2.4: 3D zinc electrode before packaging and silicon etching. Dark region represents area of zinc deposition.

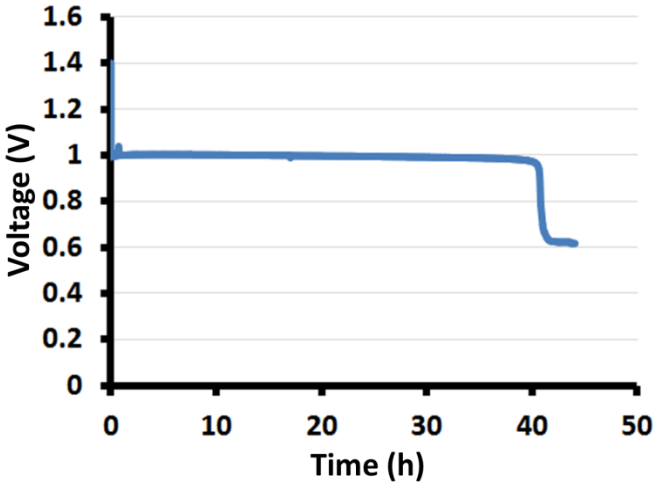

Figure 5.2.5: Discharge profile of 3D zinc-air battery at a current density of 0.28 mA/cm^2 or C/47 rate.

changed from gray to white. The dark coloring at the bottom of the posts suggests that the discharge process begins at the top of the posts. SEM reveals the extensive structural changes that zinc posts are subjected to during discharge. It is quite evident that the zinc oxide posts are much larger than the original zinc posts owing to the difference density between the two. The images also suggest the zinc has been completely discharged, supporting the theory of a top-down discharge process. It appears that the slow discharge rate allows the zinc and oxygen diffusion processes reach completion and retain the original post structure. It has been previously shown that fast discharge rates do not allow the system to reach equilibrium and creates hollow post structures due to the different diffusion constants of zinc in the metal and the oxide [10].

Commercial Energizer zinc air cells were discharged at C/100, C/70 and C/30 rates.

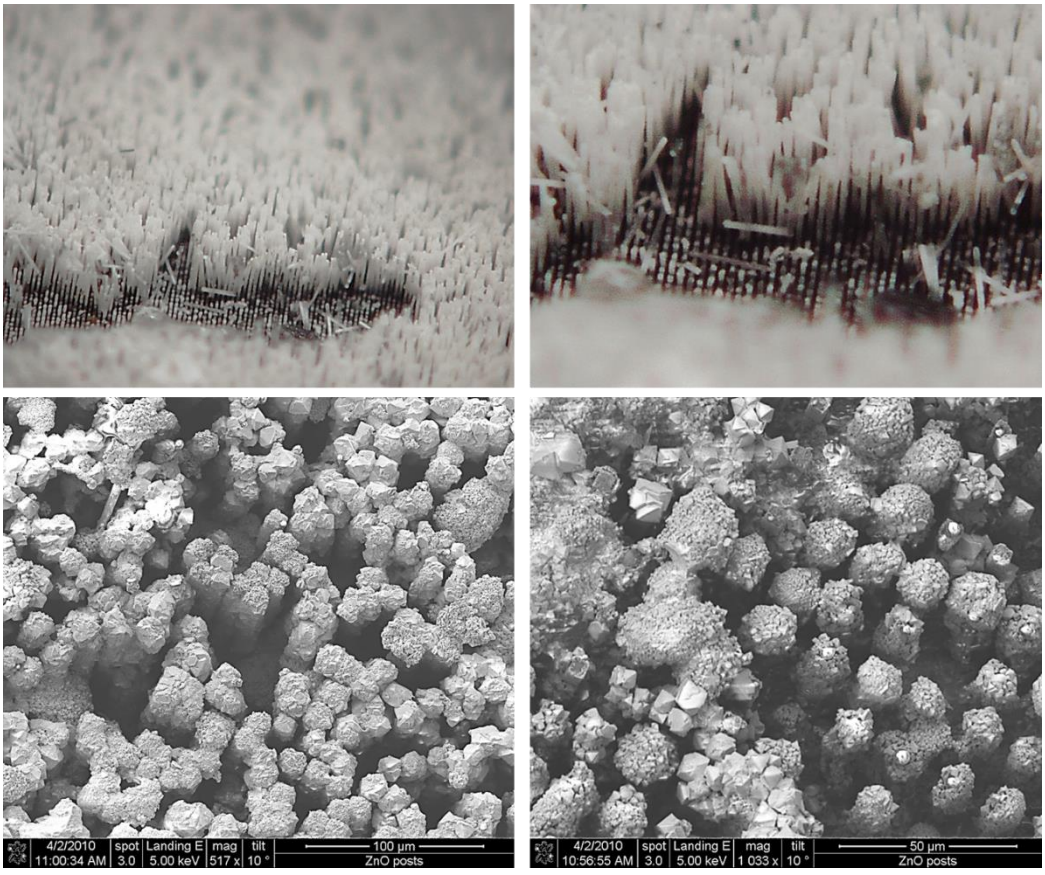

Figure 5.2.6: Discharged zinc posts imaged with optical (top) and electron (bottom) microscopes reveals dramatic changes in the microstructure.

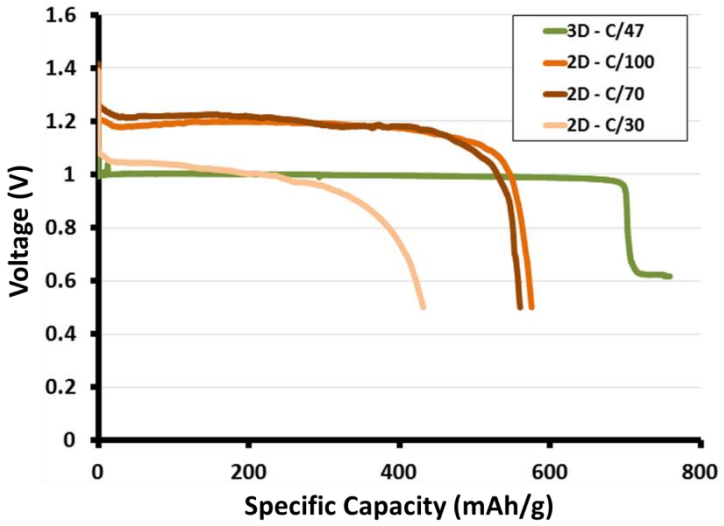

Figure 5.2.7: Specific capacity vs voltage discharge profiles comparing 2D cell and commercial zinc-air batteries. A 3D structure utilizes the zinc more efficiently.

Figure 5.2.7 compares discharge profiles of the three commercial cells and a 3D zinc cell. It can be seen that the commercial powder anode suffers from massive material utilization loss at rates faster than C/70. Even at a C/100 rate, the commercial anode only obtains 560 mAh/g, or 68% of the theoretical capacity. Comparatively, the 3D anode obtains 759 mAh/g, or 93% of the theoretical capacity. This translates into a specific energy of 760 Wh/kg normalized to the mass of zinc. This is also much larger than the commercial cells which only achieved a high of 692 Wh/kg. The high material utilization is attributed to the fact that the zinc structures are constantly in electrical contact with the current collector. During discharge, the post maintains a conductive zinc core that acts as a direct path for electrons. Furthermore, the posts do not suffer from large resistances because of the conductive nature of metallic bonding. Therefore, it is believed that the 3D zinc electrode, unlike the 3D MCMB electrode, structure can sustain large current densities. Unfortunately, the low operating voltage of the 3D zinc electrode results in a power that is on par with the commercial cells. A summary of the physical and discharge properties for all zinc-air cells can be found in Table 5.2.1.

	3D - N	Energizer 1	Energizer 2	Energizer 3
Mass (g)	0.004	0.825	0.34	0.34
Volume of Zinc (mL)	0.00056	0.115546	0.047619	0.047619
Voltage (V)	1	1.2	1.2	1
Area (cm^2)	0.25	1.06	0.466	0.466
Current Density (mA/cm^2)	0.28	6.23	7.94	17.2
Current Density (mA/g)	17.5	8.0	10.9	23.5
Areal Capacity (mAh/cm^2)	12.2	435.8	420.6	315.5
Volumetric Capacity (mAh/mL)	5426.4	3998.4	4116.0	3087.0
Gravimetric Capacity (mAh/g)	760.0	560.0	576.5	432.4
Energy Density (mWh/cm^2)	12.2	523.0	504.7	315.5
Energy Density (Wh/L)	5426.4	4798.1	4939.2	3087.0
Specific Energy (Wh/kg)	760.0	672.0	691.8	432.4
Power Density (mW/cm^2)	0.28	7.5	9.5	17.2
Power Density (W/L)	125.0	68.5	93.2	168.0
Specific Power (W/kg)	17.5	9.6	13.1	23.5

Table 5.2.1: Summary of physical and discharge properties of 3D and commercial zinc-air batteries

The low discharge voltage may be explained by the presence of a thin silicon dioxide layer left on portions of the zinc. This layer would act as a kinetic barrier to the zinc reaction thus pushing the potential more negative. The SiO_2 layer would also protect the zinc from corrosion, explaining why the cell did not fail early in the discharge like other 3D samples. However, since KOH etches SiO_2, zinc would gradually be exposed during the discharge process.

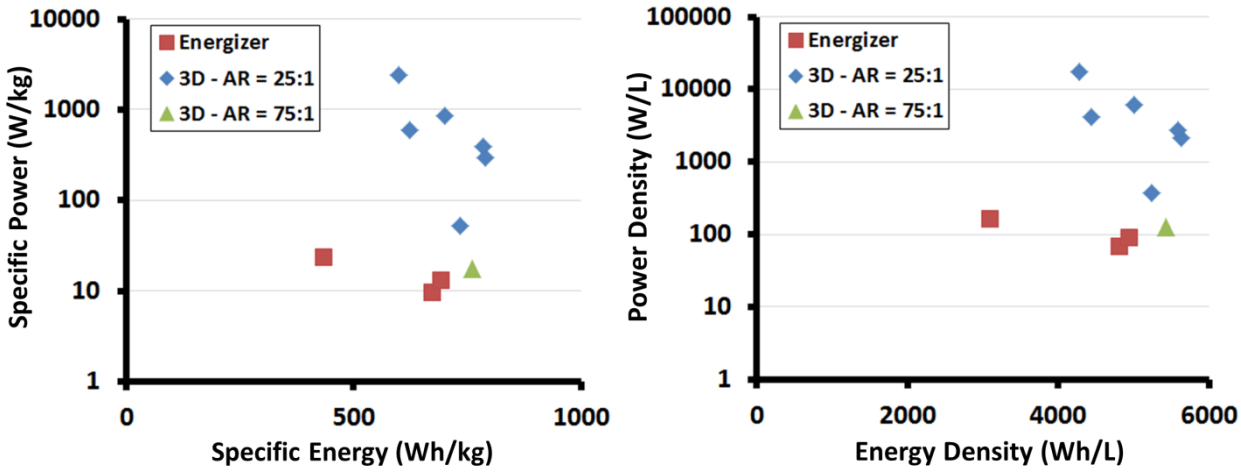

Figure 5.2.8: Zinc-air Ragone plot normalized by mass of active zinc (left) and volume of active zinc (right)

Figure 5.2.8 shows updated Ragone plots comparing the discharge characteristics of commercial and 3D zinc air cells [11]. All data is normalized to the mass and volume of active zinc and does not take into consideration any of the cell packaging. Previous 3D data was obtained by Dr. Derek Min of Prof. Bruce Dunn's lab. Although the 75:1 aspect ratio 3D electrode obtained a larger capacity than the 25:1 electrodes, the low voltage restricted the new data point within the original 3D data points. Regardless, both plots clearly show that 3D electrodes are capable of utilizing the zinc more efficiently than commercial batteries.

5.3 Zinc Corrosion Inhibitors

5.3.1 Zinc Reactions in KOH

Zinc exposed to potassium hydroxide spontaneously oxidizes and releases two electrons at 0.2V vs NHE through the following reaction [12],

$$Zn + 4OH^- \leftrightarrow Zn(OH)_4^{2-} + 2e^- \quad 5.3.1$$

$$Zn(OH)_4^{2-} \leftrightarrow ZnO + H_2O + 2OH^- \quad 5.3.2$$

In a zinc-air battery, the electrons are used to reduce oxygen by,

$$O_2 + 2H_2O + 4e^- \leftrightarrow 4OH^- \quad 5.3.3$$

This reaction occurs at -1.4V vs. NHE to give a cell EMF of 1.6V. However, hydrogen evolution on zinc electrodes in KOH occurs at -0.8V vs NHE through the following reaction [13],

$$2H_2O + 2e^- \leftrightarrow H_2 + 2OH^- \quad 5.3.4$$

This is equivalent to a corrosion reaction and can limit a battery's available energy density as well as its shelf life. Hydrogen gas evolution on zinc is typically slow enough to ignore when needed for immediate use. However, for long term storage, commercial companies saturate the electrolyte with zincate and alloy the zinc with other inactive metals known to have large hydrogen overpotentials, such as mercury.

High aspect ratio zinc rods improve the kinetics of hydrogen evolution due to the large increase of surface area. Upon introducing the electrodes to electrolyte, hydrogen bubbles immediately form, indicative of a parasitic corrosion reaction. New methods are required to suppress gas evolution without the use of toxic or inactive materials. Recent research suggests organic polymer additives such as PEG600 may act as corrosion inhibitors by coating the surface of the electrode with long polymer chains [14] [15] [13]. This layer can prevent the electrolyte from reacting with the zinc, thus creating an overpotential for gas evolution. Previous reported

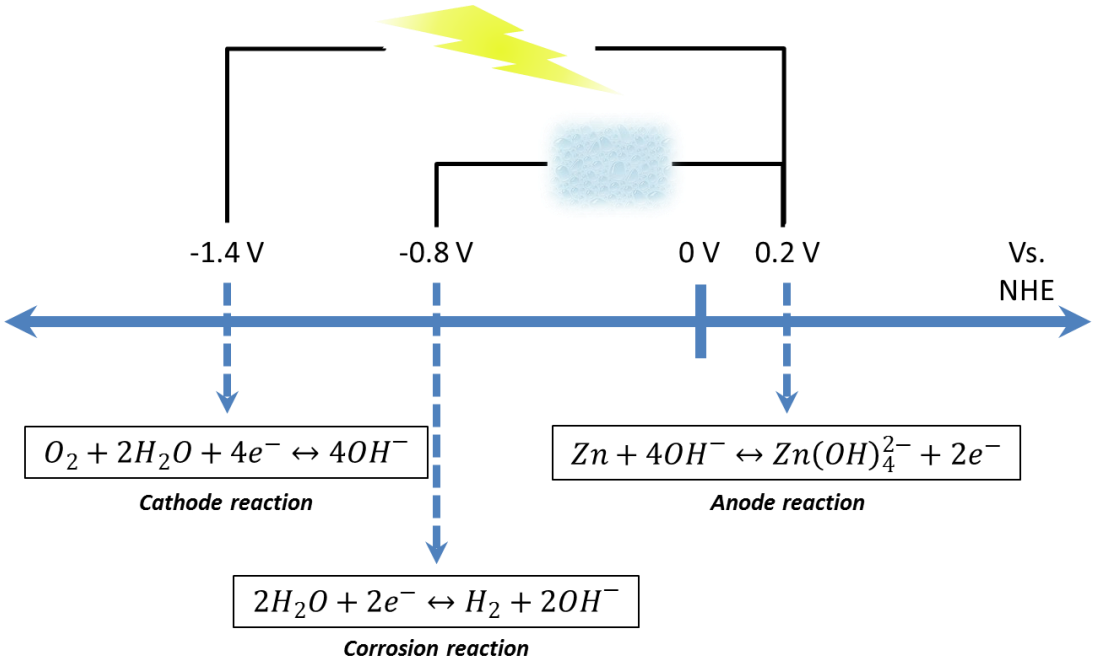

Figure 5.3.1: Potential scale showing source of competing reactions. The corrosion reaction is thermodynamically more favorable but kinetically less favorable than the cathode reaction. The high surface area of 3D zinc electrodes allows the corrosion reaction to also be kinetically favorable.

results had suggested a 0.2% solution of PEG600 in KOH yields the most favorable results. However, the electrolytes were also saturated with zincate molecules which can lead to Zn plating when polarized beyond -1.2V (Fig 5.3.1). Therefore, a more in depth study is required to determine the corrosion inhibitor properties of such additives.

5.3.2 Tafel Extrapolation

As discussed earlier, the Butler-Volmer (BV) equation describes the current response of a polarized reversible electrode undergoing a redox reaction. In the limiting case of large overpotentials, the BV equation can be simplified to its respective anodic and cathodic currents [7],

$$i = i_o exp\left(\frac{\alpha z F \eta}{RT}\right) \qquad 5.3.5$$

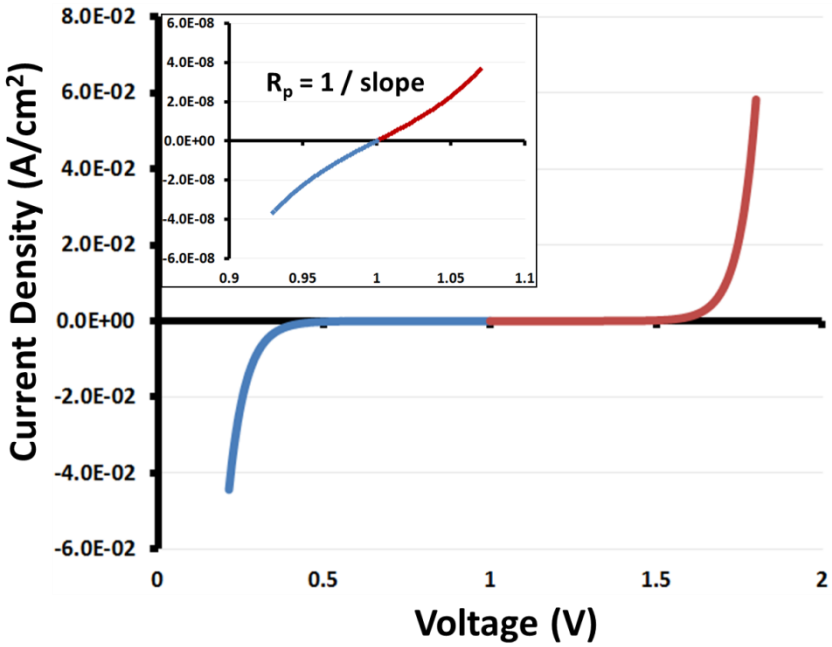

Figure 5.3.2: Hypothetical **l**inear polarization curves for negative sweep (blue) and positive sweep (red). Inset shows linear relationship for low overpotentials which can be used to determine polarization resistance.

$$i = i_o exp\left(-\frac{(1-\alpha)zF\eta}{RT}\right) \quad 5.3.6$$

Solving for overpotential yields the Tafel equation

$$\eta = a + b\log(i) = b\log\left(\frac{i}{i_o}\right) \quad 5.3.7$$

where

$$a = -2.3\frac{RT}{\alpha zF}\log(i_o) \quad 5.3.8$$

$$b = 2.3\frac{RT}{\alpha zF} \quad 5.3.9$$

for anodic currents and

$$a = 2.3\frac{RT}{(1-\alpha)zF}\log(i_o) \quad 5.3.10$$

$$b = -2.3\frac{RT}{(1-\alpha)zF} \quad 5.3.11$$

for cathodic currents. In both instances, b is known as the Tafel slope [16].

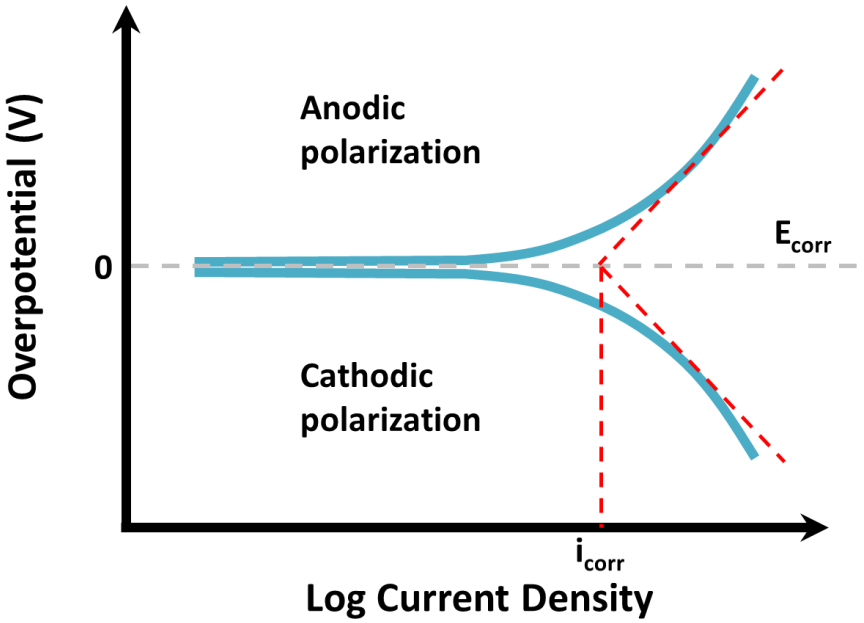

Figure 5.3.3: Stern diagram displaying method for determining corrosion current

Linear polarization experiments yield curves that look like those in Figure 5.3.2. The linear response at low overpotentials can be used to determine the polarization resistance, as shown in the inset. A Stern diagram (Fig 5.5.3) can then be used to estimate the corrosion current and potential [17]. The slopes of the linear regions at high overpotentials represent the Tafel slopes for the respective reaction. For a one-electron process where $\alpha = 0.5$, Tafel slopes should be about 118 mV/decade. In practice, Tafel slopes fluctuate due to mixed potentials of multiple reactions [16]. The intersection of the anodic and cathodic Tafel slopes yields the corrosion current, as shown in Figure 5.3.3.

5.3.3 Experimental

Linear sweep voltammetry experiments were performed on a three electrode cell connected to a potentiostat (VMP3, Biologic USA). Zinc foil and platinum mesh were used for the working and counter electrode, respectively. The surface of the zinc foil was scratched using

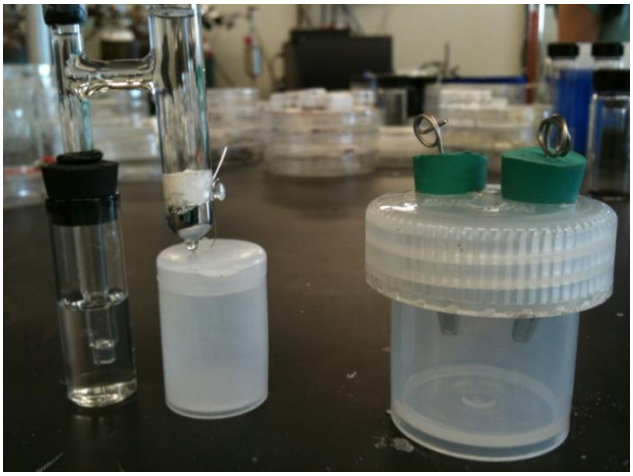

Figure 5.3.4: Experimental setup for linear polarization experiments. Saturated calomel reference electrode is on the left, testing cell is on the right.

a dremmel and subsequently cleaned using various solvents. A saturated calomel electrode (SCE) was used as the reference electrode (Fig 5.3.4). A salt bridge was used to protect the porous Vycor frit at the end of the reference electrode. The frit of the salt bridge was replaced every six experiments to maintain an accurate voltage reading. A new zinc sample was used for every test, and the platinum was cleaned with various solvents between each experiment.

6M potassium hydroxide (KOH) was prepared by mixing KOH pellets in deionized water (DI). The necessary amounts of PEG 600 were added to make solutions of 0.2%, 1.0% and 3.0%. Solutions were then sonicated for 1 hour or until the PEG was dissolved. New electrolyte solutions were prepared every 7-10 days to ensure proper concentrations.

5.3.4 Results of Corrosion Inhibitor Experiments

Linear polarization experiments were performed to determine the inhibitor capabilities of various PEG600 concentrations. The reference, counter and working electrodes were saturated calomel (SCE), platinum mesh and zinc foil (0.5 cm^2), respectively. Samples were swept cathodically to -2.4V and anodically to -1.5V at a rate of 2 mV/s with an OCP step between each

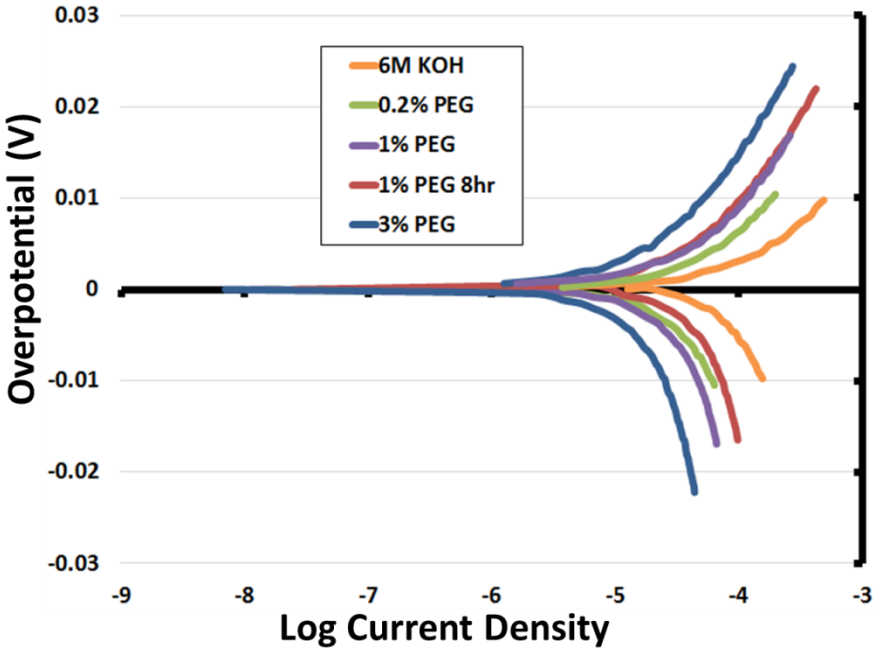

Figure 5.3.5: Stern diagram for linear sweep experiments testing corrosion inhibition properties of PEG 600 dispersed in 6M KOH

sweep. The platinum mesh was thoroughly washed using a sonication treatment alternating between acetone, water and isopropanol prior to each experiment. Approximately 8mL of 6M KOH was used as the electrolyte and purged with argon for at least 10 minutes. The appropriate amount of PEG600 was introduced to the KOH and allowed to disperse for at least 2 hours. For soaking experiments, electrodes sat in solutions of PEG600 and deionized water for the desired length of time. All graphs are the average of at least 2 experiments.

Stern diagrams for various PEG concentrations are shown in Figure 5.3.5. Using the methods described, the respective polarization resistance and corrosion current were determined for 6M KOH electrolyte solutions containing 0%, 0.2%, 1% and 3% PEG 600. Table 5.3.1 summarizes the corrosion inhibition properties. A pure KOH solution yielded a polarization resistance of 47.8 Ω and a corrosion current of 0.076 mA. As the PEG concentration is increased, the polarization resistance increases and corrosion current decreases, thus concluding PEG 600

Electrolyte Solution	Polarization Resistance (Ω)	Corrosion Potential (V)	Corrosion Current (mA)
6M KOH	47.8	-1.614	0.076
0.2% PEG	111.1	-1.582	0.018
1% PEG	135.1	-1.582	0.025
1% PEG 8 hr soak	112.4	-1.595	0.036
3% PEG	277.8	-1.603	0.015

Table 5.3.1: Summary of corrosion inhibition properties for solutions containing 0%, 0.2%, 1% and 3% PEG 600.

may be an appropriate gas suppressant when added to an aqueous electrolyte. The 3% PEG concentration displayed the most effective corrosion inhibition properties, increasing the polarization resistance by 480% and decreasing the corrosion current by 80%. Interestingly, it appears that soaking the electrode in a PEG solution prior to testing decreases the inhibitor properties of the polymer, as seen by the poor values obtained by the sample soaked in a 1% solution for 8 hours.

5.4 Conclusions

Zinc-air batteries have high energy density owing to the large specific capacity of zinc and the small, low weight air cathode. Commercial coin cells use a high surface area zinc powder to overcome the kinetic overpotentials associated with the chemical reaction. Unfortunately, this arrangement causes the cell to experience a gradual increase in resistance during discharge as zinc oxide forms around each particle. Unless discharged at extremely slow rates, the battery utilizes only a fraction of the available capacity.

A three-dimensional zinc air cell was fabricated using a commercial cathode and packaged in an epoxy unit. The 3D zinc posts were made through a combination of MEMS lithographic techniques and electrodeposition. The resulting electrode was composed of zinc posts 450 μm tall and 6 μm in diameter. When discharged at a rate of 0.28 mA/cm^2, the battery achieved a benchmark areal capacity of 12.1 mAh/cm^2 at an average voltage of 1.0V. This is equivalent to an energy density of 40 J/cm^2. When comparing material utilization efficiencies, the 3D electrode obtained 93% of the expected capacity whereas the 2D electrode only achieved 68% of the expected capacity when discharged at a slower rate. This is possible since the zinc posts have a direct electrical connection to the current collector by means of a solid metallic core. During discharge, the core remains intact until it is converted to zinc oxide. Unfortunately, the 3D electrode had an operating voltage of only 1.0 V, compared with the 1.2 V of the commercial battery.

The high surface area 3D zinc electrodes are susceptible to corrosion side reactions with the electrolyte. This is evident by the formation of hydrogen gas bubbles upon introducing the electrolyte. PEG 600 was investigated as an organic additive that may act as corrosion inhibitor.

Using linear sweep voltammetry and Tafel analysis, it was determined that adding any amount of PEG 600 increases the polarization resistance, with a maximum occurring at a concentration of 3%.

It has been shown that a 3D zinc array has superior discharge characteristics to a commercial cell. Unfortunately, the methods of preparing the electrode are not capable of including the typical corrosion inhibitors. The addition of PEG into the electrolyte solution has been shown to be a possible simple solution to this problem. Zinc air cells have the potential to impact a large portion of the battery market. Before this can happen, we must learn to engineer the cells in a way that takes advantage of the battery chemistry rather than compensate for it. Three dimensional cells take a giant first step in this direction.

5.5 References

[1] C. Daniel and J. Besenhard, The Handbook of Battery Materials, Wiley-VCH, 2011.

[2] R. Huggins, Advanced Batteries: Materials Science Aspects, Springer, 2009.

[3] E. Sayligan, T. Kukrer, G. Civelekoglu, F. Ferella, A. Akcil, F. Veglio and M. Kitis, "A review of technologies for the recovery of metals from spent alkaline and zinc-carbon batteries," *Hydrometallurgy,* vol. 97, p. 158, 2009.

[4] G. Zhang and X. Zhang, "MnO2/MCMB electrocatalyst for all solid state alkaline zinc-air cells," *Electrochimica Acta,* vol. 49, p. 873, 2004.

[5] S. Eom, C. Lee, M. Yun and Y. Sun, "The roles and electrochemical characterization of activated carbon in zinc air battery cathodes," *Electrochimica Acta,* vol. 52, p. 1592, 2006.

[6] F. Mansfeld and S. Gilman, "The effect of several electrode and electrolyte additives on the corrosion and polarization behavior of alkaline zinc electrode," *Journal of Electrochemical Society,* vol. 117, no. 10, 1970.

[7] A. Bard and L. Faulkner, Electrochemical Methods: Fundamentals and Applications, John Wiley and Sons, 2001.

[8] J. Cooper, "Powering future vehicles with the refuelable zinc/air battery," *Science and Technology Review,* vol. October, 1995.

[9] J. Gilliam, J. Graydon, D. Kirk and S. Thorpe, "A review of specific conductivities of potassium hydroxide solutions for various concentrations and temperatures," *International Journal of Hydrogen Energy,* vol. 32, p. 359, 2007.

[10] W. Wang, M. Dahl and Y. Yin, "Hollow nanocrystals through the nanoscale kirkendall effect," *Chemistry of Materials,* 2012.

[11] F. Chamran, H. Min, B. Dunn and C.-J. Kim, "Zinc-air microbattery with electrode array of zinc microposts," in *MEMS*, Kobe, 2007.

[12] J. Wang, Y. Horng, Y. Lin and R. Lin, "Effects of organic corrosion inhibitors on the electrochemical characteristics of zinc in alkaline media," *Corrosion,* vol. 64, no. 1, p. 51, 2008.

[13] G. Bereket, M. Gulec and A. Yurt, "Inhibition efficiencies of some organic compounds on the corrosion of zinc in alkaline media," *Anti-Corrosion Methods and Materials,* vol. 56, no. 1, p. 52, 2006.

[14] M. Auinat and Y. Ein-Ely, "Enhanced inhibition of zinc corrosion in alkaline solutions containing carboxylic acid modified PEG," *Journal of Electrochemical Society,* vol. 152, no. 6, 2005.

[15] Y. Ein-Eli and M. Auinat, "The behavior of zinc metal in alkaline solution containing organic inhibitors," *Journal of Electrochemical Society,* vol. 150, no. 12, 2003.

[16] G. Kear and F. Walsh, "The characteristics of a true Tafel slope," *Corrosion and Materials,* vol. 30, no. 6, 2005.

[17] N. Perez, Electrochemistry and Corrosion Science, Kluwer Academic Publishers, 2004.

Chapter 6

CONCLUSIONS AND FUTURE DIRECTIONS

It is apparent that today's batteries fall short of the energy and power requirements for mobile electronics. Three-dimensional batteries address this issue by renovating traditional battery designs to include nonplanar interfaces. Manipulating feature sizes to control transport distances and mass loadings can maximize a battery's performance without the costly and time-consuming process of developing new materials. Many 3D electrode designs have demonstrated superior qualities compared to 2D electrodes. Despite the few full 3D batteries that have been realized, the promise of high power and energy is enough to ensure a promising future for the technology.

Unlike most three dimensional electrodes in literature, the 3D concentric tube design does not require the presence of inactive scaffolding materials to provide the three-dimensional structure. By including only typical battery components, we can ensure the highest possible energy density. In addition, the ordered structure allows us to accurately estimate the loaded energy density based on the geometry and size of the 3D features. In fact, it is possible to prepare an electrode with a desired capacity using more than one structural blueprint. The concentric tube design is also compatible with any other active materials that can be prepared as a slurry. Therefore, it is possible to introduce new, high-capacity materials into the fabrication process as they are developed. This ensures sustainable long-term processing that is required for mass production.

Three dimensional carbon electrodes were fabricated using traditional MEMS techniques. Probe measurements revealed that individual post resistivity was higher than that of conventional electrodes but should have little effect on the electrochemical performance at low currents. 3D electrodes exhibited areal capacities up to 8.1 mAh/cm^2 at current densities much greater than those advertised for commercially available batteries. When compared to planar electrodes tested under similar conditions, 3D electrodes provided over 600% more areal capacity. The high surface area post structures proved to facilitate lithium intercalation by preserving small diffusion distances normally associated with thin electrodes. In doing this, mass loadings greater than 20 mg/cm^2 are possible. When assembled as a battery, the cell discharged an energy density of 40 J/cm^2 at power densities of 3.1, 0.71 and 0.35 mW/cm^2, proving that 3D electrodes can obtain high power without sacrificing energy.

A central theme of 3D batteries is the ability to increase the capacity of an electrode by layering material in a vertical fashion. This theory was tested by comparing electrodes with varying post heights and diameters. As expected, the electrode composed of the smallest posts obtained an average stable capacity of 1.2 mAh/cm^2 while the electrode with the largest posts obtained 2.7 mAh/cm^2. The electrode with feature sizes between the two achieved a stable capacity of 1.4 mAh/cm^2. It was determined that an important parameter for 3D electrode performance is network connectivity. Results showed that higher porosity slurries had lower specific capacities due to poor particle contact. It is apparent that keeping a dense, intact structure is more important than improving electrolyte penetration.

The assembly of a 3D concentric tube battery has been broken into three distinct steps. The most difficult step involves the conformal deposition of a solid electrolyte separator. A novel electrochemical technique has been shown to successfully characterize the quality of

various deposited films. When possible, these findings were supported visually through the use of electron microscopy. By effectively introducing the cathode material, a 3D concentric tube battery prototype was built, confirming the concept's feasibility.

Three dimensional electrodes may potentially lead to high power applications for zinc-air batteries. Restructuring the active zinc metal into vertically aligned rods ensures direct electronic connection with the current collector. This approach yielded a specific capacity of over 750 mAh/g at a C/47. In comparison, a commercial zinc air battery utilized only 560 mAh/g of material when discharged at half the rate of the 3D sample. It is evident that 3D electrodes can lead to more efficient zinc-air batteries. In addition, it was shown that controlling zinc corrosion for enhanced shelf-life may be as simple as adding the proper amounts of PEG600 to the electrolyte.

The presented results give a positive picture about the progress of 3D batteries. It has been shown that, of the many 3D designs that exist, the concentric tube strategy can obtain the highest energy density. However, issues regarding post resistivity and material utilization may place inherent limits on the battery structure. Therefore, it is important to evolve the design in ways that can overcome potential pitfalls.

Although the post resistivity should currently not drastically affect the electric potential distribution, it will eventually become a large source of ohmic loss. One method to increase the areal capacity without increasing the post resistance is to load the base of the electrode with material as well. This can be done by using slurry to attach the posts to the current collector instead of silver epoxy. An early attempt is displayed in Figure 6.1. This sample was prepared using high temperatures to fuse the posts to the thin carbon layer on the backside of the mold. The end result is a 3D carbon post electrode attached to a 60 µm thick carbon layer. This layer is expected to reduce the initial cycling anomalies associated with the silver epoxy and increase the mass loading and capacity.

One of the most discussed alternative designs involves a combination of the core-shell and concentric tube designs. In this case, one would sacrifice a small amount of electrode material and replace it with a metallic rod. Adding a 3D current collector would ensure a uniform

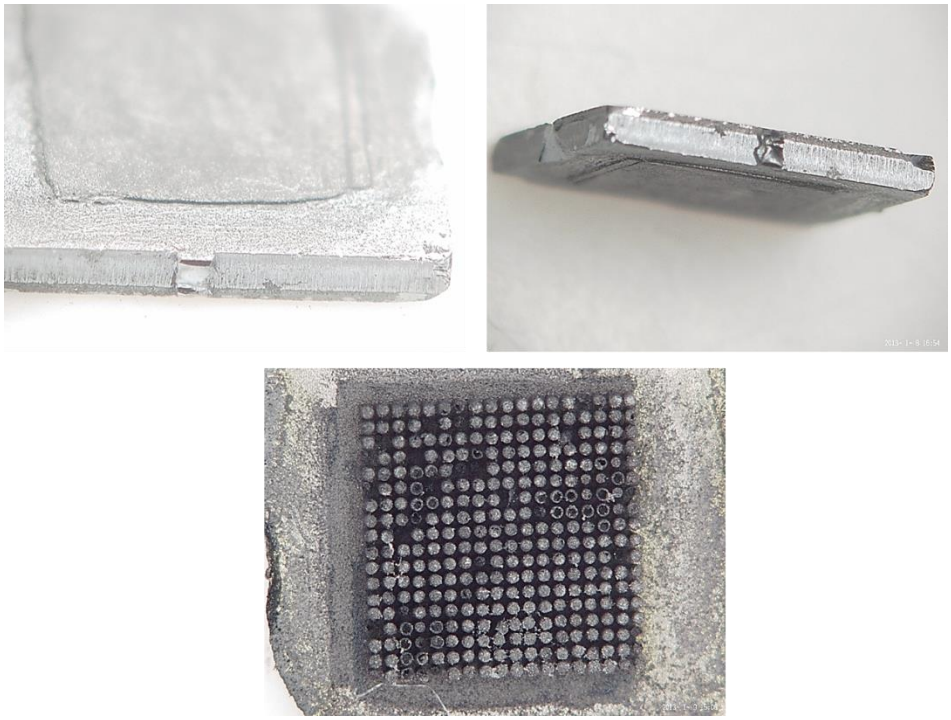

Figure 6.1: Carbon posts attached to current collector using 60 micron thick layer of carbon

current distribution along the length of the post and provide a direct highway for electron transport. Some of the sacrificed active material may potentially be compensated by using less conductive additive in the slurry. One possible way of building an electrode of this type is outlined in Figure 6.2. This process only differs from the current technique by three steps. Coincidentally, these steps are the exact same methods for fabricating 3D zinc posts. However, instead of anodizing the mold in HF to form the initial silicon channels, one would use FDRIE. After electrodepositing copper into the channels, a second FDRIE step can be performed to create larger channels surrounding the metallic posts. The large channels can then be filled with slurry using vacuum infiltration. The final step remains as a XeF_2 etch. Although an expensive approach, it can provide insight to the effects of a 3D current collector on the electrochemical performance of a post array.

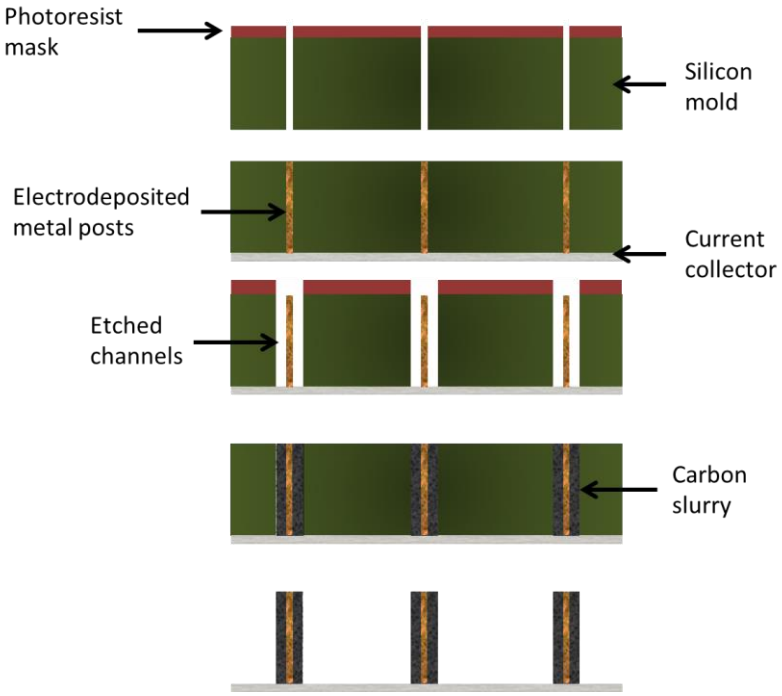

Figure 6.2: Proposed method for fabricating 3D post array with 3D current collector

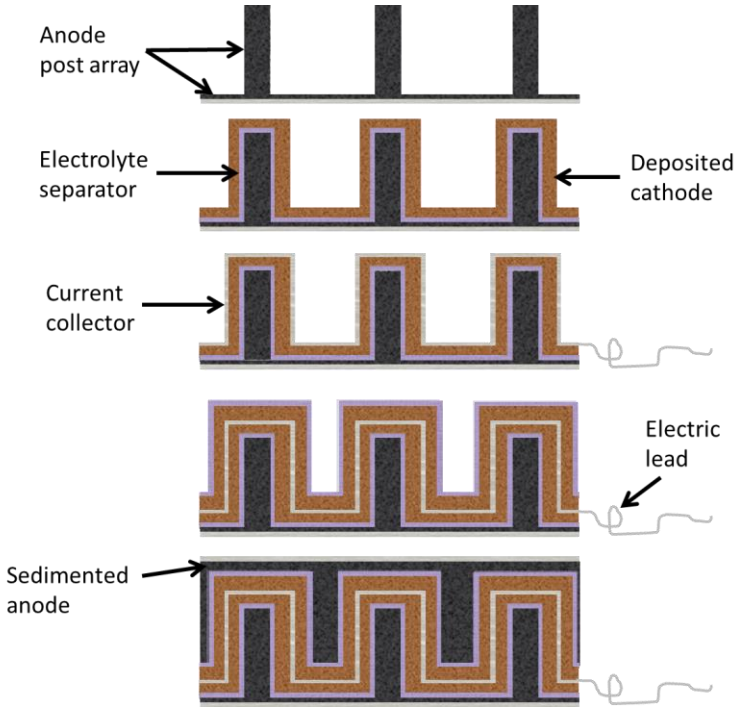

Figure 6.3: Proposal for possible packaging of two 3D concentric tube cells

It may be that inherent limits on material utilization are part of the post array design. With a slight modification, it may be possible to overcome these limits by incorporating two cells in one package (Fig 6.3). This would require the deposition of cathode material around the existing post structure rather than sedimentation throughout the entire volume. The next step would involve depositing a thin current collector and attaching a lead. The process would then be repeated in reverse, ending with sedimentation of the anode. This battery would avoid ohmic losses and large transport distances associated with an individual cell composed of posts the size of the cell. Connecting the cells in series or parallel would result in near identical energy densities as an individual cell. A battery of this type would be limited to the active materials that can be deposited in large quantities and by techniques that deposit conformal coatings.